Ph.D. Program in Civil, Chemical and Environmental Engineering

Curriculum in Chemical, Materials and Process Engineering

Department of Civil, Chemical and Environmental Engineering

Polytechnic School, University of Genoa, Italy.

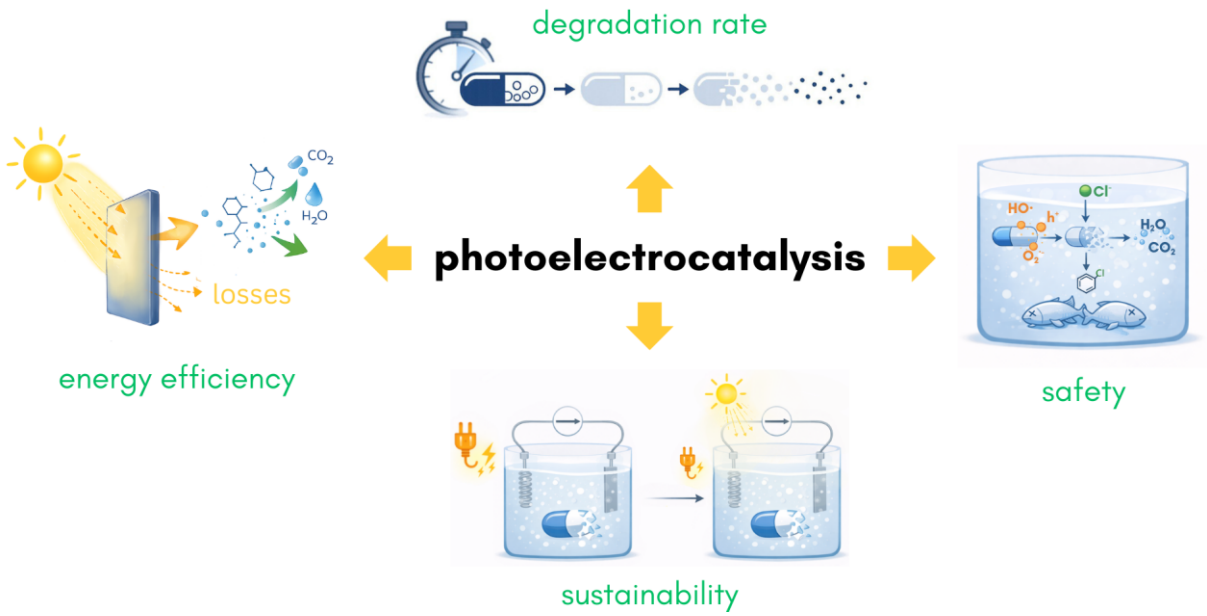

Investigation of Applicability of Photoelectrocatalysis towards Oxidation of Pharmaceutical Pollutants

Ekaterina Skolotneva

INVESTIGATION OF APPLICABILITY

OF PHOTOELECTROCATALYSIS TOWARDS OXIDATION

OF PHARMACEUTICAL POLLUTANTS

BY

EKATERINA SKOLOTNEVA

Dissertation discussed in partial fulfillment of
the requirements for the Degree of

DOCTOR OF PHILOSOPHY

Civil, Chemical and Environmental Engineering
curriculum in Chemical, Materials and Process Engineering,
Department of Civil, Chemical and Environmental Engineering, University of Genoa, Italy

May, 2026

Adviser(s):

Prof. Marco Panizza – Department of Civil, Chemical and Environmental Engineering, University of Genoa

Prof. Davide Clematis – Department of Civil, Chemical and Environmental Engineering, University of Genoa

External Reviewers:

Prof. Emmanuel Mousset – GEPEA - GEnie des Procédés Environnement – Agroalimentaire
Nantes University

Prof. Salvador Cotillas Soriano – Department of Chemical Engineering and Materials
Complutense University of Madrid

Examination Committee:

Prof. Elisabetta Finocchio (President and Internal Member) – Department of Civil, Chemical and Environmental Engineering
University of Genoa

Prof. Amirreza Khataee – Department of Chemical Engineering
Royal Institute of Technology (KTH)

Prof. Monica Puccini – Department of Civil and Industrial Engineering
University of Pisa

Prof. Ignacio Sirés Sadornil – Department of Materials Science and Physical Chemistry
University of Barcelona

Ph.D. program in Civil, Chemical and Environmental Engineering

Curriculum in Chemical, Materials and Process Engineering

Cycle XXXVIII

ACKNOWLEDGEMENTS

I would like to acknowledge the University of Genoa for granting me a PhD scholarship that made my doctoral research possible. And I would like to express my sincere gratitude to all those who supported me during my doctoral studies and contributed, in different ways, to the completion of this dissertation.

I would first like to thank Professor Marco Panizza for serving as senior supervisor of this dissertation.

My deepest gratitude goes to my supervisor Professor Davide Clematis for his constant availability, generosity with his time, and unwavering support throughout every stage of my PhD. I am deeply grateful that he gave me the opportunity to experience the genuine joy of doing science without pressure and with full freedom. I feel very fortunate to have had Professor Clematis as my supervisor, and I believe that his guidance helped me grow as a researcher and shaped the kind of scientist I hope to become.

I am also pleased to thank the other professors of the Department of Civil, Chemical and Environmental Engineering – Professor Antonello Barbucci, Professor Maria Paola Carpanese, Professor Marina Delucchi, Professor Elisabetta Finocchio, and Professor Gabriella Garbarino – for their teaching, kindness, and readiness to help whenever needed.

I am thankful to my colleagues who made my everyday working life enjoyable and helped create such a positive and friendly atmosphere. First of all, I am especially grateful to Toni (Dr. Maria Assensio) and Davide (Dr. Cademartori), whom I met at the very beginning of my PhD and who patiently helped me start this journey. My special thanks go to Juan (Dr. Basbus) for his invaluable advice and wisdom. I would also like to thank Amir Yadzani for the sense of solidarity that came from being in a similar position. And I thank Sara (Dr. Massardo) and Alberto (Prof. Lagazzo), with whom I shared an office, for making it a pleasant place to work.

I would also like to express my sincere gratitude to my host supervisor at the University of Warsaw, Professor Magdalena Skompska, without whom a substantial part of this work would not have been possible. I am deeply grateful for her genuine involvement in my research project. Her responsiveness, kindness, and outstanding scientific guidance meant a great deal to me. I am thankful for everything she taught me and for the generosity with which she shared her knowledge and experience.

I would like to acknowledge the professors at the Medical University of Warsaw with whom I had the pleasure to collaborate during this work. I am especially grateful to Professor Grzegorz Nałęcz-Jawecki for his help with the toxicological tests. Although this area lies quite far from my own specialization, he was patient and took the time to explain everything to me in a clear and accessible way. I would also like to thank Professor Joanna Giebułtowicz for her help with the HPLC-MS/MS analysis and the subsequent interpretation of the data.

I am pleased to thank the many wonderful people I met during my stay in Poland. I am grateful to Kamila (Dr. Zarębska) for her help with the practical details of laboratory work and also for showing me around Warsaw. I am thankful to Aliaksei Bohdan for his help with physical methods of analysis. My sincere thanks go to Ewelina (Dr. Wierzyńska) for helping me with the organic chemistry that was particularly challenging for me.

And I thank my loved ones. I am grateful to my friends for bringing moments of lightness and distraction from work, and for allowing me, at times, to feel carefree. I would also like to acknowledge my family for the practical help that made my move at the beginning of my PhD possible.

Finally, I thank my partner, Igor. I believe that only he truly knows how difficult this journey has been for me. I am deeply grateful for his constant support and belief in me throughout these years. I am especially grateful for the way he encouraged me whenever I was afraid to aim higher than I thought I could. His support meant more to me than I can express.

ABSTRACT

Conventional wastewater treatment technologies are ineffective in removing persistent micropollutants, necessitating the development of advanced oxidation processes capable of achieving their efficient degradation. Among emerging approaches, photoelectrocatalysis has attracted increasing attention as a promising technology that combines electrochemical approach with solar energy utilization. In this context, the present thesis investigates the applicability of photoelectrocatalysis for the degradation of pharmaceutical pollutants, with a particular focus on understanding energy consumption, degradation mechanism and safety.

The thesis begins with a comprehensive theoretical overview of photoelectrochemical systems, highlighting the fundamental differences between photoelectrocatalytic and conventional electrochemical oxidation. Special emphasis is placed on the energetic advantage of photoelectrocatalysis, which arises from the decoupling of reaction thermodynamics from the applied external potential. Despite this, experimentally measured energy consumption data for photoelectrocatalytic degradation of organic pollutants remain scarce. This work addresses this gap by systematically evaluating the energy efficiency of photoelectrocatalytic pharmaceutical degradation and demonstrating energy consumptions below 3 kWh/m^3, with typical values around 1.5 kWh/m^3 for unmodified $BiVO_4$ photoanodes.

For the first time, the impact of this substitution of oxygen evolution reaction with organic oxidation on solar conversion efficiency of photoelectrochemical system is analyzed in detail, accounting for both thermodynamic and kinetic considerations. The results reveal that replacing water oxidation with a thermodynamically more favorable organic oxidation reaction leads to a decrease in solar conversion efficiency for a given photoanode. However, in this case faster reaction kinetics may allow to achieve higher photocurrents and, thus, higher product fluxes. Moreover, organic oxidation enables the use of photoanodes with narrower band gaps than those required for water splitting, allowing absorption of a larger fraction of the solar spectrum. The formation of key reactive oxygen species is also evaluated, demonstrating that hydroxyl radical generation at high fluxes is unlikely in unbiased photocatalytic systems.

Based on the results of literature review, $BiVO_4$ is selected as a model photoanode material for experimental investigations due to its suitable semiconductor properties. Despite these advantages, experimental removal percentages for various pharmaceuticals remain below 60% after two hours of treatment. Preliminary experimental analyses reveal that the performance of $BiVO_4$ is primarily limited by low intrinsic catalytic activity towards oxidation of organic compounds, which manifests itself as low faradaic efficiency even when the process is not controlled by mass-transfer, significant surface recombination resulting in current much lower than the maximum theoretical one, and photocorrosion.

To mitigate these limitations, surface modification of $BiVO_4$ with β-FeOOH is investigated as a strategy to improve hole extraction and photoelectrode stability. While this modification leads to a 1.5-2 times photocurrent increase and stability improvement, it unexpectedly results in reduced pharmaceuticals degradation rates (from 50.6% to 34.2% for paracetamol, from 64.0% to 54.6% for sulfamethoxazole, from 53.5% to 55.2% for carbamazepine) and higher energy consumption. Mechanistic analysis demonstrates that β-FeOOH preferentially enhances water oxidation kinetics rather than organic oxidation, thereby increasing competition between the two reactions. These findings underscore that photocurrent density alone is an insufficient metric for predicting photoelectrocatalytic performance.

Finally, the role of chloride ions in photoelectrocatalytic degradation is examined on sulfamethoxazole degradation. The presence of chloride significantly accelerates oxidation through the formation of reactive chlorine species, achieving complete degradation in 60 and 20 minutes at chloride concentrations 200 and 600 mg/L Cl^-, respectively. However, the formation of highly toxic chlorination products (including halogenated acetic acids) and toxicity increase were detected. A non-linear dependence of degradation pathways on chloride concentration is elucidated for the first time, highlighting the complexity of chlorination-assisted photoelectrocatalytic processes.

Overall, this thesis provides a critical and systematic evaluation of photoelectrocatalysis for pharmaceutical pollutant degradation, combining theoretical efficiency analysis with detailed experimental investigations. The results clarify fundamental limitations, challenge common assumptions regarding photocurrent-based performance metrics, and identify key design principles for future development of selective and energy-efficient photoelectrocatalytic systems.

INDEX

INTRODUCTION

Water pollution and water scarcity remain major obstacles to achieving United Nations Sustainable Development Goal 6 (Clean Water and Sanitation) and are expected to intensify as the global population grows toward approximately 9.7 billion by 2050, thereby increasing pressure on freshwater resources and wastewater infrastructure [1,2]. Recent WHO/UNICEF monitoring estimates that in 2024, 27% of the global population (2.2 billion people) lacked “safely managed” drinking-water services, defined as an improved source on premises, available when needed (i.e., without interruptions), and free from contamination [3].

The problem is further complicated by the emergence of persistent contaminants and contaminants of emerging concern (CECs) – a broad group that includes pharmaceuticals and personal care products, endocrine-disrupting chemicals, per- and polyfluoroalkyl substances (PFAS), pesticides, and other industrial additives that are increasingly detected in surface waters, groundwater, and treated effluents. Comprehensive reviews emphasize that many CECs occur at trace levels (often ng/L-µg/L), yet can still be biologically active, and their risk is amplified by continuous discharge, mixture effects, and the formation of by-products during treatment or in the environment [4].

A key challenge highlighted in the literature is that conventional wastewater treatment was not designed to fully remove such chemically diverse, often recalcitrant compounds, so residual micropollutants may persist in reclaimed water and receiving waters. In addition, commonly applied unit processes, – including biological treatment, physical separation steps (e.g., adsorption, filtration, coagulation), and conventional chemical oxidation, – often show intrinsic limitations, such as incomplete removal of dissolved micropollutants by purely physical methods, sludge generation and disposal requirements for sorption/coagulation-based approaches, limited biodegradability of toxic or biorefractory compounds in biological systems, and the need to handle and store reactive (potentially hazardous) oxidants in chemical oxidation schemes [5,6].

Consequently, recent review work increasingly frames advanced, oxidative polishing steps – e.g., catalytic and photo-driven advanced oxidation processes (AOPs) – as important options for degrading persistent organics and improving overall removal robustness, while also stressing the need for careful assessment of by-products and operational scalability [7,8].

Among advanced oxidation processes, photoelectrocatalysis (PEC) has attracted considerable attention over the past fifteen years. The fundamental principle of photoelectrocatalysis is illustrated in Figure I-1 [9]. In this process, a semiconductor-based and therefore photoactive electrode (a photoanode in the presented scheme) absorbs incident light. Absorption of photons induces the transition of electrons from the valence band to the conduction band, resulting in the generation of electron-hole pairs (Eq. I.1). The photogenerated holes may directly oxidize organic compounds (Eq. I.2) or oxidize water molecules or radical precursors (typically electrolyte salts) to form reactive oxidative radicals (Eqs. I.3 – I.8), which subsequently contribute to the degradation of organic pollutants. Simultaneously, the photogenerated electrons are transferred through an external circuit to the cathode, where they reduce hydrogen cations

produced during the oxidation of organic compounds. The application of an external electrical bias promotes charge separation by driving electrons toward the cathode and holes toward the photoanode/solution interface, thereby suppressing electron-hole recombination and enhancing overall process efficiency.

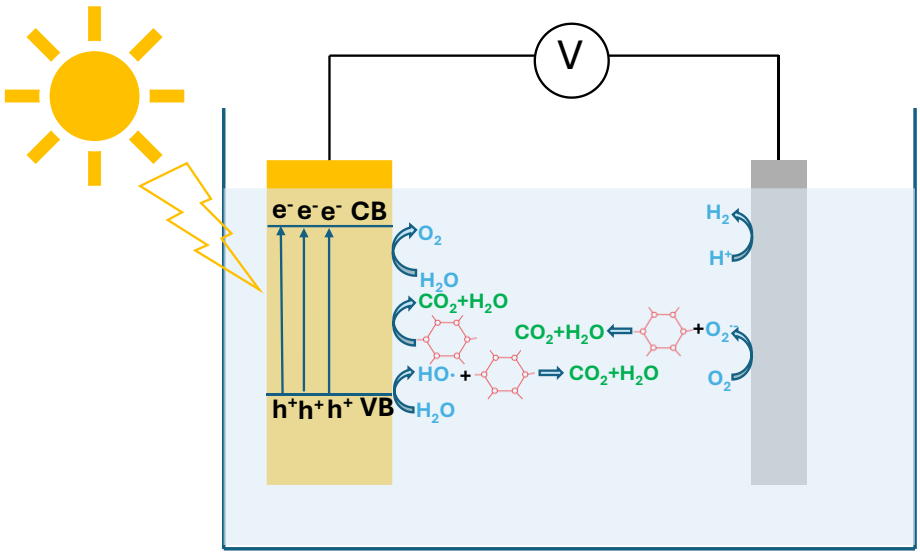

Figure I-1 Scheme of photoelectrocatalytic process.

Radicals that can be generated during photoelectrocatalysis are generally the same as those formed in other AOPs and, as mentioned above, depend on the nature of the precursor species present in the system. Among these, the most important reactive species are the hydroxyl radical ($HO^{\bullet}$) and the superoxide anion radical ($O_2^{\bullet-}$), which can be formed from water or dissolved oxygen (Eqs. I.3 and I.4). In the presence of sulfate ions – commonly used as supporting electrolytes – sulfate radicals ($SO_4^{\bullet-}$) may also be generated (Eq. I.5). In addition, chlorination reactions can occur during AOPs as a result of the oxidation of chloride ions, leading to the formation of reactive chlorine species (Eqs. I.6 – I.8).

$$Photoanode + h\nu \rightarrow h_{VB}^{+} + \overline{e}_{CB},\ h\nu > E_g \tag{I.1}$$

$$Pollutant + h_{VB}^{+} \rightarrow \ldots \rightarrow CO_2 + H_2O \tag{I.2}$$

$$h_{VB}^{+} + H_2O \rightarrow HO^{\bullet} + H^{+} \tag{I.3}$$

$$\overline{e}_{CB} + O_{2(aq)} \rightarrow O_2^{\bullet-} \tag{I.4}$$

$$h_{VB}^{+} + SO_4^{2-} \rightarrow SO_4^{\bullet-} \tag{I.5}$$

$$2h_{VB}^{+} + 2Cl^{-} \rightarrow Cl_{2(aq)} \tag{I.6}$$

$$h_{VB}^{+} + \frac{1}{2}Cl_{2(aq)} + H_2O \rightarrow HClO^{-} + H^{+} \tag{I.7}$$

$$3h_{VB}^{+} + \frac{1}{2}Cl_{2(aq)} + \frac{1}{2}H_2O \rightarrow HClO_2^{-} + 3H^{+} \tag{I.8}$$

Historically, photoelectrocatalysis was developed primarily for the water-splitting reaction [10], and to this day the majority of studies in this field have focused on photoelectrochemical water splitting for hydrogen production. Nevertheless, since the early 2010s, photoelectrocatalysis has also been increasingly investigated for the oxidation of organic compounds. This has been driven, on the one hand, by the motivation to replace the thermodynamically demanding and kinetically sluggish anodic water oxidation reaction with the thermodynamically and kinetically more favorable oxidation of organic matter. On the other hand, it has been motivated by the search for more energy-efficient alternatives to conventional electrochemical oxidation processes for organic contaminant removal. Under this approach, organic pollutants may act as sacrificial agents during hydrogen production, as they are easier oxidized at the anode with the concomitant release of protons, which are subsequently reduced at the cathode to produce hydrogen gas [11–13].

Photoelectrocatalysis can essentially be regarded as a combination of two technologies – photocatalysis and electrocatalysis and therefore exhibits several important advantages over each individual approach. A key advantage of photoelectrocatalysis over photocatalysis is the suppression of electron-hole recombination through the application of external electrical bias. This results in higher steady-state concentrations of reactive oxygen species and, consequently, in faster degradation rates and higher mineralization efficiencies. Furthermore, in conventional photocatalysis, catalysts are typically used in the form of nanoparticles dispersed in the reaction medium. In contrast, photoelectrocatalysis commonly employs photoactive materials synthesized as immobilized films on electrode substrates. This configuration is more practical, as it eliminates the need for photocatalyst recovery and separation, reduces the risk of secondary pollution associated with nanoparticle release, and enables the design of continuous-flow reactor systems [11].

Compared to conventional electrochemical oxidation, photoelectrocatalysis has an important advantage in terms of reduced energy consumption. The required external electrical bias is lower than that needed in purely electrochemical advanced oxidation processes, as the primary role of the applied bias is not to increase the overpotential of the oxidation reaction but to enhance electron-hole separation. This reduction in energy demand is widely emphasized as a key advantage of photoelectrocatalysis for sustainable wastewater treatment applications [14,15].

However, several key challenges limit the large-scale application of photoelectrocatalysis. The literature consistently identifies stability and scalability as the main constraints for practical implementation [12]. Issues such as photocorrosion, degradation of the active layer, gradual loss of catalytic activity, and insufficient mechanical stability and adhesion of the photoactive coating to the substrate remain characteristic of many photoelectrode materials. These limitations represent major barriers to practical deployment, as long-term stability and reproducibility under realistic water matrices are particularly critical for many systems [11,16]. In addition, the transition from laboratory-scale batch (“beaker”) experiments to flow-through or larger-scale systems introduces further challenges. These include non-uniform light distribution, optical losses, limitations in hydrodynamics and mass transfer, electrolyte resistance, electrode spacing, the need for membranes or compartment separation, and the selection of suitable window materials, with quartz-based components being costly. Collectively, these factors directly constrain the

performance and economic feasibility of photoelectrocatalytic systems for the degradation of organic contaminants.

The research presented in this work aims to advance the understanding of photoelectrocatalysis application for the oxidation of persistent organic contaminants. Accordingly, applicability is assessed in terms of degradation rate, energy efficiency, safety (non-toxicity) and sustainability. The following chapters are structured to address these assessment dimensions in a coherent theoretical-to-experimental progression.

The work begins with a concise overview of theoretical studies addressing the fundamental concepts of photoelectrochemical cells. This analysis is intended to clarify the origin of the energy advantage of photoelectrocatalytic systems compared to conventional electrochemical cells and to identify the key parameters that should be considered during material selection and process design. Subsequently, the most commonly employed photoelectrode materials are discussed with respect to their suitability for the photoelectrocatalytic oxidation of organic contaminants. In addition, a brief overview of state-of-the-art photoelectrocatalytic systems for organic pollutant degradation is provided in order to highlight current challenges and identify potential application areas for these photoanodes.

Chapter 2 presents a theoretical analysis of the limiting solar conversion efficiencies in photoelectrochemical systems in which organic oxidation is employed as the anodic half-reaction. The objective of this chapter is to numerically assess how replacing the conventional anodic water oxidation reaction with a thermodynamically and kinetically more favorable organic oxidation reaction affects the solar conversion efficiency. In addition, the solar conversion efficiencies of the formation of key reactive radical species are analyzed. To the best of our knowledge, such a comprehensive theoretical assessment has not been previously reported.

Chapter 3 motivates the selection of $BiVO_4$ as a reference photoanode material for subsequent investigations of photoelectrocatalytic organic pollutant degradation. This chapter provides a detailed electrochemical characterization of $BiVO_4$ and, through preliminary degradation experiments, demonstrates how performance-limiting factors manifest during photoelectrochemical degradation of organic pollutants and ultimately influence degradation efficiency. Based on these results, the main limitations that must be addressed to improve the organic degradation performance of $BiVO_4$ are identified. Furthermore, the influence of key operational parameters on both degradation rate and energy consumption is systematically investigated, and optimal conditions are determined for use in subsequent experimental studies.

Chapter 4 explores the modification of $BiVO_4$ to enhance its performance toward organic pollutant degradation. β-FeOOH was selected as a cocatalyst due to its environmental compatibility and its established relevance in both AOPs and photoelectrocatalysis. Although modification with β-FeOOH resulted in approximately a two-fold increase in photocurrent and a pronounced improvement in photoelectrode stability, the modified photoanode exhibited reduced organic oxidation performance under photoelectrocatalytic conditions compared to bare $BiVO_4$. A detailed mechanistic analysis is therefore conducted to elucidate this discrepancy. The results of this chapter demonstrate that, in the context of organic pollutant degradation, higher photocurrents do not necessarily correspond to higher degradation

efficiencies. Consequently, the competition between water oxidation and the target organic oxidation reaction is identified as a critical factor that must be carefully considered.

Chapter 5 investigates the influence of chloride ions on the photoelectrocatalytic degradation performance of $BiVO_4$ toward the pharmaceutical pollutant sulfamethoxazole, as well as on the toxicity of treated water samples. Using high-performance liquid chromatography-mass spectrometry (HPLC–MS), the transformation by-products formed during sulfamethoxazole oxidation are identified, and the effect of initial chloride concentration on the reaction pathways is examined. In addition, the ecotoxicity of treated samples is evaluated for both freshwater and marine ecosystems.

REFERENCES

1. UN, T.G.A. of U.N. Transforming Our World: The 2030 Agenda for Sustainable Development; 2015;
2. Unated Nations UN Population Deivision Data Portal Available online: https://population.un.org/dataportal/home?df=09ead4cb-eb3d-4e3d-8ad8-e0c4dc311503.
3. (WHO), W.H.O.; (UNICEF), U.N.I.C.E.F. Progress on Household, Drinking Water, Sanitation and Hygiene 2000-2024: Special Focus on Inequalities; 2025;
4. Li, X.; Shen, X.; Jiang, W.; Xi, Y.; Li, S. Comprehensive Review of Emerging Contaminants: Detection Technologies, Environmental Impact, and Management Strategies. Ecotoxicol. Environ. Saf. 2024, 278, 116420, doi:10.1016/j.ecoenv.2024.116420.
5. Martínez-Huitle, C.A.; Rodrigo, M.A.; Sirés, I.; Scialdone, O. Single and Coupled Electrochemical Processes and Reactors for the Abatement of Organic Water Pollutants: A Critical Review. Chem. Rev. 2015, 115, 13362–13407, doi:10.1021/acs.chemrev.5b00361.
6. Panizza, M.; Cerisola, G. Direct and Mediated Anodic Oxidation of Organic Pollutants. Chem. Rev. 2009, 109, 6541–6569, doi:10.1021/cr9001319.
7. Zhang, Y.; Zhang, X.; Wang, S. Recent Advances in the Removal of Emerging Contaminants from Water by Novel Molecularly Imprinted Materials in Advanced Oxidation Processes — A Review. Sci. Total Environ. 2023, 883, 163702, doi:10.1016/j.scitotenv.2023.163702.
8. Shahid, M.K.; Kashif, A.; Fuwad, A.; Choi, Y. Current Advances in Treatment Technologies for Removal of Emerging Contaminants from Water – A Critical Review. Coord. Chem. Rev. 2021, 442, 213993, doi:10.1016/j.ccr.2021.213993.
9. Palmisano, L.; Yurdakal, S. Photoelectrocatalysis. Fundamentals and Applications; Elsevier, 2023; ISBN 9780128239896.
10. Fujishima, A.; Honda, K. Electrochemical Photolysis of Water at a Semiconductor Electrode. Nature 1972, 238, 37–40, doi:10.1038/238038a0.
11. Fernandez-Ibanez, P.; McMichael, S.; Rioja Cabanillas, A.; Alkharabsheh, S.; Tolosana Moranchel, A.; Byrne, J.A. New Trends on Photoelectrocatalysis (PEC): Nanomaterials, Wastewater Treatment and Hydrogen Generation. Curr. Opin. Chem. Eng. 2021, 34, 100725, doi:10.1016/j.coche.2021.100725.
12. Sun, J.; Fu, C.; Hu, Z.; Sirés, I.; Zhou, M. Recent Advances in Photoelectrocatalysis for Simultaneous Water Purification, Energy Generation or Resource Recovery. Crit. Rev. Environ. Sci. Technol. 2025, 783–804, doi:10.1080/10643389.2025.2450128.
13. Rioja-Cabanillas, A.; Valdesueiro, D.; Fernández-Ibáñez, P.; Byrne, J.A. Hydrogen from Wastewater by Photocatalytic and Photoelectrochemical Treatment. JPhys Energy 2021, 3, doi:10.1088/2515-

7655/abceab.

14. Garcia-Segura, S.; Brillas, E. Applied Photoelectrocatalysis on the Degradation of Organic Pollutants in Wastewaters. J. Photochem. Photobiol. C Photochem. Rev. 2017, 31, 1–35, doi:10.1016/j.jphotochemrev.2017.01.005.
15. Olvera-vargas, H.; Pazos, M.; Bustos, E.; Deng, F.; Salazar-gonz, R. Recent Developments in (Photo)Electrocatalytic Materials for Wastewater Treatment and Resource Recovery. Appl. Catal. O Open 2025, 202, 207033, doi:10.1016/j.apcato.2025.207033.

CHAPTER I: LITERATURE REVIEW

1.1. ENERGETICS OF PHOTOELECTROCHEMICAL CELL

Here a brief overview of the energy diagram in a photoelectrochemical cell is presented.

The possibility of solar energy conversion is based on the ability of semiconductor materials to absorb light; therefore, in a PEC cell, at least one electrode must be a semiconductor. The configuration most often applied in water treatment – an n-type semiconductor used as the photoanode and a metal used as the cathode – is discussed here.

The most convenient way, although not the most familiar for an electrochemist, to describe the energetics of a photoelectrochemical cell is to use energy-level terminology (Figure 1-1).

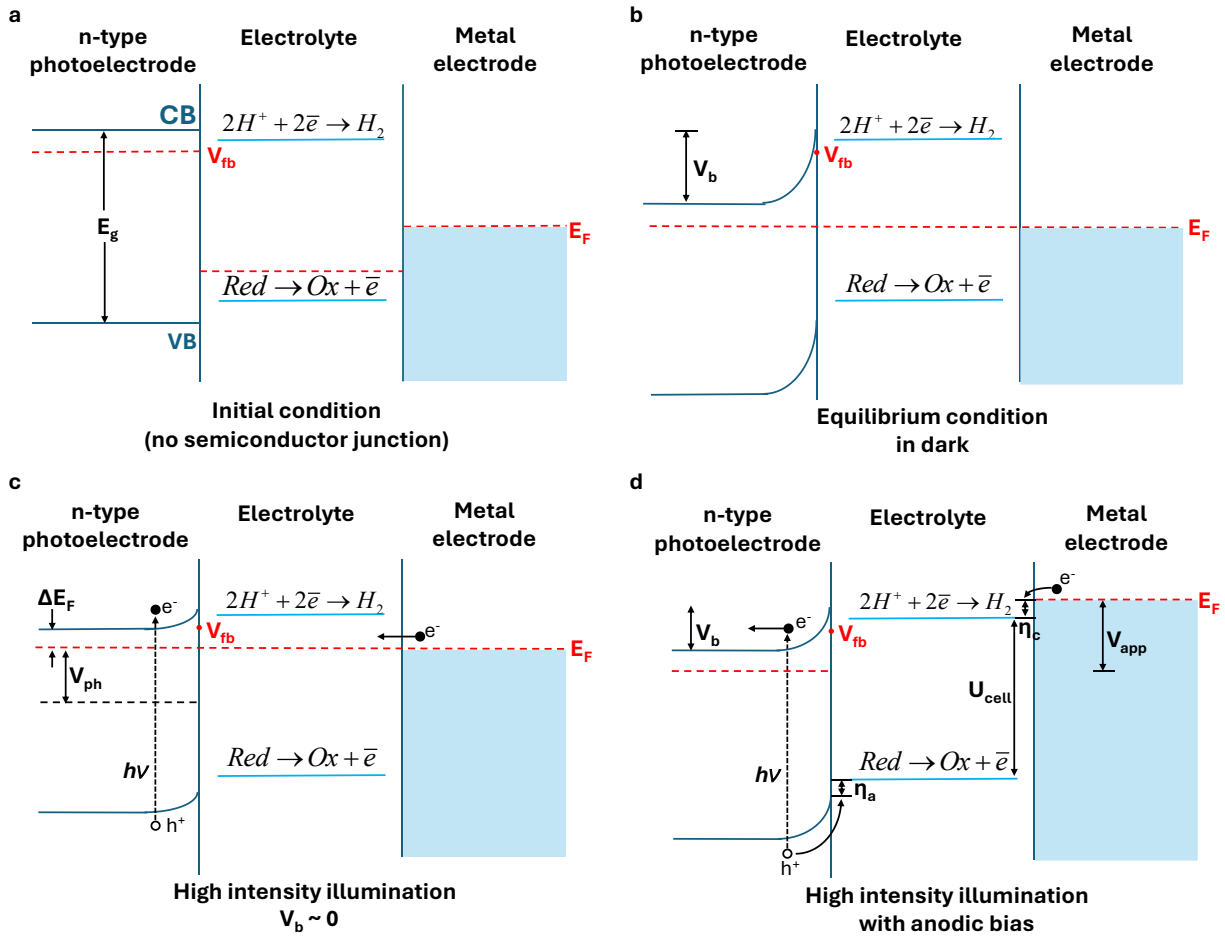

Figure 1-1 Sequence of energy level diagram for a semiconductor-metal photoelectrochemical cell from the initial condition (no contact and no chemical potentials equilibrium) (a) via equilibrium in dark (b) and under illumination without applied bias (c) to the final condition of photoelectrocatalysis with external bias.

Band theory describes how electronic energy levels are distributed in solids. In an isolated atom, electrons occupy discrete (quantized) atomic orbitals. When many identical atoms are brought together to

form a crystal, their outer orbitals overlap, and the electrons can no longer be assigned to a single atom. Because of the Pauli exclusion principle, two electrons in the whole crystal cannot occupy the same quantum state (except for opposite spin), so the originally degenerate atomic levels must split into many slightly different levels. As a result, each atomic orbital gives rise to a set of approximately N energy levels in a crystal containing N atoms. For macroscopic N, these levels become so densely spaced that they are conveniently treated as quasi-continuous energy bands. The band gap (E_g) forms because the overlap of atomic orbitals in a periodic crystal splits energies into separated bands, leaving an energy range with no allowed electronic states between them.

In semiconductor materials, filled energy states correspond to the valence band, whereas empty energy states correspond to the conduction band. In solid-state physics, the vacuum level is taken as the zero reference for energy. The band diagram of a semiconductor in vacuum is presented in Figure 1-1a. It is usually depicted by the conduction band minimum and the valence band maximum.

Another important concept depicted in Figure 1-1a is the Fermi level (E_F). Formally, it is defined as the energy of an electronic state whose probability of occupation is equal to 1/2 [1]. Practically, the Fermi energy of an electronic conductor, with respect to the lowest quantum state of the electron in vacuo is given by the negative of the work function, W, a quantity which can directly be measured by the threshold energy of photoelectron emission into vacuum: $E_F = -W$. Thus, Fermi level can be understood as electrochemical potential of electrons (Eq. 1.1). The difference between metals and semiconductors is determined by the position of the Fermi level. In metals, the Fermi level coincides with the maximum energy of electrons in the conduction band, whereas in semiconductor materials it is located between the conduction band and the valence band. In semiconductors, the position of the Fermi level is determined by the semiconductor type, its composition, temperature, and electrical potential (φ).

$$E_F = \bar{\mu}_e = \mu_e + e\varphi \tag{1.1}$$

where $\bar{\mu}_e$, μ_e, e are the electrochemical and chemical potentials of electrons and their electric charge, respectively. The term of Fermi level of electrons in solution was introduced to bridge the gap in terminology between solid state physics and electrochemistry by Gerischer [2]. In solution containing a redox couple (Eq. 1.2) at equilibrium conditions the electrochemical potential of electrons can be described by Eq. 3:

$$Ox + n\bar{e} \rightarrow Red \tag{1.2}$$

$$\bar{\mu}_e = \frac{\bar{\mu}_{Red} - \bar{\mu}_{Ox}}{n} \tag{1.3}$$

Taking into account the definition of the electrochemical potential (Eq. 1.4 and 1.5) and considering that the species are present in the same phase, so that the electrical potential component is identical, a complete expression for the electrochemical potential of electrons in solution can be obtained (Eq. 1.6):

$$\bar{\mu}_{Red} = \mu_{Red} + nF\varphi^{sol} = \mu^{\circ}_{Red} + RT\ln C_{Red} + nF\varphi^{sol} \tag{1.4}$$

$$\bar{\mu}_{Ox} = \mu_{Ox} + nF\varphi^{sol} = \mu^{\circ}_{Ox} + RT\ln C_{Ox} + nF\varphi^{sol} \tag{1.5}$$

$$\bar{\mu}_e = \frac{\mu_{Red} - \mu_{Ox}}{n} = \frac{\mu^{\circ}_{Red} - \mu^{\circ}_{Ox}}{n} + \frac{RT}{n}\ln\frac{C_{Red}}{C_{Ox}} \tag{1.6}$$

where $\bar{\mu}_{Red}$ and $\bar{\mu}_{Ox}$ are electrochemical potentials of reduced and oxidized species, μ_{Red}, μ_{Ox}, μ°_{Red} and μ°_{Ox} are their chemical and standard chemical potentials, C_{Red} and C_{Ox} are their concentrations, n is a number of transferred electrons, R is a gas constant, T is temperature.

Remembering that standard electrode potential of redox couple may be defined as $U^{\circ}_{Red/Ox} = \frac{\mu^{\circ}_{Red} - \mu^{\circ}_{Ox}}{nF}$ [3], a well-known Nernst equation can be derived:

$$\frac{\bar{\mu}_e}{F} = U^{\circ}_{Red/Ox} + \frac{RT}{nF}\ln\frac{C_{Red}}{C_{Ox}}\Bigg|\cdot\frac{F}{N_A e} \tag{1.7}$$

where F is Faraday's constant.

It is important to note that in Eq. (1.1), since it belongs to solid-state physics, all quantities are expressed as the energy required to transfer a single particle; therefore, the electrochemical potential has the dimension of electronvolts (eV). In Eq. (1.7), which is derived from the fundamental postulates of electrochemistry that operate with moles of species, potentials are expressed in volts, while the electrochemical potential is given in J/mol. In order to convert all quantities into electronvolts, Eq. (1.7) must be multiplied by $F/(N_A e)$, which is equal to unity (N_A is a Avogadro's number). Another important point is that, according to electrochemical convention, the standard electrode potential is measured relative to the reversible hydrogen electrode (RHE), whose potential is taken as zero. As mentioned above, in solid-state physics the zero potential is assumed to be in vacuum. Therefore, to translate electrochemical quantities into the language of solid-state physics, a correction of −4.44 eV must be applied, corresponding to the Fermi redox potential of H^+/H_2 couple [4].

$$E_{F,Red/Ox} = -4.4eV + E^{\circ}_{F,Red/Ox} + \frac{k_B T}{ne}\ln\frac{C_{Red}}{C_{Ox}} \tag{1.8}$$

where k_B is Boltzmann's constant.

Electrons in an electrolyte are localized on redox ions and are not free to move, in contrast to electrons in an electronically conductive phase, for which the concept of the Fermi level was originally introduced. However, the reduced species can be considered as occupied states, whereas the oxidized species can be considered as empty states. These two states possess different charges and, consequently, different energies. More precisely, the electronic energies of these states change continuously due to fluctuations of solvent dipoles, a phenomenon described by Marcus theory. As a result, the energy levels can be represented by Gaussian probability functions $W(E)$, corresponding to the density of states (DOS), as depicted in Figure 1-2 [5]. For identical concentrations of Ox and Red species, the probability distributions exhibit the same maximum (Figure 1-2a). The redox Fermi level is located at the intersection of the distribution curves, and electron transfer between the species involves fluctuations of the energy from the most probable values, represented by the distribution peaks, to the isoenergetic crossing point.

According to the Franck-Condon principle, an electron transfer occurs with the highest probability when the energy levels of the electron in the initial and final states are equal, so no energy loss occurs during the transition. This condition is satisfied because the timescale of electron transfer (~10^{-15} s) is much shorter than the timescale of solvent dipole reorganization (~10^{-13} s). Therefore, the Gerischer model assumes that electron transfer takes place from an occupied state in the metal or semiconductor to an empty state in the redox system with the same energy, or vice versa – from an occupied state in the redox system to an empty state in the solid. Within this approach, the rate of electron transfer (i.e., the number of single-electron transfer events per second) is determined by the density of energy states on both sides of the interface. Consequently, the rate constant is essentially governed by the relative positions of the energy states on either side of the interface [5–7].

For described case, since two redox couples are present in the electrolyte, the initial Fermi level in the electrolyte can be located anywhere between them, depending on the initial relative concentrations of H_2 and *Red* in the cell. For this schematic explanation, it can be assumed that it is slightly higher than the *Ox*/*Red* Fermi redox level.

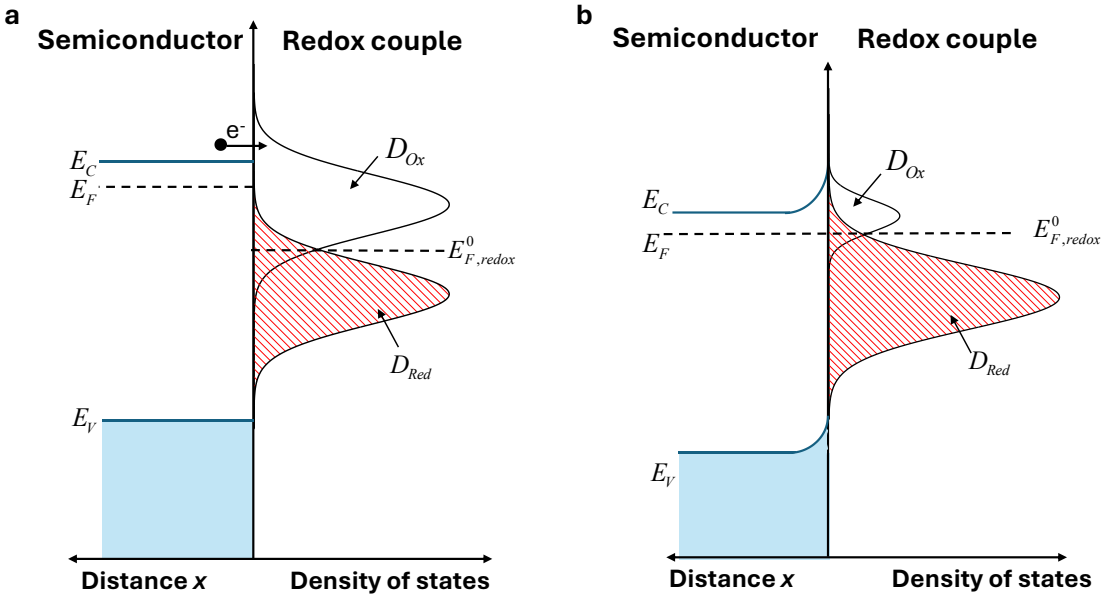

Figure 1-2 Electron transfer at the semiconductor–electrolyte interface. (a) n-type semiconductor before contact with a redox couple in solution at equal initial concentrations; (b) semiconductor–electrolyte interface after charge redistribution in the system and establishment of equilibrium.

When a semiconductor, a metal electrode, and a solution containing a redox couple are brought into contact (Figure 1-1b), the difference between their Fermi levels creates a gradient in the electrochemical potential and drives electron transfer toward the phase with the lower Fermi level. This process continues until the Fermi levels in all phases, i.e. the electrochemical potential of electrons, become equal, that is, until equilibrium is established (Figure 1-1b).

Because the density of states in the solution, metal, and semiconductor differs by several orders of magnitude (DOS_{Me}>>DOS_{sol}>>DOS_{SC}: 10^{23} cm^{-3} for metal, 10^{20}-10^{21} cm^{-3} for solution and 10^{15}-10^{19} cm^{-3} for semiconductor [8]), it can schematically be assumed that the equilibrated Fermi level of the system is

determined by the Fermi level of the metal. This assumption is justified because the relative change in electron concentration induced by electron redistribution in the system is negligible for the metal, small for the solution, and significant for the semiconductor.

Figure 1-2b shows how the Fermi level of the solution is changed. When oxidized species are reduced, their concentration is decreased and the concentration of reduced species is increased, thus, the interception point of energy distribution curves moves upward and the Fermi level in the solution is increased.

Because the semiconductor loses a fraction of its majority charge carriers under the action of the gradient of electrochemical potential of electrons, a depletion region (space-charge region) is formed near the surface. In this region, positively charged ionized lattice ions remain uncompensated by mobile electrons; therefore, local electroneutrality no longer holds and a space-charge region is established. The positive charge in the semiconductor space-charge region is balanced by a net charge of opposite sign in the electrolyte. This charge separation across the semiconductor-electrolyte junction gives rise to an internal electric field and an associated potential drop within the semiconductor. This potential drop increases the electrostatic barrier for further charge transfer and thus enables the establishment of equilibrium. The potential drop across the semiconductor space-charge region is commonly referred to as the band-bending potential (V_b), and it is equal to the difference between the initial Fermi levels in the semiconductor and the metal (or between the semiconductor and the solution).

It must be considered that, in general, variations induced by a change in the semiconductor potential do not affect the energies of the band-edge positions at the interface, which are therefore said to be pinned, unless surface states are not involved. Under these conditions, the entire potential change – caused by contact of the semiconductor with the solution, subsequent illumination, or application of an external bias – drops across the semiconductor space-charge region and results exclusively in band bending modification, while the potential drop across the Helmholtz layer remains unchanged [8,9].

When this system is illuminated (Figure 1-1c), the equilibrium is shifted. The reason is the generation of additional charge carriers: when the semiconductor absorbs photons with energies exceeding the band-gap energy, electron-hole pairs are generated. Under illumination, the hole concentration can increase by several orders of magnitude relative to dark conditions, whereas the change in electron concentration is negligible. The photogenerated holes are efficiently driven by the built-in electric field in the space-charge region toward the semiconductor-electrolyte interface, where they participate in interfacial processes and/or discharge negatively charged surface states and the charge at the electrolyte interface, while electrons are driven toward the bulk. This redistribution of charge carriers leads to a reduction of the space-charge region in the semiconductor and, consequently, to a decrease in the built-in electric field and the band bending.

On an energy diagram, this looks like an upward shift of the semiconductor potential, accompanied by a corresponding rise of the Fermi level, which is shifted by the same value due to the electric potential term in Eq. (1.1). Physically, the difference between the semiconductor potential in the dark and under illumination is defined as the photovoltage (V_{ph}): illumination reduces the electrostatic barrier in the space-charge region, causing the Fermi level in the semiconductor bulk to rise toward the flat-band potential (V_{fb}). The flat-band potential is defined as the potential at which no excess charge exists on the semiconductor side of the junction and, consequently, no in-built electric field is present. Therefore, it represents the maximum Fermi level attainable in the cell. It should be noted that, in Figure 1-1, the flat-band potential

lies below the redox Fermi level of the H^+/H_2 couple. Thus, even if illumination is sufficiently intense to completely flatten the bands, electrons transferred to the metal from the semiconductor conduction band do not possess enough energy to drive hydrogen reduction. As a result, the spontaneous process is not possible in this cell, and no photocurrent is recorded under these conditions.

In order to drive an electrochemical process in this cell, an external bias must be applied. Upon application of a voltage, both electrodes in the system are polarized. On the energy diagram, this is represented by further band bending in the semiconductor, corresponding to a downward shift of the semiconductor potential due to anodic polarization, and by an upward shift of the metal potential due to cathodic polarization. Supplying of an external voltage enables the energy of electrons in metal become sufficient for hydrogen reduction. After polarization, the Fermi levels in the different phases are no longer equal, which creates a gradient in the electrochemical potential of electrons and thereby induces the flow of electrical current [10].

Thus, an external bias must be applied to drive the photoelectrochemical process if:

1) Band gap is narrower than the potential difference between the cathodic and anodic reaction, i.e. required cell voltage ($E_g < U_{cell} = E_{F,Redox} - E_{F,H^+/H_2}$);
2) Flat band potential of n-type semiconductor (photoanode) is more positive than potential of cathodic reaction (or flat band potential of p-type semiconductor is less positive than potential of anodic reaction).

It should be noted that if the valence band of an n-type semiconductor is not sufficiently positive to drive the anodic reaction, the application of an external potential cannot compensate for this limitation, because it does not alter the band-edge positions. In this case, the process is not possible.

1.2. ORIGIN OF ENERGY GAIN IN PHOTOELECTROCHEMICAL SYSTEM COMPARED TO CONVENTIONAL ELECTROCHEMICAL CELL

Owing to the features of the photoelectrochemical cell, described in detail above, application of the photoelectrochemical process for the oxidation of organic pollutants can reduce energy consumption compared to a conventional electrochemical cell.

In a conventional electrochemical cell, an external bias is applied to provide cathodic electrons with sufficient energy to drive hydrogen reduction (or the reduction of other species) and to create free energy levels that can be occupied by electrons from reduced species at the anode, i.e., to ensure the oxidation reaction. In contrast, in a photoelectrochemical cell, provided that the valence-band position is favourable, photogenerated holes possess sufficient energy to oxidize reduced species even in the absence of an external bias. In this case, the role of the external bias is different: it supplies additional energy to electrons at the cathode to drive the reduction reaction and increases band bending, thereby enhancing electron-hole separation. Thus, the application of an external potential does not influence the oxidation reaction, since it does not shift the position of the valence-band edge [11]. Figure 1-3 illustrates that, in a conventional electrochemical cell, all the energy required to drive the electrochemical process is supplied exclusively by the applied external potential, whereas in a photoelectrochemical cell the major part of this energy is provided by solar illumination.

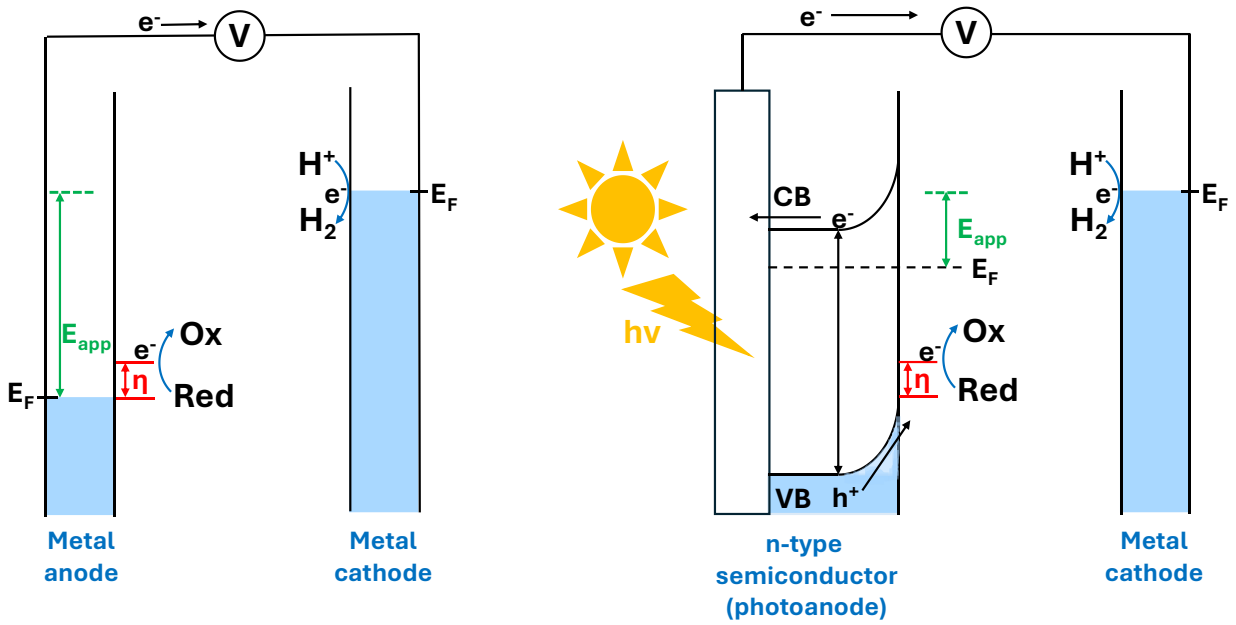

Figure 1-3 Schematic comparison of energy diagram of (a) conventional electrochemical cell and (b) photoelectrochemical cell.

1.3. CRITERIA FOR CHOICE OF SEMICONDUCTOR MATERIAL FOR IMPLEMENTATION IN PEC SYSTEM FOR WATER TREATMENT

Based on described above theoretical principles of PEC functionality the following criteria can be identified for choice of photoelectrode.

Thermodynamic feasibility

To ensure thermodynamical possibility of a semiconductor to drive an electrochemical reaction, semiconductor material with appropriate band edges should be chosen [10,12]. If the system employs photoanode, the bottom of its valence band should be enough positive to ensure direct oxidation of organic pollutant by holes, or generation of hydroxyl radicals (or other ROS). If the system employs photocathode, the top of conduction band should be negative enough to ensure hydrogen/oxygen or pollutant reduction.

Band gap should also be narrow enough to ensure sufficient light absorption and, thus, decent current density and fluxes of products both on anode and cathode. For other hand, it is well-known that semiconductors with narrower band gap suffer more from photocorrosion [13]. Therefore, a trade-off between high productivity and photostability should be optimized.

As described above, in the case of photoelectrocatalysis there is no strict requirement that both the valence band and the conduction band of the semiconductor must be positioned so as to enable both the anodic and cathodic reactions, nor is there a strict requirement that the band-gap width must exceed the required cell voltage. These conditions are mandatory for an unbiased photoelectrochemical cell, whereas upon application of an external bias both constraints become less stringent, allowing greater flexibility in

the choice of semiconductor material. Nevertheless, to minimize energy consumption, the selected semiconductor should be as close as possible to fulfilling these requirements.

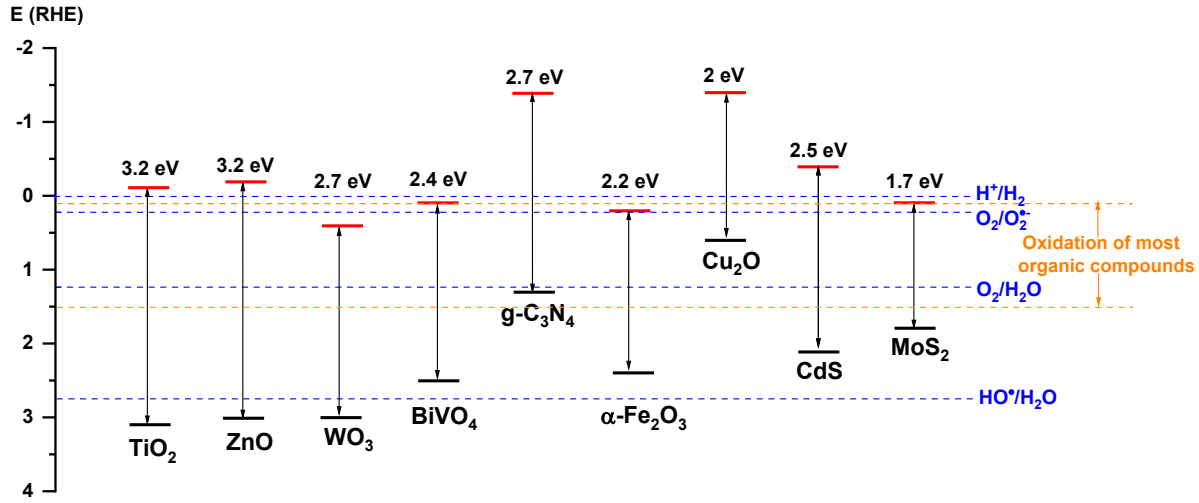

Figure 1-4 Band gap and band edge positions of different semiconductor materials. Data from [14,15].

Figure 1-4 shows the band-gap values and band-edge positions of the most commonly used photoactive materials. Analysis of this diagram allows the prediction that oxidation of organic compounds by photogenerated holes is thermodynamically possible on all the presented semiconductors. At the same time, the formation of hydroxyl radicals is thermodynamically feasible on only ZnO, TiO_2 and WO_3, since the valence-band edges of these semiconductors are located at potentials more positive than 2.73 V (vs NHE), which is required for the oxidation of H_2O to $HO^{\bullet}$. Due to the favourable position of the conduction-band edge, tuning of the Fermi level of the metallic cathode to enable hydrogen reduction is not required for ZnO, TiO_2, whereas small external potentials below 0.5 V are required to drive the cathodic reaction in the case of WO_3. Nevertheless, spontaneous operation on ZnO or TiO_2 is unlikely, since their band gap is approximately 3.2 eV and, consequently, they are able to absorb only about 3% of the standard solar spectrum, resulting in a maximum theoretical photocurrent of ~1 mA/cm^2. Moreover, it should be noted that water splitting, which is a parasitic reaction in the case of organic pollutant removal is thermodynamically possible on these semiconductors. In contrast, valence bands of Cu_2O and g-C_3N_4 are positioned too negatively to oxidize water (in the case of g-C_3N_4 this oxidation is thermodynamically allowed but unlikely due to the small overvoltage). In principle, they are capable of oxidizing organic pollutants by photogenerated holes without charge losses due to parasitic water oxidation.

Catalytic activity

Reaction rate of (photo)electrocatalyst system depends on two main factors: number of active sites in the system (electrochemically active surface area) and intrinsic catalytic activity of the material [16].

The electrochemical surface area (ECSA) is generally not an intrinsic property of a material but rather a design feature of the electrode architecture. The ECSA can be significantly increased through various

synthesis strategies, so that reasonable values can be achieved even for materials that do not initially possess highly developed surfaces. It should be noted that, in the photoelectrocatalysis literature, several families of semiconductor materials are repeatedly reported to exhibit high ECSA as a result of appropriate architectures, such as nanorods, nanotubes, nanowires, and nanosheets, including TiO_2, ZnO, WO_3, MoS_2, and g-C_3N_4 etc. It should also be noted that an increase in ECSA is typically achieved by reducing the grain size of the material. This reduction is beneficial for electron-hole separation when the characteristic grain size is smaller than the diffusion length of the minority charge carrier. However, it can negatively affect charge transfer, since transport across grain boundaries hinders overall charge transport, and light absorption, due to light attenuation at grain interfaces [17].

Oxidation of organic compounds can proceed either via their reaction with reactive oxygen species, the most important of which is the hydroxyl radical (HO•), or via direct electron transfer, i.e., direct oxidation by photogenerated holes [18]. Accordingly, when selecting a photocatalyst, one should focus either on promoting ROS formation reactions or on achieving specific selectivity toward a particular organic oxidation reaction.

Siahrostami et al. [19] developed a thermodynamic picture of the catalyst properties that determine selectivity towards one, two- or four-electron water oxidation leading to hydroxyl radical, hydrogen peroxide or oxygen formation, respectively. The results are presented in Figure 1-5a. They proposed a criterion for forming hydroxyl radicals is that the free energy of OH* on the catalyst surface is higher the free energy of HO•(aq) which is ~ 2.4 eV. Among all semiconductor materials for which authors made their calculations, the only one which is close to the region where formation of HO• is kinetically favourable is TiO_2, while other popular semiconductors like WO_3, $BiVO_4$, MnO_2 and SnO_2 are prone to hydrogen peroxide formation. This conclusion is widely evidenced in the experiments. It is interesting to note, that the DFT calculations of free energy diagram for water oxidation reaction on boron-doped diamond electrode gives the free energy of HO* formation equal to 2.83 eV, one more time proving excellent ability of this material to form free hydroxyl radicals (Figure 1-5b) [20].

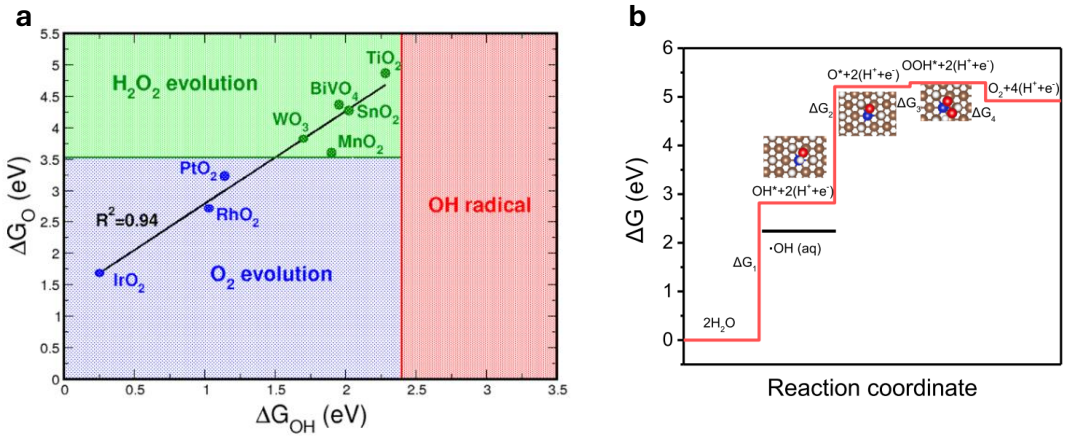

Figure 1-5 Phase diagram in terms of the binding energies of O* versus OH* (a) adapted from [19]. Free energy diagram for water oxidation reaction on BDD surface (b) adapted from [20].

As in heterogeneous catalysis in general, the reaction free energies and activation barriers of the individual elementary steps involved in the oxidation of organic compounds depend on the binding strength of reaction intermediates at the active site(s) on the surface of the photocatalyst. Because the nature of this bonding can vary significantly between different crystallographic facets, it is essential to characterize both the morphology and surface structure of semiconductor crystals. According to the Sabatier principle, optimal catalytic performance requires a balanced interaction between the catalyst surface and both reactants and products: adsorption must be sufficiently strong to enable activation, yet not so strong as to poison the surface or hinder product desorption, and sufficiently weak interactions must be avoided to prevent catalytic inactivity. At present, the quantitative determination of material properties such as binding energies and reaction free energies is largely achievable only through theoretical calculations.

Electron-hole recombination and charge-transport

The rate of charge-carrier recombination plays a decisive role in determining whether photogenerated electrons and holes remain available to participate in electrochemical reactions. If these charge carriers recombine before reaching the electrode/electrolyte interface, the corresponding redox reactions cannot proceed. Consequently, efficient photoelectrocatalysis requires semiconductor materials characterized by long minority-carrier lifetimes or, equivalently, large carrier diffusion lengths.

From a materials perspective, an indirect band gap is advantageous in terms of minimizing charge-carrier recombination probability, whereas a direct band gap is generally more favorable for maximizing light absorption [21]. Thus, an appropriate balance between optical absorption and charge-carrier dynamics is required.

Rapid charge-carrier transport is essential to minimize resistive losses during photoelectrocatalytic operation and to achieve sufficiently high photocurrents. The conductivity type of the semiconductor (p-type or n-type) further determines whether the material is suitable for use as a photocathode or a photoanode. Accordingly, materials with high electrical conductivity and appropriately chosen conduction type are required to ensure efficient degradation of organic pollutants.

Stability

For industrial-scale applications, semiconductor materials must exhibit sufficient chemical and mechanical stability under prolonged operation. This includes stability over a wide pH range, tolerance to the application of an external electrical bias, strong adhesion to the substrate, resistance to mechanical erosion, and the ability to withstand extensive gas evolution at the electrode surface [22,23].

In addition, semiconductor materials employed in photoelectrochemical systems must be photostable. Photocorrosion refers to the process in which photogenerated charge carriers drive the self-oxidation or self-reduction of the photoelectrode material. Anodic photocorrosion occurs when photogenerated holes oxidize lattice species, whereas cathodic photocorrosion arises when photogenerated electrons reduce lattice cations. Photocorrosion is therefore considered as a parasitic process, as it competes with the target reaction for photogenerated charge carriers, leading to reduced Faradaic efficiency. Moreover, photocorrosion results in degradation of the semiconductor lattice, leaching of lattice ions into the electrolyte (an undesirable outcome for water treatment applications), photocurrent decay, and potential changes in surface phase composition (e.g., $Cu_2O \rightarrow Cu/CuO$).

Thermodynamically, photocorrosion occurs when the decomposition potentials of a semiconductor are suitably aligned with its conduction and/or valence band positions, such that photogenerated charge carriers possess sufficient energy to drive self-redox reactions [24–26]. Consequently, the selection of semiconductor materials for photoelectrochemical applications should ideally be guided by knowledge of their decomposition potentials, with preference given to materials for which photocorrosion is thermodynamically unfavorable. In practice, however, this condition is rarely fully met. Therefore, careful kinetic control becomes essential: when the desired interfacial reaction is slow, charge carriers may accumulate at the surface, rendering parasitic self-redox reactions competitive. Under such conditions, enhancing surface reaction kinetics can significantly improve photoelectrode stability.

The risk of photocorrosion generally increases for narrow-bandgap semiconductor and especially p-type semiconductors employed as photocathodes often suffer from severe photocorrosion in aqueous environments [10,21].

Practicality: sustainability and scale-up

A set of material properties governing large-scale applicability must be considered. These properties represent fundamental practical constraints, as the successful upscaling of materials that perform well at the laboratory scale to industrial-scale applications is often hindered by a mismatch between excellent intrinsic performance and industrial requirements.

First, the material should be composed of earth-abundant elements, be derived from inexpensive precursors, and exhibit low toxicity [27]. In addition, fabrication methods should be cost-effective while enabling the production of uniform and adherent coatings over large surface areas. Such methods must also be compatible with industrially relevant substrates, such as titanium and transparent conducting oxides (e.g., FTO – fluorinated tin oxide or ITO – indium tin oxide) [10].

1.4. PHOTOANODE MATERIALS USED FOR PHOTOELECTROCATALYTIC WATER TREATMENT

Guided by the criteria discussed above, five semiconductors dominate the literature as photoanodes for PEC water remediation: TiO_2, WO_3, ZnO, g-C_3N_4 and $BiVO_4$. Other frequently reported photoanodes include α-Fe_2O_3, Cu_2O, CdS and MoS_2 (Figure 1-6). The prevalence of the “top five” reflects a practical balance between photochemical robustness under anodic bias, sufficient oxidative driving force for organics oxidation, accessible fabrication as immobilized electrodes, and cost/availability; importantly, each material represents a different compromise between stability, light harvesting, and charge-transport/kinetic limitations (Table 1-1). The following sections briefly summarize the key advantages and bottlenecks of each photoanode.

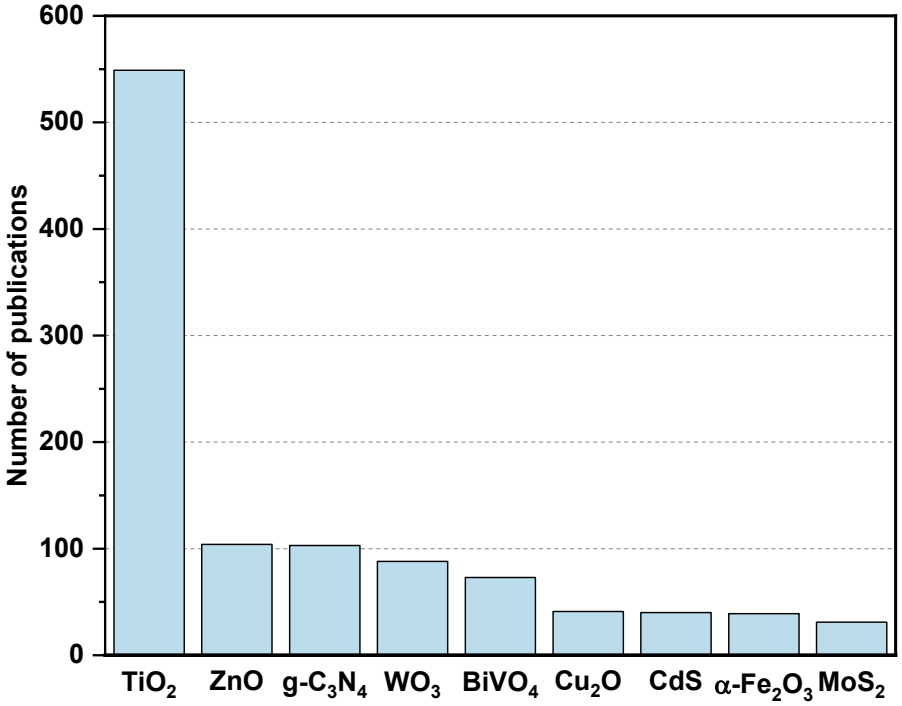

Figure 1-6 Comparison of the number of publications between nine main photoanodes used in water treatment. Data from 2010 to January 2026, according to the Web of Science database. Keywords: (wastewater OR pollutant) AND (photoanode OR photoelectrocatalysis OR photoelectrocatalytic) NOT (water oxidation OR water splitting).

Titanium dioxide (TiO_2) remains the benchmark photoanode material for photoelectrocatalytic oxidation of organic pollutants because it combines exceptional chemical/photochemical stability under anodic polarization with high oxidative power of photogenerated holes, enabling robust $HO^{\bullet}$-driven (and direct hole) oxidation pathways without rapid photo-corrosion [27–30]. TiO_2 is also abundant, inexpensive, and relatively non-toxic**,** which makes it attractive for water-treatment deployment compared with many narrow-bandgap semiconductors. From an engineering point of view, TiO_2 is beneficial due to the fact that it allows easily control the electrode architecture and it can be fabricated as strongly adherent, immobilized photoelectrodes (films, nanotube arrays, nanostructured layers on Ti substrates), providing large interfacial area, improved mass transfer, and easy recovery – key advantages over slurry photocatalysis for practical PEC reactors [29]. Although pristine TiO_2 is limited by its wide bandgap (~3.2 eV) and recombination losses, the literature consistently highlights that defect engineering, doping, and heterojunction design can extend spectral response and accelerate charge separation while preserving TiO_2's intrinsic stability – precisely why TiO_2 is so widely used as the "workhorse" photoanode platform for PEC organic oxidation [31].

Although ZnO has the bandgap slighly wider than the one of TiO_2 (~3.2-3.3 eV), it is still considered as a photoanode for photoelectrocatalytic oxidation of organic pollutants because it combines strong oxidative valence-band holes (able to drive direct oxidation and $HO^{\bullet}$-mediated pathways) with high charge-carrier mobility (higher than the one of TiO_2) and the ability to more precisely control the arcitecture [27,32]. It is also far more cheaper and the least toxic than other photocatalyst materials due to its wide abundance in the nature [28]. However, the reviews also emphasize that ZnO's broader use is constrained by photocorrosion/chemical instability in certain aqueous environments, motivating common stabilization

strategies (nanostructuring, heterojunctions/coatings, and operational control) to preserve activity during repeated oxidation runs [14][33]. Despite this, ZnO remains attractive due to its low cost, abundance, biocompatibility and scalable electrode fabrication for PEC organic oxidation [27].

WO_3 is widely used as visible-light-active photoanodes for photoelectrocatalytic oxidation of organic pollutants because it is an n-type semiconductor with a moderate bandgap (~2.6–2.8 eV), enabling absorption into the blue/visible region, and its valence-band holes are strongly oxidizing [31,34,35]. In addition, WO_3 can be prepared as robust, immobilized thin films/nanostructures on conductive substrates and many reviews highlight WO_3's good stability under anodic conditions in acidic media relative to several other visible-light semiconductors. However, WO_3 also has important limitations: its conduction band is relatively positive, making cathodic H_2 evolution thermodynamically challenging without appropriate cell design/applied bias, and its performance can be constrained by short hole diffusion length/recombination losses and surface-kinetic bottlenecks, often motivating heterojunctions (e.g., with $BiVO_4$), defect/oxygen-vacancy engineering, or co-catalyst strategies to improve charge separation and interfacial charge transfer. Finally, multiple reviews note that WO_3 can suffer from chemical instability in alkaline conditions (dissolution to tungstate species), which restricts operating pH windows and influences real-wastewater applicability [36].

Graphitic carbon nitride (g-C_3N_4) is increasingly explored as a PEC photoanode component for organic oxidation because it is a metal-free, earth-abundant, chemically robust polymeric semiconductor with intrinsic visible-light absorption (typically attributed to its moderate bandgap ~2.7 eV) and a π-conjugated, N-rich heptazine/tri-s-triazine framework that can be readily chemically tuned (doping/functionalization/defect engineering) and integrated into thin-film electrodes [14,31,37]. In water treatment discussions, the key practical advantage is that g-C_3N_4 can be engineered into 2D/porous architectures and heterojunctions (including Z-scheme/S-scheme designs) to enhance light harvesting and promote interfacial oxidation by improving charge separation-features [38]. However, the same reviews emphasize important limitations that often prevent bare g-C_3N_4 from being a high-performance stand-alone photoanode: low intrinsic electrical conductivity and high recombination**,** poor charge transport through thick/bulk layers, and electrode integration issues (adhesion, stability and activity losses unless immobilized and coupled to a better conducting scaffold/oxide). Consequently, g-C_3N_4 is most often chosen because its visible-light response and highly tailorable chemistry make it an effective photoactive "building block" in composite photoanodes for PEC oxidation, where bias plus rational interface engineering can convert its photogenerated carriers into higher organic-oxidation rates [27,30].

$BiVO_4$ is a visible-light-driven photoanode for photoelectrocatalytic oxidation of organic pollutants because its moderate bandgap (~2.4–2.5 eV) enables efficient absorption in the visible region and its valence-band holes are sufficiently oxidizing to drive direct organic oxidation under anodic bias [27,31,39,40]. Its appeal is strengthened by the fact that $BiVO_4$ is commonly described as comparatively stable and low-toxicity among visible-light semiconductors, and it can be fabricated as immobilized thin films/nanostructured electrodes on conductive substrates. However, the same reviews emphasize key limitations that often down the performance: $BiVO_4$ suffers from poor electron transport/low electron mobility and significant bulk/surface recombination, so photocurrents and oxidation rates are frequently limited by charge-separation and surface-kinetic bottlenecks. As a result, high-performing $BiVO_4$ PEC

photoanodes typically rely on nanostructuring (to shorten transport distances), doping/alloying and defect control, surface passivation/cocatalysts, and heterojunction architectures (including tandem/stacked designs) to accelerate charge extraction and interfacial oxidation while maintaining stability [14,41]. Taken together, $BiVO_4$ is used so extensively for PEC organic oxidation because it offers a rare combination of visible-light activity, strong oxidative holes, and practical electrode manufacturability, but it generally requires materials engineering to overcome intrinsic transport and recombination constraints for high-rate pollutant removal.

Table 1-1 Semiconductor properties of five most used photoanode materials for water treatment.

	TiO_2	**WO_3**	**$BiVO_4$**	**ZnO**	**g-C_3N_4**
Percentage of standard solar spectra absorbed, %	3.4	8.7	18	3.4	10.9
Maximum theoretical current density, mA/cm^2	1.1	3.1	7.5	1	4
Hole diffusion length, nm	10000 [36]	150 [36]	70-100 [42]	400-2500 [43]	1000 [44]
Electron mobility, $cm^2/(V \cdot s)$	0.1 [45]	12 [46]	0.01 [47]	200 [48]	2.43 [49]
Stability	Highly stable pH 0-14	Stable at pH≤4 [50]	Stable at 4<pH<11 [51]	Stable at 5<pH<12 [33]	Stable at pH 0-14
Morphology control	Very good (thin film formation, strong adhesion, versatile nanostructuring: nanorods, nanowires, nanotubes, layering)	Possible (thin film formation, strong adhesion, moderate morphology control)	Possible (thin film formation, strong adhesion, moderate morphology control)	Excellent (thin film formation, strong adhesion, nanostructuring: nanorods, nanowires, nanotubes, layering)	Possible (thin film formation, poor adhesion, limited morphology control)

In the field of electrochemical oxidation of organic pollutants, it is common to classify anodes as active or non-active, depending on the mechanism of the oxygen evolution reaction (OER) and, consequently, on whether the electrode material is capable of generating hydroxyl radicals [52]. Such a classification is not typically applied in photoelectrocatalysis; however, it could be interesting to consider the most frequently used semiconductor materials from this perspective. Table 1-2 summarizes the thermodynamic and

catalytic characteristics of these photoactive materials relevant to hydroxyl radical generation, as well as experimental data on HO· radical detection. The thermodynamic feasibility of hydroxyl radical formation is determined by the position of the valence-band edge, which must be more positive than the standard potential for hydroxyl radical formation (2.73 V vs RHE [53]) in order for photogenerated holes to possess sufficient energy to oxidize water to HO·. The catalytic predisposition of a material toward hydroxyl radical formation is governed by the free energy of the adsorbed HO* intermediate. If this free energy is higher than that required for the formation of a free aqueous HO· radical (2.4 eV), desorption of the HO species into the solution is thermodynamically favored; if it is lower, the HO species preferentially remains adsorbed on the semiconductor surface [16]. Finally, among the various experimental methods used to detect HO· radicals in solution – such as scavenging experiments with ethanol or tert-butanol, terephthalic acid probe-molecule oxidation, and scanning electrochemical microscopy – electron paramagnetic resonance (EPR) spectroscopy combined with DMPO (5,5-dimethyl-1-pyrroline N-oxide) spin trapping is considered the most representative technique [54].

Table 1-2 Hydroxyl radicals' formation on most used photoanode materials in PEC for water treatment.

	TiO_2	**WO_3**	**$BiVO_4$**	**ZnO**	**g-C_3N_4**
VB, V vs NHE	2.83	>3	2.68 [55]	>3	1.1
ΔG_{HO*}, eV	~2.4 [19]	1.7 [56]	1.95 [19]	1.98 [57]	0.2 [58]
DMPO-HO·spin aduct detection	Yes [59–61]	Yes [62,63]	No [59]	Yes [64,65]	No [63]

Analysis of Table 1-2 shows that the formation of free hydroxyl radicals is thermodynamically allowed on TiO_2, WO_3, and ZnO anodes, whereas it is not feasible on $BiVO_4$ and g-C_3N_4. At the same time, the strength of hydroxyl radical adsorption on the photocatalyst surface increases in the row WO_3<ZnO<TiO_2. This trend suggests that the lowest amount of free hydroxyl radicals is expected to be generated on WO_3, while the highest amount is expected on TiO_2. These conclusions are supported by experimental hydroxyl radical detection using EPR spin-trapping techniques. Although a small amount of adsorbed hydroxyl radicals on the $BiVO_4$ surface is detected by SECM [66], no DMPO-HO· spin adduct is observed, indicating the absence of free hydroxyl radical formation. Under illumination of g-C_3N_4, small peaks attributed to the DMPO-HO· adduct are reported [51]; however, these signals are assigned to hydroxyl radicals generated indirectly via $O_2{\cdot}^-$, since the conduction-band position of g-C_3N_4 allows the reduction of dissolved oxygen to superoxide species, and a large amount of DMPO–$O_2{\cdot}^-$ is detected in a separate experiment. Upon illumination of WO_3, low-intensity peaks corresponding to the DMPO–HO· adduct are detected [62,63], which is consistent with the assumption that hydroxyl radical formation on WO_3 is thermodynamically possible but not catalytically favored. In contrast, ZnO and TiO_2 actively generate hydroxyl radicals with the highest reported concentrations (7-11 mM) [59–61,64,65]. Thus, using the classification commonly employed in the field of electrochemical oxidation of organic pollutants, TiO_2 and ZnO would be classified as non-active anodes, $BiVO_4$ and g-C_3N_4 as active anodes, and WO_3 as having mixed behavior.

The analysis presented above allows the preferred application areas of these photoanodes to be rationalized. TiO_2, as already discussed, is the most commonly used photoanode in water treatment due to its high rate of hydroxyl radical generation, which results in high oxidation efficiency and low selectivity toward organic compounds. In contrast, WO_3 and $BiVO_4$ are considered preferable photoanodes for chlorination photoelectrochemical systems, since their band-edge positions enable the formation of active chlorine species, while the absence of hydroxyl radicals suppresses the formation of toxic chlorate and perchlorate species [14].

1.5. OVERVIEW OF TOP-PERFORMING PEC SYSTEMS FOR ORGANIC POLLUTANTS REMOVAL

Photoelectrochemical systems have been extensively investigated for water treatment applications, including the removal of heavy metals and organic pollutants. They have been tested for the degradation of organic dyes [67–69], pesticides [70], pharmaceutical contaminants [71–73], PFAS [74], phenolic compounds [75,76], and real wastewater samples [77,78]. Here, attention is focused on the top-performing PEC cells that achieve the highest percentage of removal of organic pollutants (in most cases >90%) to attempt to identify the factors responsible for their high performance. Table 1-3 provides an overview of such systems, considering key PEC parameters such as the type of light source, applied external bias, the ratio of geometric photoanode surface area to treated solution volume, the pseudo-first-order apparent degradation rate, and energy consumption.

Considering the PEC systems employing TiO_2-based photoanodes presented in this overview, it can be concluded that the most important factors enhancing the performance of TiO_2 are the increase in active surface area and improved light harvesting. For example, Hu et al. built 3D “facet-heterojunction” TiO_2/Ti, 3D structure of which strongly boosts adsorption capacity and exposes more reactive sites, while the facet heterojunction helps spatially separate photogenerated charges [79]. As a result, they fasten the Bisphenol A oxidation compared to a conventional 2D TiO_2/Ti electrode. Franz et al. used plasma electrolytic oxidation to grow porous, electrically continuous TiO_2 coatings on Ti meshes and achieved 99% removal of carbamazepine in 55 min [73]. Another successful strategies was doping of TiO2 in order to increase electorn-hole separation that allowed to use very low external bias [80] and construction of heterojunction with visible-light semiconductor in order to increase the fraction of absorbed light [81].

Across presented studies, ZnO performance gains for organic oxidation come less from “changing ZnO itself” and more from engineering its interfaces and architecture to extract charges faster under bias, increase light harvesting and mitigate ZnO’s known instability. An example is a spray-pyrolyzed ZnO/FTO thin film, where optimizing an adherent, hydrophilic film enables steady PEC oxidation of terephthalic acid and reasonable reusability [82]. Another improvement route is substrate/interlayer engineering: introducing a conductive and robust Ti/MMO (Ru-Ti oxide) interlayer beneath ZnO increases effective interfacial charge transfer and stabilizes ZnO under illumination and anodic polarization, which is reflected in markedly higher apparent kinetics [83]. The third route is heterojunction/composite design to address recombination and expand activity under visible light: Ti/Ce-ZnO/g-C_3N_4 yields higher visible-light photocurrent and strong oxidation/mineralization performance with good cycling stability [84], Ce-ZnO/MoS_2/Ti furthermore improves performance towards degradation of the same pharmaceutical [85].

WO_3-based photoanodes reviewed here are improved by engineering the electrode architecture and electronic structure to mitigate WO_3's intrinsic recombination and interfacial charge-transfer losses. In one approach, WO_3 is nanostructured into anodized nanorod arrays, where tuning the anodization conditions controls the nanorod morphology/defect density and translates into higher PEC activity, enabling complete degradation of the organophosphorus pesticide fenamiphos under anodic bias (1 V vs Ag/AgCl) in acidic medium [86]. A more direct strategy is defect engineering: generating oxygen-deficient WO_{3-x} anoplate-array films introduces oxygen vacancies that facilitate charge transport and interfacial transfer under bias, yielding a clear kinetic advantage for chlorophenol oxidation compared with stoichiometric WO_3 [87]. Finally, heterojunction construction (Ag_3PO_4/WO_3) strengthens visible-light utilization and charge separation and it substantially increases both pollutant removal and mineralization rates for recalcitrant dichlorophenol relative to the individual components [88]. As was stated above, WO_3 photoanodes are suitable for chlorination, therefore, high removal rates can be also achieved in the systems containing chloride ions without semiconductor modification. For example, Koo et al. [89] showed that the rate of organic pollutants oxidation on bare WO_3 in the presence of chloride species is faster than in the electrolyte containing only sulfate and, in the chloride-containing electrolyte it was possible to reach 100% degradation of Bisphenol A in 60 minutes and 100% degradation of Paracetamol and Carbamazepine in 30 minutes. Xiao et al. [90] employed WO_3 photoanode in saline water together with the carbon felt cathode and at optimized 92% of TOC removal of Bisphenol A was achieved in 120 minutes.

In the reviewed PEC studies, g-C_3N_4 is not employed as a bare photoanode; instead, its performance in organic oxidation is enhanced by coupling it with other semiconductors to improve charge separation and suppress electron-hole recombination. Consequently, g-C_3N_4 is most commonly incorporated into heterostructured systems [84,91–93], where such modifications improve band alignment and charge-carrier separation. In addition, modification of wide-band-gap semiconductors such as TiO_2 and ZnO with g-C_3N_4 extends light absorption into the visible range. Because g-C_3N_4 is intrinsically limited by poor electrical conductivity and inefficient charge-carrier transport, electrode-engineered architectures have been explored to overcome these drawbacks. For example, g-C_3N_4 nanosheet arrays grown directly on conductive carbon fibers have been reported; this immobilization strategy enhances electron collection and enables stable operation over repeated cycles during nitrophenol degradation [94].

$BiVO_4$, while being an efficient visible-light-absorbing photocatalyst, is limited by rapid electron-hole recombination and low electrical conductivity. Consequently, PEC oxidation performance is predominantly enhanced through the construction of heterojunctions and/or the incorporation of electron sinks or plasmonic metals to improve charge separation and interfacial charge transfer. For example, Ag_3PO_4 nanoparticles grown on $BiVO_4$ ($Ag_3PO_4/BiVO_4$) increase the photocurrent and accelerate PEC oxidation kinetics, enabling complete removal of norfloxacin within 90 min at a relatively low applied bias [72]. A closely related approach involves p-n coupling with a narrow-band-gap chalcogenide ($BiVO_4/Ag_2S$), where the heterointerface enhances photocurrent generation and supports faster PEC degradation compared with the individual components under visible or simulated solar irradiation [95]. The introduction of plasmonic Ag into a $BiVO_4$-based p-n junction (Ag-$BiVO_4$/BiOI) further improves visible-light absorption and forms a Schottky barrier that facilitates electron extraction, resulting in higher diclofenac removal efficiencies (92% within 120 min) [96]. Finally, tandem oxide heterostructures such as $WO_3/BiVO_4$ are employed to

optimize band alignment and charge-carrier collection under practical bias conditions, with layer thickness optimization identified as a critical design parameter for achieving enhanced photocurrent and PEC activity under simulated sunlight [97].

In general, effective enhancement of organic compound oxidation is achieved by addressing the specific weaknesses of the photoanode rather than by further improving properties that are already intrinsically strong (Table 1-3). For TiO_2 and ZnO, efforts should primarily focus on improving light absorption, whereas for WO_3, g-C_3N_4, and $BiVO_4$, enhancement of charge transport and electron-hole separation is of greater importance. As noted above, the appropriate selection of semiconductor materials for reactions that match their intrinsic properties can also lead to high oxidation performance, even without additional material modification.

It should also be noted that many of the studies reviewed here are conducted under experimental conditions that are primarily designed to demonstrate the potential of photoelectrochemical systems and to achieve enhanced performance metrics, although these conditions are far from industrial application. In particular, a light source with an irradiance exceeding that of the standard solar spectrum is often employed, which increases the number of charge carriers available for electrochemical reactions and facilitates higher reaction rates. While such conditions are valuable for fundamental studies, they may differ from those typically encountered in practical applications. In addition, a relatively high ratio of geometric electrode surface area to the volume of the treated solution is frequently used, which is beneficial for maximizing reaction efficiency at the laboratory scale but intrinsically limits process productivity at the industrial scale. Finally, in some cases, comparatively high external potentials are applied, leading to increased pollutant removal efficiencies, although this approach may involve trade-offs with respect to material stability and energy consumption.

Another important conclusion drawn from the literature analysis is that, although it is frequently stated that the use of photoelectrochemical processes instead of purely electrochemical ones can significantly reduce energy consumption, measurements of energy consumption are reported only rarely. As a result, this widely postulated advantage is often not quantitatively substantiated, which complicates a direct and meaningful comparison of the actual energy efficiencies of different systems. Addressing this aspect would significantly strengthen future studies in this field. Nevertheless, the reported energy consumption values for PEC systems are promising, as they are on the order of a few kWh/m^3, whereas conventional electrochemical oxidation typically requires tens to hundreds of kWh/m^3.

Table 1-3 Summary of essential characteristics of top-performing PEC cells for organic pollutants degradation
*Energy consumption of UV-lamp is also considered.

Anode	**Cathode**	**Light source**	**E_{app}**	**S_{anode}/V_{sol} Electrolyte**	**Pollutant**	**Degradation rate**	**Apparent degradation rate constant**	**Energy consumption**	**Reference**
Ti/FH-**TiO_2**	Pt	300 W Xenon lamp λ=320-780 nm	+0.4 V vs SCE	17.5 m^{-1} 50 mL 0.1 M Na_2SO_4	Bisphenol-A 5 mg/L	97.04% (60 min)	0.084 min^{-1}	-	[79]
Ru-dopped Ti/**TiO_2**	Pt	UV-C λ=254 nm	-0.2 V vs 3 M Ag/AgCl	10 m^{-1} 20 mL 0.05 M Na_2SO_4	Terasil Blue dye 0.011 mM	98% (120 min)	-	-	[80]
Ti/**TiO_2**	Ti	14 W UV lamp λ=275 nm	8 V vs cathode (*4 cells in series*)	25.6 m^{-1} 1 L 0.02 Na_2SO_4	Paracetamol 10 mg/L	95% (300 min)	$8.52 \cdot 10^{-3}$ min^{-1}	67 kWh m^{-3} $order^{-1}$*	[98]
FTO/Mo-**$BiVO_4$/TiO_2**	Pt foil	300 W Xe lamp 400 nm filter 100 mW/cm^2	1 V vs Ag/AgCl	- 36 mL 0.1 M $NaHCO_3$ (pH=4)	Ibuprofen 5 mg/L	100% (120 min)	0.0212 min^{-1}	-	[81]
Ti/**TiO_2**	Stainless steel	30 W Hg UVC lamp λ=254 nm	4 V vs cathode	10.9 m^{-1} 3 L	Carbamazepine 100 мg/L	99% (55 min)	0.076 min^{-1}	7.58 kWh/m^{3}*	[73]

W/**WO_3**	Pt	AM 1.5 G	1 V vs 3 M Ag/AgCl	- 14 mL H_2SO_4 (pH=1)	Fenamiphos 20 mg/L	100% (120 min)	-	-	[86]
WO_{3-x}	Stainless steel	AM 1.5 G	1.2 V vs SHE	10 m^{-1} 80 mL 0.1 M Na_2SO_4	4-chlorophenol 10 mg/L	85.5% (120 min)	0.0157 min^{-1}	1.31 kWh/m^3	[87]
FTO/**WO_3**	Pt wire	300 W Xe lamp λ>420 nm	0.5 V vs Ag/AgCl	4 m^{-1} 50 mL 0.1 M Na_2SO_4 + 50 mM NaCl (pH=4)	Bisphenol A Paracetamol Carbamazepine 50 μM	100% (60 min) 100% (30 min) 100% (30 min)	0.09 min^{-1} 0.125 min^{-1} 0.085 min^{-1}	-	[89]
FTO/**WO_3**	Carbon felt	300 W Xe lamp 100 mW/cm^2	-0.5 V vs Ag/AgCl	- 25 cm^2 anode 200 mM NaCl	Bisphenol A 10 mg/L	95.5% (120 min) 92% TOC (120 min)	0.078 min^{-1}	-	[90]
Ag_3PO_4/**WO_3**	CuO-modified hydrophobic carbon cloth	300 W Xe lamp Sunlight filter 200 mW/cm^2	1.8 V vs cathode	- 0.1 M Na_2SO_4	2,5-dichlorophenol 20 mg/L	91.2% (90 min)	0.0263 min^{-1}	-	[88]
Ti/MoS_2/Ce-**ZnO**	Pt	Visible light 72 W	0.9 V vs Ag/AgCl	192 m^{-1} 100 mL 35 mM Na_2SO_4 (pH=3)	Cefixime 2 mg/L	87% (120 min)	-	-	[85]

Ti/MMO/**ZnO**	Pt	UVC lamp 9W λ=254 nm	0.2 V vs Ag/AgCl (sat. KCl)	4.2 m^{-1} 150 mL 0.1 M Na_2SO_4 (pH=9)	Levofloxacin 20 mg/L	99.2% (240 min)	1.206 min^{-1}	-	[99]
Ti/MMO/**ZnO**	Pt	UVC lamp 9W (20 mW/cm^2) λ=254 nm	0.5 V vs Ag/AgCl (sat. KCl)	4.2 m^{-1} 150 mL 0.1 M Na_2SO_4	Clopyralid 20 mg/L	77% (240 min)	0.388 min^{-1}	-	[83]
FTO/**ZnO**	Stainless steel	UV	1.5 V vs cathode	21.3 m^{-1} 300 mL water	Terephthalic acid 0.5 mM	91% (400 min)	$2.52 \cdot 10^{-5}$ min^{-1}	-	[82]
Ti/Ce-**ZnO/g-C_3N_4**	Pt plate	Fluorescent lamp 18 W λ=425, 500, 550, 600 nm	0.9 V vs Ag/AgCl (sat)	29.1 m^{-1} 120 mL 35 mM Na_2SO_4	Cefixime 10 mg/L	80% (180 min) 100% 96% TOC (330 min)	-	-	[84]
(**TiO_2/g-C_3N_4**)/CQDs:N,P	Pt wire	LED visible light ≥400 nm 80-85 mW/cm^2	1.2 V vs cathode	45.3 m^{-1} 20 mL 0.1 M Na_2SO_4	1,4-dioxane 100 mg/L	97% (720 min)	0.0089 min^{-1}	-	[92]
FTO/Zn-MOF@**g-C_3N_4**	Pt wire	100 W Xe lamp UV-vis	0.1 V vs 3 M Ag/AgCl	- 100 mL 0.1 M Na_2SO_4	Naproxen 10 mg/L	97.52% (120 min)	-	-	[91]
Ti/**TiO_2/g-C_3N_4** QDs	Pt plate	Xe lamp	0.6 V vs SCE	20 m^{-1}	Phenol	98.6%	0.0361 min^{-1}	-	[93]

		100 mW/cm^2		20 mL 0.1 M Na_2SO_4	5 mg/L	(120 min)			
carbon-fiber/**g-C_3N_4**	carbon fiber textiles	70 W lamp Simulated sunlight	2 V vs cathode	12.5 m^{-1} 100 mL Na_2SO_4	2,4-dinitrophenol 20 mg/L	99.5% (240 min)	0.0221 min^{-1}	-	[94]
FTO/**Ag-$BiVO_4$**/BiOI	Ag-BiOI	Solar simulator 100 W Xe lamp	1 V vs 3 M Ag/AgCl	13 m^{-1} 50 mL 0.1 M Na_2SO_4	Diclofenac 10 mg/L	92% (120 min)	0.0173 min^{-1}	0.928 kWh/g TOC	[96]
FTO/ Ag_3PO_4/**$BiVO_4$**	Pt wire	300 W Xe lamp λ≥420 nm	0.5 V vs SCE	- 10 mM $NaClO_4$	Norfloxacin 5 mg/L	100% (90 min)	$2.63\cdot10^{-2}$ min^{-1}	-	[72]
Ti/blue-**TiO_2**/RuO_2/**$BiVO_4$**	Pt foil	Xe lamp λ≥420 nm	2 V vs SCE	- 0.1 M NaCl (pH=5)	Paracetamol 332 mg/L	100% (180 min)	0.0388 min^{-1}	0.02 kWh/g COD 3.54 kWh/m^3	[100]
FTO/**WO_3**/**$BiVO_4$**	Pt wire	AM 1.5 G	1.75 vs RHE	- 1 M NaCl	Sodium 2-naphthalenesulfonate 50 мg/L Benzyl alkyl dimethylammonium compounds 50 мg/L	100% (60 min) 100% (90 min)	-	-	[97]
FTO/**$BiVO_4$**/Ag_2S	Pt sheet	Solar simulator 100 W Xe lamp	1.2 V vs 3 M Ag/AgCl	13 m^{-1} 0.1 M Na_2SO_4	Sulfamethoxazole 10 mg/L	86% (120 min)	0.0147 min^{-1}	-	[95]

1.6. PHARMACEUTICAL POLLUTION OF NATURAL WATERS

Pharmaceutical residues are considered as one of the most common groups of contaminants of emerging concern. They enter the environment continuously, and therefore they are frequently detected at low concentrations in natural waters. Even at these trace concentrations, they can degrade water quality and may pose risks to drinking-water resources, aquatic ecosystems, and human health [101–105].

Pharmaceuticals enter waters mostly because modern society uses large volumes of medicines and many active ingredients are not fully broken down before reaching the environment. Across the European Union, pharmaceutical use can reach the kilotonne scale (e.g., paracetamol sales up to ~10,000 tonnes/year in France) and official surveillance reports veterinary antimicrobial sales in the hundreds of tonnes per country per year [106,107], while in the United States consumers purchased more than 25 billion doses of acetaminophen-containing products annually (implying multi-kilotonne annual use) [108]. After intake, pharmaceuticals are partially absorbed and subjected to metabolic degradation in humans and animals; however, substantial fractions are often excreted as parent compounds or active metabolites via urine or feces and subsequently discharged into raw sewage, which may or may not undergo treatment [102]. Conventional water treatment plants are not designed to remove pharmaceutical pollutants, consequently, many compounds are only partially eliminated and can enter natural waters with treated effluents [103,104]. Additional sources of pharmaceutical contamination include the flushing and improper disposal of unused medications [105]. Moreover, antibiotics, antiparasitics, hormones, and anti-inflammatories used in animals can reach water via runoff from fields fertilized with manure, leakage from storage, or direct release in aquaculture [104].

A key problem for ecosystem is that many pharmaceuticals are biologically active by design (they act on receptors/enzymes that often exist in wildlife too), and aquatic organisms can face lifelong exposure to complex mixtures at low but continuous concentrations. Although only little is known about ecotoxicological effects of pharmaceuticals on aquatic and terrestrial organisms and wildlife, several adverse effects have already been documented. The fish feminization and disrupt reproduction was recorded at exposure to synthetic estrogens (notably ethinylestradiol, EE2) at extremely low concentrations [109]. Psychoactive drugs (e.g., antidepressants or illicit drugs) can alter fish risk-taking, feeding, reproduction, and predator avoidance – effects that matter for survival even when animals don't "die" outright [110–112]. Some drugs (e.g., anti-inflammatories like diclofenac) are linked with oxidative stress and tissue impacts in aquatic organisms; risk depends on local concentrations, season, and dilution [113].

Human risk is more complicated: concentrations in treated drinking water are usually very low, but concerns persist because exposure is chronic, mixtures are common, and some endpoints (like antimicrobial resistance) are indirect but serious [104,114]. Antibiotics in water don't just affect microbes directly – they can select for resistant bacteria and resistance genes, which can then move through wastewater systems and into natural waters [115,116]. This is now framed as a One Health issue connecting environment, animals, and humans.

A global-scale study conducted in 2022 investigated pharmaceutical contamination in rivers worldwide by analyzing water samples collected from 1,052 locations across 258 rivers in 104 countries [117]. The water samples were analyzed for 61 active pharmaceutical ingredients. The most frequently detected in this

study pharmaceuticals are carbamazepine (found in 66.2% of sampled locations), metformine (61.1% locations), caffeine (56.1%), gabapentin (41.6%), nicotine (43.5%), trimethoprim (39.9%), sulfamethoxazole (40.7%). and paracetamol (36.8%). The highest measured concentrations were measured for paracetamol (mean and median concentrations of 3.10 and 2.11 mg/L, respectively), caffeine (2.50 and 2.06 mg/L), metformin (2.36 and 2.06 mg/L), fexofenadine (0.66 and 0.62 mg/L), sulfamethoxazole (0.53 and 0.44 mg/L), metronidazole (1.20 and 0.82 mg/L), gabapentin (0.48 and 0.41 mg/L), nicotine (0.44 and 0.31 mg/L) and carbamazepine (0.11 and 0.09 mg/L).

Based on the results of this study, paracetamol, sulfamethoxazole, and carbamazepine were selected as model contaminants to investigate the applicability of photoelectrocatalysis for the oxidation of pharmaceutical pollutants. These compounds were chosen due to their high global occurrence, highest environmental concentrations, and representation of major pharmaceutical classes: analgesic and anti-inflammatory (paracetamol), antibiotic (sulfamethoxazole), and psychotropic (carbamazepine). The global distribution of these pharmaceuticals is illustrated in Figure 1-7.

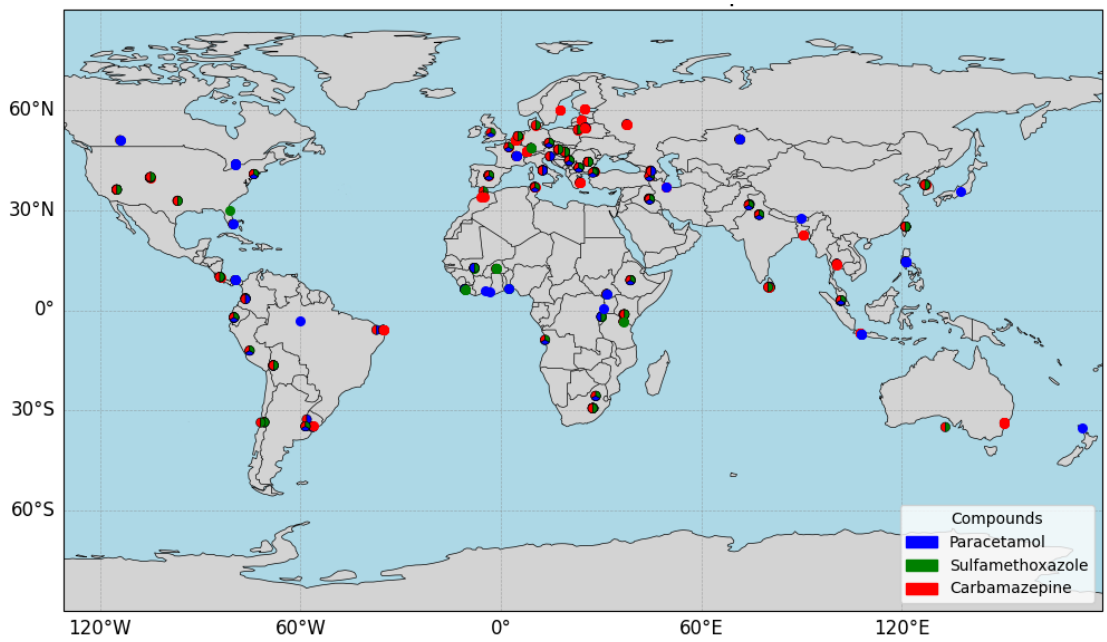

Figure 1-7 Locations of paracetamol (blue), sulfamethoxazole (green) and carbamazepine (red) detection in rivers. According to the database collected in [117].

CONCLUSIONS

– The enhancement in energy efficiency observed in photoelectrochemical systems arises from the fact that photogenerated holes already possess sufficient energy to drive oxidation reactions. In this context, the applied external potential primarily serves to improve charge separation rather than to supply additional energy required to overcome intrinsic energetic barriers.

- Most photoanode materials commonly employed for the oxidation of organic pollutants thermodynamically allow parallel water oxidation. Therefore, this process can occur concurrently and it represents a parasitic reaction that competes with the target oxidation of organic species.
- Photoelectrocatalysis enables a more flexible selection of semiconductor materials compared to unbiased photocatalytic systems. In particular, strict requirements on the simultaneous alignment of valence and conduction bands for both oxidation and reduction reactions, as well as on the band-gap width exceeding the required cell voltage, are relaxed, since the applied external bias can partially compensate for energetic mismatches.
- An ideal photoanode would simultaneously combine optimal band-edge positions, high photostability, efficient charge separation, strong light absorption, large electrochemically active surface area, and high catalytic ability. In practice, achieving all of these properties within a single material remains challenging.
- The most frequently investigated photoanode materials for the oxidation of organic pollutants include TiO_2, ZnO, g-C_3N_4, WO_3 and $BiVO_4$, as they offer a favourable balance between energetic alignment, stability, catalytic activity, and material availability.
- Using the terminology commonly employed in the field of electrochemical oxidation of organic pollutants, TiO_2 and ZnO can be classified as non-active anodes, $BiVO_4$ and g-C_3N_4 as active anodes, while WO_3 exhibits mixed behavior.
- High photoelectrochemical efficiencies have been reported in the literature, with degradation efficiencies approaching 100% within tens of minutes and total organic carbon (TOC) removal reaching up to 70% within approximately two hours under optimized conditions.
- Although it is often stated in the literature that the application of photoelectrochemical processes leads to reduced energy consumption compared to purely electrochemical approaches, quantitative assessments of energy consumption are reported only in a limited number of studies on PEC systems. Inclusion of such analyses would enable a more comprehensive evaluation and comparison of system performance.
- Many studies demonstrating high oxidation efficiencies employ experimental conditions that are particularly favourable at the laboratory scale, such as illumination intensities exceeding standard solar irradiance, high ratios of geometric electrode surface area to treated solution volume, or relatively high applied biases. While these approaches are effective for revealing performance limits, future investigations conducted under more realistic and, where possible, standardized conditions would facilitate a more accurate assessment of the practical potential of photoelectrochemical oxidation processes.

REFERENCES

1. Jiang, P.; Zheng, H.-Z. The Physics of Semiconductors; 1993; ISBN 9783319238791.
2. Gerischer, H.; Ekardt, W. Fermi Levels in Electrolytes and the Absolute Scale of Redox Potentials. Appl. Phys. Lett. 1983, 43, 393–395, doi:10.1063/1.94356.
3. Bard, A.J.; Faulkner, L.R. Electrochemical Methods : Fundamentals and Applications; Second Ed.; John Wiley&Sons, Inc.: New York, USA, 2001; ISBN 9781118312803.
4. Trasatti, S. THE ABSOLUTE ELECTRODE POTENTIAL: AN EXPLANATORY NOTE. Int. Union Pure Appl. Chem. 1986, 58, 955–966, doi:10.1351/pac198658070955.
5. Memming, R. Semiconductor Electrochemistry; Wiley-VCH, 2015; ISBN 9783319296418.
6. Nozik, A.J.; Memming, R. Physical Chemistry of Semiconductor - Liquid Interfaces. J. Phys. Chem. 1996, 100, 13061–13078.
7. Pleskov, Y. V.; Gurevich, Y.Y. Semiconductor Photoelectrochemistry; Springer, 1986; ISBN 978-1468490800.
8. Nozik, A.J. Physical Chemistry of Semiconductor - Liquid Interfaces. 1996, 3654, 13061–13078.
9. Hariprasad, N.; Viswanathan, K.; Krishnamurthy, K.R.; Harindranathan, N. Understanding Reaction Mechanism in Photon-Assisted Reduction of Carbon Dioxide. In Photocatalytic Nanomaterials for Environmental Applications; 2018; pp. 175–211 ISBN 9781945291586.
10. Palmisano, L.; Yurdakal, S. Photoelectrocatalysis. Fundamentals and Applications; Elsevier, 2023; ISBN 9780128239896.
11. Cha, H.G.; Choi, K.S. Combined Biomass Valorization and Hydrogen Production in a Photoelectrochemical Cell. Nat. Chem. 2015, 7, 328–333, doi:10.1038/nchem.2194.
12. Гуревич, В.А.; Плесков, Ю.В. Фотоэлектрохимия Полупроводников; 1983;
13. Memming, R. Energy Production by Photoelectrochemical Processes. In Philips Technical review; 1978; Vol. 38, pp. 160–177.
14. Liu, J.; Wu, H.; Sun, J.; Li, S.; Hassani, A.; Zhou, M. Non-TiO2-Based Photoanodes for Photoelectrocatalytic Wastewater Treatment: Electrode Synthesis, Evaluation, and Characterization. EES Catal. 2025, 3, 921–942, doi:10.1039/d5ey00068h.
15. Kamble, G.S.; Natarajan, T.S.; Patil, S.S.; Thomas, M.; Chougale, R.K.; Sanadi, P.D.; Siddharth, U.S.; Ling, Y.C. BiVO4 As a Sustainable and Emerging Photocatalyst: Synthesis Methodologies, Engineering Properties, and Its Volatile Organic Compounds Degradation Efficiency. Nanomaterials 2023, 13, doi:10.3390/nano13091528.
16. She, Z.W.; Kibsgaard, J.; Dickens, C.F.; Chorkendorff, I.; Nørskov, J.K.; Jaramillo, T.F. Combining Theory and Experiment in Electrocatalysis: Insights into Materials Design. Science (80-.). 2017, 355,

doi:10.1126/science.aad4998.

17. Splitting, E.; Hu, J.; Zhao, S.; Zhao, X.; Chen, Z. Strategies of Anode Materials Design towards Improved Photoelectrochemical Water. 2019.
18. Panizza, M.; Cerisola, G. Direct and Mediated Anodic Oxidation of Organic Pollutants. Chem. Rev. 2009, 109, 6541–6569, doi:10.1021/cr9001319.
19. Siahrostami, S.; Li, G.L.; Viswanathan, V.; Nørskov, J.K. One- or Two-Electron Water Oxidation, Hydroxyl Radical, or H2O2 Evolution. J. Phys. Chem. Lett. 2017, 8, 1157–1160, doi:10.1021/acs.jpclett.6b02924.
20. Liu, G.; Zhang, C.; Zhou, Y.; Yan, Q. Insight into the Overpotential and Thermodynamic Mechanism of Hydroxyl Radical Formation on Diamond Anode. Appl. Surf. Sci. 2021, 565, 150559, doi:10.1016/j.apsusc.2021.150559.
21. Govind Rajan, A.; Martirez, J.M.P.; Carter, E.A. Why Do We Use the Materials and Operating Conditions We Use for Heterogeneous (Photo)Electrochemical Water Splitting? ACS Catal. 2020, 10, doi:10.1021/acscatal.0c01862.
22. Chi, J.; Jiang, Z.; Yan, J.; Larimi, A.; Wang, Z.; Wang, L.; Shangguan, W. Recent Advancements in Bismuth Vanadate Photoanodes for Photoelectrochemical Water Splitting. Mater. Today Chem. 2022, 26, doi:10.1016/j.mtchem.2022.101060.
23. Schneider, J.; Bahnemann, D.; Ye, J.; Li Puma, G.; Dionysiou, D. Photocatalysis. Fundamentals and Perspectives; 2016; ISBN 978-1-78262-041-9.
24. Bard, A.J.; Wrighton, M.S. Thermodynamic Potential for the Anodic Dissolution of N-Type Semiconductors: A Crucial Factor Controlling Durability and Efficiency in Photoelectrochemical Cells and an Important Criterion in the Selection of New Electrode/Electrolyte Systems. J. Electrochem. Soc. 1977, 124, 1706–1710, doi:10.1149/1.2133140.
25. Fan, F.R.F.; Bard, A.J. Semiconductor Electrodes. 24. Behavior of Photoelectrochemical Cells Based on p-Type Gallium Arsenide in Aqueous Solutions. J. Am. Chem. Soc. 1980, 102, 3677–3683, doi:10.1021/ja00531a002.
26. Nozik, A.J. Photoelectrochemical Cells. Philos. Trans. R. Soc. A Math. Phys. Eng. Sci. 1980, 295, 453–470.
27. Fernandez-Ibanez, P.; McMichael, S.; Rioja Cabanillas, A.; Alkharabsheh, S.; Tolosana Moranchel, A.; Byrne, J.A. New Trends on Photoelectrocatalysis (PEC): Nanomaterials, Wastewater Treatment and Hydrogen Generation. Curr. Opin. Chem. Eng. 2021, 34, 100725, doi:10.1016/j.coche.2021.100725.
28. Garcia-Segura, S.; Brillas, E. Applied Photoelectrocatalysis on the Degradation of Organic Pollutants

in Wastewaters. J. Photochem. Photobiol. C Photochem. Rev. 2017, 31, 1–35, doi:10.1016/j.jphotochemrev.2017.01.005.

29. Liang, X.; Yu, S.; Meng, B.; Wang, X.; Yang, C.; Shi, C. Advanced TiO2-Based Photoelectrocatalysis: Material Modifications, Charge Dynamics, and Environmental – Energy Applications. Catalysis 2025, 15, 542, doi:10.3390/catal15060542.
30. Olvera-vargas, H.; Pazos, M.; Bustos, E.; Deng, F.; Salazar-gonz, R. Recent Developments in (Photo)Electrocatalytic Materials for Wastewater Treatment and Resource Recovery. Appl. Catal. O Open 2025, 202, 207033, doi:10.1016/j.apcato.2025.207033.
31. Liu, Y.; Xu, X.; Sun, X.; Li, W.; Duan, J. Recent Research Progress of Photoelectrocatalysis Technology in the Removal of Organic Pollutants from Water. J. Water Process Eng. 2025, 75, 107911, doi:10.1016/j.jwpe.2025.107911.
32. Chauke, N.M.; Raphulu, M. Simultaneous “One-Pot” Pollution Mitigation and Hydrogen Production from Industrial Wastewater Using Photoelectrocatalysis Process. Mater. Today Catal. 2024, 5, 100052, doi:10.1016/j.mtcata.2024.100052.
33. Dimitropoulos, M.; Aggelopoulos, C.A.; Sygellou, L.; Tsantis, S.T.; Koutsoukos, P.G. Unveiling the Photocorrosion Mechanism of Zinc Oxide Photocatalyst : Interplay between Surface Corrosion and Regeneration. J. Environ. Chem. Eng. 2024, 12, 112102, doi:10.1016/j.jece.2024.112102.
34. Rioja-Cabanillas, A.; Valdesueiro, D.; Fernández-Ibáñez, P.; Byrne, J.A. Hydrogen from Wastewater by Photocatalytic and Photoelectrochemical Treatment. JPhys Energy 2021, 3, doi:10.1088/2515-7655/abceab.
35. Dang, Q.; Wang, L.; Liu, J.; Wang, D.; Chai, J.; Wu, M.; Tang, L. Recent Progress of Photoelectrocatalysis Systems for Wastewater Treatment. J. Water Process Eng. 2023, 53, 103609, doi:10.1016/j.jwpe.2023.103609.
36. Liu, X.; Wang, F.; Wang, Q. Nanostructure-Based WO3 Photoanodes for Photoelectrochemical Water Splitting. PCCP 2012, 14, 7894–7911, doi:10.1039/c2cp40976c.
37. Sun, J.; Fu, C.; Hu, Z.; Sirés, I.; Zhou, M. Recent Advances in Photoelectrocatalysis for Simultaneous Water Purification, Energy Generation or Resource Recovery. Crit. Rev. Environ. Sci. Technol. 2025, 783–804, doi:10.1080/10643389.2025.2450128.
38. Zhang, Y.; Lian, P.; Hao, X.; Zhang, L.; Yang, L.; Jiang, L.; Zhang, K.; Liao, L. Modification Strategies of G-C3N4-Based Materials for Enhanced Photoelectrocatalytic Degradation of Pollutants: A Review. Inorganics 2025, 13, 225.
39. Orimolade, B.O.; Arotiba, O.A. Bismuth Vanadate in Photoelectrocatalytic Water Treatment Systems for the Degradation of Organics: A Review on Recent Trends. J. Electroanal. Chem. 2020, 878, doi:10.1016/j.jelechem.2020.114724.

40. Ali, A.Z.; Mohapatra, S.; Hoek, J.P. Van Der; Spanjers, H. BiVO4-Based Photoanodes for the Photoelectrocatalytic Removal of Trace Organic Pollutants from Water : A Mini Review on Recent Developments. Curr. Opin. Environ. Sci. Heal. 2025, 45, 100615, doi:10.1016/j.coesh.2025.100615.
41. Bai, Y.; Fang, Z.; Fang, Y.; Lin, C.; Bai, H.; Fan, W. Recent Advances in BiVO4-Based Heterojunction Photocatalysts for Energy and Environmental Applications. Chem. Commun. 2025, 61, 5264–5280, doi:10.1039/d4cc06798c.
42. Kim, T.W.; Choi, K.S. Nanoporous BiVO4 Photoanodes with Dual-Layer Oxygen Evolution Catalysts for Solar Water Splitting. Science (80-.). 2014, 343, 990–995, doi:10.1126/science.1246913.
43. Lopatiuk-Tirpak, O.; Chernyak, L. Studies of Minority Carrier Transport in ZnO. Superlattices Microstruct. 2007, 42, 201–205, doi:10.1016/j.spmi.2007.04.030.
44. Ruan, Q.; Bayazit, M.K.; Kiran, V.; Xie, J.; Wang, Y.; Tang, J. Key Factors Affecting Photoelectrochemical Performance of G-C3N4 Polymer Films. Chem. Commun. 2019, 55, 7191–7194, doi:10.1039/c9cc03084k.
45. Tang, H.; Prasad, K.; Sanjinès, R.; Schmid, P.E.; Lévy, F. Electrical and Optical Properties of TiO2 Anatase Thin Films Ellectrical and Optical Properties of Ti02 Anatase Thin Films. J. Appl. Phys. 1994, 75, 2042–2047, doi:10.1063/1.356306.
46. Zhao, Y.; Balasubramanyam, S.; Sinha, R.; Lavrijsen, R.; Verheijen, M.A.; Bol, A.A. Physical and Chemical Defects in WO3 Thin Films and Their Impact on Photoelectrochemical Water Splitting. ACS Appl. Energy Mater. 2018, 1, 5887–5895.
47. Chen, D.; Xie, Z.; Tong, Y.; Huang, Y. Review on BiVO4-Based Photoanodes for Photoelectrochemical Water Oxidation: The Main Influencing Factors. Energy and Fuels 2022, doi:10.1021/acs.energyfuels.2c02119.
48. Rahman, A.A. RBS and Channeling Study of Single Crystal ZnO, 2009.
49. Noda, Y.; Merschjann, C.; Tarábek, J.; Amsalem, P.; Koch, N.; Bojdys, M.J. Directional Charge Transport in Layered, Two-dimensional Triazine-based Graphitic Carbon Nitride. Angew. Chemie - Int. Ed. 2019, 58, 9394–9398.
50. Knöppel, J.; Zhang, S.; Speck, F.D.; Mayrhofer, K.J.J.; Scheu, C.; Iek-, H.E.R.E.; Jülich, F. Time-Resolved Analysis of Dissolution Phenomena in Photoelectrochemistry – A Case Study of WO3 Photocorrosion. Electrochem. commun. 2018, 96, 53–56, doi:10.1016/j.elecom.2018.09.008.
51. Toma, F.M.; Cooper, J.K.; Kunzelmann, V.; McDowell, M.T.; Yu, J.; Larson, D.M.; Borys, N.J.; Abelyan, C.; Beeman, J.W.; Yu, K.M.; et al. Mechanistic Insights into Chemical and Photochemical Transformations of Bismuth Vanadate Photoanodes. Nat. Commun. 2016, 7, doi:10.1038/ncomms12012.

52. Sirés, I.; Brillas, E.; Oturan, M.A.; Rodrigo, M.A.; Panizza, M. Electrochemical Advanced Oxidation Processes: Today and Tomorrow. A Review. Environ. Sci. Pollut. Res. 2014, 21, 8336–8367, doi:10.1007/s11356-014-2783-1.

53. Armstrong, D.A.; Huie, R.E.; Koppenol, W.H.; Lymar, S. V; Neta, P.; Ruscic, B.; Stanbury, D.M.; Wardman, P. Standard Electrode Potentials Involving Radicals in Aqueous Solution : Inorganic Radicals (IUPAC Technical Report). Pure 2015, 87, 1139–1150, doi:10.1515/pac-2014-0502.

54. Janzen, E.G. Spin Trapping. Acc. Chem. Res. 1971, 50, 31–40.

55. Łęcki, T.; Hamad, H.; Zarębska, K.; Wierzyńska, E.; Skompska, M. Mechanistic Insight into Photochemical and Photoelectrochemical Degradation of Organic Pollutants with the Use of BiVO4 and BiVO4/Co-Pi. Electrochim. Acta 2022, 434, doi:10.1016/j.electacta.2022.141292.

56. Siahrostami, S.; Bjorketun, M.E.; Strasse, P.; Greeley, J.; Rossmeisl, J. Tandem Cathode Fo Proton Exchange Membrane Fuel Cells. Phys. Chem. Chem. Phys. 2013, 15, 9326–9334, doi:10.1039/c3cp51479j.

57. Kelly, S.R.; Shi, X.; Back, S.; Vallez, L.; Park, S.Y.; Siahrostami, S.; Zheng, X.; Nørskov, J.K. ZnO As an Active and Selective Catalyst for Electrochemical Water Oxidation to Hydrogen Peroxide. ACS Catal. 2019, 9, 4593–4599, doi:10.1021/acscatal.8b04873.

58. Tian, J.; Zhou, Z.; Zhang, S.; Li, Z.; Shi, L.; Li, Q.; Wang, J. Synergistic Modulation of Metal-Free Photocatalysts by the Composition Ratio Change and Heteroatom Doping for Overall Water Splitting. J. Mater. Chem. A 2021, 9, 11753–11761, doi:10.1039/d1ta01978c.

59. Saison, T.; Chemin, N.; Chane, C.; Brezova, V.; Jolivet, J. New Insights Into BiVO4 Properties as Visible Light Photocatalyst. J. Phys. Chem. C 2015, 119, 12967–12977, doi:10.1021/acs.jpcc.5b01468.

60. Brezova, V.; Stasko, A. Spin Trap Study of Hydroxyl Radicals Formed in the Photocatalytic System TiO2-Water-p-Cresol-Oxygen. J. Catal. 1994, 147, 156–162, doi:10.1006/jcat.1994.1125.

61. Morelli, R.; Renato, I.; Maria, C.; Alborghetti, S. EPR Spin-Trapping of Hydroxyl Radicals onto Photocatalytic Membranes Immobilizing Titanium Dioxide , and Spin Adduct Competition , as a Probe of Reactivity with Aqueous Organic Micropollutants. J. Photochem. Photobiol. A Chem. 1998, 112, 271–276, doi:10.1016/S1010-6030(97)00287-6 Get rights and content.

62. Guo, W.; Wei, Q.; Li, G.; Wei, F.; Hu, Z. A Bulk Oxygen Vacancy Dominating WO3−x Photocatalyst for Carbamazepine Degradation. Nanomaterials 2024, 14, 923, doi:10.3390/nano14110923.

63. Lu, Y.; Gao, S.; Ma, T.; Zhang, J.; Liu, H.; Zhou, W. A Z-Scheme Heterojunction g-C3N4/WO3 for Efficient Photodegradation of Tetracycline Hydrochloride and Rhodamine B. Nanomaterials 2025, 15, 410, doi:10.3390/nano15050410.

64. Ancona, A.; Dumontel, B.; Garino, N.; Demarco, B.; Chatzitheodoridou, D.; Fazzini, W.; Engelke, H.; Cauda, V. Lipid-Coated Zinc Oxide Nanoparticles as Innovative ROS-Generators for Photodynamic Therapy in Cancer Cells. Nanomaterials 2018, 8, 143, doi:10.3390/nano8030143.

65. Rutile, Z.T.; Mediouni, N.; Dappozze, F.; Khrouz, L.; Parola, S.; Ben, A.; Amara, H.; Rhaiem, H. Ben; Jaffrezic-renault, N.; Namour, P.; et al. Correlation between Photocatalytic Properties of ZnO and Generation of Hydrogen Peroxide — Impact of Composite. Catal. Today 2022, 12, 1445, doi:10.3390/catal12111445.

66. Ahn, H.S.; Bard, A.J. Surface Interrogation Scanning Electrochemical Microscopy of Ni1-xFexOOH (0. J. Am. Chem. Soc. 2016, 138, 313–318.

67. Obregón, S.; Barriga-castro, E.D.; Mendoza-reséndez, R.; Luna, C. Enhanced Photocatalytic Behavior of BiVO4 through Photoinduced Charge Transfer to Amorphous β-FeOOH Nanoparticles. Ceram. Int. 2016, 42, 17773–17780, doi:10.1016/j.ceramint.2016.08.105.

68. Bacha, A.U.R.; Cheng, H.; Han, J.; Nabi, I.; Li, K.; Wang, T.; Yang, Y.; Ajmal, S.; Liu, Y.; Zhang, L. Significantly Accelerated PEC Degradation of Organic Pollutant with Addition of Sulfite and Mechanism Study. Appl. Catal. B Environ. 2019, 248, 441–449, doi:10.1016/j.apcatb.2019.02.049.

69. Deshpande, N.G.; Ahn, C.H.; Koli, R.R.; Jamadar, A.S.; Kim, D.S.; Kim, Y.B.; Jung, S.H.; Cho, H.K. Controlled Nanostructured Morphology of BiVO4 Photoanodes for Efficient On-Demand Catalysis in Solar Water-Splitting and Sustainable Water-Treatment. Appl. Surf. Sci. 2020, 514, 146075, doi:10.1016/j.apsusc.2020.146075.

70. Zanoni, M.V.B.; Irikura, K.; Perini, J.A.L.; Bessegato, G.G.; Sandoval, M.A.; Salazar, R. Recent Achievements in Photoelectrocatalytic Degradation of Pesticides. Curr. Opin. Electrochem. 2022, 35, 101020, doi:10.1016/j.coelec.2022.101020.

71. Orimolade, B.O.; Zwane, B.N.; Koiki, B.A.; Tshwenya, L.; Peleyeju, G.M.; Mabuba, N.; Zhou, M.; Arotiba, O.A. Solar Photoelectrocatalytic Degradation of Ciprofloxacin at a FTO/BiVO4/MnO2 Anode: Kinetics, Intermediate Products and Degradation Pathway Studies. J. Environ. Chem. Eng. 2020, 8, doi:10.1016/j.jece.2019.103607.

72. Cao, D.; Wang, Y.; Qiao, M.; Zhao, X. Enhanced Photoelectrocatalytic Degradation of Norfloxacin by an Ag3PO4/BiVO4 Electrode with Low Bias. J. Catal. 2018, 360, 240–249, doi:10.1016/j.jcat.2018.01.017.

73. Franz, S.; Falletta, E.; Arab, H.; Murgolo, S.; Bestetti, M.; Mascolo, G. Degradation of Carbamazepine by Photo(Electro)Catalysis on Nanostructured TiO2 Meshes: Transformation Products and Reaction Pathways. Catalysis 2020, 10, 169, doi:10.3390/catal10020169.

74. Earn, C.; Valiyaveettil, R.; Ryu, B.; Abd, N.; Yeon, S.; Byum, S.; Tiek, K. A Systematic Review on Photo-Based Advanced Oxidation Processes for per- and Polyfluoroalkyl Substances Removal. J.

Environ. Manage. 2025, 394, 127241.

75. Bennani, Y.; Perez-rodriguez, P.; Alani, M.J.; Smith, W.A.; Rietveld, L.C.; Zeman, M.; Smets, A.H.M. Photoelectrocatalytic Oxidation of Phenol for Water Treatment Using a BiVO 4 Thin-Film Photoanode. J. Mater. Res. 2016, 31, 2627–2639, doi:10.1557/jmr.2016.290.
76. Bennani, Y.; Perez-Rodriguez, P.; Alani, M.J.; Smith, W.A.; Rietveld, L.C.; Zeman, M.; Smets, A.H.M. Photoelectrocatalytic Oxidation of Phenol for Water Treatment Using a BiVO4 Thin-Film Photoanode. J. Mater. Res. 2016, 31, 2627–2639, doi:10.1557/jmr.2016.290.
77. Collivignarelli, M.C.; Abbà, A.; Miino, M.C.; Bertanza, G.; Sorlini, S.; Damiani, S.; Arab, H.; Bestetti, M.; Franz, S. Photoelectrocatalysis on TiO2 Meshes: Different Applications in the Integrated Urban Water Management. Environ. Sci. Pollut. Res. 2021, 59452–59461.
78. Dong, T.; Zheng, Z.; Man, J.H.K.; Lo, I.M.C. A Low-Carbon-Emission Photoelectrochemical System Using Ov-Fe2O3@BiVO4 Photoanode for Integrated Multiple Pollutant Removal and Energy Harvesting from Real Saline Sewage. Chem. Eng. J. 2024, 499, 155840, doi:10.1016/j.cej.2024.155840.
79. Hu, Y.; Jin, Y.; Zhang, P.; Zhang, Y.; Zhao, G. Efficient Removal of Bisphenol A and Cr(VI) Simultaneously in an Advanced Redox Photoelectrocatalytic System over Dual 3D TiO2 Photoelectrodes. Appl. Catal. B Environ. 2023, 322, 122102, doi:10.1016/j.apcatb.2022.122102.
80. García-ramírez, P.; Ramírez-morales, E.; Cortazar, C.J.S.; Sires, I.; Silva-Martinez, S. Influence of Ruthenium Doping on UV- and Visible-Light Photoelectrocatalytic Color Removal from Dye Solutions Using a TiO2 Nanotube Array Photoanode. Chemosphere 2021, 267, 128925, doi:10.1016/j.chemosphere.2020.128925.
81. Pylarinou, M.; Sakellis, E.; Gardelis, S.; Psycharis, V.; Kostakis, M.G.; Thomaidis, N.S.; Likodimos, V. Bilayer TiO2/Mo-BiVO4 Photoelectrocatalysts for Ibuprofen Degradation. Materials (Basel). 2025, 18, 344, doi:10.3390/ma18020344.
82. Hunge, Y.M. A Multifunctional ZnO Thin Film Based Devices for Photoelectrocatalytic Degradation of Terephthalic Acid and CO2 Gas Sensing Applications. Sensors Actuators B. Chem. 2018, 274, 1–9, doi:10.1016/j.snb.2018.07.117.
83. Santos, O.S.; Eguiluz, K.I.B.; Goulart, L.A.; Salazar-banda, G.R.; Lanza, M.R. V; Saez, C.; Rodrigo, M.A. Towards a Higher Photostability of ZnO Photo-Electrocatalysts in the Degradation of Organics by Using MMO Substrates. Chemosphere 2021, 271, 129451, doi:10.1016/j.chemosphere.2020.129451.
84. Sheydaei, M.; Ayoubi-feiz, B.; Abbaszade-fakhri, G. A Visible-Light Active g-C3N4/Ce–ZnO/Ti Nanocomposite for Efficient Photoelectrocatalytic Pharmaceutical Degradation : Modelling with Artificial Neural Network. Process Saf. Environ. Prot. 2021, 149, 776–785,

doi:10.1016/j.psep.2021.03.037.

85. Moharramkhani, P.; Sheydaei, M.; Ayoubi, B.; Farhad, F. Visible-light Photoelectrocatalytic Properties of Bifacial Immobilized Ce–ZnO/MoS2/Ti Electrode in Degradation of Cefixime : Taguchi Optimization Method. J. Iran. Chem. Soc. 2022, 19, 2769–2778, doi:10.1007/s13738-022-02498-8.
86. Rosello-Marquez, G.; Fernandez-Domene, R.M.; Sanchez-Tovar, R.; Garcia-Anton, J. Photoelectrocatalyzed Degradation of Organophosphorus Pesticide Fenamiphos Using WO3 Nanorods as Photoanode. Chemosphere 2020, 246, 125677, doi:10.1016/j.chemosphere.2019.125677.
87. Liu, X.; Zhou, H.; Pei, S.; Xie, S.; You, S. Oxygen-Deficient WO3−x Nanoplate Array Film Photoanode for Efficient Photoelectrocatalytic Water Decontamination. Chem. Eng. J. 2020, 381, 122740, doi:10.1016/j.cej.2019.122740.
88. Yan, K.; Li, S.; Liu, J.; Liu, X.; Zhang, J. Integration of Ag3PO4/WO3 Photoanode with Bifunctional CuO Cathode Exhibiting Photocatalytic and Peroxidase-Mimetic Properties for Nanozyme-Coupled Photoelectrocatalytic Degradation of Persistent Pollutant. J. Colloid Interface Sci. 2025, 681, 356–364, doi:10.1016/j.jcis.2024.11.171.
89. Koo, M.S.; Chen, X.; Cho, K.; An, T.; Choi, W. In Situ Photoelectrochemical Chloride Activation Using a WO3 Electrode for Oxidative Treatment with Simultaneous H2 Evolution under Visible Light. Environ. Sci. Technol. 2019, 53, 9926–9936, doi:10.1021/acs.est.9b02401.
90. Xiao, K.; Liang, H.; Chen, S.; Yang, B.; Zhang, J.; Li, J. Enhanced Photoelectrocatalytic Degradation of Bisphenol A and Simultaneous Production of Hydrogen Peroxide in Saline Wastewater Treatment. Chemosphere 2019, 222, 141–148, doi:10.1016/j.chemosphere.2019.01.109.
91. Ambaye, A.D.; Zikalala, S.A.; Mashiloane, K.C.; Nure, J.F.; Kebede, M.A.; Mokrani, T.; Nxumalo, E.N. Development of Engineered Zn-MOF/g-C3N4 Based Photoelectrochemical System for Real-Time Sensors and Removal of Naproxen in Wastewater. Talanta Open 2024, 10, 100371, doi:10.1016/j.talo.2024.100371.
92. Su, Y.; Ye, Y.; Lin, S.; Lu, Y.; Luo, H.; Liu, G. Surface Modification of TiO2/g-C3N4 Electrode with N, P Codoped CQDs for Photoelectrocatalytic Degradation of 1,4-Dioxane. Water 2023, 15, 2837, doi:10.3390/w15152837.
93. Sun, B.; Lu, N.; Su, Y.; Yu, H.; Meng, X.; Gao, Z. Decoration of TiO2 Nanotube Arrays by Graphitic-C3N4 Quantum Dots with Improved Photoelectrocatalytic Performance. Appl. Surf. Sci. 2017, 394, 479–487, doi:10.1016/j.apsusc.2016.10.121.
94. Xi, X.; Lu, Z.; Chen, H.; Tian, W.; Yang, Y. Flexible Carbon-Fiber/g-C3N4 Nanosheet Array as Recyclable Photocatalysts and Photoelectrocatalysts. Sci. Rep. 2025, 15, 21090, doi:10.1038/s41598-025-04701-1 1.
95. Orimolade, B.O.; Arotiba, O.A. Towards Visible Light Driven Photoelectrocatalysis for Water

Treatment: Application of a FTO/BiVO4/Ag2S Heterojunction Anode for the Removal of Emerging Pharmaceutical Pollutants. Sci. Rep. 2020, 10, 5348, doi:10.1038/s41598-020-62425-w.

96. Orimolade, B.O.; Arotiba, O.A. Enhanced Photoelectrocatalytic Degradation of Diclofenac Sodium Using a System of Ag-BiVO4/BiOI Anode and Ag-BiOI Cathode. Sci. Rep. 2022, 12, 4214, doi:10.1038/s41598-022-08213-0.
97. Davies, K.R.; Allan, M.G.; Nagarajan, S.; Townsend, R.; Asokan, V.; Watson, T.; Godfrey, A.R.; Maroto-valer, M.M.; Kuehnel, M.F. Photoelectrocatalytic Surfactant Pollutant Degradation and Simultaneous Green Hydrogen Generation. Ind. Eng. Chem. Res. 2023, 62, 19084–19094, doi:10.1021/acs.iecr.3c00840.
98. Compound, N.D.; Reactor, E.; Cotillas, S.; Westerho, P.; Garcia-segura, S. Scaling up Photoelectrocatalytic Reactors: A TiO2 Degrades Acetaminophen. Water 2019, 1–14, doi:10.3390/w11122522.
99. Goulart, L.A.; Moratalla, A.; Lanza, M.R. V; Cristina, S.; Rodrigo, M.A. Photoelectrocatalytic Treatment of Levofloxacin Using Ti/MMO/ZnO Electrode. Chemosphere 2021, 284, 131303, doi:10.1016/j.chemosphere.2021.131303.
100. Sun, X.; Su, T.; Cui, X.; Yu, H.; Lu, Y.; Qin, W.; Huo, M. A TiO2 Nanotube Photoanode (Blue TiO2 Nanotube/RuO2/BiVO4) for Efficient Acetaminophen Degradation and Nitrogen Removal. J. Water Process Eng. 2024, 60, 105230, doi:10.1016/j.jwpe.2024.105230.
101. Rivera-Utrilla, J.; Sánchez-Polo, M.; Ferro-García, M.Á.; Prados-Joya, G.; Ocampo-Pérez, R. Pharmaceuticals as Emerging Contaminants and Their Removal from Water. A Review. Chemosphere 2013, 93, 1268–1287, doi:10.1016/j.chemosphere.2013.07.059.
102. Halling-Sorensen, B.; Nors Nielsen, S.; Lanzky, P.F.; Ingerslev, F.; Holten Lutzeheft, H.C.; Jorgensen, S.E. Occurance, Fate and Effects of Pharmacettical Substances in the Environment - A Review. Chemosphere 1998, 36, 357–393.
103. Nikolaou, A.; Meric, S.; Fatta, D. Occurrence Patterns of Pharmaceuticals in Water and Wastewater Environments. Anal. Bioanal. Chem. 2007, 387, 1225–1234, doi:10.1007/s00216-006-1035-8.
104. Zechariah Wada, O.; Bamidele Olawade, D. Recent Occurrence of Pharmaceuticals in Freshwater , Emerging Treatment Technologies, and Future Considerations: A Review. Chemosphere 2025, 374, 144153, doi:10.1016/j.chemosphere.2025.144153.
105. Khetan, S.K.; Collins, T.J. Human Pharmaceuticals in the Aquatic Environment: A Challenge to Green Chemisty. Chem. Rev. 2007, 107, 2319–2364, doi:10.1021/cr020441w.
106. Moore, A.; Moore, N. Paracetamol and Pain: The Kiloton Problem. Eur. J. Hosp. Pharm. 2016, 23, 187–188.

107. Sales of Veterinary Antimicrobial Agents in 31 European Countries in 2021. Eur. Med. Agency 2022.

108. Babak, J.O.; McLeod, M. Chandler MacLennan, P.A.; Lee, W.M.; Fontana, R.J.; Karvellas, C.J.; McGuire, Brendan M. Lewis, C.E.; Terrault, N.M.; Locke, J.E. Association of FDA Mandate Limiting Acetaminophen (Paracetamol) in Prescription Combination Opioid Products and Subsequent Hospitalizations and Acute Liver Failure. JAMA 2023, 329, 735–744, doi:10.1001/jama.2023.1080.

109. Kidd, K.A.; Blanchfield, P.J.; Mills, K.H.; Palace, V.P.; Evans, R.E.; Lazorchak, J.M.; Flick, R.W. Collapse of a Fish Population after Exposure to a Synthetic Estrogen. PNAS 2007, 104, 8897–8901, doi:10.1073/pnas.0609568104.

110. Brodin, T.; Fick, J.; Jonsson, M.; Klaminder, J. Dilute Concentrations of a Psychiatric Natural Populations Drug Alter Behavior of Fish from Natural Populations. Science (80-.). 2013, 814–815.

111. Liu, Y.; Lv, J.; Guo, C.; Jin, X.; Zuo, D.; Xu, J. Environmental Behavior, Risks, and Management of Antidepressants in the Aquatic Environment. Environ. Sci. Process. Impacts 2025, 27, 1196–1228, doi:10.1039/d4em00793j.

112. Horký, P.; Grabic, R.; Grabicova, K.; Brooks, B.W.; Douda, K.; Hubena, P.; Santos, E.M.S.; Randak, T. Methamphetamine Pollution Elicits Addiction in Wild Fish. J. Exp. Biol. 2021, 224, doi:10.1242/jeb.242145.

113. Duarte, C.; Lorenzo, T. Di; Reboleira, A.S.P.S. Environmental Risk of Diclofenac in European Groundwaters and Implications for Environmental Quality Standards. Sci. Rep. 2024, 14, 20689, doi:10.1038/s41598-024-71747-y.

114. Coderre, M.; Fortin, A.-S.; Morency, L.-D.; Roy, J.; Sirois, C. Pharmaceuticals in Drinking Water: A Scoping Review to Raise Pharmacists' Public Health and Environmental Awareness on Contamination in Groundwater, Surface Water, and Other Sources. Int. J. Pharm. Pract. 2025, 33, 360–368, doi:10.1093/ijpp/riaf038.

115. Zhu, C.; Wu, L.; Ning, D.; Tian, R.; Gao, S.; Zhang, B.; Zhao, J.; Zhang, Y.; Xiao, N.; Wang, Y.; et al. Global Diversity and Distribution of Antibiotic Resistance Genes in Human Wastewater Treatment Systems. Nat. Commun. 2025, 16, 4006, doi:10.1038/s41467-025-59019-3.

116. Bracing for Superbugs: Strengthening Environmental Action in the One Health Response to Antimicrobial Resistance. United Nations Environ. Program. 2023.

117. Wilkinson, J.L.; Boxall, A.B.A.; Kolpin, D.W.; Leung, K.M.Y.; Lai, R.W.S.; Wong, D.; Ntchantcho, R.; Pizarro, J.; Mart, J.; Echeverr, S.; et al. Pharmaceutical Pollution of the World ' s Rivers. 2022, 119, 1–10, doi:10.1073/pnas.2113947119/-/DCSupplemental.Published.

CHAPTER II: CRITICAL ANALYSIS ON SOLAR CONVERSION EFFICIENCY IN PHOTOELECTROCHEMICAL SYSTEMS FOR ORGANIC OXIDATION

2.1. INTRODUCTION

Photoelectrochemical (PEC) water splitting is widely investigated as a route for renewable hydrogen generation, with hydrogen serving as a clean fuel and energy carrier that can substitute carbon-based fossil resources. However, the solar-to-hydrogen efficiency and the economic viability of PEC water splitting remain insufficient for large-scale applications.

Although the oxidation of organic compounds is thermodynamically and kinetically more favorable than water splitting, it is less frequently employed as the anode reaction in PEC systems. Moreover, in the literature, it is sometimes suggested that substituting water oxidation with thermodynamically more favorable anodic reactions, such as organic oxidation, increases solar conversion efficiency or enhances hydrogen production [1,2]. Consistently, experimental studies report that this substitution is associated with higher photocurrents and/or increased hydrogen evolution rates. Nevertheless, while theoretical calculations of solar conversion efficiencies (SCE) for water splitting on different semiconductors are available (Figure 2-1), analogous calculations for organic oxidation reactions are still lacking.

To address this gap, the solar conversion efficiency and productivity for the unbiased photoelectrocatalytic oxidation of organic compounds are calculated, and process losses are evaluated using two models: absorbed photon energy balance (APEB) and modified detailed balance (MDB).

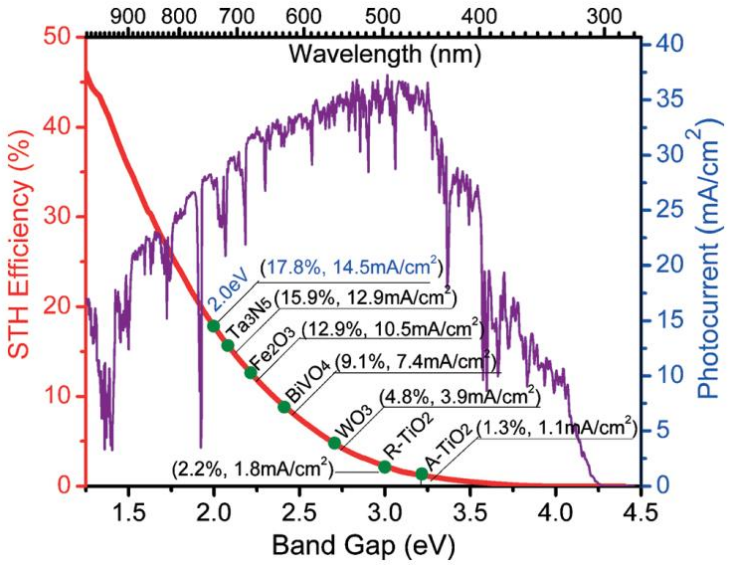

Figure 2-1 Solar-to-hydrogen conversion efficiency (STH) and maximum current density calculated for water splitting reaction depending for different semiconductor materials under standard solar spectra AM 1.5 G. Adapted from [3].

2.2. METHODS

2.2.1. Solar energy absorption efficiency

Extensive studies on the thermodynamic limits for solar energy conversion efficiencies are available in the literature [4–9]. Here a brief overview of the main concepts is provided.

The solar energy available to drive an electrochemical reaction is determined by the solar spectral distribution and irradiance, which are influenced by atmospheric conditions and by the orientation of the absorbing surface relative to the sun. To enable reliable comparison of efficiencies reported by different laboratories, a reference spectrum (AM 1.5G, Figure 2-2) is chosen in photovoltaic applications and is also adopted for photoelectrochemical systems. Accordingly, efficiency measurements (and calculations) are performed using illumination sources that reproduce this spectral distribution and irradiance as closely as possible.

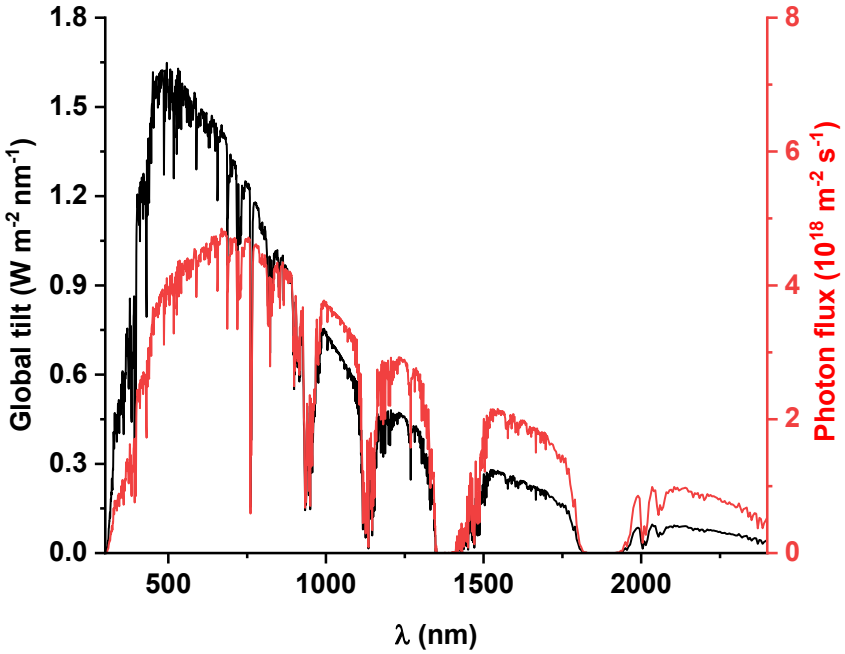

Figure 2-2 AM 1.5G spectra http://rredc.nrel.gov/solar/spectra/am1.5/.

The total irradiance (or incident power density) P_{in} (W/m^2) can be calculated as follows (Eq. 2.1):

$$P_{in} = \int_0^\infty P(\lambda) d\lambda \tag{2.1}$$

Where $P(\lambda)$ is the spectral irradiance (W m^{-2} s^{-1} nm^{-1}) and λ is the wavelength (nm). The total irradiance of AM 1.5G is 1001 W/ m^2, considering a wavelength range 0.3-4 μm, which is usually normalized to 1000 W/m^2, and set equivalent to 1 Sun.

The most critical phenomenon in photo-based systems is the absorption of photons by semiconductors. These materials absorb only the photons with an energy higher than a threshold – band gap energy (E_g). Assuming that all photons with an energy higher than E_g are absorbed without losses, and considering the relation $E_g = \frac{hc}{\lambda_g}$, the absorbed photon flux (J_{ph}) of the semiconductor with the band gap energy E_g is defined as:

$$J_{ph} = \int_0^{\lambda_g} J_{in}(\lambda) d(\lambda) \tag{2.2}$$

where J_{in} is the incident spectral photon flux ($m^{-2}\ s^{-1}\ nm^{-1}$).

When a semiconductor absorbs a photon with an energy higher than the band gap energy, only one electron-hole pair is generated, with the electron's energy equal to the top of conduction band (i.e. the energy increment of electron equal to E_g), and the excess of photon energy is lost as heat. Thus, it is possible to define the solar energy absorption efficiency, η_E:

$$\eta_E = \frac{J_{ph} \cdot E_g}{P_{in}} \tag{2.3}$$

When not all incident photons above semiconductor bandgap are absorbed, a non-unity absorption fraction, f_{abs}, is introduced in nominator of Eq. 2.3.

2.2.2. Absorbed photon energy balance

This section considers an energy balance for an absorbed photon (Figure 2-3) [10]. The energy received by the system is $h\upsilon = E_g$. However, as all the energy conversion processes, only a fraction of this energy will be available to drive the electrochemical reaction. It must be considered that in the reference condition, all the electrons in the system are in equilibrium, and the Fermi level's position is determined by the metal's Fermi level. Thus, during the electron transfer from the conduction band of semiconductor to the Fermi level of the metal, the energy loss ($E_{loss,et}$) is:

$$E_{loss,et} = V_b + (E_C - E_F) \tag{2.4}$$

Thus, the energy balance of an absorbed photon in the system is described by:

$$E_g - V_b - (E_c - E_F) = e\left(\frac{\triangle G}{nF} + \eta_a + \eta_c + iR\right) \tag{2.5}$$

where each contribution is defined as follows:

- V_b band bending energy (eV), spent on the charge separation in the space charge region;
- $(E_c - E_F)$ is the energy loss of electron (eV) in transfer from the CB of SC to the Fermi level of metal;
- $e\frac{\Delta G}{nF}$ is the free energy of electrode reaction (eV), normalized to the unity of charge;
- $e(\eta_a + \eta_c)$ are the overpotential for anodic and cathodic reactions (eV);
- eiR are the Ohmic losses (eV).

The left-hand part of the Eq. 2.5 represents the net available energy for the electrochemical reaction after all the losses in semiconductor-metal contact are accounted for. The right-hand part of the Eq. 2.5 represents the energy required to drive an electrochemical reaction considering all losses associated with electrochemical process. Thus, the minimum band gap energy required to drive the reaction is:

$$E_g = e\left(\frac{\triangle G}{nF} + \eta_a + \eta_c + iR\right) + V_b + (E_c - E_F) \tag{2.6}$$

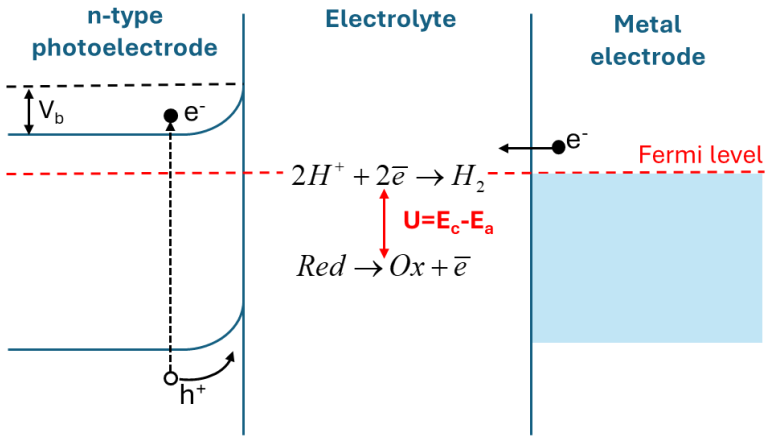

Figure 2-3 Energy diagram of a photoelectrochemical cell.

The chemical efficiency of the process can be calculated as a ratio of energy required to drive chemical reaction (i.e. free Gibbs energy) to the supplied energy (E_g):

$$\eta_{Chem} = \frac{\triangle G / (nF)}{E_g} \tag{2.7}$$

and then the overall solar conversion efficiency can be presented as:

$$SCE = \eta_E \eta_{Chem} \tag{2.8}$$

2.2.3. Modified detailed balance model for photoelectrochemical cell

The detailed balance model is widely applied in photovoltaics community [11]. Introduced by Shockley and Queisser [12], the method balances the photocurrent generated from absorbed sunlight with the radiative dark current associated with black-body emission for a given band gap. Thus, under the assumption that the only loss is radiative recombination, it allows to present the efficiency limits of a solar cell device as a function of a single parameter – semiconductor band gap. However, for photoelectrochemical system due to its complexity and multicomponent nature, it is impossible to obtain analog of detailed balance. Recently, Fountain et al. derived a model on the basis of the same postulates but it represents the efficiency limit as a function of six parameters – semiconductor band gap, semiconductor absorption fraction (f_{abs}), semiconductor external radiative efficiency (ERE), series resistance (R_S), shunt resistance (R_{Sh}) and catalytic exchange current density [8]. In this formulation band gap and semiconductor absorption fraction govern the operation-light absorption of a semiconductor,

external radiative efficiency, series and shunt resistances represent the charge carrier transport, while exchange current densities are account for electrochemical kinetics.

Here a summary of a model formulation is presented.

The voltage generated by the photoelectrochemical cell, thus, the energy available to be converted into the chemical energy, V_{PEC}, depends on device current density, j, and can be presented as follows:

$$V_{PEC}(j) = V_{PV}(j) - V_{cat,a}(j) - V_{cat,c}(j) - V_{series}(j) \tag{2.9}$$

where each contribution is defined as follows:

- V_{PV} is an inverse current-voltage relationship of a photodiode;
- $V_{cat,a}$ is an anodic overpotential;
- $V_{cat,c}$ is a cathodic overpotential;
- V_{series} is a series resistance due to the electrolyte transport through solution, calculated as jR_S.

The photodiode voltage is derived as an inverse formulation of a diode equation [13] with the incorporation of series and shunt resistances taking into account also the semiconductor absorption fraction and external radiative efficiency:

$$V_{PV}(j) = \frac{k_B T}{q_e} \ln\left[\frac{f_{abs} j_L - j - (V_{PV} + jR_S)/R_{Sh}}{j_0 / ERE} + 1 \right] \tag{2.10}$$

where

k_B is a Boltzmann's constant, J/K;

T is a temperature, K;

q_e is an electron charge, J;

j_L is a photocurrent, A/m^2;

j_0 is a saturated (dark) current, A/m^2;

R_s is a series resistance, Ohm;

R_{sh} is a shunt resistance, Ohm.

Series resistance in PEC cell is representative of ohmic losses (the movement of current through the emitter and base, the contact resistance between the metal contact and semiconductor). The shunt resistance is caused by leakage across the *pn*-junction due to crystal defects and impurities within the junction region. The main impact of series and shunt resistance is to reduce the fill factor, i. e. the power of PEC cell.

A detailed balance model for the photodiode dark current assuming only radiative recombination into the semiconductor:

$$j_0(E_g) = \frac{q_e}{4\pi^2 \hbar^3 c^2} \int_{E_g}^{\infty} \frac{E^2}{e^{E/k_B T} - 1} dE \tag{2.11}$$

where

$\hbar$ is the reduced Planck constant, J·s;

c is the light velocity, m/s;

E is the energy, J.

ERE means the fraction of the total (radiative and non-radiative) recombination which is represented by the detailed balance radiative recombination. Thus, to obtain the real dark current the ideal one calculated by Eq. 2.11 should be divided by ERE.

To calculate the electrocatalytic overvoltage the reverse formulation of Butler-Volmer equation in assumption that forward and reverse electron transfer coefficients are equal is used:

$$V_{cat}(j) = \frac{RT}{\alpha n_e F} \sinh^{-1}\left(\frac{j}{2 j_{0,cat}}\right) \tag{2.12}$$

where

R is a gas constant, J/(mol·K);

α is an electron transfer coefficient;

n_e is a number of electrons participating in the reaction;

$j_{0,cat}$ is the exchange current density, A/m^2;

The reaction occurs when the voltage of a photoelectrochemical cell is no less than the standard electrode reaction $V_{PEC}(j) \geq E^0$. In turn, the maximum efficiency occurs when the cell voltage equals to the standard electrode reaction: $V_{PEC}(j_{op}) = E^0$. j_{op} is the optimum current density, thus, taking into account also the Faradic efficiency, f_{FE}, the solar conversion efficiency can be calculated according to equation (2.13). Note that substituting of Eq. (2.3) and Eq. (2.7) into Eq. (2.8) gives the same formula.

$$SCE = \frac{E^0 j_{op} f_{FE}}{P_{in}} \cdot 100\% \tag{2.13}$$

2.2.4. Productivity calculations

Another key parameter in photoelectrochemical process is the productivity of the process, that can be estimated as the hydrogen production rate. To produce one molecule of hydrogen, two electrons are required. Thus, assuming all generated electrons participate in the target chemical reaction (i. e. semiconductor absorption fraction, charge separation efficiency, the injection yield and the faradaic efficiency equal to 1) the maximum hydrogen production rate can be calculated as follows:

$$J_{H_2} = \frac{J_{ph}}{2 \cdot N_A} \tag{2.14}$$

where N_A is the Avogadro number.

2.3. RESULTS AND DISCUSSION

In this section, the efficiency and productivity of different chemical reactions occurring at the photoanode are compared. Two scenarios are considered: (i) an idealized case, in which all photons with energies above the semiconductor band gap are fully absorbed, electron–hole recombination is purely radiative, overpotentials are negligible (i.e., kinetic limitations are absent), and no additional losses are included; and

(ii) a realistic case, in which 90% of photons with energies above the band gap are absorbed, overpotentials are present (reflecting kinetic constraints), non-radiative recombination occurs, and series and shunt losses are taken into account. At the cathode, the hydrogen evolution reaction is assumed in all cases, and its characteristics are kept constant across the investigated systems. Table 2-1 summarizes the reactions considered, together with their Gibbs free energies, standard electrode potentials, numbers of transferred electrons, and exchange current densities.

Table 2-1 Thermodynamical and kinetics parameters of reactions under investigation.

Oxidized compound	**Reaction of oxidation to hydrogen**	**ΔG, kJ/mol**	**E°, V**	**n**	**j_0, mA/cm²**
Water	$H_2O(l) = \frac{1}{2}O_2(g) + H_2(g)$	237	1.23	2	10^{-5} [14]
Methanol	$CH_3OH(l) + H_2O(l) = CO_2(g) + 3H_2(g)$	9.18	0.016	6	1 [15]
Acetic acid	$CH_3COOH(l) + 2H_2O(l) = 2CO_2(g) + 4H_2(g)$	75.59	0.098	8	$7.90 \cdot 10^{-3}$ [16]
Acetaldehyde	$CH_3CHO(l) + 3H_2O(l) = 2CO_2(g) + 5H_2(g)$	50.97	0.052	10	$2.76 \cdot 10^{-5}$ [17]
Ethanol	$CH_3CH_2OH(l) + 3H_2O(l) = 2CO_2(g) + 6H_2(g)$	97.60	0.082	12	$31.6 \cdot 10^{-5}$ [18]
Urea	$CO(NH_2)_2(l) + H_2O(l) = CO_2(g) + N_2(g) + 3H_2(g)$	214.2	0.37	6	$7.14 \cdot 10^{-3}$ [19]

2.3.1. Calculations by absorbed photon energy balance model

To evaluate V_b we have to consider the space charge width (L_{sc}) given by equation (2.15):

$$L_{sc} = \sqrt{\frac{2\varepsilon_0 \varepsilon_{sc} V_b}{eN_D}} \tag{2.15}$$

where ε_0 is the vacuum permittivity (F/m), ε_{sc} is the relative permittivity of a semiconductor, N_D is the doping level (J^{-1} m^{-3}).

The value of V_b determines the width of the space-charge region, which in turn affects the charge separation efficiency. Thus, there is a trade-off between minimizing losses and ensuring good charge separation. It has been assumed that a value of 0.2 eV is optimal to address this issue in real systems [10,20,21].

The value E_c-E_F can be approximately evaluated by the equation (2.16) [22]:

$$E_c - E_F = \frac{k_B T}{e} \ln \frac{N_C}{N_D} \tag{2.16}$$

where E_c – conduction band edge position (eV), E_F – Fermi level (eV), k – Boltzmann's constant (J/K), e – electron charge (C), N_c – density of states in CB (J^{-1} m^{-3}).

As seen from Eq. 2.16, it is possible to decrease E_c-E_F value by increasing the concentration of n-type dopants N_D. This increases the concentration of electrons in the conduction band, and to maintain Fermi-Dirac statistics, the Fermi level must move closer to the bottom of the conduction band. However, adding dopants will also decrease the space charge width (Eq. 2.15): a higher concentration of charge carriers provides better screening, leading to a more rapid decay of the electrostatic potential away from the interface. Thus, the same trade-off exists here. The value of 0.2 eV is accepted as appropriate for real systems [10,20,21].

Ohmic losses are assumed to be zero for idealized case and 0.05 eV for real case [10,20].

For idealized case, no kinetic limitations are assumed, thus, all overpotentials equal 0. For real case, all overpotentials have been calculated using hypersinus approximation of Butler-Volmer equation (2.17), as this form gives a better approximation for unequal electron transfer coefficients [8]. The total current density is chosen to be 50 mA/cm^2, which is the upper estimate of realistic possible current in a PEC system (maximum light current of photoelectrode with E_g=1 eV). The electron transfer coefficients are assumed to be 0.5. The exchange current density for hydrogen and oxygen evolution reactions is 1 mA/cm^2 and 10^{-5} mA/cm^2, respectively. It is reported that these values can be achieved using Earth-abundant catalysts (such as NiMo for HER and NiZn, CoFe and NiMoFe for OER) [14]. The number of electrons participating in the reactions equals to two to be consistent with the literature [8]. The exchange current densities of organic oxidation are found in the literature for electrochemical oxidation of these compounds on different electrocatalysts as an estimate. The number of electrons participating in electrochemical reaction is assumed to be one, as it is unlikely that more electrons would participate in one elementary step, and the rate-determining step is always considered.

$$\eta = \frac{RT}{\alpha nF} \sinh^{-1}\left(\frac{j}{2j_0}\right) \tag{2.17}$$

where R – gas constant, 8.314 J/(mol K); T – temperature, 298 K; α – electron transfer coefficient, 0.5; n – number of electrons participating in elementary step, 2; F – Faraday's constant, 96485 C/mol; j – total current density, mA/cm^2; j_0 – exchange current density, mA/cm^2.

Thus, for the reaction of water oxidation, the losses are estimated to be about 0.95 eV, which is in good agreement with previous works and estimates [9,10]. For the oxidation reactions of organic compounds the losses are lower due to the better kinetics and lower anodic overvoltages (in the range between 0.59 eV for the fastest reaction of methanol oxidation and 0.93 eV for the slowest reaction of acetaldehyde oxidation).

2.3.2. Calculations by modified detailed balance model

For idealized case, only radiative recombination is considered, which is expressed by dark current, thus, ERE=1. Fraction of absorbed photons equal to 1, overpotentials equal to 0. Series and shunt resistances are 0 and ∞, respectively. This converts Eq. 2.10 into ideal diode equation and all voltage generated by the photoelectrochemical system is fully spent to drive electrochemical reaction.

For realistic case, series and shunt resistance are normalized to the ideal diode resistance, which is the ratio of the open circuit voltage and the short circuit current density. This normalization is needed to make the fill-factor reduction independent of bandgap energy. The normalized values are taken to be 0.1 and 10 [8]. Each of this contribution gives 10% reduction in fill-factor. ERE is taken to be 10^{-6} which is in agreement with the literature reports for the state-of-the-art PEC cells [23]. Fraction of absorbed photons equal to 0.9. All overpotentials are calculated by Eq. 2.17 with the same values discussed in the previous section.

2.3.3. Influence of thermodynamics: Idealized case

First, to investigate solely the effect of thermodynamic parameters of electrochemical reaction on solar conversion efficiency, the idealized case with no kinetic limitations (overpotentials equal to zero) is considered.

The results of this analysis for the oxidation of water, urea, acetic acid, and methanol are presented in Figure 2-4a. Both models describe the process in a similar manner, consistent with the literature [5,8,10]. A sharp cut-off in efficiency is observed at band gaps below the efficiency maximum, because photons absorbed at these band gaps do not provide sufficient energy to drive the electrochemical reaction; under these conditions, the process cannot proceed. At band gaps above the efficiency maximum, the efficiency also decreases due to the reduced fraction of absorbed solar energy (η_E in Eq. 2.8 decreases). Overall, the efficiency curves follow the solar energy absorption efficiency trend (Figure 2-4d) scaled by a reduction factor given by the chemical efficiency (Eq. 2.8).

The two models differ mainly in the turn-on band gap and in the shape and magnitude of the efficiency peak. The minimum band gap predicted by the APEB model is approximately 0.2 eV lower than that predicted by the MDB model. This difference is attributed to the underlying assumptions: in the APEB model, entropy-related losses are not included, whereas they are incorporated in the diode equation (Eq. 2.10). In addition, recombination can be neglected in the APEB framework, while Eq. 2.11 includes radiative recombination even under ideal conditions. Moreover, within the MDB approach, the efficiency peak is less sharp, and the maximum efficiency is typically 3–5% lower than that obtained from the APEB model at the same minimum band gap. In the MDB description, the operating point is constrained by the reaction voltage requirement; when E_g is too small, the required voltage is not reached, or, when it is approached, diode recombination increases and reduces the photocurrent. As a result, the operating current density (j_{op}, Eq. 2.13) and the efficiency decrease. In contrast, the APEB model evaluates primarily whether the required photovoltage can be generated, without explicitly accounting for the current-voltage dependence. Accordingly, the APEB model is used as a transparent and illustrative framework, whereas the detailed balance model is used as a more precise and realistic description. In the following sections, the analysis is mainly based on the second model, while the first one is also employed to support a more comprehensive interpretation of the results.

For water oxidation (E°=1.23 V), the maximum solar conversion efficiency is 30.6% for a semiconductor with a band gap of 1.59 eV, whereas for urea oxidation (0.37 V) it is 22.3% at 0.69 eV. For reactions with even lower standard electrode potentials, the maximum SCE shifts to band gaps below 1 eV, that is out of the range relevant for semiconductors, and they are less than 7%. This demonstrates that the employment

of thermodynamically more favorable reactions does not lead to higher SCE. According to Eq. 2.7, a lower Gibbs free energy at a fixed band gap decreases the chemical efficiency of the process and, consequently, reduces the solar conversion efficiency. This behavior is expected because, regardless of the energy required per elementary reaction step ($\Delta G/nF$), an energy equal to the band gap (E_g) is required to generate one electron-hole pair in the semiconductor. Therefore, a larger mismatch leads to higher losses and lower solar conversion efficiency.

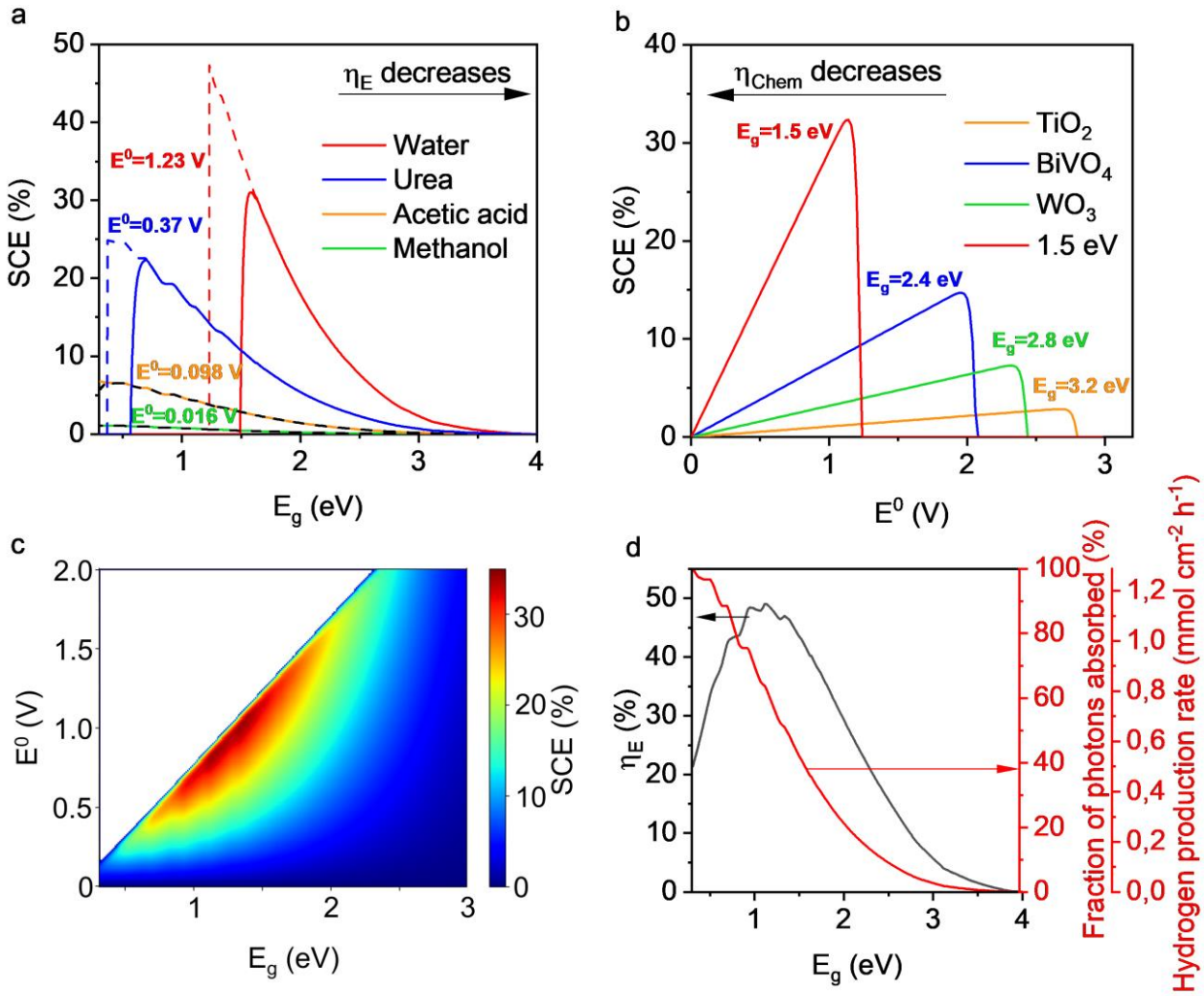

Figure 2-4 The theoretical solar conversion efficiencies calculated by absorbed photon energy balance model (dashed line) and modified detailed balance model (solid line) for ideal case in dependence on band gap energy for anodic reactions of water (red) urea (blue), acetic acid (orange) and methanol (green) oxidation (a); the theoretical solar conversion efficiencies calculated by modified detailed balance model in dependence of standard potential of anodic reaction for TiO_2/ZnO (orange), $BiVO_4$ (blue), WO_3 (green) and semiconductor with band gap 1.5 eV (red) (b); maximum theoretical efficiency versus semiconductor band gap and standard electrode potential of anodic reaction (c); dependence of hydrogen production rate on band gap energy (d).

Accordingly, at a fixed semiconductor band gap, replacing water splitting with thermodynamically more favorable anodic reaction results in a decrease in solar conversion efficiency. This trend is illustrated in Figure 2-4b, where the maximum theoretical solar conversion efficiencies of common semiconductors are plotted as a function of the standard electrode potential of the anodic reaction. The maximum is obtained

when the reaction potential matches the maximum photovoltage that can be generated by a semiconductor with the given band gap. Reactions with higher thermodynamic requirements cannot be driven, leading to a sharp efficiency drop. For reactions with lower standard electrode potentials, the efficiency decreases approximately linearly, reflecting the linear decrease of η_{Chem}.

Figure 2-4c shows how the ratio between the standard electrode potential of the anodic reaction and the semiconductor band-gap energy affects solar conversion efficiency. The upper-left white region corresponds to conditions under which the band-gap energy is insufficient to drive the electrochemical reaction. The maximum solar conversion efficiency of 34.5% is obtained for a reaction requiring 0.99 V when carried out on a semiconductor with a band gap of 1.34 eV (η_{Chem}=73.9% and η_E=46.5%). Notably, this value is slightly higher than the maximum solar conversion efficiency for water oxidation shown in Figure 2-4a (30.6%).

However, the use of reactions with lower thermodynamic requirements is expected to provide important advantages. In particular, a lower reaction free-energy demand allows the process to be driven on a narrower-band-gap photoelectrode. As indicated by the solar energy absorption efficiency curve (Figure 2-4d), solar energy is absorbed most effectively by semiconductors with band gaps in the range of 0.9-1.5 eV, with a maximum absorption efficiency of 49.11% at 1.12 eV. This implies that anodic reactions with small standard electrode potentials can be operated using photoelectrodes with band gaps that are optimal for solar energy absorption. The broader spectral absorption of such electrodes increases charge-carrier generation, thereby enabling higher hydrogen evolution rates (or higher yields of other valuable cathodic products) and higher oxidation fluxes of the target organic molecules.

2.3.4. Influence of kinetics: Realistic case

In this section, the influence of a kinetic parameter, namely the exchange current density, is investigated.

First, experimentally measured exchange current densities (Table 2-1), together with the series and shunt resistances, are considered to explain the deviation of the realistic case (Figure 2-5a) from the idealized case (Figure 2-4a). Although the trends observed under ideal conditions remain – qualitative agreement between the two models, a sharp efficiency decline at band gaps below the optimum, and a more gradual decrease at band gaps above the optimum following the decrease in solar absorption efficiency – the efficiencies are markedly lower and the minimum required band gaps are higher. In addition, the quantitative discrepancy between the two models increases. When additional losses are included, more energy is required to initiate the process; therefore, a higher photovoltage must be generated, which corresponds to a larger required band gap. The use of wider-band-gap semiconductors reduces light absorption and decreases the chemical efficiency. Within the modified detailed balance framework, when losses are introduced, the available voltage is progressively reduced, and the sharp cut-off is broadened into a wider, nearly symmetric peak. In contrast, the absorbed photon energy balance model can predict a minimum required band gap close to that obtained from the MDB model, but it does not capture the additional efficiency loss caused by reduced fill factor.

It is also observed that the inclusion of kinetic parameters changes the dependence of process efficiency on the standard potential of anodic reaction. In the idealized case, the highest solar conversion efficiency is obtained for the reaction with the largest thermodynamic requirement (water oxidation), due to its higher

chemical efficiency. In the realistic case, however, the highest efficiency can be achieved for urea oxidation (6.4% at 1.7 eV for urea oxidation versus 5.8% at 2.49 eV for water splitting). This is attributed to better reaction kinetics of urea oxidation: compared with the idealized case, the efficiency of water oxidation decreases faster than that of urea oxidation when kinetic losses are included. Therefore, the interplay between thermodynamic and kinetic parameters and its impact on solar conversion efficiency should be investigated.

Figure 2-5b presents the solar conversion efficiency as a function of the semiconductor band gap, the standard potential of the anodic reaction (thermodynamic parameter), and the exchange current density (kinetic parameter). At a fixed exchange current density, the cross-sections show the same qualitative behavior as in the idealized case (Figure 2-4c). However, as the exchange current density decreases, losses increase substantially; consequently, the minimum required band gap increases and the solar conversion efficiency decreases markedly. This trend is consistent with the findings of Fountain et al., who identify kinetic parameters as the most influential factors affecting efficiency [8]. Accordingly, the highest efficiency (16.53%) is obtained at the largest considered exchange current density (10 mA/cm^2) for a reaction with a standard electrode potential of 0.7 V on a photoanode with a band gap of 1.48 eV. Compared with the idealized case (Figure 2-4c), the maximum efficiency is reduced by almost a factor of two. This reduction is primarily associated with a lower chemical efficiency: the optimum remains in a band gap range with high solar absorption, where – after accounting for all losses – the process can be sustained only for reactions with lower thermodynamic requirements than in the idealized case (η_{Chem}=47.3% and η_E=43.8%).

Figures 2-5c,d illustrate the interplay between thermodynamic and kinetic parameters for reactions occurring on a single photoanode ($BiVO_4$, E_g=2.4 eV). The white region corresponds to conditions under which the process is thermodynamically forbidden because the semiconductor device cannot generate a sufficient photovoltage. Hydrogen production rate and SCE exhibit opposite trends with respect to the standard potential of the anodic reaction: SCE decreases as the standard potential decreases, whereas the hydrogen production rate increases. This illustrates how thermodynamics affects the kinetics: the same semiconductor can provide higher overpotential (which is the difference between valence band position and equilibrium potential) for the reaction with lower energy demand. This interplay leads to the fact that the system less efficient in usage of solar energy (lower SCE) can still be more efficient in terms of hydrogen production (higher generation rates). By contrast, both metrics show the same dependence on the exchange current density, increasing as it increases. For each value of the standard electrode potential, a threshold exchange current density is observed, above which further increases do not lead to a noticeable improvement in efficiency. In general, increasing the exchange current density beyond approximately 5 mA/cm^2 does not result in a higher solar conversion efficiency.

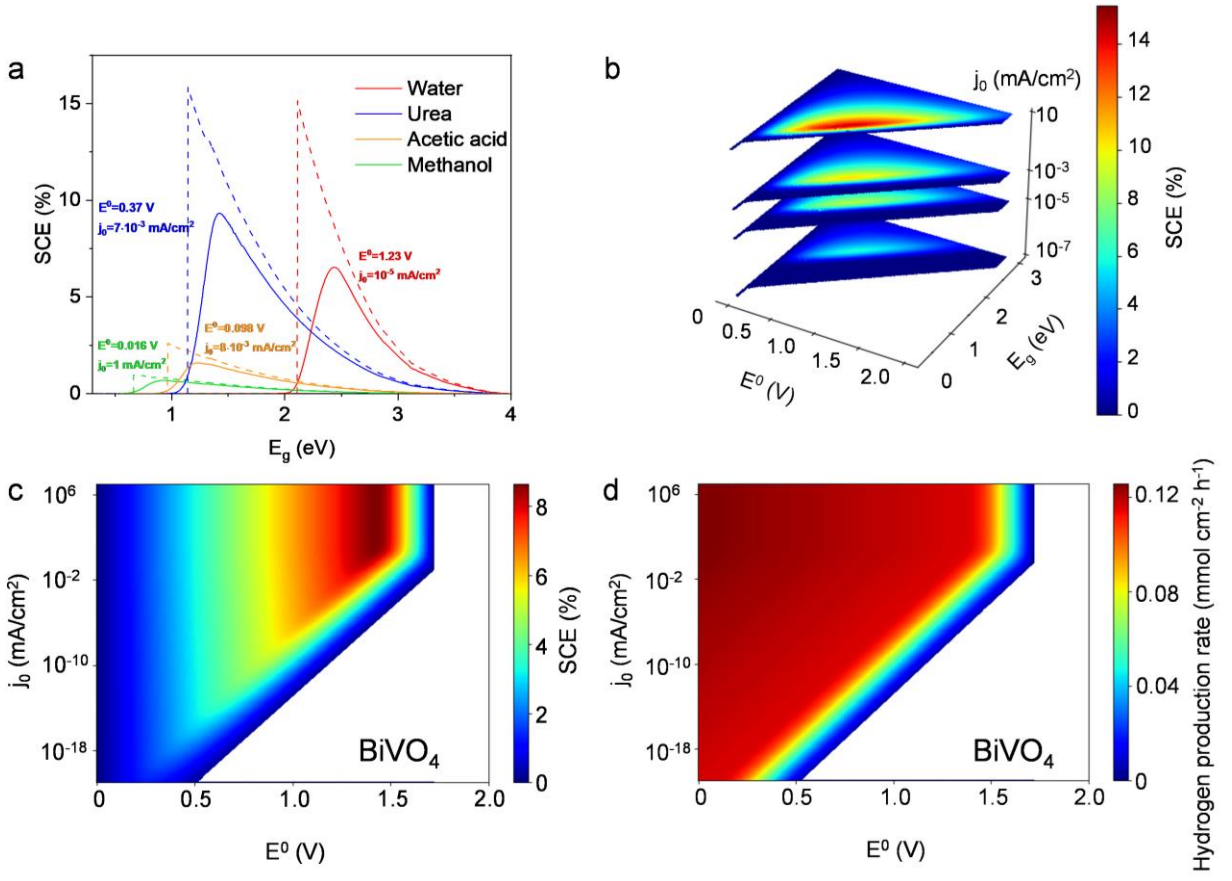

Figure 2-5 The theoretical solar conversion efficiencies calculated by absorbed photon energy balance model (dashed line) and modified detailed balance model (solid line) for real case in dependence on band gap energy for anodic reactions of water (red) urea (blue), acetic acid (orange), methanol (green), and acetaldehyde (purple) oxidation (a); the theoretical solar conversion efficiencies calculated by modified detailed balance model versus band gap, standard electrode potential and exchange current density of anodic reactions (b); effect of standard electrode potential and exchange current density on maximum theoretical solar conversion efficiency (c) and hydrogen production rate (d) of $BiVO_4$ (E_g=2.4 eV)

2.3.5. Comment on experimental data

Experimental results are considered to assess whether the tendencies described above are observed in practice.

The effect of faster kinetics is illustrated by Mohapatra et al. [24]. In this study, the influence of organic additives (methanol, glycerol, and ethylene glycol) on the photocurrent density of TiO_2 is examined (Figure 2-6a). The dependence on ethylene glycol concentration is also investigated, and an increase in concentration is shown to increase the photocurrent density. The substitution of water oxidation with glycerol oxidation is widely reported; for example, for $BiVO_4$ photoanodes, up to a threefold increase in current density at 1.2 V vs RHE is observed by different authors [25–27]. Lhermitte et al. show that the oxidation of the biomass-derived compound 2,5-hydroxymethylfurfural (HMF), which can be converted into key monomers for polyester production, efficiently suppresses water oxidation on WO_3, resulting in an approximately 30% increase in photocurrent [28].

Photocatalysis, in which both half-reactions occur on the same photocatalyst surface and the process operates without an external bias, shows the same qualitative trend as biased PEC systems: replacing water oxidation with organic oxidation increases the measured productivity, primarily due to more favorable reaction kinetics. Figure 2-6b summarizes the study by Zhang et al. on the oxidation of an organic pollutant (Reactive Red X-3B) using four commercial TiO_2 modifications; in all cases, water oxidation results in lower hydrogen production rates [29].

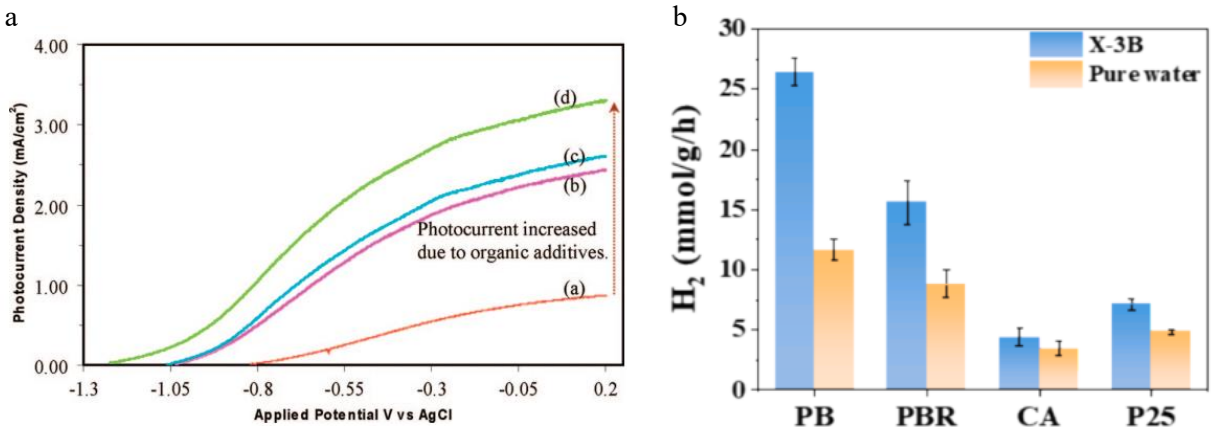

Figure 2-6 Influence of organic additives on productivity of PEC cells. (a) With external bias. Photocurrent density of TiO_2 photoanode in the absence of organic compounds (orange curve), with the addition of methanol (purple curve), glycerol (blue curve) and ethylene glycol (green curve). Adapted from [24] (b) Without external bias. Hydrogen generation rate on four commercial TiO_2 photocatalyst (PB – porous brookite, PBR – porous brookite/rutile, CA – commercial anatase, P25 – commercial P25) for the water oxidation reaction (orange bar) and oxidation of X-3B – organic pollutant Reactive Red X-3B. Adapted from [29].

A direct comparison of photocurrent density, SCE or hydrogen production rate of the same system employing different anodic reactions – water splitting or organic oxidation – in unbiased PEC cell was not found in the literature. The extensive review of Vilanova et al. (2024) [30] states that the highest reported solar-to-hydrogen efficiency of direct water splitting in unbiased PEC cell is 19.3% with an operating current of 15.4 mA/cm^2 and hydrogen production rate of 0.3 mmol/(h·cm^2) [31]. This was monolithic dual junction device RuO_2–GaAs/GaInAs/GaInP/AlInP–anatase TiO_2–Rh (dual-junction device). Noteworthy, Ko et al. [32] reported 1.40 mmol/(h·cm^2) hydrogen production rate with the photocurrent of 43.4 mA/cm^2 for the single junction device employing the PtC/Ni/c-Si as photoanode and Cu mesh as a cathode and anodic half reaction of furfural oxidation (E°=0.02 V vs RHE). One of the benefits of this device is the use of crystal silicon – a material of high industrial maturity. However, this device is not suitable for water splitting due to the too narrow band gap (1.1 eV). Therefore, replacement of the OER by a less thermodynamically demanding anodic reaction is required. Usage of semiconductor with narrower bandgap which was allowed by low energy requirements of furfural oxidation resulted in 4.9-times higher hydrogen production rate than the one of the record unbiased water-splitting device. Choi et al. [33] employed a single junction device with a perovskite photocathode (1.6 eV) and carbon nanotube anode. Again, this device cannot drive water splitting reaction; thus, it was replaced by the oxidation of phosphomolybdic acid – the derivative of lignocellulosic biomass. Narrow bandgap allowed to reach photocurrent of 19.8 mA/cm^2 and hydrogen production rate of 0.51 mmol/(h·cm^2). Moon et al. developed a device using perovskite as a cathode and NiO/NF as anode to drive furfural oxidation reaction resulting in 23.5 mA/cm^2 1.2

mmol/(h·cm^2). Overall, these examples prove that single-junction unbiased systems employing organic oxidation can exceed the productivity of unbiased dual-junction PEC cells operating with the OER, because narrower-band-gap semiconductors can be used.

It is also noted that replacing the OER with organic oxidation can lead to hydrogen formation not only via proton reduction at the cathode, but also as a by-product of the anodic oxidation process [34]. This effect can contribute to apparent hydrogen production rates that exceed the value expected from the measured photocurrent assuming 100% Faradaic efficiency, as reported, for example, in [32].

2.3.6. On the solar conversion efficiency of formation of key reactive oxygen species

In this section, the solar conversion efficiency of the formation of the most important reactive oxygen species (ROS) is considered.

Equation (2.18) describes the formation of hydroxyl radicals (HO$^\bullet$) – the most important radical in water treatment with the highest oxidative ability. Equation (2.19) describes the formation of sulfate radical anion ($SO_4^{2-\bullet}$), which can be generated in sodium sulfate – the most often used supporting electrolyte. Equation (2.20) represents the formation of superoxide anion radical ($O_2^{-\bullet}$) – radical which is formed at the cathode. Equations (2.21) and (2.22) show the hypochlorite/chlorite formation ($HClO^-$/$HClO_2^-$) – anions that are formed in chloride-containing water matrix and that are not only able to oxidize organic compounds but also act as disinfectant agent, i.e. are able to deactivate viruses, bacteria, fungi and macrobacterium.

$$HO^\bullet + H^+ + e^- \rightarrow H_2O \qquad E°=2.73\ V \qquad (2.18)$$

$$SO_4^{2-} + e^- \rightarrow SO_4^{\bullet -} \qquad E°=2.44\ V \qquad (2.19)$$

$$O_{2(aq)} + e^- \rightarrow O_2^{\bullet -} \qquad E°=-0.35\ V \qquad (2.20)$$

$$H^+ + HOCl + e^- \rightarrow \frac{1}{2}Cl_{2(g)} + H_2O \qquad E°=1.63\ V \qquad (2.21)$$

$$3H^+ + HClO_2^- + 3e^- \rightarrow \frac{1}{2}Cl_{2(g)} + \frac{1}{2}H_2O \qquad E°=1.64\ V \qquad (2.22)$$

Figure 2-7 demonstrates the solar conversion efficiency of this ROS neglecting kinetic limitations. The minimum band gap required to drive reaction (2.18) is 3.09 eV, which implies that only semiconductors absorbing less than 4.6% of the incident solar energy are able to sustain this reaction. As a consequence, the maximum solar conversion efficiency for hydroxyl radical formation is limited to 2.85% for a semiconductor with a band gap of 3.18 eV. This corresponds to a hydroxyl radical generation flux of 0.11 mmol/(m^2·s). This is an important observation posing that a generation of sufficiently high hydroxyl radical fluxes in unbiased systems is intrinsically limited and unlikely possible.

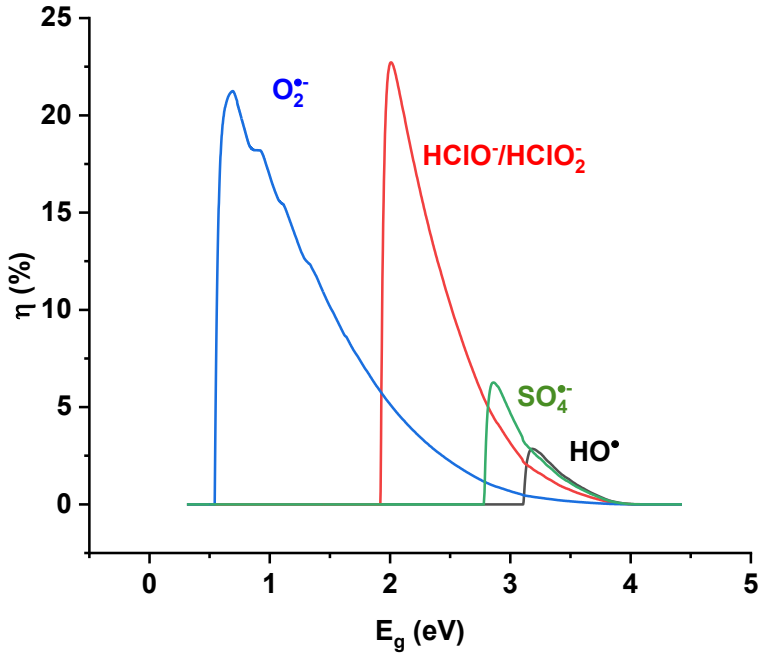

Figure 2-7 Solar conversion efficiency of formation of the most important reactive oxygen species: hydroxyl radical ($HO^{\bullet}$), sulfate radical anion ($SO_4^{\bullet-}$), superoxide anion radical ($O_2^{\bullet-}$), hypochlorite/chlorite formation ($HClO^-/HClO_2$). Calculations are performed using modified detailed balance model under idealized conditions

The formation of sulfate radicals requires semiconductors with band gaps larger than 2.77 eV, which corresponds to absorption of less than 4.8% of the incident solar energy, and results in a maximum solar conversion efficiency of 6.25% at a band gap of 2.86 eV. Therefore, their generation in unbiased PEC cells is also unlikely. Hypochlorite and chlorite formation requires a minimum band gap of 1.90 eV and reaches a maximum solar conversion efficiency of 22.73% at 2.0 eV. This value is the highest among the considered reactive oxygen species, although it is approximately 10% lower than the maximum theoretical solar conversion efficiency of a PEC cell operating with the oxygen evolution reaction as the anodic half-reaction. Consequently, the formation of these oxyanions is more probable than that of the previously discussed species. Finally, the formation of superoxide anion radicals requires semiconductors with a minimum band gap of 0.53 eV and reaches a maximum solar conversion efficiency of 21.2% at a band gap of 0.68 eV. However, materials with band gaps below 1 eV are metallic and not photoactive; therefore, this maximum efficiency is not achievable in practice. Nevertheless, superoxide formation is thermodynamically allowed over the entire range of semiconductor band gaps considered. This implies that, in any unbiased PEC cell with a conduction band edge positioned above -0.35 V vs RHE, the formation of superoxide anion radicals is thermodynamically feasible.

2.4. CONCLUSIONS

- For a given semiconductor photoelectrode, replacing the electrochemical reaction with a thermodynamically more favourable one does not lead to an increase in solar conversion efficiency; instead, it results in a decrease due to the reduction in chemical efficiency. Irrespective of the energy required to drive the electrochemical reaction, an energy equal to the semiconductor band gap (E_g)

is required to generate one charge carrier. The difference between these energies is dissipated as losses.

- Reactions with lower thermodynamic requirements can be performed on semiconductors with narrower band gaps, which are able to absorb a larger fraction of the solar spectrum. As a result, higher photocurrents and higher product fluxes can be achieved.
- The largest fraction of the solar spectrum is absorbed by semiconductors with band gaps in the range of 0.9–1.5 eV. When losses are taken into account, reactions requiring potentials of approximately 0.1–1.0 V are optimally matched with photoanodes in this band-gap range. Such thermodynamic requirements are characteristic of the oxidation of organic compounds.
- In the idealized case, where losses are neglected and kinetic limitations are absent, the maximum solar conversion efficiency reaches 34.5% for an anodic reaction requiring 0.99 V on a semiconductor with a band gap of 1.34 eV (η_{Chem}=73.9% and η_E=46.5%). In the realistic case, the maximum solar conversion efficiency decreases to 16.53% and is obtained at the highest considered exchange current density (10 mA/cm^2) for a reaction with a standard electrode potential of 0.7 V on a photoanode with a band gap of 1.48 eV (η_{Chem}=47.3% and η_E=43.8%).
- These conclusions are supported by experimental results. The highest reported solar-to-hydrogen efficiency for direct water splitting in an unbiased PEC cell is 19.3%, with a hydrogen production rate of 0.3 mmol/(h·cm^2). In contrast, replacing the oxygen evolution reaction with less thermodynamically demanding anodic reactions (such as furfural or phosphomolybdic acid oxidation) enables the use of narrower-band-gap photoelectrodes and results in significantly higher hydrogen production rates (1.40, 1.20, and 0.51 mmol/(h·cm^2)), although the corresponding solar conversion efficiencies are substantially lower (below 2%).
- Kinetics exerts a stronger influence on efficiency and productivity than thermodynamics. When reaction kinetics is slow, photogenerated charge carriers cannot be extracted efficiently from the semiconductor surface, leading to reduced photocurrent, productivity, and overall efficiency.
- The formation of hydroxyl radicals in unbiased PEC systems is unlikely to occur at sufficiently high fluxes.
- Hypochlorite and chlorite formation exhibits the highest solar conversion efficiency among the considered reactive oxygen species (22.73%) and requires semiconductors with band gaps larger than 1.9 eV. In contrast, superoxide anion radicals can be formed across the entire range of band gaps corresponding to semiconducting materials.

REFERENCES

1. Shi, Q.; Duan, H. Recent Progress in Photoelectrocatalysis beyond Water Oxidation. Chem Catal. 2022, 2, 3471–3496, doi:10.1016/j.checat.2022.11.007.
2. Papagiannis, I.; Doukas, E.; Kalarakis, A.; Avgouropoulos, G.; Lianos, P. Photoelectrocatalytic H2 and H2O2 Production Using Visible-Light-Absorbing Photoanodes. Catalysts 2019, 9, 243, doi:10.3390/catal9030243.
3. Li, J.; Wu, N. Semiconductor-Based Photocatalysts and Photoelectrochemical Cells for Solar Fuel Generation: A Review. Catal. Sci. 2015, 5, 1360–1384, doi:10.1039/c4cy00974f.
4. Bolton, J.R. Solar Fuels. Science (80-.). 1978, 202, 705–711.
5. Bolton, J.R.; Strickler, S.J.; Connolly, J.S. Limiting and Realizable Efficiencies of Solar Photolysus of Water. Nature 1985, 316, 495–500.
6. Murphy, A.B.; Barnes, P.R.F.; Randeniya, L.K.; Plumb, I.C.; Grey, I.E.; Horne, M.D.; Glasscock, J.A. Efficiency of Solar Water Splitting Using Semiconductor Electrodes. Int. J. Hydrogen Energy 2006, 31, 1999–2017, doi:10.1016/j.ijhydene.2006.01.014.
7. Varghese, O.K.; Grimes, C.A. Appropriate Strategies for Determining the Photoconversion Efficiency of Water Photoelectrolysis Cells: A Review with Examples Using Titania Nanotube Array Photoanodes. Sol. Energy Mater. Sol. Cells 2008, 92, 374–384, doi:10.1016/j.solmat.2007.11.006.
8. Fountaine, K.T.; Lewerenz, H.J.; Atwater, H.A. Efficiency Limits for Photoelectrochemical Water-Splitting. Nat. Commun. 2016, 7, 1–9, doi:10.1038/ncomms13706.
9. Pleskov, Y. V. Solar Energy Conversion in Photoelectrochemical Cells with Semiconductor Electrodes. Prog. Surf. Sci. 1984, 15, 401–456, doi:10.1016/0079-6816(84)90005-4.
10. Nozik, A.J. Photoelectrolysis of Water Using Semiconducting TiO2 Crystals. Nature 1975, 257, 383–386.
11. Nelson, J. The Physics of Solar Cells; 2003; Vol. 01; ISBN 1860943403.
12. Shockley, W.; Queisser, H.J. Detailed Balance Limit of Efficiency of P-n Junction Solar Cells. 1961, 32, 510–519, doi:10.1063/1.1736034.
13. Honsberg, S.B.; Bowden, S.G. Photovoltaics Education Website Available online: www.pveducation.org.
14. McCrory, C.C.L.; Jung, S.; Ferrer, I.F.; Chatman, S.M.; Peters, J.C.; Jaramillo, T.F. Benchmarking Hydrogen Evolving Reaction and Oxygen EvolvingReaction Electrocatalysts for Solar Water Splitting Devices. J. Am. Chem. Soc. 2015, 137, 4347–4357.
15. Bekmezci, M.; Yildizay, H.; Kokoglu, B.; Sen, F. Nanoengineered Pt – V Catalysts Promote Efficient Methanol Oxidation in Carbon Nanotubes †. RSC Adv. 2025, 15, 27848–27863,

doi:10.1039/d5ra03938j.

16. Alshammari, B.H.; Begum, H.; Ibrahim, F.A.; Hamdy, M.S.; Oyshi, T.A.; Khatun, N.; Hasnat, M.A. Electrocatalytic Hydrogen Evolution Reaction from Acetic Acid over Gold Immobilized Glassy Carbon Surface. Catalysts 2023, 13, 744, doi:10.3390/catal13040744.
17. Communication, I.C.; Karim-nezhad, G.; Pashazadeh, A. Kinetic Study of the Electrocatalytic Oxidation of Acetaldehyde at Ni/Al Layered Double Hydroxide Modified Sol-Gel Derived Carbon Ceramic Electrode. Iran. Chem. Commun. 2015, 3, 103–113.
18. Habibi, B.; Ghaderi, S. Ethanol Electrooxidation on the Co@Pt Core-Shell Nanoparticles Modified Carbon-Ceramic Electrode in Acidic and Alkaline Media. Iran. J. Hydrog. Fuel Cell 2016, 1, 19–31, doi:10.22104/ijhfc.2016.314.
19. El-lateef, H.M.A.; Khalaf, M.M.; Mohamed, I.M.A. Advances in Phosphorus-Based Catalysts for Urea Electrooxidation : A Pathway to Sustainable Waste to Energy Conversion Through Electrocatalysis. Catalysts 2024, 14, 937, doi:10.3390/catal14120937.
20. Anderson, W.W.; Chai, Y.G. Becquerel Effect Solar Cell. Energy Convers. 1976, 15, 85–94, doi:10.1016/0013-7480(76)90020-6.
21. Гуревич, В.А.; Плесков, Ю.В. Фотоэлектрохимия Полупроводников; 1983;
22. Memming, R. Semiconductor Electrochemistry; Wiley-VCH, 2015; ISBN 9783319296418.
23. Green, M.A. Radiative Efficiency of State-of-the-art Photovoltaic Cells. Prog. Photovoltaics Res. Appl. 2012, 20, 472–476, doi:10.1002/pip.1147.
24. Mohapatra, S.K.; Raja, K.S.; Mahajan, V.K.; Misra, M. Efficient Photoelectrolysis of Water Using TiO2 Nanotube Arrays by Minimizing Recombination Losses with Organic Additives. J. Phys. Chem. C 2008, 112, 11007–11012, doi:10.1021/jp7100539.
25. Liu, D.; Liu, J.; Cai, W.; Ma, J.; Yang, H. Bin; Xiao, H.; Huang, Y.; Liu, B. Selective Photoelectrochemical Oxidation of Glycerol to High Value-Added Dihydroxyacetone. Nat. Commun. 2019, 10, 1779, doi:10.1038/s41467-019-09788-5.
26. Yi-Hsuan, W.; Kuznetsov, D.A.; Pflug, N.C.; Alexey, F.; Muller, C.R. Solar-Driven Valorisation of Glycerol on BiVO4 Photoanodes: Effect of Co-Catalyst and Reaction Media on Reaction Selectivity. J. Mater. Chem. A 2021, 9, 6252–6260, doi:10.1039/d0ta10480a.
27. Bora, D.K.; Nadjafi, M.; Armutlulu, A.; Hosseini, D.; Castro-Fernandez, P.; Toth, R. Photoelectrochemical Glycerol Oxidation on Mo-BiVO4 Photoanodes Shows High Photocharging Current Density and Enhanced H2 Evolution. Energy Adv. 2022, 1, 715, doi:10.1039/d2ya00077f.
28. Lhermitte, C.R.; Plainpan, N.; Canjura, P.; Boudoire, F.; Sivula, K. Direct Photoelectrochemical Oxidation of Hydroxymethylfurfural on Tungsten Trioxide Photoanodes. RSC Adv. 2021, 11, 198–

202, doi:10.1039/d0ra09989a.

29. Zhang, X.; Cheng, Z.; Bo, C.; Sun, Y.; Piao, L. The Photocatalytic Wastewater Hydrogen Production Process with Superior Performance to the Overall Water Splitting. J. Colloid Interface Sci. 2025, 677, 189–197, doi:10.1016/j.jcis.2024.06.039.
30. Vilanova, A.; Dias, P.; Lopes, T.; Mendes, A. The Route for Commercial Photoelectrochemical Water Splitting: A Review of Large-Area Devices and Key Upscaling Challenges. Chem Soc Rev 2024, 53, 2388–2434, doi:10.1039/d1cs01069g.
31. Cheng, W.-H.; Richter, M.H.; May, M.M.; Ohlmann, J.; Lackner, D.; Dimroth, F.; Hannappel, T.; Atwater, H.A.; Lewerenz, H. Monolithic Photoelectrochemical Device for Direct Water Splitting with 19% Efficien. ACS Energy Lett. 2018, 3, 1795–1800, doi:10.1021/acsenergylett.8b00920.
32. Ko, M.; Lee, M.; Kim, T.; Jin, W.; Jang, W.; Hwang, S.W.; Kim, H.; Kwak, J.H.; Cho, S.; Seo, K.; et al. Coupling Furfural Oxidation for Bias-Free Hydrogen Production Using Crystalline Silicon Photoelectrodes. Nat. Commun. 2025, 16, 2701, doi:10.1038/s41467-025-58000-4.
33. Choi, Y.; Mehrotra, R.; Lee, S.; Vu, T.; Nguyen, T.; Lee, I.; Kim, J.; Yang, H.; Oh, H.; Kim, H.; et al. Bias-Free Solar Hydrogen Production at 19.8 MA Cm-2 Using Perovskite Photocathode and Lignocellulosic Biomass. Nat. Commun. 2022, 13, 5709, doi:10.1038/s41467-022-33435-1.
34. Costantino, F.; Kamat, P. V Do Sacrificial Donors Donate H 2 in Photocatalysis? ACS Energy Lett. 2022, 7, 242–246, doi:10.1021/acsenergylett.1c02487.

CHAPTER III: KEY OPERATIONAL PARAMETERS AND INHERENT LIMITATIONS OF $BiVO_4$ PHOTOANODES IN ORGANIC POLLUTANTS DEGRADATION

3.1. INTRODUCTION

Based on the results of the literature review, $BiVO_4$ was selected as a reference semiconductor material for the experimental investigation of the photoelectrocatalytic oxidation of pharmaceutical pollutants.

$BiVO_4$ fulfils the key sustainability and practicality requirements for potential large-scale applications. It is a non-toxic material composed of earth-abundant elements, cost-efficient [1]. In addition, it can be synthesized in the form of both powders and thin films using scalable techniques such as electrodeposition [2], sol-gel techniques [3], hydrothermal synthesis [4], and spin-coating [5,6].

The choice of $BiVO_4$ is primarily motivated by its relatively narrow band gap (E_g~2.4 eV, absorption edge at λ<520 nm), which allows it to absorb a significant fraction of the standard solar spectrum (approximately 18%). This value is higher than that of many other photoactive materials used for the oxidation of organic pollutants in photoelectrocatalysis (Chapter I, Table 1-1). As a result, $BiVO_4$ can potentially operate under natural sunlight, whereas TiO_2 and ZnO – are activated only under UV irradiation ((E_g~3.2 eV, absorb at λ<400 nm) and therefore require artificial light sources, which are associated with additional energy costs.

In contrast to ZnO, which undergoes photocorrosion in aqueous solutions [7], and WO_3, which requires strongly acidic conditions (pH<4) to maintain stability [8], $BiVO_4$ remains stable within a relatively wide pH window (5<pH<11), which makes it suitable for application in real wastewater treatment systems [9].

Furthermore, the conduction and valence band edges of $BiVO_4$ are located at approximately 0.1 V and 2.5 V vs. SHE, respectively [5,9]. The oxidation potentials of many organic compounds fall within this potential range, which makes $BiVO_4$ a suitable photoanode for the removal of organic pollutants. Numerous studies have confirmed that unmodified $BiVO_4$ is capable of oxidizing a variety of organic contaminants, although with modest efficiency. Reported degradation efficiencies include approximately 50% degradation of sulfamethoxazole within 2 h [10], 70% degradation of ciprofloxacin within 2 h [11], 70% degradation of phenol within 4 h [12], up to 32% degradation of a range of polycyclic aromatic hydrocarbons within 8 h [13], and 88% degradation of isopropanol within 12 h [14]. However, these degradation rates remain insufficient for large-scale practical applications.

Therefore, the aim of this chapter is to establish the foundation for the subsequent experimental studies by identifying the key factors limiting the performance of bare $BiVO_4$ towards oxidation of organic pollutants and determine the optimal values of operational parameters for the further degradation experiments.

This chapter begins with the electrochemical characterization of $BiVO_4$, aimed at describing its photoelectrochemical behavior and identifying the intrinsic factors that limit its performance.

Subsequently, the chapter provides an analysis of preliminary experiments on oxidation of simple organic model compounds, aimed at assessing how the performance-limiting factors identified for $BiVO_4$ manifest themselves during, and ultimately influence, its photoelectrochemical degradation activity.

Finally, an analysis of the key operational parameters influencing the photoelectrochemical oxidation of organic compounds is presented. Based on this assessment, the most suitable values of these parameters are determined.

3.2. MATERIALS AND METHODS

3.2.1. Materials

All reagents were of analytical grade and used without further purification. Bismuth nitrate pentahydrate ($Bi(NO_3)_3 \cdot 5H_2O$), potassium iodide (KI), vanadyl acetylacetonate ($VO(acac)_2$), dimethyl sulfoxide (DMSO), Salicylic acid ($C_7H_6O_3$), Phenol (C_6H_6O), Congo Red, sodium sulfate (Na_2SO_4), sodium sulfite (Na_2SO_3) and fluorine-doped tin oxide (FTO) coated glass substrates with a surface resistance of 7 $\Omega \cdot cm^{-2}$ were purchased from Sigma-Aldrich. Benzoic acid (C_5H_5COOH) ans sodium hydroxide (NaOH) were purchased from Carlo Erba (Reagents s.r.l, Italy). Aqueous solutions were prepared using distilled water (DW).

3.2.2. Synthesis procedure

$BiVO_4$ samples for preliminary investigations (Section 3.2 Electrochemical Characterization and Section 3.3 Preliminary Organic Compound Oxidation Experiments) were synthesized using the Successive Ionic Layer Adsorption and Reaction (SILAR) method [3].

FTO glass substrates were cleaned according to the following procedure: ultrasonic treatment in acetone for 15 min, followed by ultrasonic treatment in ethanol for 15 min, and finally ultrasonic treatment in distilled water for 15 min. The cleaned substrates were then dried under ambient conditions.

Subsequently, a piece of cleaned FTO was vertically immersed in a 5 mM aqueous solution of $Bi(NO_3)_3 \cdot 5H_2O$ for 10 s and then transferred into a 5 mM aqueous solution of KI for an additional 10 s. This immersion sequence was repeated for 10 min, corresponding to 60 SILAR cycles, resulting in the formation of a bright orange BiOI layer on the FTO substrate.

A vanadium precursor solution (0.2 M $VO(acac)_2$ dissolved in DMSO) was drop-cast onto the BiOI-coated surface at a volume of 50 $\mu L/cm^2$. The samples were then annealed in air at 450 °C for 2 h, with a heating rate of 2 °C/min.

The resulting $BiVO_4$ films were immersed in 1 M NaOH solution for 30 min under gentle stirring to remove residual V_2O_5. The samples were subsequently rinsed thoroughly with distilled water and dried in air.

The experiments presented in Section 3.4 Operational parameters were carried out with the use of $BiVO_4$ and $BiVO_4$/β-FeOOH samples prepared by synthesis procedures described in detail in the following chapter (Chapter 4, Section 4.2.2 $BiVO_4$ thin film synthesis and Section 4.2.3 β-FeOOH deposition).

3.2.3. Experimental set-up

Both electrochemical characterization and preliminary degradation experiments were conducted in 300 mL beaker containing 200 mL of solution in a typical three-electrode configuration. Reference electrode is 3 M KCl Ag/AgCl (0.21 V vs SHE), counter electrode is platinum mesh cylinder.

The characterization was performed in 0.1 M Na_2SO_4 solution with a natural pH (5.6-6.4). When required, 0.2 M Na_2SO_3 was added as a hole scavenger. An Autolab PGSTAT302N was used. Ossila Solar Simulator imitating AM 1.5G Standard solar spectra (irradiance 100 mW/cm^2) was used as a light source in characterization experiments. The surface area of working electrode for characterization experiments is 1 cm^2.

Degradation experiments were carried out under continuous magnetic stirring at 800 rpm. Illumination was supplied by a 36 W light-emitting diode lamp with a wavelength of 455 nm. The surface area of working electrode for characterization experiments is 6 cm^2. Aqueous solutions containing various organic contaminants (salicylic acid, benzoic acid, phenol, and Congo red) were prepared at an initial concentration of 20 mg/L in 0.1 M N_2SO_4 electrolyte.

The concentration of target organic compunds was monitored during the experiment by UV-vis spectroscopy using spectrophotometer Jasco V-630 operated in a transmission mode. The normalized concentration C/C_0 was obtained from the ratio of absorbances A/A_0, according to the Beer's law ($A=lc\varepsilon$).

All degradation experiments were performed for a total duration of 240 min. Aliquots were collected at reaction times of 0, 10, 20, 30, 40, 60, 90, 120, 180, and 240 min for analysis..

A detailed description of the experimental setup and operating conditions used in the studies presented in Section 3.4 Operational Parameters is provided in Chapter 4, Section 4.2.5 Photocatalytic and Photoelectrocatalytic Degradation of Pharmaceuticals.

3.3. ELECTROCHEMICAL CHARACTERIZATION OF $BIVO_4$ PHOTOANODE

3.3.1. Linear Sweep Voltammetry

Electrochemical characterization of bare $BiVO_4$ provides insight into the main factors that limit its photoelectrochemical performance. Although most electrochemical characterization experiments are carried out in buffered electrolytes to ensure a defined pH and to allow conversion of potentials to the RHE scale, all experiments in this work are performed under conditions typical for electrochemical oxidation, i.e., in a common supporting electrolyte (0.1 M Na_2SO_4) at its natural pH (without adjustment). Consequently, the potentials versus RHE are only estimated using pH ≈ 5.8 and E (3 M KCl Ag/AgCl vs RHE)=0.209 V according to the following formula:

$$E(\text{vs RHE}) = E\ (\text{vs Ag/AgCl}) + E_{Ag/AgCl}(\text{vs RHE}) + 0.059\,pH \tag{3.1}$$

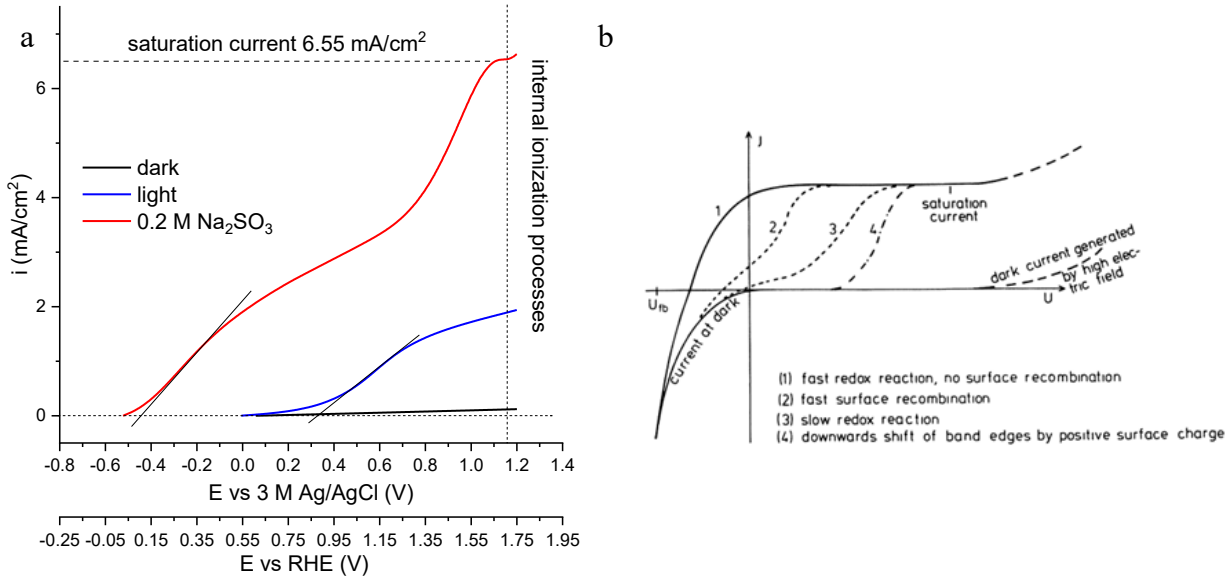

Figure 3-1 (a) Linear sweep voltammetry of a bare $BiVO_4$ photoelectrode. Back illumination by a solar simulator with a standard spectra AM 1.5G (100 mW/cm^2). Counter electrode – Pt mesh cylinder, reference electrode – 3 M KCl Ag/AgCl, 200 ml of 0.1 M Na_2SO_4 with addition of 0.2 M Na_2SO_3 (red), scan rate 100 mV/s. Natural pH around 5.8. (b) Theoretical prediction of different shapes of LSV curves [15].

Figure 3-1a shows typical LSV curves for bare, unmodified $BiVO_4$. As predicted by the semiconductor electrochemistry [16], in the case of photoactive material the water oxidation begins before the standard electrode potential E°=1.23 V (vs RHE) (Figure 3-1a blue curve). This behavior is explained by the valence band edge of $BiVO_4$ being located at approximately 2.5 V vs RHE, so the photogenerated holes already possess sufficient energy to oxidize water prior to the application of any external bias. The applied bias does not change the overpotential, as the overpotential is determined solely by the positions of the semiconductor band edges, which are pinned and independent of the applied potential. Instead, the applied bias enhances the separation of charge carriers. Therefore, the increase in current with increasing potential is attributed to the greater number of charge carriers available to participate in the electrochemical reaction [17].

However, theory predicts that water oxidation starts at the flat band potential, which for $BiVO_4$ is approximately -0.53 V vs 3 M Ag/AgCl [18], whereas in our case the photocurrent onset potential is observed at around 0.34 V vs 3 M Ag/AgCl and 0.89 V vs RHE. This discrepancy is attributed to slow kinetics: when charge carriers are not injected into the solution through the electrochemical reaction, they accumulate at the surface, and this excess surface carrier concentration drives surface recombination [19,20]. The surface recombination can be considered as an alternative carrier sink to the photocurrent leaving the semiconductor. Therefore, additional potential is required to suppress the surface recombination and to allow photocurrent to flow.

Although theoretical photocurrent density for $BiVO_4$ under the standard AM 1.5G solar spectra is calculated to be 7.5 mA/cm^2, the experimental values of bare $BiVO_4$ do not reach this value. Typically, the photocurrent does not exceed 2 mA/cm^2 at E=1.23 V vs RHE and in our case at such electrode potential it equals to 1.25 mA/cm^2. As already stated, even when electron–hole pairs reach the semiconductor/solution interface, not all of them are consumed by the electrochemical water-oxidation reaction because of the high

kinetic barrier. This limitation can be illustrated by introducing a component whose oxidation is much easier than water oxidation and which therefore removes the kinetic constraints. The red curve in Figure 3-1a shows LSV recorded with the addition of a hole scavenger, sodium sulfite, which is exclusively oxidized when it is present due to its much more favorable kinetics compared to the one of water oxidation. In this case the photocurrent is significantly enhanced, confirming that the limiting factor of $BiVO_4$ photoelectrode performance is its poor catalytic activity towards water oxidation [21].

It is also observed that the current onset potential in the presence of sulfite is shifted to -0.44 V vs 3 M Ag/AgCl towards flat band potential (-0.53 V vs 3 M Ag/AgCl). This result is expected, since surface recombination and photocurrent generation are two processes competing for the same charge carriers; therefore, when the electrochemical reaction is promoted, fewer carriers remain available for recombination, and consequently less potential is required to suppress it.

Comparison of the experimental curves (Figure 3-1a) with the theoretically predicted ones (Figure 3-1b) shows that, in the absence of hole scavenger the $BiVO_4$ performance is governed by slow reaction kinetics (blue experimental curve corresponds to the third curve in the theoretical plot), whereas when the kinetic barriers are largely removed, the behavior still deviates from the ideal case due to the fast surface recombination (red experimental curve corresponds to the second theoretic curve). This is an interesting observation, as it leads to the conclusion that passivation of surface recombination centers represents an alternative strategy to cocatalyst modification for enhancing the photocurrent [22,23].

It is particularly interesting to observe the short plateau of a saturated current predicted by theory, during which all absorbed photons are converted into charge carriers that contribute to the photocurrent. The value of this saturation current is close to the calculated maximum theoretical current for $BiVO_4$ (6.55 mA/cm^2 vs 7.5 mA/cm^2), and the deviation is explained by the fact that not all photons capable of being absorbed are actually absorbed. The potential range over which saturation is achieved is short – 1.11-1.16 V vs 3 M Ag/AgCl (1.66-1.73 V vs RHE) – and the potential required to completely suppress recombination is high. In the literature, there are examples of much more efficient energy usage where bare $BiVO_4$ (however, modified by nanostructuring [2] or introduction of oxygen vacancies [24]) reaches >90% electron-hole separation efficiency at lower potentials around 1.23 V vs RHE. At the potential higher than 1.16 V vs 3 M Ag/AgCl the photocurrent exceeds the saturation value. This behavior is attributed to the application of a strong electric field which induces internal ionization processes leading to the generation of additional minority carriers. The application of such strong fields is undesirable, as it may result in semiconductor lattice damage and rapid photoanode degradation.

3.3.2. Chronoamperometry

The measurement of chopped photocurrent chronoamperometry provides information about surface recombination and photocorrosion occurring in the system.

Figure 3-2a presents the chopped LSV curve recorded with a very low scan rate (0.005 V/s) to unsure current stabilization at each potential. It is observed that, throughout the entire studied potential range, the photocurrent decays from the maximum value reached upon illumination to a stabilized value. This decay is determined by the rate at which holes are trapped at the semiconductor surface [25], which explains why

the decay becomes faster at lower applied potentials. After stabilization, the current reaches a steady-state value that depends on the relative rates of recombination and charge transfer to redox species [26].

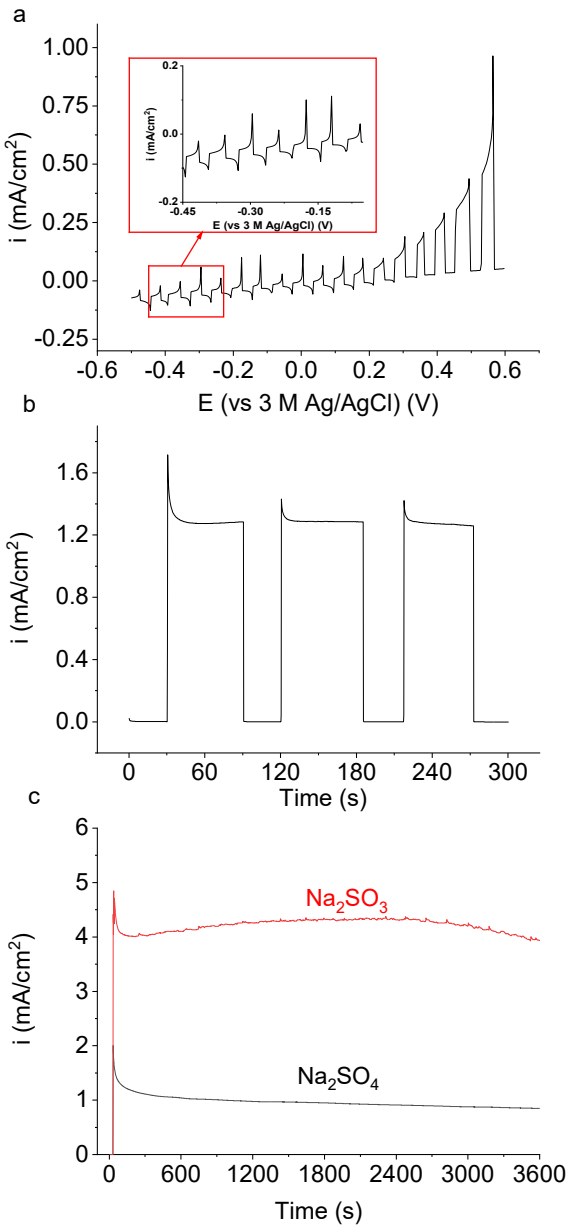

Figure 3-2 (a)Chopped linear sweep voltammetry (0.005 V/s); (b) chopped chronoamperometry, E=0.8 V vs RE; (c) chronoamperometry without (black) and with hole scavenger (red). WE – $BiVO_4$, CE – Pt wire, RE – 3 M Ag/AgCl, 0.1 M Na_2SO_4 (+0.2 M Na_2SO_3), diode 400 nm 100 mW/cm^2, natural pH~5.8.

In the vicinity of flat band potential the anodic transients are increased and the cathodic transient occurs after the light is switched off. This behavior is attributed to the increased relaxation time that results from reduced band bending. The origin of the cathodic negative transient is explained by the fact that, once the light is turned off, the trapped holes can no longer move, whereas electrons can still diffuse from the bulk and oxidize these trapped holes, thereby generating a negative photocurrent [27].

It is noteworthy that even at potentials far from the flat-band potential, where the cathodic transient photocurrents are diminished, the anodic photocurrent decay remains evident, once again emphasizing that surface recombination plays a major role in the performance of $BiVO_4$ (Figure 3-2b). This photocurrent decay does not represent a constant value; depending on the sample, it can reach up to 30% within 2 minutes.

Figure 3-2c shows the chronoamperometry recorded at longer times. Although at short time scales it is observed that, after the rapid decrease in current following illumination, the current reaches a steady-state value (Figure 3-2b), at longer times a continuous and very slow current decay is observed. This slower decay is attributed to the photocorrosion of $BiVO_4$ [5,28]. Holes accumulated at the surface destabilize the lattice and lead to the bulk dissolution of $BiVO_4$; the resulted Bi- and, particularly, V- vacancies act as additional recombination centers, further decreasing the number of charge carriers and thus photocurrent. This hypothesis is supported by the fact that in the presence of hole scavenger (0.2 M Na_2SO_3) the current decay is reduced. In the absence of hole scavenger, the current decreases by 32% from the steady-state value reached 2 minutes after illumination over the course of 1 hour, whereas in the presence of the scavenger the decay is only about 3% over 1 hour.

3.4. PRELIMINARY ORGANIC COMPOUNDS OXIDATION EXPERIMENTS

To preliminarily evaluate the potential of $BiVO_4$ for photoelectrochemical degradation of organic pollutants, experiments with different model organic compounds are performed. According to the literature, bare $BiVO_4$ exhibits low activity in the visible-light degradation of organic pollutants; therefore, to obtain conclusive results on the factors limiting the performance of unmodified $BiVO_4$, the experiments are carried out under strict illumination using a 455 nm diode with a light power exceeding 1 Sun, instead of a solar simulator.

Different aromatic compounds are selected for the initial evaluation: one with an electron-donating substituent (phenol), one with an electron-withdrawing substituent (benzoic acid), and two compounds containing both types of functional groups (salicylic acid and Congo red). The degradation results are shown in Figure 3-3a. It is observed that 6% of benzoic acid, 5% of phenol, 23% of salicylic acid, and 31% of Congo red are removed in four hours. These values are very low, and the degradation performance cannot be considered efficient.

It is worth noting that in all cases the measured current varies in a quite wide range, owing to the low reproducibility of the samples (which is common for photoelectrocatalytic materials). However, no relationship is observed between the total charge passed through the system and the absolute number of degraded moles: 210 C are passed to remove 2 μmol of benzoic acid, 117 C are passed to remove 6 μmol of salicylic acid, 65 C are passed to remove 2.4 μmol of phenol, and 47 C are passed to remove 1.72 μmol of Congo red. This observation may indicate that oxidation in the system is selective, and that certain compounds are oxidized more readily than others due to more favorable interactions with the surface layer of the semiconductor electrode.

Figure 3-3c and 3-3d show the results of the kinetic analysis for the degradation of these four compounds. It should be noted that the absorbance of phenol increases during the first hour of the experiment and

decreases afterwards. This behavior is occasionally observed in the photodecomposition of phenolic compounds and is likely caused by the formation of an oxidation by-product that absorbs at the same wavelength but has a higher molar absorption coefficient. Therefore, for the kinetic analysis of phenol degradation, only the data points collected after one hour are used. The results show that zero-order oxidation occurs in all cases, which is typical for heterogeneous reactions that are not limited by mass transport.

The limiting current density for these concentrations of organic pollutants is in order of tens мA/cm^2. This estimation is made assuming mass transport coefficient k_m=10^{-6} m/s for mixed-tank reactor [30] and complete mineralization, thus, for phenol, salicylic acid, benzoic acid and Congo red limiting currents are 57.4, 39.1, 47.4 and 38.2 мA/cm^2, respectively. The generated photocurrents are much higher than these limiting currents (Figure 3-3b) and the fact that in these conditions system demonstrates the behavior typical for the regime operating under kinetic control indicates poor catalytic properties of $BiVO_4$ towards oxidation of organic compounds.

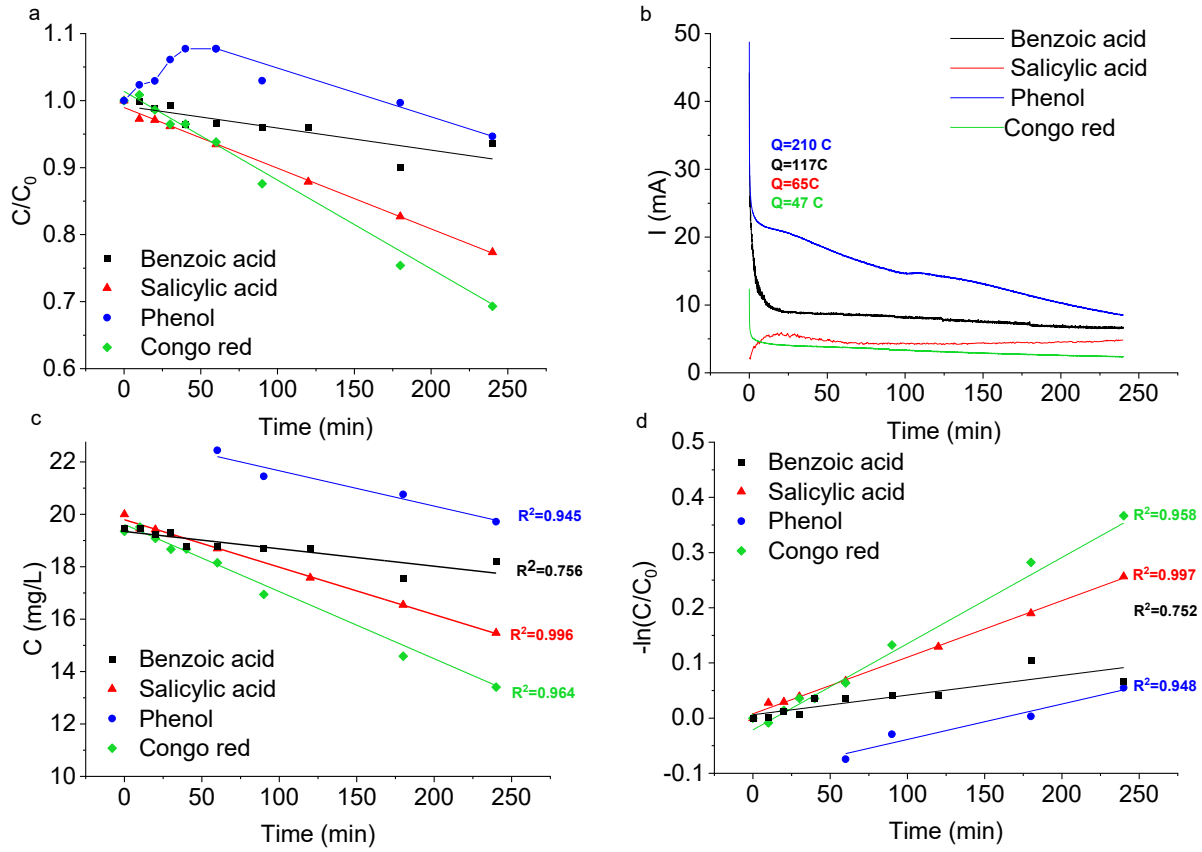

Figure 3-3 Study of model organic compounds (benzoic acid – black squares, salicylic acid – red triangles, phenol – blue triangles, Congo red – green rhombus) photoelectrochemical oxidation on bare $BiVO_4$. Degradation (a), current density evolution during degradation (b), zero-order kinetics (c), first-order kinetics (d).

3.5. OPERATIONAL PARAMETERS

3.5.1. Influence of light source placement

It is observed that the position of the light source influences the photocatalytic degradation efficiency. Without the application of external bias, front illumination favors degradation compared to back illumination. This effect is attributed to light absorption. The number of absorbed photons per unit volume (I) decreases with increasing distance (x) from the illuminated surface x [17]:

$$I = I_0 \exp(-\alpha x) \tag{3.2}$$

where I_0 is the photon flux density of the light source entering the sample, α is the absorption coefficient of the material.

Under back illumination, most photons are absorbed at the photocatalyst/FTO interface, and their number then decreases exponentially toward the photocatalyst/electrolyte interface. Consequently, the generated electron-hole pairs follow the same spatial distribution. In the absence of an electric field, there is no movement of charges from the photocatalyst/FTO interface toward the photocatalyst/electrolyte interface, and those charges that do not participate in the electrochemical reaction and remain in the bulk of the semiconductor rapidly recombine. Thus, the number of charge carriers available at semiconductor/ electrolyte interface is very low and it corresponds to a small fraction of absorbed photons. Under front illumination, most photons are absorbed at the photocatalyst/electrolyte interface and thus most of the electron-hole pairs become immediately available for the electrochemical reaction at semiconductor/electrolyte interface. Therefore, in PC front illumination mode should be more efficient than back illumination mode.

Figure 3-4 supports this conclusion. In the photocatalytic degradation of paracetamol both on bare $BiVO_4$ and on modified $BiVO_4$/β-FeOOH, front illumination leads to faster degradation than back illumination.

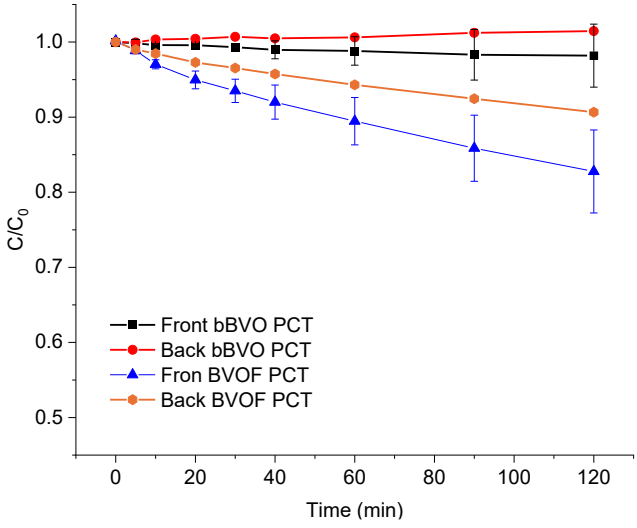

Figure 3-4 Photocatalytic oxidation of PCT on bare $BiVO_4$ and modified $BiVO_4$/β-FeOOH photoelectrodes under front (black and blue) and back (red and orange) illumination modes.

In photoelectrocatalytic experiments, i.e., when an external bias is applied, an increase in photocurrent is observed when the $BiVO_4$ photoelectrode is illuminated from the back. This effect is well known for $BiVO_4$, as poor electron mobility is recognized as one of the major factors limiting its performance. Under front illumination, electrons must travel through the entire depth of the semiconductor, whereas under back illumination electron-hole pairs are generated at the substrate/photocatalyst interface, increasing the flux of electrons entering the external circuit and consequently increasing the total current [29]. In this case, the number of charge carriers available for electrochemical reaction is also increased. Therefore, improved degradation of an organic compound is expected under back illumination in PEC process.

Figure 3-5 supports this expectation. In all cases on modified $BiVO_4$/β-FeOOH photoanode, the degradation of both compounds – paracetamol and sulfamethoxazole – is improved and accelerated under back illumination conditions. However, this increase in current also leads to an increase in specific energy consumption (Table 3-1). Because the distribution of current between the two electrochemical reactions involved– water splitting and organic oxidation – is not changed when the total current increases, the majority of the current continues to be directed toward the parasitic reaction of water oxidation. Therefore, as the total current increases, the amount of wasted current increases as well.

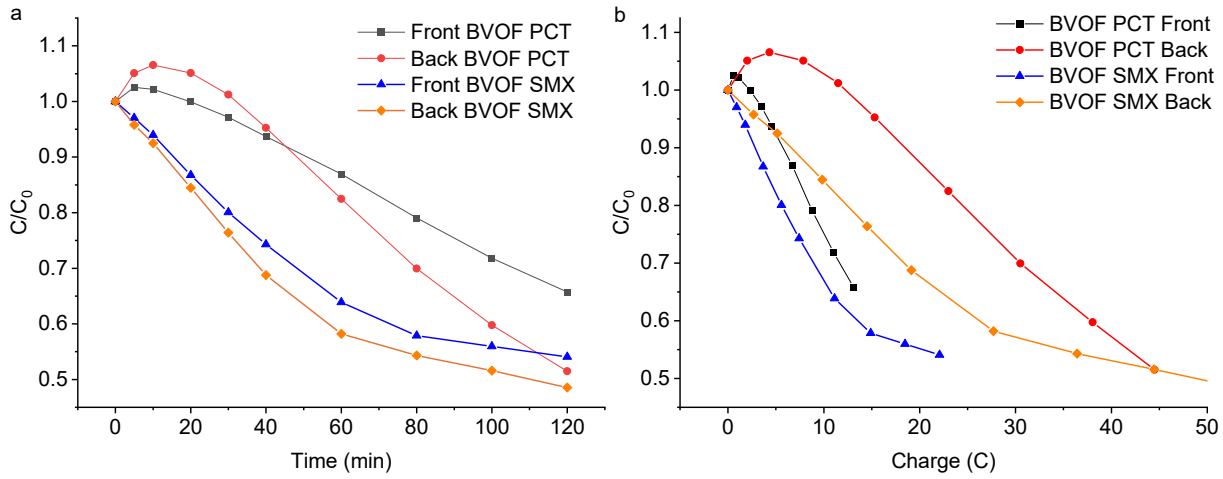

Figure 3-5 Photoelectrocatalytic oxidation of PCT and SMX on bare $BiVO_4$ photoelectrodes under front (black and blue) and back (red and orange) illumination modes.

Thus, to unsure more efficient energy consumption and, more importantly, better conditions for comparison of PC and PEC experiments, the front illumination mode is chosen for both PC and PEC experiments.

Table 3-1 Comparison of energy utilization efficiency of photoelectrocatalytic degradation in front and back illumination modes. Degradation of PCT and SMX on $BiVO_4$/β-FeOOH photoanode under application of 0.8 V vs Ag/AgCl is presented.

	PCT Front	**PCT Back**	**SMX Front**	**SMX Back**
Removal rate, %	34.2	48.5	45.9	51.4
Total charge, C	13.11	44.49	22.07	52.90
Energy consumption, kW/m3	1.38	4.82	2.40	8.56
Energy consumption for 1 mg of pollutant removal, Wh/mg	1.2	3.0	1.6	5.0

3.5.2. Influence of applied bias

In the case of photoelectrocatalytic system the external bias may be required for two reasons:

(1) The band positions do not allow electrochemical reactions. The energy of electrons (holes) in conduction (valence) band is not enough to drive reduction (oxidation). In this case the application of external bias is needed to change the quasi-Fermi level of electrons (holes) to make the corresponding half-reaction possible.

(2) To increase the electron-hole separation to raise the total number of charge curriers in the system.

In the case of $BiVO_4$ used as a photoanode, the conduction band (CB) is positioned at 0.09 V vs RHE and the valence band (VB) at 2.49 V vs RHE [30,31]. Thus, the band positions of $BiVO_4$ are sufficient to allow the oxidation of water and most organic compounds, whereas the CB position slightly differs from the potential required for the hydrogen evolution reaction. Therefore, a small external bias of approximately –0.1 V is required to drive hydrogen reduction. When the overpotential is taken into account (which for a Pt counter electrode is assumed to be -0.1 V), the total potential necessary to overcome this limitation is equal to -0.2 V [32].

To roughly estimate the theoretical potential required to achieve complete electron-hole separation, a brief analysis of Figure 3-6 is conducted. Electron-hole pairs are generated throughout the region where photons are absorbed; therefore, the thickness of the generation zone is taken as the absorption depth, which is defined as the inverse of the absorption coefficient (α^{-1}). As a first approximation, it is assumed that within the space charge region (L_{sc}), all generated electron-hole pairs are separated by the internal electric field. The hole diffusion length (L_p) defined as $L_p = \sqrt{D_p \tau_p}$, where D_p is the hole diffusion coefficient in SC (m/s^2) and τ_p is the hole lifetime (s) represents the average distance a hole is able to travel before it is recombined with an electron. Consequently, the total thickness of the separation zone is taken as $L_{sc}+L_p$.

The following conditions can therefore be described:

- Electron-hole pairs are generated at x< α^{-1};
- At x< L_{sc}, electron-holes are separated by electric field;
- At L_{sc}<x< L_{sc}+L_p carriers are transported to the space charge region by diffusion and, subsequently, reach the interface without recombination being preserved by electric field;
- At x> L_{sc}+ L_p recombination occurs, making it unlikely for the carriers to reach the interface.

Thus, two possible relationships exist between the thicknesses of the generation and separation zones. When the separation zone is thinner than the generation zone $L_{sc}+L_p<\alpha^{-1}$, (Figure 3-6a) not all electron-holes reach the interface. Most holes generated outside the separation zone recombine before reaching the interface and therefore do not contribute to the photocurrent. In contrast, when the separation zone is thicker than the generation zone (Figure 3-6b), all generated carriers are efficiently separated, and recombination is minimized.

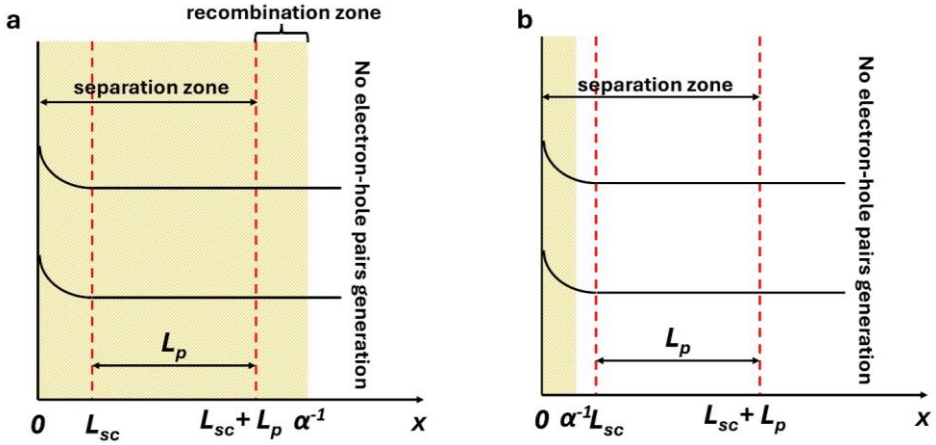

Figure 3-6 Schematic representation of the possible relationships between the absorption depth, the space charge region, and the diffusion length in a semiconductor.

The thickness of the separation zone can be varied by increasing the space charge region through the application of an external bias. The entire applied potential contributes to the change in the potential drop across the semiconductor, $\Delta\varphi_{sc}$, rather than across the Helmholtz layer; thus, $\Delta\varphi_{sc}=E_{bias}$ [25]. The space charge region depends on semiconductor potential according to the following equation:

$$L_{sc} = \sqrt{\frac{2\Delta\varphi_{sc}\varepsilon_r\varepsilon_0}{eN_D}} \tag{3.3}$$

where ε_0 is the vacuum permittivity ($8.85\cdot10^{-14}$ F·cm^{-1}), ε_r is the relative permittivity, e is the electron charge ($1.602\cdot10^{-19}$ C), N_D is the concentration of donors. Thus, the minimum estimate of potential required to apply to separate all electron-hole pairs:

$$E_{sep} = \frac{(\alpha^{-1} - L_p)^2 eN_D}{2\varepsilon_r\varepsilon_0} \tag{3.4}$$

Taking into account the parameters from Table 3-2 for $BiVO_4$, the lower estimate of the potential required for complete electron-hole separation in $BiVO_4$ is equal to 1 V vs the flat-band potential (0.09 V vs RHE for $BiVO_4$ [4]). It is noteworthy that this estimate is significantly lower than the potential for

complete charge separation shown in Figure 3-1a for unmodified $BiVO_4$ (1.7 V vs RHE), and is slightly lower than the potentials reported in the literature for complete electron-hole separation in bare $BiVO_4$ with modified nanostructures [2] or with introduced oxygen vacancies [33] (Figure 3-7), which are reported as 1.2 V vs RHE. This discrepancy is explained by the fact that the estimate is an approximation, as it does not account for recombination in the space-charge region and does not consider that, when holes accumulate at the semiconductor interface (which occurs under conditions of slow electrochemical reaction), their concentration at the boundary of the space-charge region is also increased, resulting in a reduced diffusion driving force [15]. Therefore, in practice, the potential required for complete charge separation is always higher than the estimated value. At the same time, for modified $BiVO_4$ samples in which the modification is intended to reduce recombination or charge transfer, the experimental values are close to the estimated potential, whereas in the case of unmodified $BiVO_4$ the deviation is significantly larger.

Table 3-2 Semiconductor properties of $BiVO_4$.

Parameter	Value
Absorption coefficient, cm-1	0.19·105 [34]
Relative permittivity	68 [35]
Concentration of donors, cm-3	1.4·1019 [31]
Hole diffusion length, nm	56 [34]

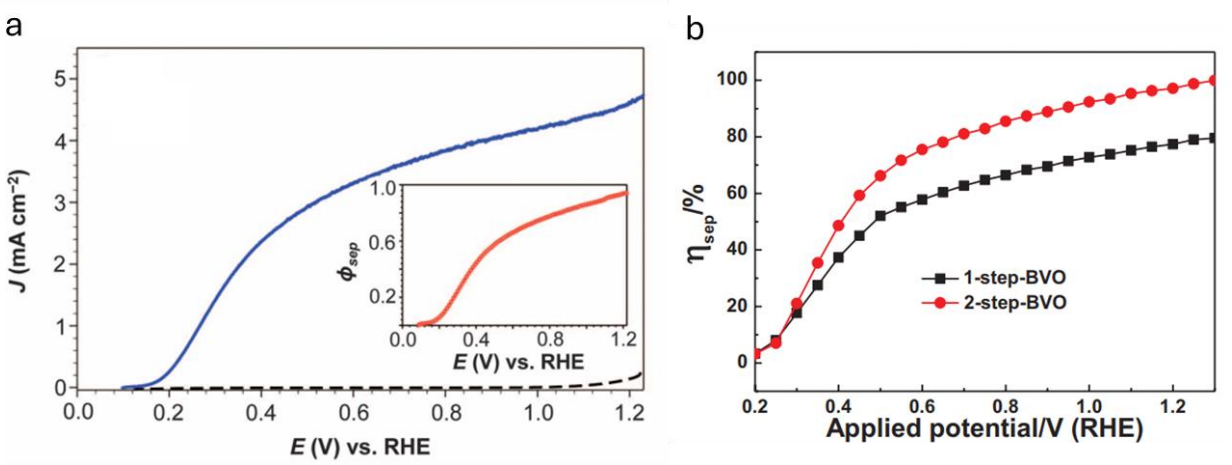

Figure 3-7 Literature data on complete electron-hole separation in $BiVO_4$ photoanode. (a) Nanoporous $BiVO_4$ measured in 0.5 M phosphate buffer (pH 7) containing 1 M Na_2SO_3 under AM 1.5G, 100 mW/cm^2 illumination [2], (b) $BiVO_4$ with introduced oxygen vacancies measured in 1 M borate buffer (pH 9) containing 0.2 M Na_2SO_3 under AM 1.5G, 100 mW/cm^2 illumination [33].

Figure 3-8 shows the dependence of the applied potential on the degradation efficiency of paracetamol (PCT) and on the photocurrent. It is observed that the application of higher potential leads to an increase in photocurrent and degradation efficiency. This result is expected, as an increased total photocurrent indicates

that more charge carriers are available for the oxidation of organic molecules and that a greater amount of oxidative species is formed. However, this also implies higher energy losses due to the increase in the partial current spent on the water oxidation reaction.

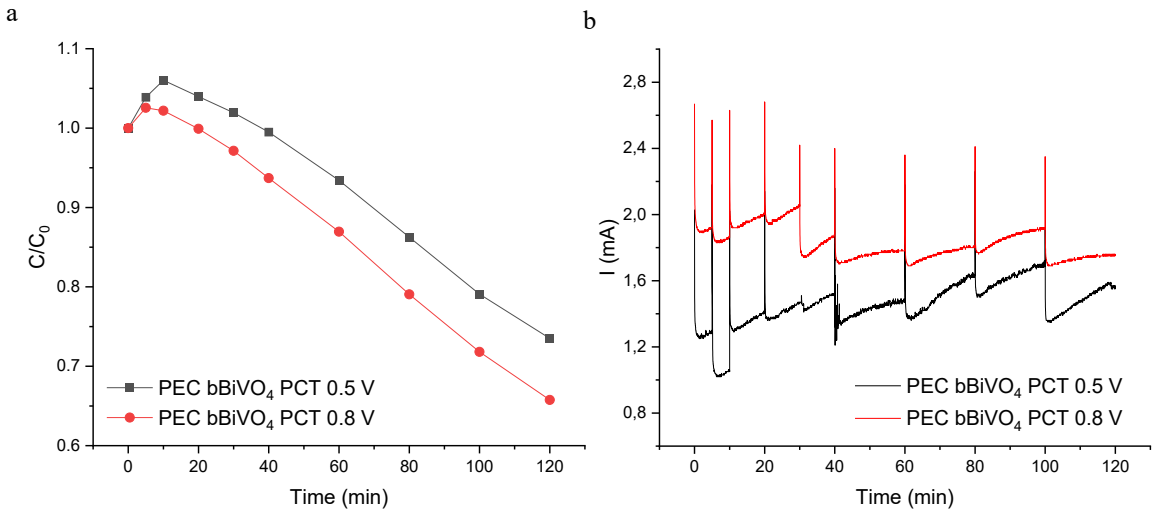

Figure 3-8 Effect of applied bias on paracetamol degradation (a) and on photocurrent (b). 6 ml 20 mg/L PCT, bare $BiVO_4$ as WE, 1 M Ag/AgCl as RE, Front illumination by 100 mW/cm^2 400 nm diode.

Nevertheless, for the subsequent experiments, a potential of 0.8 V (vs 1 M Ag/AgCl) is chosen to ensure efficient electron-hole separation and an adequate number of charge carriers available for the electrochemical reaction on one hand, and on the other hand, to remain within the potential range that does not induce an excessively strong electric field inside the semiconductor, which would lead to internal ionization and destructive processes within the lattice.

3.5.3. Influence of pH

In this study, experiments were carried out at the natural solution pH (5.6-6.4) without buffer addition. This approach is advantageous for laboratory-scale investigations because no additional species are introduced into the system; therefore, the number of possible intermediates is reduced and potential interfering effects that could complicate data interpretation are minimized. In addition, $BiVO_4$ is stable within this pH range. Working at natural pH also enables investigation under conditions that are representative of wastewaters and natural waters, which increases the practical relevance of the results. From an application perspective, avoiding pH adjustment may also reduce the operating cost at industrial scale, as no extra chemicals are required for pH control.

It is well established that pH can affect the charge carried by a compound. When pH exceeds pK_a, the compound is mainly present in its deprotonated (negatevily charged) form; when pH is below pK_a, the protonated (positevely charged) form predominates. Under anodic polarization, the $BiVO_4$ surface is positively charged. Consequently, positively charged molecules may be electrostatically repelled from the surface, which could decrease the degradation rate, whereas negatively charged molecules may experience stronger electrostatic attraction, potentially enhancing adsorption and degradation.

Carbamazepine has pK_a values of 2.3 and 13.9 between which it exists in zwitterion forms without any charge. Therefore, within the pH range used in this work it is expected to be predominantly neutral and its degradation should therefore be largely independent of electrostatic adsorption, which is consistent with literature reports [38]. Sulfamethoxazole has pK_a values of 1.7 and 5.6; thus, at pH 5.6-6.4 it is present mainly in the neutral form, with only a minor fraction in the anionic form [39]. This limited amount of negatively charged SMX is not expected to largely affect the degradation process. Paracetamol has pK_a values of 9.39 and 9.86 [40]; therefore, within the natural pH range it is expected to carry positive charge and experience an electrostatic repulsion from the positively charged $BiVO_4$ surface. However, this expectation is not supported by the experimental data: the effect of pH on the $BiVO_4$ photoelectrocatalytic oxidation of paracetamol is shown in Figure 3-9, and no significant dependence of the removal rate on pH is observed. Moreover, the current response of the system remains essentially unchanged across the studied pH values; therefore, very similar energy consumptions are obtained at different pH values.

Overall, this analysis supports the decision to conduct experiments at natural pH representative of real wastewater conditions. For the investigated pharmaceutical compounds, pH variations within 5.6-6.4 do not significantly affect oxidation performance, indicating that operation without pH adjustment is a justified and practically applicable strategy.

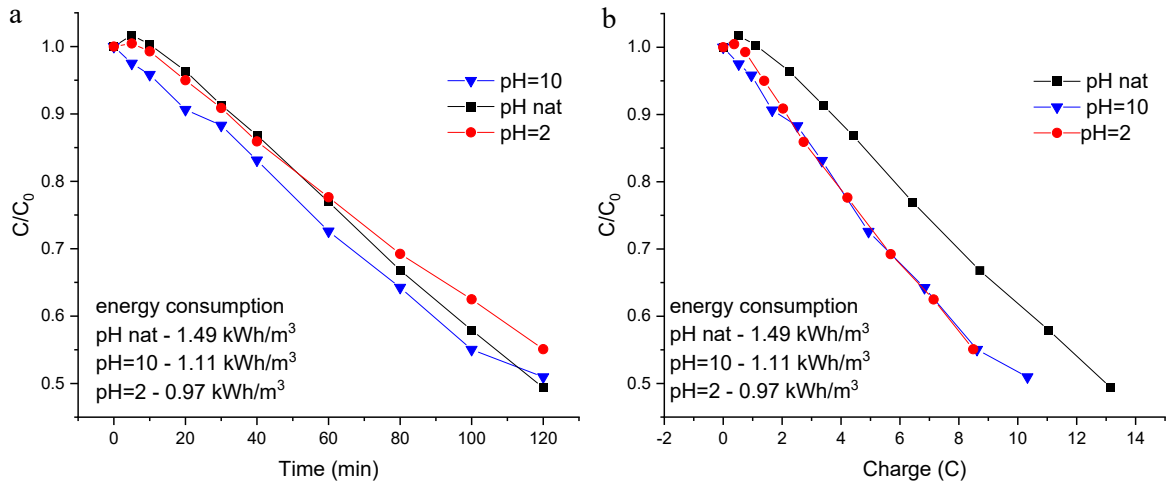

Figure 3-9 pH influence of PCT degradation efficiency and energy consumption.

3.6. CONCLUSIONS

- $BiVO_4$ exhibits low catalytic activity toward water oxidation, which results in an experimental photocurrent that is significantly lower than the theoretical value. However, this fact may have a positive effect on the oxidation of organic pollutants, since water oxidation is a parasitic reaction in this process.
- $BiVO_4$ suffers from rapid surface recombination. Even when kinetic limitations are removed and the electrochemical reaction rapidly consumes holes from the surface, a considerable potential still must be applied to achieve complete electron-hole separation and to reach saturated current. Therefore, the passivation of surface recombination centers may be considered as a strategy for improving the photoelectrochemical performance of $BiVO_4$.

- Although back illumination produces higher photocurrents, the improvement in degradation rate is modest (approximately 15%), whereas energy consumption increases dramatically (3.5 times). For this reason, front illumination is chosen for all subsequent experiments.
- The external electric potential does not affect the overpotential of the electrochemical reaction, but it is required to increase the number of available charge carriers by improving electron-hole separation. In the case of $BiVO_4$, a potential of 1 V vs the flat-band potential is considered sufficient for complete electron-hole separation. Therefore, for further experiments, 0.8 V vs 1 M Ag/AgCl is chosen as the working potential.
- The solution pH does not influence photoelectrocatalytic oxidation. Therefore, the natural pH (without the addition of buffers) is used in subsequent experiments.
- The performance of $BiVO_4$ in the oxidation of organic compounds is primarily limited by its low catalytic activity toward organic molecules oxidation, its high susceptibility to electron-hole recombination and photocorrosion. Consequently, efforts must be directed toward identifying a cocatalyst that reduces the kinetic barriers of organic oxidation and enhances the photostability of $BiVO_4$.

REFERENCES

1. Trinh, D.T.T.; Khanitchaidecha, W.; Channei, D.; Nakaruk, A. Synthesis, Characterization and Environmental Applications of Bismuth Vanadate; Springer Netherlands, 2019; Vol. 45; ISBN 0123456789.
2. Kim, T.W.; Choi, K.S. Nanoporous BiVO4 Photoanodes with Dual-Layer Oxygen Evolution Catalysts for Solar Water Splitting. Science (80-.). 2014, 343, 990–995, doi:10.1126/science.1246913.
3. Xiong, B.; Wu, Y.; Du, J.; Li, J.; Liu, B.; Ke, G.; He, H.; Zhou, Y. Cu3Mo2O9/BiVO4 Heterojunction Films with Integrated Thermodynamic and Kinetic Advantages for Solar Water Oxidation. 2020, 0–8, doi:10.1021/acssuschemeng.0c04561.
4. Kamble, G.S.; Ling, Y.-C. Solvothermal Synthesis of Facet - Dependent B Photocatalyst with Enhanced Visible - Light - Driven Photocatalytic Degradation of Organic Pollutant : Assessment of Toxicity by Zebrafish Embryo. Sci. Rep. 2020, 10, 12993, doi:10.1038/s41598-020-69706-4.
5. Toma, F.M.; Cooper, J.K.; Kunzelmann, V.; McDowell, M.T.; Yu, J.; Larson, D.M.; Borys, N.J.; Abelyan, C.; Beeman, J.W.; Yu, K.M.; et al. Mechanistic Insights into Chemical and Photochemical Transformations of Bismuth Vanadate Photoanodes. Nat. Commun. 2016, 7, doi:10.1038/ncomms12012.
6. Nguyen, T.D.; Nguyen, V.H.; Nanda, S.; Vo, D.V.N.; Nguyen, V.H.; Van Tran, T.; Nong, L.X.; Nguyen, T.T.; Bach, L.G.; Abdullah, B.; et al. BiVO4 Photocatalysis Design and Applications to Oxygen Production and Degradation of Organic Compounds: A Review. Environ. Chem. Lett. 2020, 18, 1779–1801, doi:10.1007/s10311-020-01039-0.
7. Dimitropoulos, M.; Aggelopoulos, C.A.; Sygellou, L.; Tsantis, S.T.; Koutsoukos, P.G. Unveiling the Photocorrosion Mechanism of Zinc Oxide Photocatalyst : Interplay between Surface Corrosion and Regeneration. J. Environ. Chem. Eng. 2024, 12, 112102, doi:10.1016/j.jece.2024.112102.
8. Knöppel, J.; Zhang, S.; Speck, F.D.; Mayrhofer, K.J.J.; Scheu, C.; Iek-, H.E.R.E.; Jülich, F. Time-Resolved Analysis of Dissolution Phenomena in Photoelectrochemistry – A Case Study of WO3 Photocorrosion. Electrochem. commun. 2018, 96, 53–56, doi:10.1016/j.elecom.2018.09.008.
9. Ali, A.Z.; Mohapatra, S.; Hoek, J.P. Van Der; Spanjers, H. BiVO4-Based Photoanodes for the Photoelectrocatalytic Removal of Trace Organic Pollutants from Water : A Mini Review on Recent Developments. Curr. Opin. Environ. Sci. Heal. 2025, 45, 100615, doi:10.1016/j.coesh.2025.100615.
10. Fuentes-Camargo, I.; Carrera-Crespo, J.E.; Vazquez-Arenas, J.; Romero-Ibarra, I.; Rodriguez, J.L.; Lartundo-Rojas, L.; Cardoso-Mart, J. Pulse-Plating Electrodeposition of Metallic Bi in an Organic-Free Aqueous Electrolyte and Its Conversion into BiVO4 To Improve Photoelectrochemical Activity toward Pollutant Degradation under Visible Light. J. Phys. Chem. C 2020, 124, 1421–1428, doi:10.1021/acs.jpcc.9b09898.

11. Carrera-Crespo, J.E.; Fuentes-Camargo, I.; Palma-Goyes, R.E.; García-Perez, U.M.; Vazquez-Arenas, J.; Chairez, I.; Poznyak, T.; AChairez, I.; Poznyak, T. Unrevealing the Effect of Transparent Fluorine-Doped Tin Oxide (FTO) Substrate and Irradiance Configuration to Unmask the Activity Of. Mater. Sci. Semicond. Process. 2021, 128, 105717.
12. Bennani, Y.; Perez-Rodriguez, P.; Alani, M.J.; Smith, W.A.; Rietveld, L.C.; Zeman, M.; Smets, A.H.M. Photoelectrocatalytic Oxidation of Phenol for Water Treatment Using a BiVO4 Thin-Film Photoanode. J. Mater. Res. 2016, 31, 2627–2639, doi:10.1557/jmr.2016.290.
13. Kohtani, S.; Tomohiro, M.; Tokumura, K.; Nakagaki, R. Photooxidation Reactions of Polycyclic Aromatic Hydrocarbons over Pure and Ag-Loaded BiVO4 Photocatalysts. Appl. Catal. B Environ. 2005, 58, 265–272, doi:10.1016/j.apcatb.2004.12.007.
14. Huang, C.; Pan, G.; Peng, P.; Yang, T.C. Chemical In Situ DRIFT Study of Photocatalytic Degradation of Gaseous Isopropanol over BiVO4 under Indoor Illumination. J. Mol. Catal. A. Chem. 2010, 327, 38–44, doi:10.1016/j.molcata.2010.05.009.
15. Cardon, F.; Gomes, W.P.; Dekeyser, W. Photovoltaic and Photoelectrochemical Solar Energy Conversion; NATO Advanced Study Institute on Photovoltaic and Photoelectrochemical Solar Energy Conversion, 1980; ISBN 9781461592358.
16. Гуревич, В.А.; Плесков, Ю.В. Фотоэлектрохимия Полупроводников; 1983;
17. Palmisano, L.; Yurdakal, S. Photoelectrocatalysis. Fundamentals and Applications; Elsevier, 2023; ISBN 9780128239896.
18. Łęcki, T.; Hamad, H.; Zarębska, K.; Wierzyńska, E.; Skompska, M. Mechanistic Insight into Photochemical and Photoelectrochemical Degradation of Organic Pollutants with the Use of BiVO4 and BiVO4/Co-Pi. Electrochim. Acta 2022, 434, doi:10.1016/j.electacta.2022.141292.
19. Hallstrom, L.; Tossi, C.; Tittonen, I. Computational Study Revealing the Influence of Surface Phenomena in P-GaAs Water-Splitting Cells. J. Phys. Chem. C 2021, 125, 12478–12478, doi:10.1021/acs.jpcc.1c00982.
20. Iandolo, B.; Zhang, H.; Wickman, B.; Zoric, I.; Conibeer, G.; Hellman, A. Correlating Flat Band and Onset Potentials for Solar Water Splitting on Model Hematite Photoanodes. RSC Adv. 2015, 5, 61021–61030, doi:10.1039/c5ra10215d.
21. Seabold, J.A.; Choi, K. Efficient and Stable Photo-Oxidation of Water by a Bismuth Vanadate Photoanode Coupled with an Iron Oxyhydroxide Oxygen Evolution Catalyst. 2012.
22. Zachäus, C.; Abdi, F.F.; Peter, L.M.; Van De Krol, R. Photocurrent of BiVO4 Is Limited by Surface Recombination, Not Surface Catalysis. Chem. Sci. 2017, 8, 3712–3719, doi:10.1039/c7sc00363c.
23. Garner, L.E.; Steirer, K.X.; Young, J.L.; Anderson, N.C. Covalent Surface Modification of Gallium

Arsenide Photocathodes for Water Splitting in Highly Acidic Electrolyte. ChemSusChem 2017, 10, 1–9, doi:10.1002/cssc.201601408.

24. Wang, S.; He, T.; Chen, P.; Du, A.; Ostrikov, K.; Huang, W.; Wang, L. In Situ Formation of Oxygen Vacancies Achieving Near-Complete Charge Separation in Planar BiVO4 Photoanodes. Adv. Mater. 2020, 32, 1–10, doi:10.1002/adma.202001385.
25. Memming, R. Semiconductor Electrochemistry; Wiley-VCH, 2015; ISBN 9783319296418.
26. Peter, L.M. Dynamic Aspects of Semiconductor Photoelectrochemistry. 1990, 753–769.
27. Abrantes, L.M.; Peter, L.M. Transient Photocurrents at Passive Iron Electrodes. J. Electroanal. Chem. 1983, 150, 593–601, doi:10.1016/S0022-0728(83)80238-1.
28. Tian, T.; Jiang, G.; Li, Y.; Xiang, W.; Fu, W. Unveiling the Activity and Stability of BiVO4 Photoanodes with Cocatalyst for Water Oxidation. Renew. Energy 2022, 199, 132–139, doi:10.1016/j.renene.2022.08.138.
29. Park, Y.; Kang, D.; Choi, K.S. Marked Enhancement in Electron – Hole Separation Achieved in the Low Bias Region Using Electrochemically Prepared Mo-Doped BiVO4 Photoanodes. Phys. Chem. Chem. Phys. 2014, 16, 1238–1246, doi:10.1039/c3cp53649a.
30. Cooper, J.K.; Gul, S.; Toma, F.M.; Chen, L.; Glans, P.A.; Guo, J.; Ager, J.W.; Yano, J.; Sharp, I.D. Electronic Structure of Monoclinic BiVO4. Chem. Mater. 2014, 26, 5365–5373, doi:10.1021/cm5025074.
31. Łęcki, T.; Hamad, H.; Zarębska, K.; Wierzyńska, E.; Skompska, M. Mechanistic Insight into Photochemical and Photoelectrochemical Degradation of Organic Pollutants with the Use of BiVO4 and BiVO4/Co-Pi. Electrochim. Acta 2022, 434, doi:10.1016/j.electacta.2022.141292.
32. Govind Rajan, A.; Martirez, J.M.P.; Carter, E.A. Why Do We Use the Materials and Operating Conditions We Use for Heterogeneous (Photo)Electrochemical Water Splitting? ACS Catal. 2020, 10, doi:10.1021/acscatal.0c01862.
33. Wang, S.; He, T.; Chen, P.; Du, A.; Ostrikov, K.; Huang, W.; Wang, L. In Situ Formation of Oxygen Vacancies Achieving Near-Complete Charge Separation in Planar BiVO4 Photoanodes. Adv. Mater. 2020, 32, doi:10.1002/adma.202001385.
34. Palaniselvam, T.; Shi, L.; Mettela, G.; Anjum, D.H.; Li, R.; Katuri, K.P.; Saikaly, P.E.; Wang, P. Vastly Enhanced BiVO4 Photocatalytic OER Performance by NiCoO2 as Cocatalyst. Adv. Mater. Interfaces 2017, 4, doi:10.1002/admi.201700540.
35. Zhong, D.K.; Choi, S.; Gamelin, D.R. Near-Complete Suppression of Surface Recombination in Solar Photoelectrolysis by “Co-Pi” Catalyst-Modified W:BiVO4. J. Am. Chem. Soc. 2011, 133, 18370–18377, doi:10.1021/ja207348x.

CHAPTER IV: EFFECT OF β-FEOOH MODIFICATION ON $BiVO_4$ PHOTO- AND PHOTOELECTROCATALYTIC PERFORMANCE TOWARDS DEGRADATION OF PHARMACEUTICALS

4.1. INTRODUCTION

Preliminary investigations show that the photoelectrocatalytic performance of $BiVO_4$ in organic oxidation processes is primarily limited by low intrinsic catalytic activity toward organic oxidation reactions, rapid electron-hole recombination and photocurrent decay caused by photocorrosion. Therefore, the material should be modified in a way to increase the extracting of photogenerated holes. Efficient hole extraction prevents their accumulation on the lattice surface and consequently suppresses photocorrosion and electron-hole recombination by reducing the number of holes available for these parasitic processes. In these regards, the modification with an efficient co-catalyst is necessary to ensure rapid consumption of photogenerated holes through electrochemical reactions.

β-FeOOH is a low-cost and environmentally benign material (it is one of the compounds constituting rust). It has been successfully applied as a co-catalyst for both photoactive materials [1–3] and advanced oxidation processes [4–6]. The literature reports that modification of $BiVO_4$ with β-FeOOH increases the photocurrent density by up to 2.5 times and enables stable photocurrent for up to 20 h of operation [1–3].

The degradation of organic compounds on bare β-FeOOH shows relatively modest performance (e.g., photocatalytic removal of 35% of methylene blue in 4.5 h [7] and 16.3% of oxytetracycline in 30 min [8]). However, when β-FeOOH is combined with $BiVO_4$, a significant enhancement in degradation efficiency is observed. Li et al. reported 80% degradation of oxytetracycline within 60 min on a $BiVO_4$/FeOOH photoanode in the presence of peroxomonosulfate, with stable performance over five degradation cycles [9]. Wen et al. achieved 99.1% photocatalytic degradation of ofloxacin within 15 min using a $BiVO_4$/CQDs/β-FeOOH photocatalyst [10]. Obregón et al. reported 85% degradation of methylene blue after 180 min on a $BiVO_4$/β-FeOOH photatalyst [11]. Moreover, several studies indicate that β-FeOOH possesses a suitable valence band position for the generation of hydroxyl radicals [7,12].

In addition, this modification may promote the formation of a Z-scheme heterojunction, in which less energetic holes of $BiVO_4$ recombine with less energetic electrons of β-FeOOH. Such a charge transfer pathway suppresses recombination involving the more energetic charge carriers, namely holes in β-FeOOH and electrons in $BiVO_4$, thereby preserving their high redox potential [13]. Consequently, this system may also be effective in photocatalytic processes operated without external bias.

The present chapter aims to investigate the effect of β-FeOOH modification on the photocatalytic and photoelectrocatalytic performance of $BiVO_4$ towards the degradation of selected pharmaceutical compounds, namely paracetamol, sulfamethoxazole, and carbamazepine.

The experimental work presented in this chapter is conducted during an academic mobility period at the Laboratory of Electrochemistry headed by Professor Magdalena Skompska, University of Warsaw.

4.2. MATERIALS AND METHODS

4.2.1. Materials

All reagents were of analytical grade and used without further purification. Bismuth nitrate pentahydrate ($Bi(NO_3)_3 \cdot 5H_2O$), potassium iodide (KI), p-benzoquinone (p-BQ), vanadyl acetylacetonate ($VO(acac)_2$), dimethyl sulfoxide (DMSO), iron(III) chloride ($FeCl_3$), terephthalic acid (TA), paracetamol (PCT), sulfamethoxazole (SMX), and carbamazepine (CBZ) were purchased from Sigma-Aldrich. Sodium hydroxide (NaOH), sodium sulfate (Na_2SO_4), absolute ethanol (C_2H_5OH), concentrated sulfuric acid (H_2SO_4), and concentrated nitric acid (HNO_3) were obtained from POCh S.A. Aqueous solutions were prepared using deionized (DI) water (Rephile, 18 MΩ·cm). Fluorine-doped tin oxide (FTO) coated glass substrates with a surface resistance of 20 Ω·cm-2 were purchased from Dyenamo AB (Sweden).

4.2.2. $BiVO_4$ thin film synthesis

$BiVO_4$ thin films were synthesized by a well-known electrodeposition technique [14] slightly modified in the previous work [15]: BiOI were electrodeposited on a FTO glass and then it was chemically converted to $BiVO_4$.

FTO samples of size 2.5x1 cm were first cleaned in acetone for 15 minutes in ultrasound bath, then in DI water in ultrasound bath also for 15 minutes. After that the activation of FTO surface states were made to increase the adhesion of electrodeposited film. First, samples were bathed in 3 M NaOH for 30 seconds, then they were washed with DI water. Secondly, the samples were bathed in 1 M Na_2SO_4 for 15 seconds and washed again with DI water.

The plating solution for BiOI deposition was prepared as follows: pH of 50 ml of aqueous solution of 0.4 M KI was adjusted to value 1.7 by adding few drops of HNO_3(conc). This was done to ensure the dissolution of slightly soluble $Bi(NO_3)_3 \cdot 5H_2O$ which is soluble at pH<3. The certain amount of $Bi(NO_3)_3 \cdot 5H_2O$ was added to reach 0.04 M concentration. The iodine ions form complexes with Bi ions $[BiI_4]^-$, further increasing the solubility of bismuth nitrate. The obtained solution was mixed with 20 ml of 0.23 M *p*-benzoquinone dissolved in absolute ethanol. The deep red-brown solution was obtained.

Electrodeposition was performed in a classical three-electrode cell, containing 1 M KCl Ag/AgCl as a reference electrode (RE), Pt wire as a counter electrode (CE) and cleaned and activated FTO as a working electrode (WE). The electrodeposition was performed via cyclic voltammetry (CV) in the potential range from 0.33 V to – 0.25 V during 40 cycles. The potentiodynamic method was used instead of potentiostatic one like in the original procedure [14] to prevent the stagnation of diffusion layer and increase the concentration of $[BiI_4]^-$ complex near the FTO surface. At the potentials between 0.1 and 0.33 V the reaction rate is relatively slow, thus, at this range the $[BiI_4]^-$ concentration decrease may be compensated by the diffusion of $[BiI_4]^-$ from the bulk solution to the FTO surface. On the first CV scan the loop typical for the nucleation process is observed. The charge passed through the system was around 380 mC cm^{-2} and 1.5 cm^2 surface area was covered by BiOI layer.

The following reaction occurs:

$$[BiI_4]^- + 2OH^- \rightarrow BiOI + H_2O + 3I^- \quad (4.1)$$

The *p*-benzoquinone serves as a source of OH^- ions electrogenerated during its reduction on WE. This leads only to the local change of pH in the vicinity to the WE, whereas in the bulk solution pH does not change and, thus, Bi^{3+} ions remain dissolved. The usage of *p*-benzoquinone is crucial as other sources of electrochemically generated OH^- ions (for example, nitrites) have reduction potentials lower than Bi^{3+}. The usage of *p*-benzoquinone allows one to carry out the reaction at the potentials lower than Bi^{3+} reduction, so it prevents formation of metallic Bi as impurities [16].

$$Bi^{3+} + 3\overline{e} \rightarrow Bi \quad E^0 = 0.308V(RHE) \tag{4.2}$$

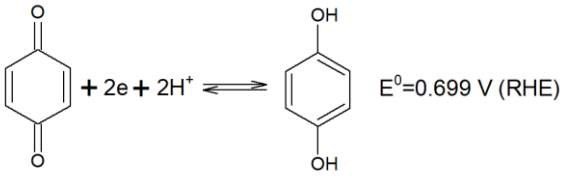

(4.3)

After the deposition bright-orange samples of FTO/BiOI were obtained (Figure 4-1a). Previous works carried out in the same laboratory showed the formation of needles-like morphology [14,15], which serves as a template for the further conversion to worm-like $BiVO_4$ and ensures the good electrochemical properties of electrodeposited $BiVO_4$ film: high porosity and, thus, developed electrochemically active surface area and improved electron-hole separation since the formed grains have the characteristic size lower than the hole-diffusion length (70-100 nm).

To convert BiOI into $BiVO_4$ the 100 μL of 0.2 M solution of $VO(acac)_2$ dissolved in DMSO was dropped on a sample. The usage of DMSO as a solvent is crucial because BiOI surface is hydrophobic and the aqueous $VO(acac)_2$ solution can not penetrate the BiOI template deeply leading to the formation of large particles of $BiVO_4$ limiting the porosity and overcoming the hole diffusion length [17]. The sample was dried on a hot plate at T=120°C until the solution becomes gel-like (Figure 4-1b). This step is required to evaporate DMSO and fix the vanadium precursor on a surface of BiOI. After that, the sample was annealed at 450°C for two hours with the rate 2°C/min.

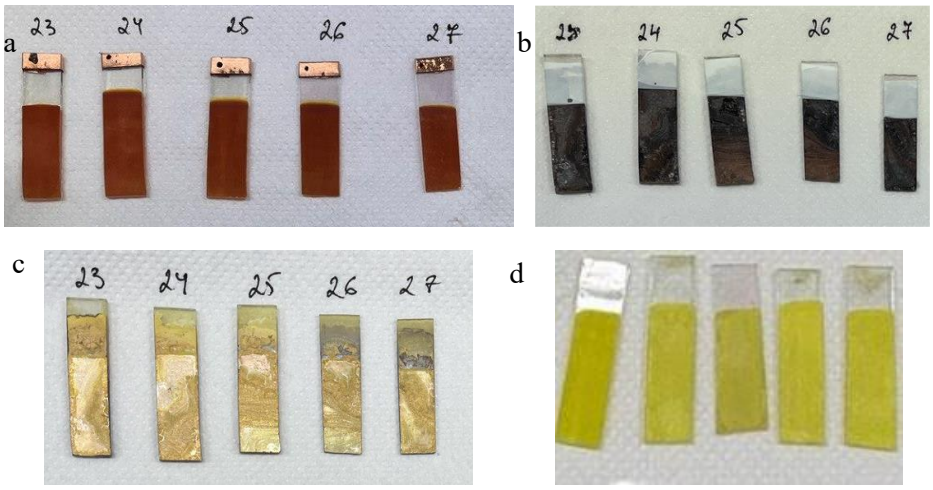

Figure 4-1 Stages of $BiVO_4$ synthesis: (a) BiOI thin film deposited on FTO, (b) BiOI covered with gel-like $VO(acac)_2$ solution after partion evaporation of DMSO, (c) $BiVO_4$ samples after furnace covered with V_2O_5, (d) resulting $BiVO_4$.

The samples after the furnace have pearl-yellow color (Figure 4-1c). To remove the excess of V_2O_5 which is soluble in alkali, the bathing of the samples with a gentle stirring in 1 M NaOH is performed for 30 minutes.

The resulting samples have yellow mate color (Figure 4-1d).

4.2.3. β-FeOOH deposition

To synthesize β-FeOOH layer $BiVO_4$ electrodes (of surface area 1.5 cm^2) were immersed in 7-9 ml of 5 mM concentrations of $FeCl_3 \cdot 6H_2O$ (Sigma Aldrich) on a hot plate (40°C) for 90 minutes until the change of solution color (from slightly yellow to bright orange) [2]. It is assumed that self-hydrolysis reaction of Fe^{3+} ions occurs in this process [18]:

$$Fe^{3+} + 2H_2O \rightarrow FeOOH + 3H^+ \quad (4.4)$$

The thickness of β-FeOOH layer can be controlled by repeating this procedure several times, thus the layer thickness was optimized.

To characterize specifically β-FeOOH material FTO/β-FeOOH samples were prepared. On a bare FTO the procedure describe above was repeated seven times to reach the bright-orange color and relatively thick layer of β-FeOOH.

4.2.4. Characterization methods

Crystallographic properties of samples were evaluated by X-Ray Diffraction (XRD) at RT in air. For this purpose, it was used a PANalytical AERIS equipment operated at 30 kV and 10 mA, with Bragg-Brentano geometry, Cu Kα radiation, angular range (2θ) of 5–80°, 0.011° step size, Ni filter and PIXcel^{1D} detector.

A field-emission scanning electron microscope FE-SEM (Carl Zeiss Sigma HV) equipped with In-lens detector at operating voltage of 5/20 kV and 5 mm working distance was used to examine the morphology of the samples.

The energy-dispersive X-ray spectroscopy (EDS) elemental analysis was performed with Quantax EDS with Bruker Nano XFlash Detector.

Diffuse reflectance spectra of the samples were recorded using UV-vis spectrometer (Shimadzu UV-3600) equipped with an integrating sphere.

Raman Spectroscopy was performed with Renishaw inVia Confocal Raman Spectrometer with 532 nm laser as an excitation source.

X-ray photoelectron spectroscopy (XPS) measurements were carried out using a PHI 5000 VersaProbe spectrometer (ULVAC-PHI). A monochromated Al Kα radiation source ($h\nu$=1486.6 eV) operating at a power of 23 W was employed for photoelectron excitation. Survey and high-resolution spectra were acquired at pass energies of 117.4 eV and 23.5 eV, respectively. Signal background subtraction was performed using the Shirley method. Peak fitting of high-resolution spectra was conducted in CasaXPS software (version 2.3) using asymmetric Gaussian-Lorentzian line shapes. All binding energy values were calibrated with respect to epy carbon C 1s peak positioned at 284.8 eV.

The photoluminescence (PL) measurements were performed using a Ti:sapphire pulsed (80 MHz frequency) laser (Coherent, USA) at a wavelength 300 nm for optical excitation. The spectral distribution of the PL was analyzed by a 300 mm monochromator and a streak camera (Hamamatsu) of about 3 ps time resolution. The measurements were performed at room temperature.

Electrochemical characterization was performed in Teflon cell with a quartz glass in a typical three-electrode configuration. Reference electrode is 1 M KCl Ag/AgCl (0.235 V vs SHE), counter electrode is platinum wire. The characterization was performed in 0.1 M Na_2SO_4 solution with a natural pH. Autolab PGSTAT302N (Metrohm, The Netherlands) was used. Diode with a wavelength of 400 nm and light intensity 100 mW/cm^2 (measured by IL1700 International Light (USA) radiometer) was used in front illumination mode.

4.2.5. Photocatalytic and photoelectrocatalytic degradation of pharmaceuticals

The photo- and photoelectro- degradation tests were performed in a quartz cuvette for fluorescence (2 cm x 1 cm with all transparent walls) containing 6 ml of 20 mg/L solution of PCT, SMX or CBZ. In the case of photocatalytic degradation, the solvent is DI water and in the case of photoelectrocatalysis – 0.1 M Na_2SO_4. The solution was magnetically rigorously stirred during the experiment.

The same diode as used in electrochemical characterization was used in the front illumination mode in both photo- and photoelectro- degradation test. The same potentiostat, reference and working electrodes were also used in photoelectrochemical degradation tests. The applied bias was 0.8 V vs reference electrode. Multimeter was used to measure the cell voltage between working and counter electrodes.

The concentration of pharmaceutical compound was monitored during the experiment by UV-vis spectroscopy using spectrophotometer Lambda 12 (Perkin Elmer) working in a transmission mode. The concentration ratio C/C_0 was obtained from the ratio of absorbances A/A_0, according to the Beer's law ($A=lc\varepsilon$).

Prior to the degradation test the initial solution of pharmaceuticals was hold in the dark in the presence of the catalyst for 30 minutes to assess the absorption. In all cases no absorption was observed. Thus, this data is not reported further.

The degradation tests were performed during 120 minutes. The probe times were 0, 5, 10, 20, 30, 40, 60, 80, 100 and 120 minutes.

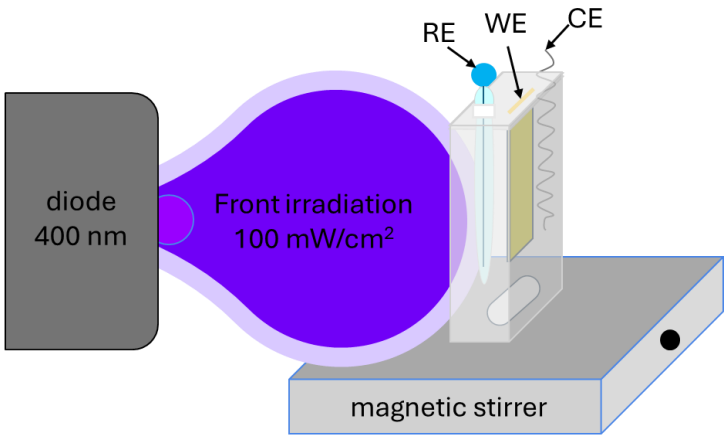

Figure 4-2 The experimental set-up for photoelectrochemical degradation experiment. Reference electrode (RE) – 1 M KCl Ag/AgCl, working electrode (WE) – $BiVO_4$ or $BiVO_4$/β-FeOOH, counter electrode (CE) – platinum wire

4.2.6. Measurements of electron-hole separation efficiency and injection yield

Assuming that each absorbed photon generates one electron-hole pair, the photocurrent (J) can be expressed as a product of absorbed current density (J_{abs}), the electron-hole separation efficiency (η_{sep}) and the charge injection yield (η_{inj}):

$$J = J_{abs} \cdot \eta_{sep} \cdot \eta_{inj} \tag{4.5}$$

For a light-emitting diode operating at a wavelength of λ=400 nm, and for $BiVO_4$ with a band gap energy E_g=2.4 eV (λ_g=506 nm), $\lambda < \lambda_g$. Therefore, all incident photons have energies exceeding the semiconductor band gap. However, not all of these photons are effectively absorbed by the semiconductor. Light harvesting efficiency (LHE) is defined as:

$$LHE = 1 - 10^{-A(\lambda)} \tag{4.6}$$

where A(λ) is the absorbance at the corresponding wavelength.

The photon flux emitted by diode (N_{ph}) is calculated according to:

$$N_{ph} = \frac{P}{hc / \lambda} \tag{4.7}$$

where P is the irradiance of the light source.

Based on this value, the incident current density is determined as:

$$J_{incident} = \mathrm{N}_{ph} \cdot q_e \tag{4.8}$$

where q_e is the electron charge.

By taking into account the non-ideal light harvesting efficiency, the absorbed current density is given by:

$$J_{abs} = J_{incident} \cdot LHE \tag{4.9}$$

The parameters calculated for the light source and the $BiVO_4$ samples used in the experiments, which define the maximum theoretical photocurrent density under the applied illumination conditions, are summarized in Table 4-1.

Table 4-1 Parameters of the light source determining the maximum theoretical current density of $BiVO_4$ under the experimental conditions.

Parameter	Value	Reference
λ, nm	400	-
P, mW/cm^2	100	-
A(λ=400 nm)	0.328	Figure 4-5a
LHE	0.53	Eq. 4.6
N_{ph}, s^{-1} m^{-2}	$2.014 \cdot 10^{21}$	Eq. 4.7
$J_{incident}$, mA/cm^2	32.26	Eq. 4.8
J_{abs}, mA/cm^2	17.11	Eq. 4.9

Adding sodium sulfite (Na_2SO_3) which is an excellent hole scavenger having very fast reaction kinetics, one can assume η_{inj}=1. In this case the photocurrent measured in this solution ($J_{Na_2SO_3}$) from Eq. (4.5):

$$J_{Na_2SO_3} = J_{abs} \cdot \eta_{sep} \tag{4.10}$$

Thus, the electron-hole separation efficiency (η_{sep}) can be determined as:

$$\eta_{sep} = \frac{J_{Na_2SO_3}}{J_{abs}} \tag{4.11}$$

The charge injection yield is evaluated by comparing the photocurrent densities measured in the presence and absence of Na_2SO_3:

$$\eta_{inj} = \frac{J_{Na_2SO_4}}{J_{Na_2SO_3}} \tag{4.12}$$

The $J_{Na_2SO_3}$ is measured in 0.1 M Na_2SO_3 and $J_{Na_2SO_4}$ is measured in 0.1 M Na_2SO_4 without buffer at natural pH (5.5-5.8).

4.2.7. Probe molecule oxidation test for the formation of hydroxyl radicals

Formation of hydroxyl radicals was estimated by the oxidation of a probe molecule – terephthalic acid. Jing Y. and Chaplin B. conducted an extensive study of various $HO^{\bullet}$ probe molecules and concluded that terephthalic acid is the most suitable probe. This conclusion is based on several factors: terephthalic acid does not undergo direct electron transfer, density functional theory calculations do not reveal any

thermodynamically favorable oxidation pathways other than hydroxyl-radical-mediated oxidation, and terephthalic acid is resistant to the Forrester-Hepburn mechanism [19]. Terephthalic acid (TA) is oxidized by hydroxyl radicals with the formation of highly fluorescent 2-hydroxyterephtalic acid (TA-HO) (Eq. 4.13).

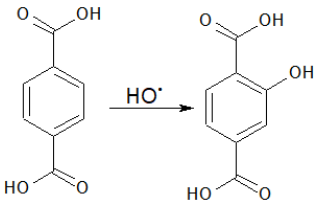

(4.13)

6 ml of $5 \cdot 10^{-4}$ M TA in 3 mM NaOH solution (to favor the solubility of TA which is slightly increased in basic media) was oxidized in photo- and photoelectrochemical experiments described above during 30 minutes. The fluorescence spectra upon excitation at 315 nm were recorded in a 1 cm quartz cuvette using the spectrofluorometer LS55 (Perkin Elmer) with the scanning rate 200 nm/min and the slit width 5 nm. The emission peak by which the concentration of TA-OH is determined: λ=425 nm.

4.3. MATERIALS CHARACTERISATION

4.3.1. Evidence for β-FeOOH formation

Formation of β-FeOOH polymorph is proved by physical technics such as Raman spectroscopy, X-ray diffraction (XRD), Energy Dispersive X-ray spectroscopy (EDS) and Scanning Electron Microscopy (SEM).

XRD results show that after the $BiVO_4$ modification only one additional peak (11.8°) occurs on a scan, all other peaks are related to $BiVO_4$ (PDF 01-075-1866) and FTO (PDF 00-041-1445) (Figure 4-3a). This additional peak, most probably, belongs to β-FeOOH phase (PDF 00-034-1266). The presence of only one additional peak is, probably, associated with a very thin layer of β-FeOOH.

Raman spectroscopy was performed on FTO/β-FeOOH sample, as on a BiVO4/β-FeOOH sample the thickness of β-FeOOH is too small and signal from $BiVO_4$ marks the signal from β-FeOOH. Raman shifts correspond to the value reported in the literature for β-FeOOH phase [20] (Figure 4-3b).

SEM revealed flake-like β-FeOOH nanoparticles (5-70 nm) on the worm-like $BiVO_4$ surface (Figure 4-3c). The coverage greatly varies with the thickness of β-FeOOH layer as well as an electrochemical performance. Thus, further layer thickness optimization is needed.

EDS analysis was performed for $BiVO_4$ modified with a thick layer of β-FeOOH. The elemental analysis reveals the presence of noticeable amount of Fe atoms and the increased oxygen content compared with bare $BiVO_4$ (Table 4-2), which is attributed to the formation of β-FeOOH. Elemental mapping further confirms the SEM observations, showing that β-FeOOH nanoparticles are uniformly distributed over the $BiVO_4$ surface (Figure 4-3d).

Table 4-2 Results of elemental analysis of $BiVO_4$/β-FeOOH obtained from EDS measurements.

Element	Weight, %	Atomic, %
O	20.1	57.2
Si	2.8	4.5
V	9.2	8.2
Fe	19.1	7.3
Sn	28.6	6.2
Bi	41.5	12.7

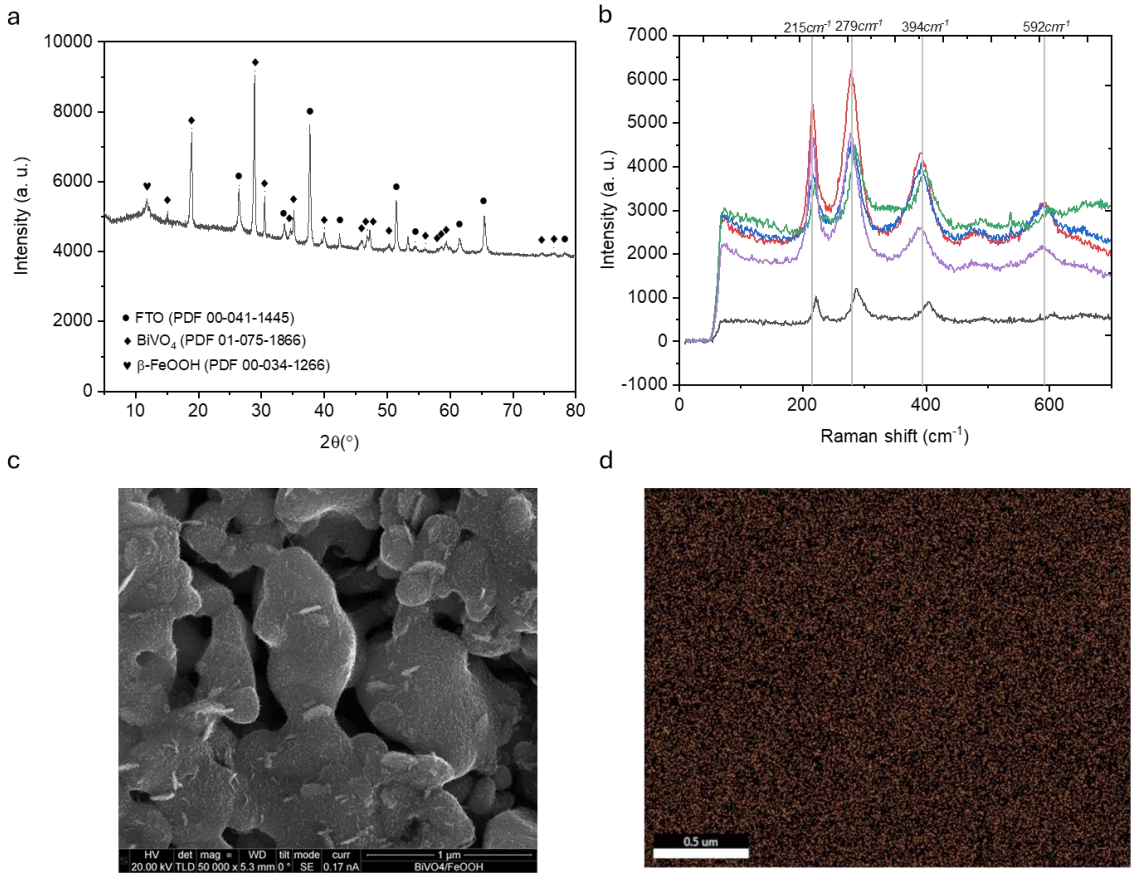

Figure 4-3 Physical characterization of $BiVO_4$/β-FeOOH sample. (a) Raman spectra of FTO/β-FeOOH (drop cast synthesis) taken at λ=523 nm; (b) XRD analysis of the $BiVO_4$/β-FeOOH sample; (c) SEM image of $BiVO_4$/β-FeOOH sample; (d) EDS picture of Fe atoms distribution on a surface of $BiVO_4$/β-FeOOH sample.

XPS analysis was performed on a thick layer of β-FeOOH deposited on an FTO substrate. The corresponding spectra are shown in Figure 4-4. The O 1s spectrum can be deconvoluted into three distinct peaks (Figure 4-4a). The peak at 530.1 eV is assigned to oxygen atoms bonded to metal cations (O1). The

peak at 531.5 eV is attributed to defect sites with low oxygen coordination (O2). The peak at 532.6 eV corresponds to surface hydroxyl groups and adsorbed water molecules. Notably, the relative area of the O2 component is substantial compared to that of the O1 peak, indicating a high concentration of oxygen vacancies in the β-FeOOH material synthesized using this procedure. The Fe 2p spectrum further supports this conclusion (Figure 4-4b). The peak at 711.9 eV is assigned to Fe^{2+} species, while the peak at 714.1 eV corresponds to Fe^{3+} species. The significant presence of Fe^{2+} is consistent with the formation of oxygen vacancies in the β-FeOOH structure, in agreement with previous reports [2].

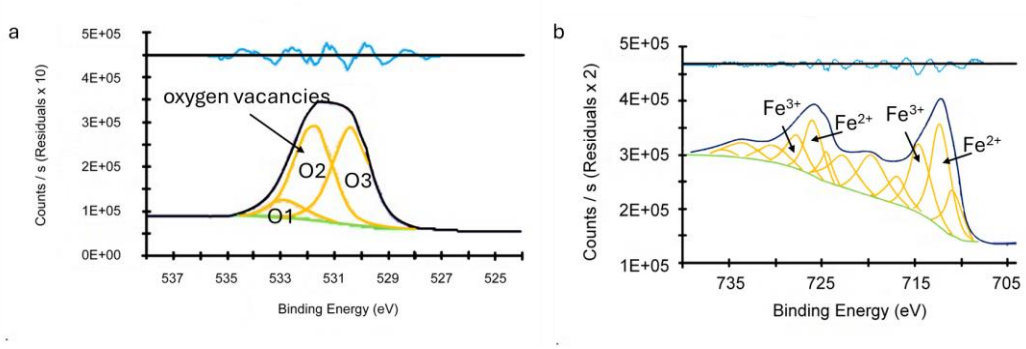

Figure 4-4 XPS high-resolution measurement results. O 1s (a) and Fe 2p (b) spectra of β-FeOOH.

UV-vis absorption of FTO/β-FeOOH and $BiVO_4$/β-FeOOH were measured. Figure 4-5a shows that the thin layer of β-FeOOH does not affect the $BiVO_4$ absorption. Thus, to evaluate the band gap of β-FeOOH the absorption of FTO/β-FeOOH was measured. The Tauc plot obtained from this measurement and built in assumption of direct electron transition is presented in Figure 5-5b. The value of band gap equal to 2.17 eV and adsorption adage around 571 nm correspond well with the literature values [7].

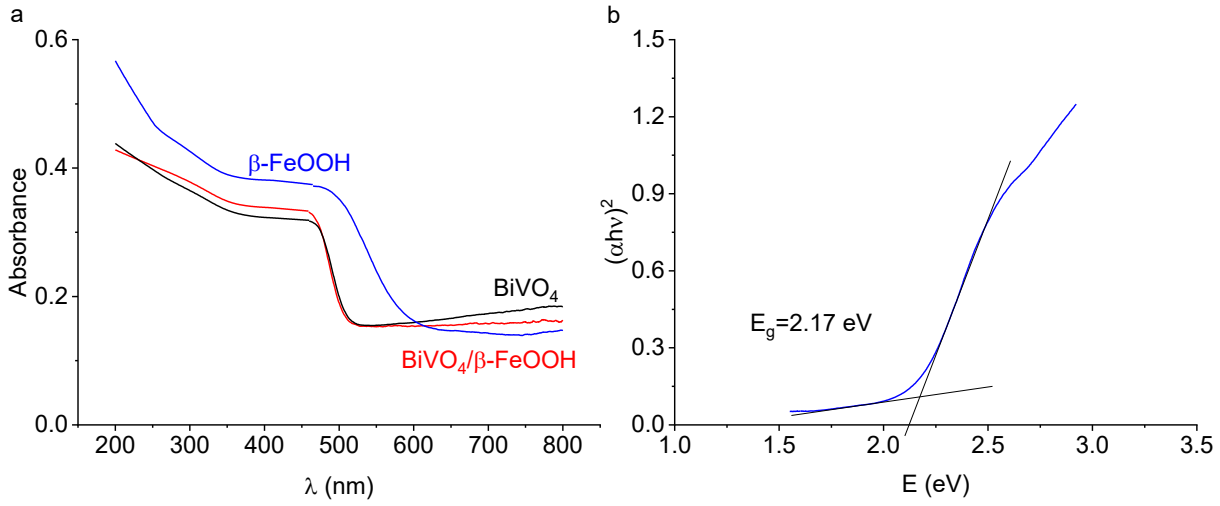

Figure 4-5 Influence of β-FeOOH cocatalyst deposition on (a) UV-vis absorbance of $BiVO_4$ and (b) Tauc plot of β-FeOOH film.

4.3.2. Optimization of β-FeOOH layer thickness

It is possible to control the thickness of the β-FeOOH layer by repeating the synthesis procedure several times. During one cycle, after 90 minutes of slow heating, the $FeCl_3$ solution changes color from pale yellow to bright orange. We refer to this single cycle as "one run". By immersing the sample in a fresh solution and repeating the 90-minute heating, additional runs can be carried out. With an increasing number of runs, the β-FeOOH layer becomes thicker. This is visible to the naked eye: after 1 run the sample appears yellow, while subsequent runs gradually turn it more orange. Figure 4-6 compares the β-FeOOH thickness after 1 run (a) and 4 runs (b) of deposition. After 1 run, separate flake-like β-FeOOH nanoparticles and initial nuclei can be observed on the worm-like surface of bare $BiVO_4$, with parts of the $BiVO_4$ surface still exposed. After 4 runs of deposition, however, the pores of $BiVO_4$ are completely filled with β-FeOOH nanoparticles, leaving no access to the bare $BiVO_4$ surface.

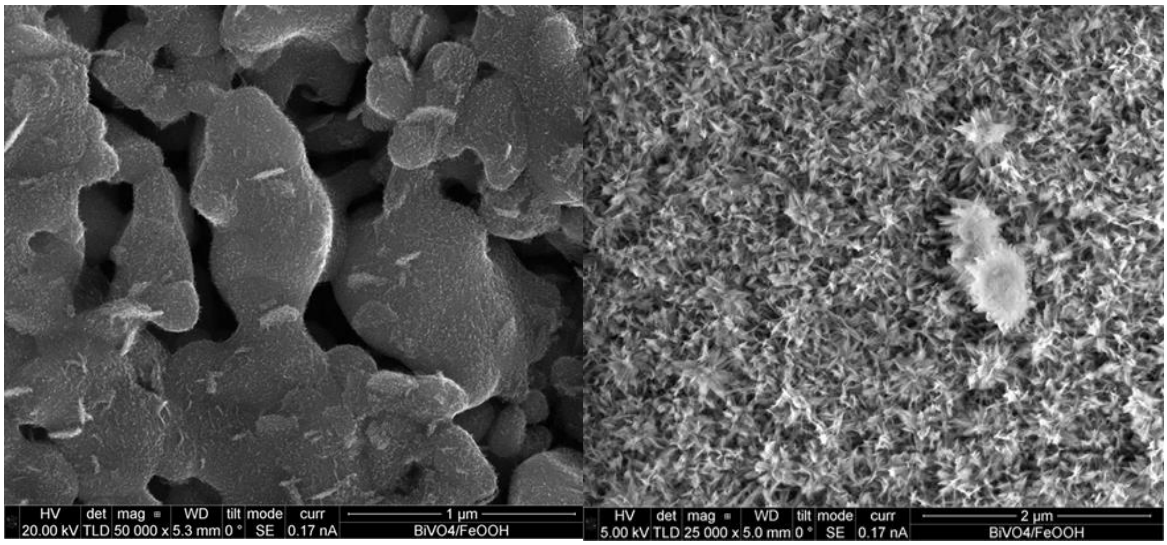

Figure 4-6 SEM image of nanoparticles of β-FeOOH. (a) 1 run deposition layer of β-FeOOH and (b) 4 runs deposition layer of β-FeOOH.

As shown in Figure 4-7, increasing the β-FeOOH layer thickness leads to a decrease in photocurrent. This effect is attributed to the reduced light absorption caused by the deposition of a thick β-FeOOH layer, which is poorly photoactive.

Therefore, one repetition of the synthesis procedure (1 run) was selected as the optimal condition, providing a co-catalyst layer of suitable thickness.

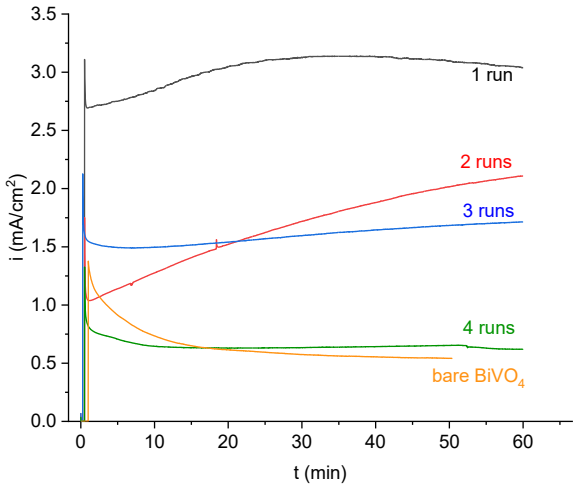

Figure 4-7 Influence of β-FeOOH thickness on electrochemical performance. Chronoamperometry is performed in 0.1 M Na_2SO_4 at E=0.8V vs 1 M KCl Ag/AgCl.

4.3.3. Electrochemical characterization

Electrochemical characterization demonstrates that modification of $BiVO_4$ with β-FeOOH leads to substantial improvement in both photocurrent density and operational stability (Figure 4-8).

Although cyclic voltammetry indicates an approximately twofold increase in current density at the potential used for the degradation test (E=0.8 V vs 1 M Ag/AgCl), long-term chronoamperometric measurements reveal that the actual enhancement is significantly larger. For bare $BiVO_4$, a rapid decrease in current density is observed within the first few minutes, followed by stabilization at a low current value. In contrast, the $BiVO_4$/β-FeOOH photoelectrode exhibits an initial increase in photocurrent, which is likely associated with the activation of surface sites, and subsequently stabilizes at a higher current density. As a result, on longer time scales the effective improvement reaches a factor of approximately six: after one hour, the current density is about 0.5 mA/cm^2 for bare $BiVO_4$ and 3 mA/cm^2 for $BiVO_4$/β-FeOOH at E=0.8 V vs 1 M Ag/AgCl).

It is also important to note that, for $BiVO_4$/β-FeOOH, the photocurrent onset potential is cathodically shifted compared with bare $BiVO_4$, from 0.32 V to −0.09 V (vs 3 M Ag/AgCl). This behaviour is attributed to the same underlying reason as in the case of Na_2SO_3 addition (Chapter 3, Section 3.2.1), namely enhanced reaction kinetics. When the electrochemical reaction proceeds faster, photogenerated charge carriers are extracted more rapidly from the photoanode surface; consequently, fewer carriers remain available for recombination, and a lower applied potential is required to suppress this parasitic process. The difference lies in the origin of the kinetic enhancement: in the case of SO_3^{2-} addition, the kinetics are improved by replacing the intrinsically slow H_2O/O_2 redox couple with the intrinsically faster SO_3^{2-}/SO_4^{2-} couple, whereas in the present case the same reaction (OER) is accelerated through $BiVO_4$ surface modification with β-FeOOH.

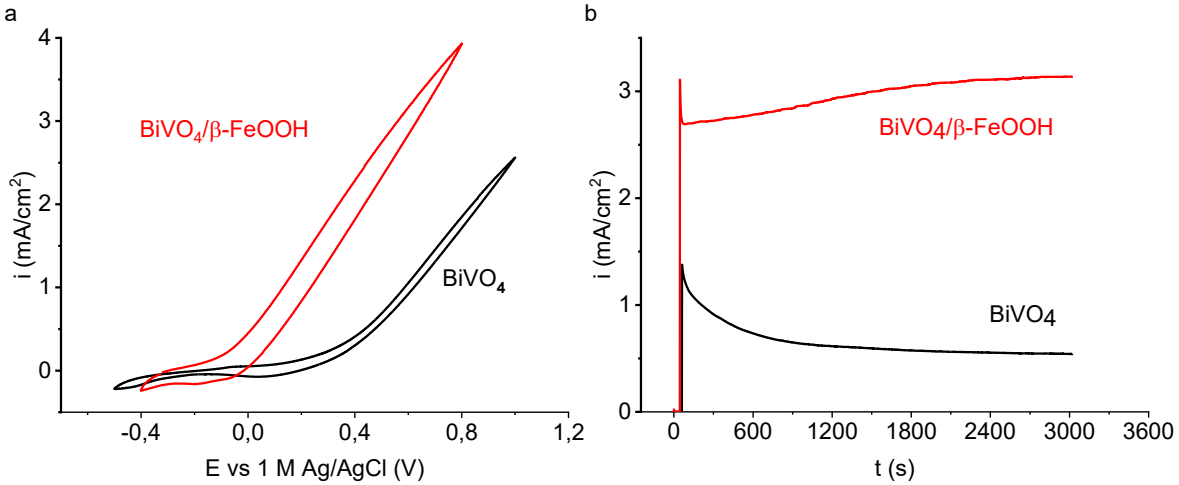

Figure 4-8 Electrochemical characterization of bare BiVO4 (black line) and BiVO4/β-FeOOH (red line). (a) Cyclic voltammetry illuminated, (b) illuminated chronoamperometry.

4.4. PHARMACEUTICALS DEGRADATION

4.4.1. Photolysis of pharamaceuticals

To ensure that the observed degradation of the pharmaceutical compounds is attributed solely to the photo- or photoelectrocatalytic effect, a photolysis test was performed. The solution was illuminated by the diode (the same which was used in photo and photo-electrocatalytic degradation experiments) in the absence of any catalyst. It was found that none of these compounds undergo photolysis under the illumination of a used light source.

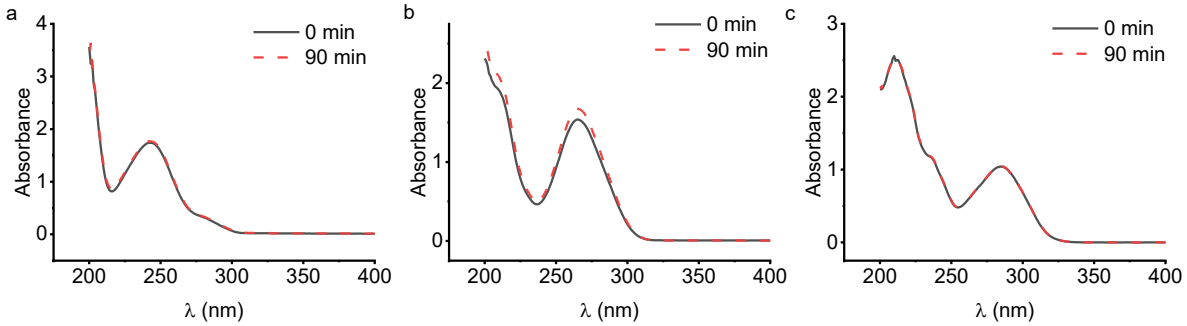

Figure 4-9 Photolysis of 20 mg/L of PCT (a), SMX (b), CBZ (d) dissolved in distilled water under the illumination of diode with λ=400 nm (100 mW/cm^2).

4.4.2. Estimation of pharmaceuticals oxidation potentials

The complete mineralization of PCT, SMX, and CBZ are as follows Eq. 4.14-16, respectively:

$$C_8H_9NO_2 + 17H_2O \rightarrow 8CO_2 + NO_3^- + 43H^+ + 42\bar{e} \quad (4.14)$$

$$C_{10}H_{11}N_3O_3S + 30H_2O \rightarrow 10CO_2 + 3NO_3^- + 71H^+ + 68\bar{e} \quad (4.15)$$

$$C_{15}H_{12}N_2O + 35H_2O \rightarrow 15CO_2 + 2NO_3^- + 82H^+ + 80\bar{e} \quad (4.16)$$

To estimate the upper limit of the oxidation current for these pharmaceutical compounds, the maximum number of electrons required for their complete mineralization was considered (i.e., 42 for PCT, 68 for SMX, and 80 for CBZ). The mass transport coefficient is assumed k_m=10^{-6} m/s for mixed-tank reactor [21]. The typical studied concentration of 20 mg/L is considered. The limiting current was then estimated according to the following equation:

$$i_{\text{lim}} = nFk_m c \quad (4.17)$$

where F is Faraday constant (96485 C/mol) and c is concentration in mol/L. The estimation gives the maximum values of limiting current equal to 53.6 μA/cm^2 for PCT, 50.3 μA/cm^2 for SMX and 65.3 μA/cm^2 for CBZ.

For the maximum current that may be recorded in cyclic voltammetry, peak currents by Randles-Ševčík equation are estimated. The maximum studied concentration (100 mg/L), maximum scan rate (100 mV/s) n=1 are taken for the calculations. Diffusion coefficient for PCT is $6.64 \cdot 10^{-10}$ m^2/s [22], for SMX is $7 \cdot 10^{-10}$ m^2/s [23] and for CBZ is $5.8 \cdot 10^{-10}$ m^2/s [24]. Thus, the upper estimation of peak currents on CV curves is 29, 18 and 17 μA/cm^2 for PCT, SMX and CBZ, respectively.

Meanwhile, on the bare $BiVO_4$ photoelectrode within the studied potential range, the current associated with water oxidation can reach up to 2 mA/cm^2. Therefore, the investigation of the oxidation kinetics of the studied pharmaceuticals directly on $BiVO_4$ or $BiVO_4$/β-FeOOH photoanodes is not feasible, since the small oxidation currents of these compounds are "masked" by the much larger water oxidation current.

Therefore, to obtain an approximate estimate of the oxidation potentials of the studied compounds, cyclic voltammograms were recorded using a conventional glassy carbon electrode at potentials below the onset of water oxidation. Although such data does not provide precise information on the standard oxidation potentials of these compounds (due to the overvoltage on the glassy carbon electrode), they allow one to assess whether these potentials fall within the energy window between the conduction and valence bands of the photoelectrode, where oxidation by holes and direct electron transfer is possible.

Figure 4-10 presents the cyclic voltammetry curves of PCT, SMX and CBZ recorded on glassy carbon working electrode in dependence on different concentrations and scan rates. In all cases the peak current gradually increases with increase of concentration or scan rate. The linear dependence of peak current on concentration and scan rate (Figure 4-10 g, h, i) confirms that this peak current is associated with PCT, SMX or CBZ oxidation, respectively.

Therefore, the oxidation potentials about 0.48 V (vs Ag/AgCl) or 1.13 V (vs RHE) for PCT, 1.04 V (vs Ag/AgCl) or 1.69 V (vs RHE) for SMX and 1.26 V (vs Ag/AgCl) and 1.91 V (vs RHE) for CBZ are determined. These values fall in the potential range where the direct electron transfer is possible on $BiVO_4$ photoanode.

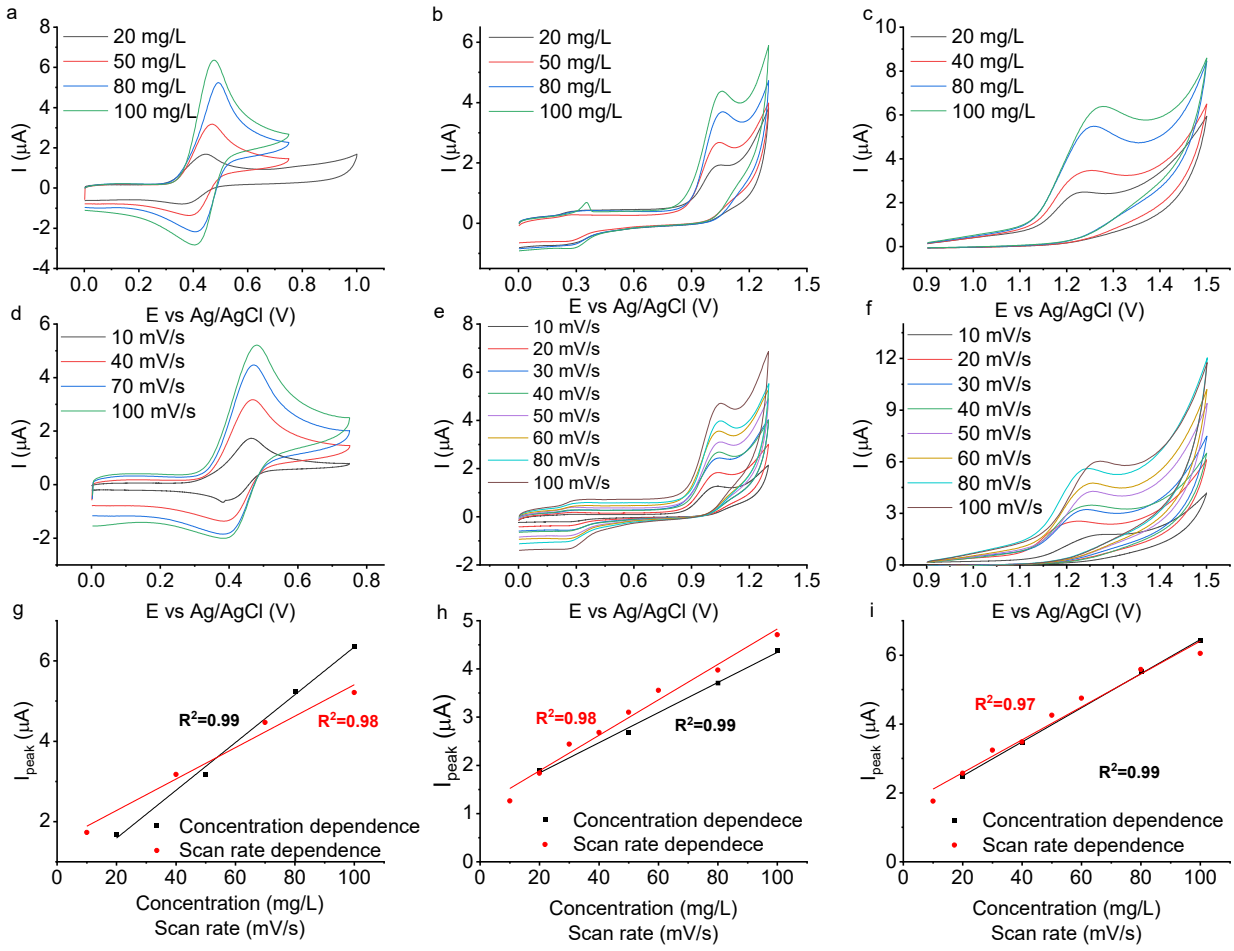

Figure 4-10 Cyclic voltammetry of PCT (a, d), SMX (b, e) and CBZ (c, f) varying the concentration at 40 mV/s scan rate (a, b, c) and varying the scan rate at 50 mg/L concentration (d, e, f). The linear dependencies of peak current on concentration and scan rate are presented on (g, h, i).

4.4.3. Kinetic analysis of pharmaceuticals degradation

Paracetamol degradation

Figure 4-11 shows the evolution of the UV-vis spectra of an aqueous solution initially containing 20 mg/L of PCT during photocatalytic and photoelectrocatalytic degradation on bare $BiVO_4$ and $BiVO_4$/β-FeOOH photoanodes. It can be observed that, in all cases, oxidation proceeds through similar mechanisms.

The initial spectrum of PCT exhibits a major peak at λ=244 nm, corresponding to the n→π* transition of C=O group and a shoulder of a most intensive peak at λ=196 nm corresponding to the π→π* transition of an aromatic ring which is in good agreement with the literature [25,26]. In all cases, no shift of the main absorption peak attributed to PCT is observed during the degradation.

During photocatalytic oxidation of paracetamol on bare $BiVO_4$, the positions of the characteristic absorption peaks remain unchanged. It is noteworthy that, in all cases, an increase in the intensity of the minimum at λ=215 nm is observed. In the paracetamol oxidation profile obtained in the PC process on $BiVO_4$/β-FeOOH, the formation of two well-defined isosbestic points at λ=224 nm and λ=267 nm is clearly visible. This behavior is indicative of a single transformation of the chromophore, suggesting a relatively

simple reaction pathway and the formation of a single oxidation by-product in the system. Interestingly, in paracetamol oxidation under PEC conditions, where a more strongly oxidative environment is generated, the intensity at λ=215 nm initially increases and subsequently decreases. This behavior is attributed to the further oxidation of the initially formed by-product. The same effect accounts for the blurring of the isosbestic points in PEC, which are clearly observed during the slower oxidation process in the photocatalytic regime. It is interesting to note that absorption bands at 215 nm and 276 nm correspond to 1,2,4-trihydroxybenzene, a known oxidation product of paracetamol formed via hydroxyl radical attack, which has been reported in multiple paracetamol oxidation pathways proposed in the literature [27,28].

During photoelectrocatalysis, the maximum at λ=243 nm increases within the first 20 minutes of the experiment. This unusual hyperchromic effect can be attributed to the formation of tautomer or isomer that absorb at the same wavelength as paracetamol but having the higher molar absorption coefficient [29]. After 20 minutes, these compounds likely begin to degrade, resulting in a decrease in the PCT peak intensity. Therefore, only the data obtained after 20 minutes were considered for the kinetic analysis of photoelectrocatalytic oxidation of PCT.

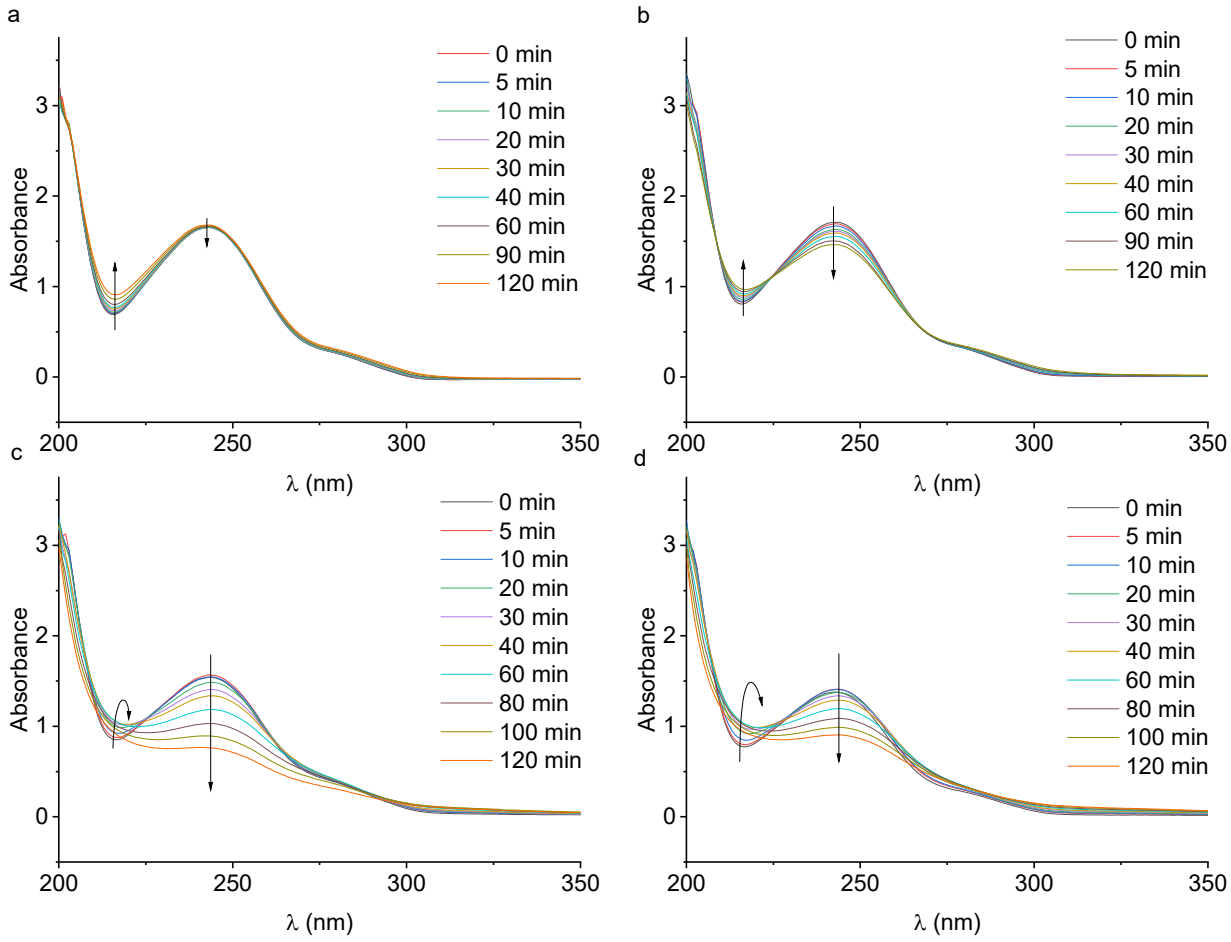

Figure 4-11 UV-vis spectra evolution during photocatalytical (a, b) and photoelectrocatalytic (c, d) degradation of PCT on bare $BiVO_4$ (a, c) and $BiVO_4$/β-FeOOH (b,d) photoelectrodes.

Figure 4-12 presents the results of the kinetic analysis of PCT degradation obtained by fitting the experimental data with different kinetic models. Both photocatalytic and photo electro catalytic oxidation of PCT is found to follow zero-order kinetics.

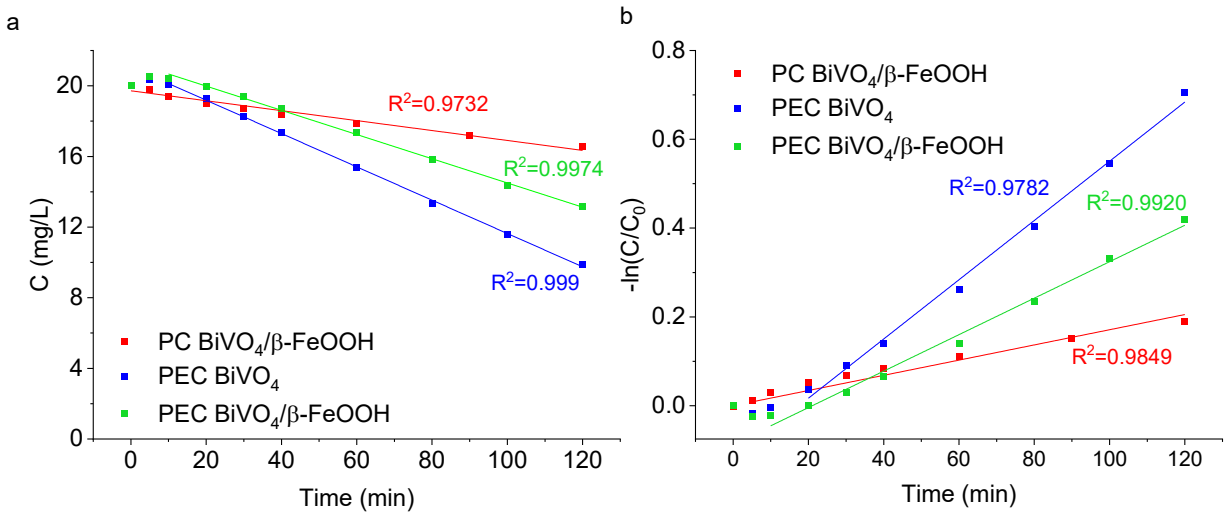

Figure 4-12 (a) Zero order and (b) 1st order kinetic analysis of PCT degradation in photocatalytic process on $BiVO_4$/β-FeOOH (red) and in photoelectrocatalytic process on bare $BiVO_4$ (blue) and on $BiVO_4$/β-FeOOH (green)

Sulfamethoxazole degradation

Figure 4-13 shows the evolution of the UV–vis spectra of an aqueous solution initially containing 20 mg L^{-1} of SMX during photocatalytic and photoelectrocatalytic degradation on bare $BiVO_4$ and $BiVO_4$/β-FeOOH photoanodes. It can be observed that, in all cases, oxidation proceeds through similar mechanisms.

The initial spectrum of SMX exhibits a peak at λ=263 nm, corresponding to the π→π* transition of the aniline part of the molecule, which is in good agreement with the literature [30–32]. In all cases, no shift of the main absorption peak attributed to SMX is observed during the degradation.

During the degradation experiment the main peak of SMX at λ=263 nm gradually decreases. In photocatalytic process on both bare and modified photoanode formation of two isosbestic points at λ=220 nm and λ=293 nm is observed, meaning the formation of a by-product in a single chromophore transformation process [33]. In photoelectrocatalytic process where the oxidation is more efficient, these isosbestic points are also blurred, probably due to the further degradation of a by-product. The increase of the absorbance in wavelength region 290-400 nm is observed. This increase was also observed in the literature and attributed to the formation of some oxidized oligomeric species [30].

As can be seen from Figure 4-14 both photocatalytic and photoelectrocatalytic degradation of SMX on obeys a pseudo-first order kinetics.

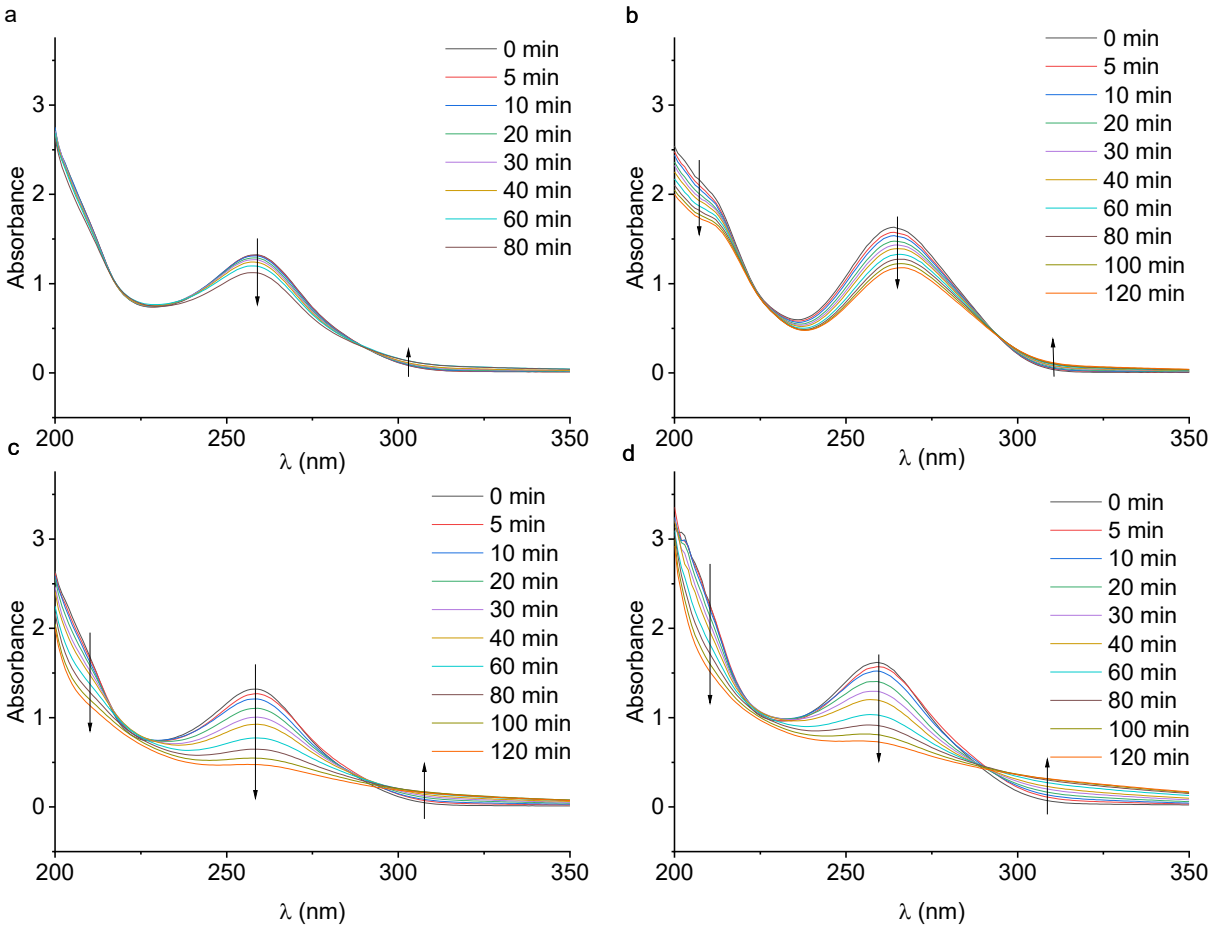

Figure 4-13 UV-vis spectra evolution during photocatalytic (a, b) and photoelectrocatalytic (c, d) degradation of SMX on bare $BiVO_4$ (a, c) and $BiVO_4$/β-FeOOH (b, d) photoelectrodes.

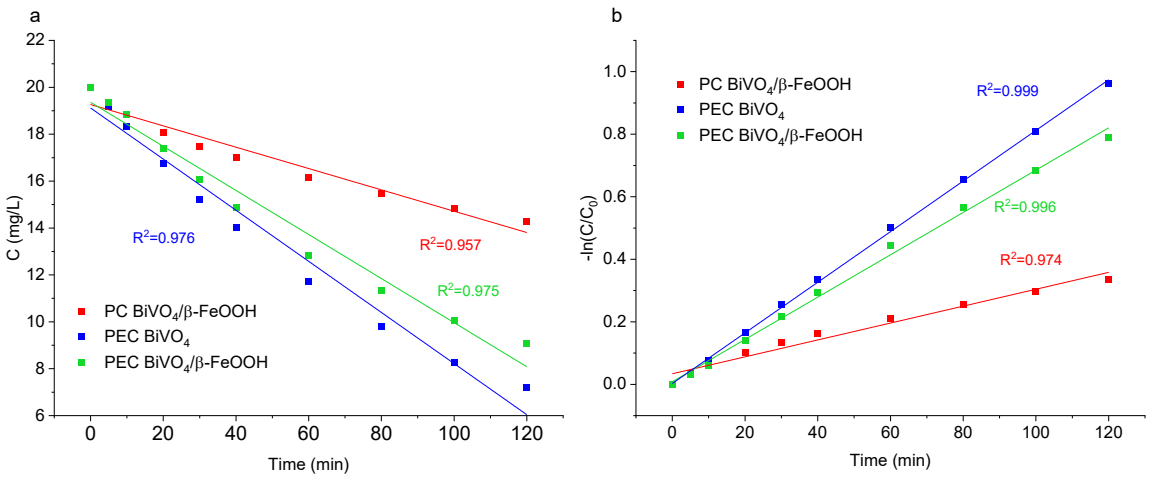

Figure 4-14 (a) Zero order and (b) 1st order kinetic analysis of SMX degradation in photocatalytic process on bare $BiVO_4$ (black) and $BiVO_4$/β-FeOOH (red) and in photoelectrocatalytic process on bare $BiVO_4$ (blue) and on $BiVO_4$/β-FeOOH (green).

Carbamazepine degradation

Figure 4-15 shows the evolution of the UV-vis spectra of an aqueous solution initially containing 20 mg L^{-1} of CBZ during photocatalytic and photoelectrocatalytic degradation on bare $BiVO_4$ and $BiVO_4$/β-FeOOH photoanodes. It can be observed that, in all cases, oxidation proceeds through similar mechanisms.

The initial spectrum of CBZ exhibits three peaks at λ=210 nm, λ=236 nm and λ=285 nm, corresponding to the π→π*, n→σ* (due to the presence of chromophore groups C=C, C=O and C=N) and n→π*(free electron doublet of the nitrogen atom) transitions, respectively, which is in good agreement with the literature [34]. In all cases, no shift of these absorption peaks attributed to CBZ is observed. The concentration of CBZ is determined by the change of peak intensity at λ=285 nm.

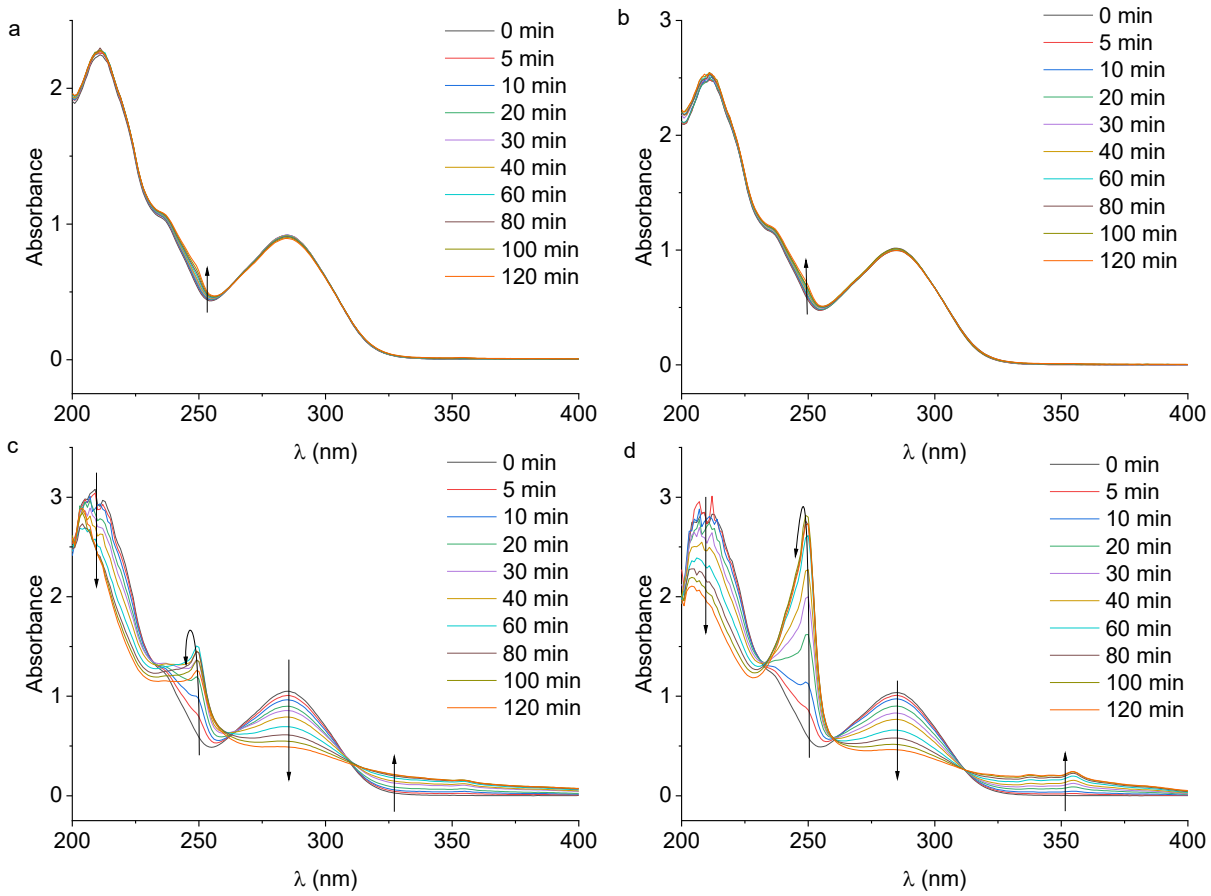

Figure 4-15 UV-vis spectra evolution during photocatalytic (a, b) and photoelectrocatalytic (c, d) degradation of CBZ on bare $BiVO_4$ (a, c) and $BiVO_4$/β-FeOOH (b, d) photoelectrodes.

During photocatalysis on both photocatalysts there is no change of main peaks intensity. In photoelectrochemical process major changes are observed. There is a decrease of characteristic peak at λ=285 nm intensity and also decrease of the lower wavelength band at λ=210 nm meaning the degradation of carbamazepine. We also observe formation of three isosbestic points at λ=232 nm, λ=260 nm and λ=312 nm, imposing the single chromophore transformation and formation of a carbamazepine degradation by-product. This by-product gives the high intensity peak at λ=250 nm which is very well seen. It is clearly

seen that this peak starts to decrease meaning that the oxidation of this compound is also occurred. This also cause the blurring of isosbestic points.

Li et al. made an extensive meta-review of 64 papers studying the degradation of CBZ in different processes (AOPs, Photocatalysis, Fenton and sulfate radical based AOPs) by means of LC/MS or GC/MS, identifying oxidation by-products and revealing the CBZ oxidation pathway [35]. They also made the DFT calculation to generalize the experimental results. Authors concluded that although the oxidative species and their concentration in different processes are different, the identified degradation pathways have a high similarity. Thus, it was possible to identify the most probable pathway of CBZ oxidation (Figure 4-16). The fourth by-product in this scheme – acridine – was identified in 59% of reviewed papers used AOPs for CBZ degradation, in 71% reviewed papers used photocatalysis and in 52% of papers used Fenton or sulfate radicals based AOPs. Figure 4-17a presents the comparison of UV-vis spectra of treated solution after 120 minutes of CBZ photoelectrocatalytic degradation on $BiVO_4$/β-FeOOH and UV-vis spectra of acridine. It is seen that the shape of spectra and peak positions (λ=250 nm, λ=338 nm, λ=345 nm, λ=354 nm) are completely coincided. The divergence in peak intensity can be explained by the interference with the initial CBZ compound spectra. Thus, the peak formed during the photoelectrocatalysis of CBZ may be attributed to acridine. It is interesting to note, that although there is a small oxidation of acridine, in our process it is essentially the final product of CBZ oxidation (Figure 4-17b).

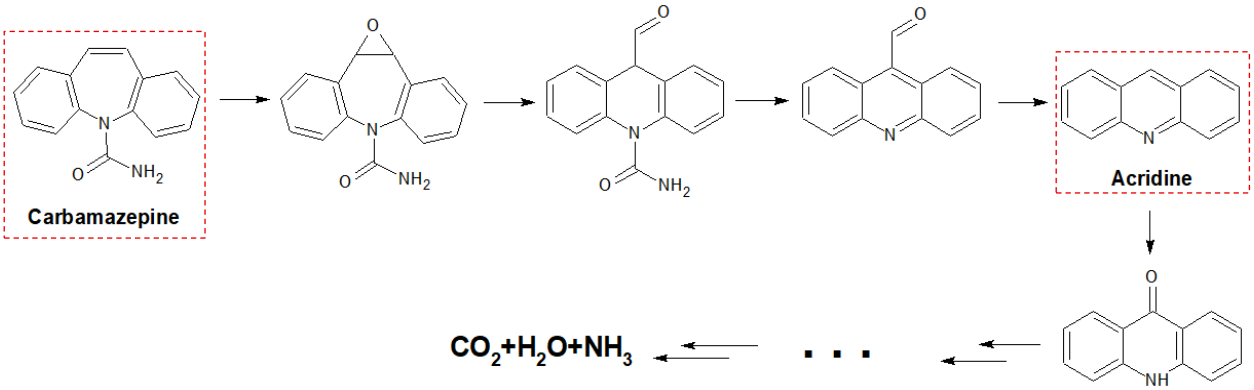

Figure 4-16 Most probable degradation pathway of carbamazepine [32]. In dashed frame the compounds seen on UV-vis spectra is highlighted.

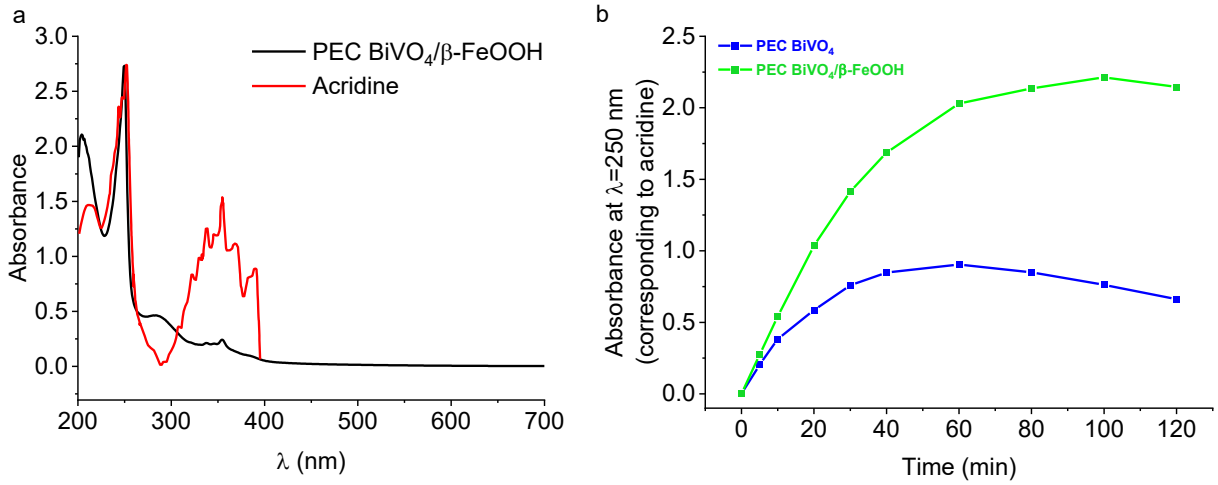

Figure 4-17 (a) Comparison of the UV-vis spectra after 120 minutes of CBZ photoelectrocatalytic oxidation on $BiVO_4$/β-FeOOH (black) and UV-vis spectra of acridine (red) and (b) evolution of acridine absorbance in photoelectrocatalytic oxidation of CBZ on bare $BiVO_4$ (blue) and on $BiVO_4$/β-FeOOH (green)

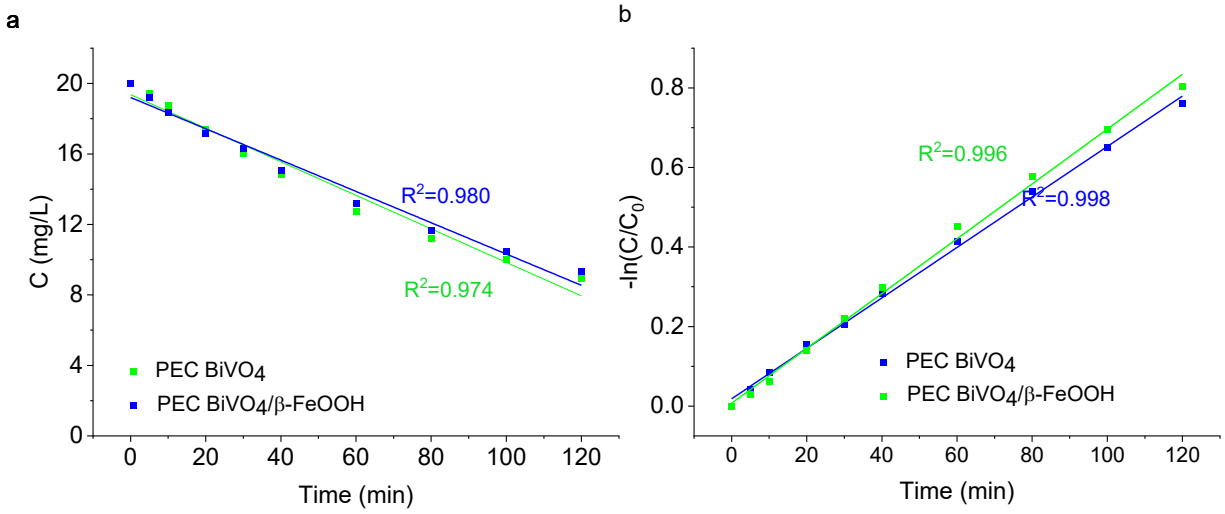

Figure 4-18 (a) Zero order and (b) 1st order kinetic analysis of CBZ degradation in photoelectrocatalytic process on bare $BiVO_4$ (blue) and on $BiVO_4$/β-FeOOH (green).

As can be seen from Figure 4-18 photoelectrocatalytic degradation of CBZ on both photoanodes obeys a pseudo-first order kinetics.

4.4.4. Photocatalytic and photoelectrocatalytic degradation of pharmaceuticals

Figure 4-19 shows the results of PCT, SMX and CBZ oxidation in different conditions. On bare $BiVO_4$ (black and blue curves) and on $BiVO_4$/β-FeOOH (red and green curves) photoanodes. In the case of zero applied bias (black and red curves) and at 0.8 V vs Ag/AgCl (blue and green).

One can observe that bare $BiVO_4$ without co-catalyst modification and without applied bias does not oxidize anything at all. This may occur due to poor charge separation and low catalytic activity.

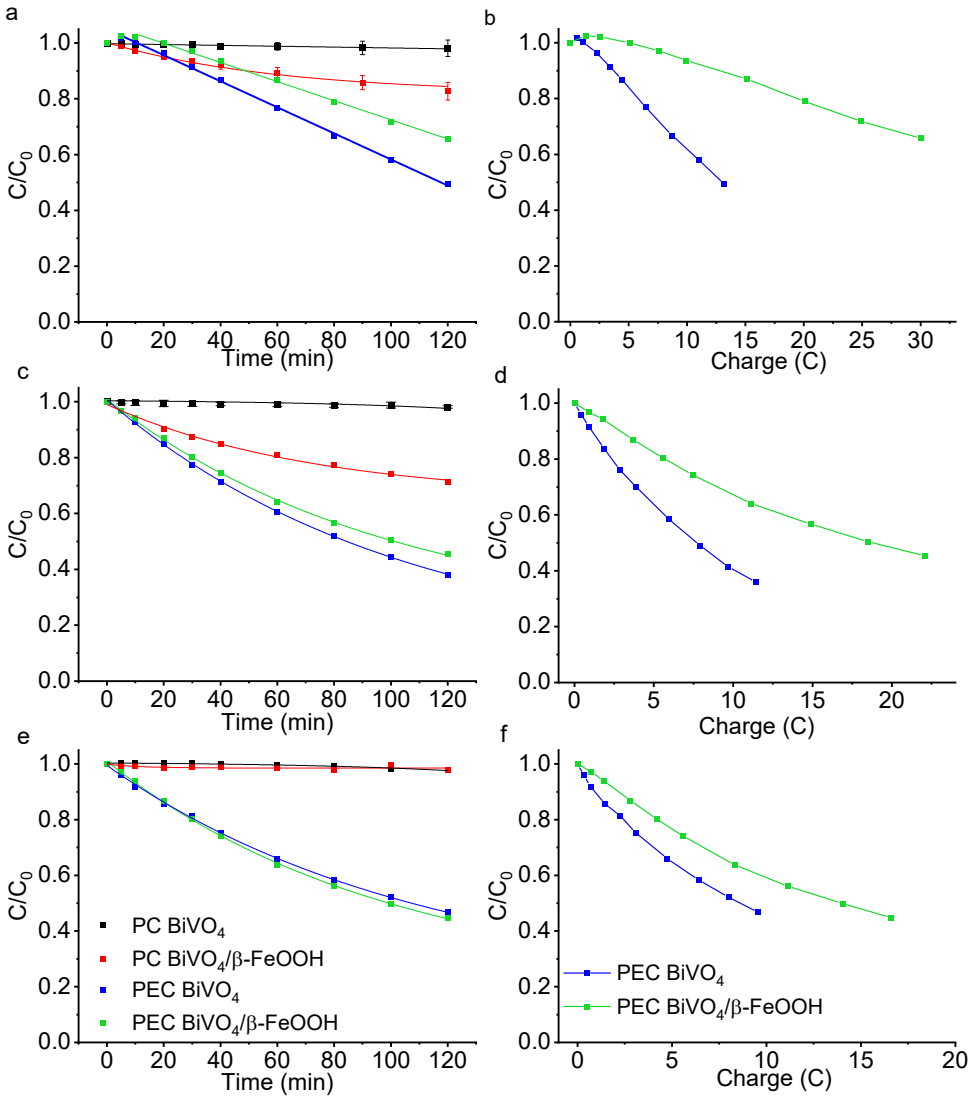

Figure 4-19 Degradation rate of paracetamol (a), sulfamethoxazole (c) and carbamazepine (e); dependence of degradation rate of paracetamol (b), sulfamethoxazole (d) and carbamazepine (f) on charge passed through the system. Black line corresponds to photocatalytic oxidation on bare $BiVO_4$, red line – photocatalytic oxidation on $BiVO_4$/β-FeOOH, blue line – photoelectrochemical oxidation on bare $BiVO_4$ and green line – photoelectrochemical oxidation on $BiVO_4$/β-FeOOH.

Modification of $BiVO_4$ with β-FeOOH leads to a slight improvement in photocatalytic performance: the removal rates increase to 17.2% for paracetamol and 28.6% for sulfamethoxazole while for CBZ it does not have any effect.

The application of external bias to bare $BiVO_4$ has much bigger effect than modification with co-catalyst, confirming that fast of electron-hole recombination is the main limitation factor of $BiVO_4$ photocatalytic performance. In all cases PEC on bare $BiVO_4$ gives the best percentage of removal: 50.6% for PCT, 64% for SMX and 53.3% for CBZ.

β-FeOOH modification leads to a decrease in photoelectrochemical performance, despite the fact that the current in the modified system is 1.5-2 times higher. This is especially clear from the plots showing the

dependence of organic oxidation on the charge passed through the system (Figure 4-19 b,d,f). The percentage of removal decreases from 50.6% for bare $BiVO_4$ to 34.2% for $BiVO_4$/β-FeOOH in the case of PCT photoelectrocatalytic degradation and from 64.0% to 54.6% in the case of SMX, while for CBZ it remains the same.

Kinetic analysis shows that in all cases except the PEC oxidation of PCT, the oxidation of pharmaceuticals follows pseudo-first order kinetics. In the systems under investigation, two reaction mechanisms may result in apparent pseudo-first order reaction kinetics.

First is the heterogeneous reaction of oxidation by holes. In this case the Langmuir-Hinshelwood model can be applied which assumes that the reactant is rapidly adsorbed on the catalyst surface and subsequently undergoes a slower surface reaction with rate *r*:

$$r = -\frac{dc}{dt} = k\frac{Kc}{1+Kc} \tag{4.19}$$

where *k* is the reaction rate constant, *K* is the adsorption-desorption equilibrium constant. For the diluted solutions, i.e. for $c<<10^{-3}$ M (20 mg/L of PCT, SMX and CBZ equivalent to $1.3\cdot10^{-4}$ M, $7\cdot10^{-5}$ M and $8.5\cdot10^{-5}$ M, respectively), equation (4.19) converts in:

$$r = kKc = k_{app}C \tag{4.20}$$

The second is the oxidation mediated by hydroxyl radicals. The oxidation of aromatic compounds in electrochemical advanced oxidation processes generally proceeds according to pseudo-first-order kinetics, as a steady-state concentration of hydroxyl radicals can be achieved in these systems. This is because hydroxyl radicals cannot accumulate due to their high reactivity, resulting in a dynamic equilibrium between their continuous generation and consumption [36].

$$r = k[HO^{\bullet}]C = k_{app}C \tag{4.21}$$

On the basis of the observation described above, several aspects require further clarifications and are addressed in the following sections (Section 4.5 Fundamental understanding of the observed behavior):

1) With the exception of photoelectrocatalytic PCT degradation, the oxidation of pharmaceutical compounds is found to follow apparent pseudo-first-order kinetics. Such behavior is characteristic of electrochemical advanced oxidation processes dominated by hydroxyl radical mediated pathways, but it may also originate from Langmuir-Hinshelwood-type heterogeneous kinetics in dilute solutions. In the present system, both effects may cause the observed kinetic behavior. The underlying origin of the apparent pseudo-first-order kinetics is therefore should be examined.
2) Modification of $BiVO_4$ with β-FeOOH results in a moderate enhancement of photocatalytic performance, whereas this improvement is not preserved under applied bias conditions. The mechanisms responsible for this behavior are analyzed in the following sections.
3) Under PEC conditions, photoanode exhibiting higher photocurrent densities ($BiVO_4$/β-FeOOH) is observed to display lower pharmaceutical degradation efficiencies. The origin of this discrepancy between photocurrent generation and degradation performance is investigated below.

4.4.5. Energy consumption analysis

As the degree of oxidation is unknown only the range of current efficiency can be estimated. The lower estimate of current efficiency is based on the assumption that only one electron leads to the degradation of initial molecule to the further by-products which do not absorb light at the characteristic wavelength. The upper estimate assumes that all electrons necessary for complete mineralization of the molecule participate in the reaction. The current efficiency, then, can be calculated as follows:

$$CE = \frac{nF(C_0 - C_{120})V}{M \cdot \text{Charge}} \cdot 100\% \quad (4.22)$$

where n – is the number of electrons participating in the reaction; F – Faraday's constant; C_{120} – concentration after 120 min of degradation experiment, g/l; C_0 – initial concentration, 0.02 g/l; V – cell volume, l; M – molar mass of the compound, g/mol.

Table 4-3 shows that in all cases the current efficiency is very low. For the best case (CBZ oxidation on bare $BiVO_4$) the upper estimate does not overcome 22% while for the worst case (PCT oxidation on $BiVO_4$/β-FeOOH) the lower estimate is 0.09%. This means that the parasitic reaction – water oxidation consumes most of the current.

It is seen that in the case of modified $BiVO_4$/β-FeOOH the current efficiency is lower while the energy consumption is higher than the ones of bare $BiVO_4$. This means that the modification with β-FeOOH strongly promotes the water oxidation reaction which is parasitic in the case of organic oxidation.

However, the measured energy consumption for the oxidation of pharmaceuticals on the bare $BiVO_4$ have very competitive values compared to conventional electrochemical oxidation process (1.48 kWh/m^3 for PCT, 1.22 kWh/m^3 for SMX and 1.12 kWh/m^3 for CBZ). This means that PEC can be considered if not as more efficient alternative to electrochemical oxidation but as a way to reduce energy costs.

Table 4-3 Parameters of pharmaceutical degradation. PC – photocatalytic degradation, PEC – photoelectrocatalytic degradation. The experiments are performed during 120 minutes in front illumination by 400 nm 100 mW/cm^2 diode under strong magnetic stirring. In the case of PEC, 0.8 V vs 1 M Ag/AgCl is applied.

	Percentage of removal, %	**Charge passed, C**	**Energy consumption, kWh/m^3**	**Energy consumption, mWh/mg**	**Current efficiency, %**
PCT $BiVO_4$	50.6	13.16	1.48	0.88	0.29-12.37
PCT $BiVO_4$/β-FeOOH	34.2	30.0	3.19	2.80	0.09-3.67
SMX $BiVO_4$	64.0	11.42	1.22	0.57	0.26-16.9
SMX $BiVO_4$/β-FeOOH	54.6	22.07	2.40	1.32	0.11-7.46
CBZ $BiVO_4$	53.3	9.56	1.12	0.63	0.27-21.86
CBZ $BiVO_4$/β-FeOOH	55.2	16.61	1.74	0.94	0.16-13.03

It should be noted that including the energy consumption of the artificial lamp would substantially increase the overall energy demand of the process, by approximately 567 kWh/m^3, according to the general formula $P_{lamp} \cdot t / V_{solution}$ [37]. For the present laboratory-scale setup, which was not designed as an optimized or scalable reactor configuration, such a value is not unexpected. In particular, the current geometry does not provide optimized light distribution or an improved $S_{anode}/V_{solution}$ ratio, both of which would be essential for reducing the specific energy demand in a practical reactor design. More importantly, as discussed above, $BiVO_4$ is a suitable photoactive material to be used without artificial light source as its narrow bandgap allows to absorb about 19% of standard solar spectra giving decent maximum theoretical values of photocurrent (about 7.5 mA/cm^2). Therefore, the artificial lamp in the present work should be regarded primarily as a laboratory tool used to intensify the degradation process and to eliminate other limiting parameters when investigating the changes in photoanode kinetic properties after its modification. In this sense, the reported lamp-related energy consumption reflects the conditions of mechanistic laboratory investigation rather than those of a realistic application scenario. For practical large-scale implementation of $BiVO_4$-based systems, the use of an artificial light source is not an intrinsic requirement as the solar light usage is possible and desired, and thus consideration of the electrical energy associated with the applied external bias is a more relevant metric for assessing process energy consumption.

FUNDAMENTAL UNDERSTANDING OF THE OBSERVED BEHAVIOUR

Investigation of effect of β-FeOOH on electron-hole separation and catalytic activity, determination of band diagram of β-FeOOH, probe molecule and quenching experiments have been done in order to understand the processes underlying behavior described in the previous section.

A deeper understanding of the effect of β-FeOOH modification can be obtained through the analysis of its band diagram, which allows one to: (i) compare the band positions of $BiVO_4$ and β-FeOOH to determine the type of heterojunction formed; (ii) compare the valence band position of β-FeOOH with the standard electrode potential for hydroxyl radical formation to assess whether their generation is thermodynamically possible; and (iii) compare the conduction band position of β-FeOOH with the standard electrode potential for superoxide anion formation to evaluate the thermodynamic possibility of their generation; (iv) access the possibility of pharmaceuticals oxidation by holes.

The band positions may be predicted by knowing the flat band potential (V_{fb}) which can be determined theoretically from the values of electronegativity (Butler-Ginley method) and experimentally by electrochemical techniques such as measurement of photocurrent onset potential and illuminated open circuit potential, and Mott-Schottky analysis. Another approach to evaluate band positions is to perform valence band XPS measurements.

Thus, the thick layer of β-FeOOH was deposited on the bare FTO substrate by the same procedure as for modification of $BiVO_4$. This FTO/β-FeOOH electrode was further investigated by different electrochemical techniques and XPS measurements to determine the band positions of β-FeOOH.

4.4.6. Electron-hole separation and catalytic activity

Electron-hole separation efficiency is evaluated using two independent approaches: photoluminescence spectroscopy and measurements performed in the presence of Na_2SO_3. Both techniques yield consistent results, indicating that electron-hole separation is not affected by the deposition of β-FeOOH and remains essentially unchanged.

Radiative recombination of electron-hole pairs is accompanied by photon emission, giving rise to photoluminescence (PL). Accordingly, analysis of PL spectra provides information on recombination processes and, indirectly, on charge separation efficiency. Figure 4-20a presents the PL spectra of bare $BiVO_4$, β-FeOOH and $BiVO_4$/β-FeOOH. All spectra exhibit broad emission bands, indicating the presence of multiple recombination pathways. An emission maximum around 570 nm is observed for β-FeOOH, which corresponds closely to its absorption edge (Figure 4-5a), suggesting that band-to-band recombination is the dominant process. In contrast, the PL spectrum of bare $BiVO_4$ displays an emission maximum at approximately 620 nm, which is red-shifted by nearly 100 nm relative to its absorption edge. This shift indicates the involvement of sub-band-gap energy states in the recombination process. Importantly, the PL spectrum of $BiVO_4$/β-FeOOH coincides with that of bare $BiVO_4$, indicating that the surface modification does not alter the recombination characteristics of the semiconductor.

Consistent results are obtained from measurements of electron-hole separation efficiency in Na_2SO_3 solution. As shown in Figure 4-20b, the separation efficiency curves for bare $BiVO_4$ and $BiVO_4$/β-FeOOH closely overlap. Taken together, the agreement between the two independent experimental techniques demonstrates that modification of $BiVO_4$ with a thin β-FeOOH layer does not affect its intrinsic electron-hole separation properties.

Catalytic activity is also evaluated using two independent techniques: electrochemical impedance spectroscopy and measurement of the charge injection yield in Na_2SO_3 solution. Both approaches provide consistent results.

The Nyquist plot shown in Figure 4-10c indicates that $BiVO_4$/β-FeOOH exhibits a markedly smaller semicircle than bare $BiVO_4$. The reduced arc diameter corresponds to a significantly lower charge-transfer resistance, indicating improved interfacial charge transport compared with pristine $BiVO_4$. These observations are consistent with the injection yield measurements performed in Na_2SO_3, as shown in Figure 4-20d. The $BiVO_4$/β-FeOOH photoanode exhibits a substantially higher injection yield, indicating that a larger fraction of photogenerated charge carriers is transferred from the semiconductor into the electrolyte as a result of the electrochemical reaction.

Taken together, both experimental techniques demonstrate that modification of $BiVO_4$ with β-FeOOH facilitates the release of photogenerated charge carriers into the solution, which is attributed to the enhanced catalytic activity of the photoanode.

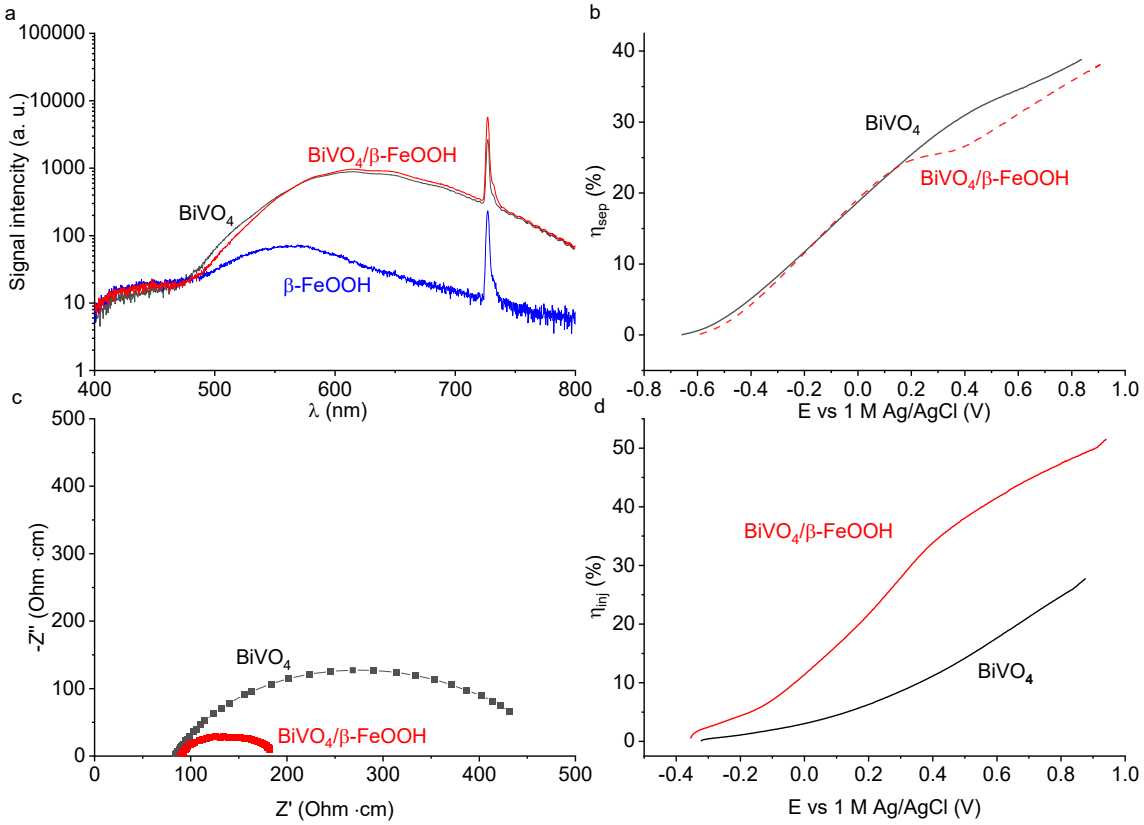

Figure 4-20 Electron-hole separation and catalytic activity of bare $BiVO_4$ (black) and modified $BiVO_4$/β-FeOOH (red). Photoluminescence spectra (a); electron-hole separation efficiency measured in 0.2 M Na_2SO_3 solution (b); EIS spectra under illumination (c); injection yield (d).

4.4.7. Theoretical evaluation of flat band potential of β-FeOOH by Butler Ginley method

Theoretically flat band potential of β-FeOOH can be evaluated from its electronegativity and band gap values, according to the equation (4.23) [38]:

$$V_{fb}[V\ vs\ RHE]=\frac{1}{e}\left(\chi-\frac{1}{2}E_g-E^e-\triangle E\right) \tag{4.23}$$

where e – is the electron charge (1.602 10^{-19} C), χ – electronegativity of a semiconductor material, E_g – band gap energy of a semiconductor, E^e is the free electron energy vs RHE (4.44 eV), ΔE is the difference between Fermi level and the bottom of a conduction band (for heavily dopped semiconductors it's generally assumed to be about 0.1 eV).

The electronegativity of the semiconductor is defined as the geometric mean of the electronegativities of the constituent neutral atoms χ(M). Accordingly, the electronegativity of for β-FeOOH may be calculated from the equation (4.24):

$$\chi=\left[\chi(Fe)\cdot\chi(O)^2\cdot\chi(H)\right]^{1/4} \tag{4.24}$$

According to the Mulliken's definition, the atomic electronegativity χ(M) is given by the arithmetic mean of the electron affinity (EA) and the first ionization energy (IE), both expressed in eV [39]. The values of EA, IE and χ(M) for Fe, O and H are listed in Table 4-4.

Table 4-4 The values of EA and IE are taken from www.nuclear-power.com.

Element	Electron affinity, eV	First ionization energy, eV	Electronegativity, eV
Fe	0.163	7.902	4.032
O	1.461	13.61	7.536
H	0.133	13.598	6.866

Thus, the calculated electronegativity of β-FeOOH is 6.297 eV which is in agreement with literature data [40].

Therefore, the flat band potential of β-FeOOH calculated by equation (4.23) equals to 0.672 V (vs RHE) or 0.024 V (vs 1 M KCl Ag/AgCl).

The theoretical model does not account for the possible adsorption of hydroxyl ions on the semiconductor surface (the point of zero charge of β-FeOOH is about 8.4 [41]) or for surface composition which can vary with the synthesis route. Moreover, it is known that β-FeOOH may exist in the form of four polymorphs (goethite (α-FeOOH), akaganeite (β-FeOOH), lepidocrocite (γ-FeOOH), and δ-feroxyhyte) having different band gaps and different location of the band edges [7]. Therefore, it is not straightforward to relate the calculated value to the material's surface crystallography and its surface charge characteristics.

4.4.8. Experimental determination of flat band potential by electrochemical techniques

Experimentally flat band potential can be determined by electrochemical techniques such as photocurrent onset potential measurements, measurements of illuminated open circuit potential and Mott-Schottky analysis.

The flat-band potential was estimated from the open-circuit potential measured under illumination (Figure 4-21a). Measurements were carried out in a deaerated electrolyte to prevent dissolved oxygen from scavenging photogenerated electrons, which would reduce the photovoltage. The data in Figure 4-21a were collected at a light intensity high enough to achieve complete band flattening. The obtained value of -0.13 V is slightly more positive than the value of photocurrent onset potential (-0.15 V, as shown in Figures 4-21 b and c). Thus, the mean value of these two measurements (-0.14 V vs 1 M KCl Ag/AgCl or 0.51 V vs RHE) was assumed as a flat band position of a β-FeOOH deposited on FTO.

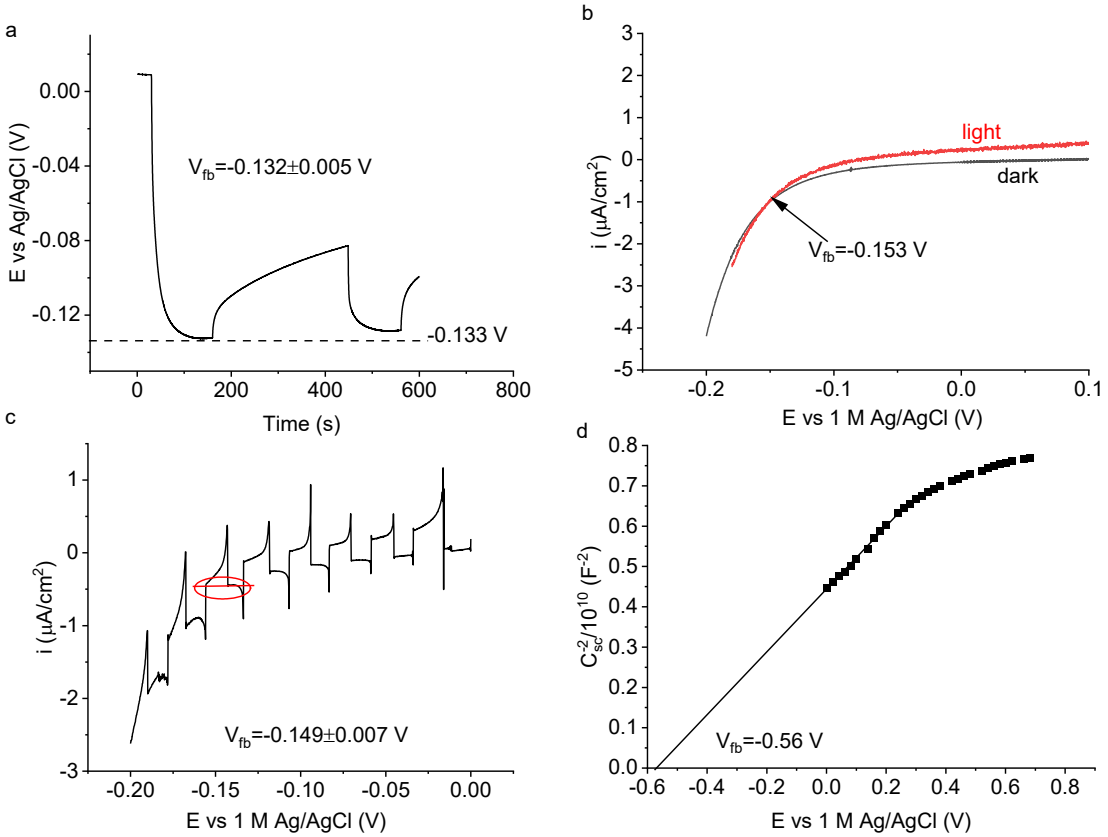

Figure 4-21 Electrochemical determination of flat band potential of β-FeOOH. (a) Illuminated open circuit potential recorded in deaerated solution; (b) linear sweep voltammetry in dark (black line) and illuminated (red line), scan rate 20 mV/s; (c) chopped linear sweep voltammetry, scan rate 5 mV/s; (d) Mott-Schottky plot fitted with the equivalent circuit.

The Mott-Schottky plots obtained at five different frequencies are presented in Figure 4-22a. It can be observed that the intersection point with the potential axis varies with frequency, indicating a deviation from ideal Mott-Schottky behavior. Among the possible reasons of such deviation described in [42], the presence of non-stoichiometric ions and surface states has been pointed out. As determined by high-resolution XPS measurements (Section 4.3.1, Figure 4-4), the applied β-FeOOH synthesis procedure led to the formation of significant amount of oxygen vacancies and Fe^{2+} ions in the crystal lattice. Therefore, it is assumed that the observed deviation from ideal Mott-Schottky behaviour arises from these surface defects.

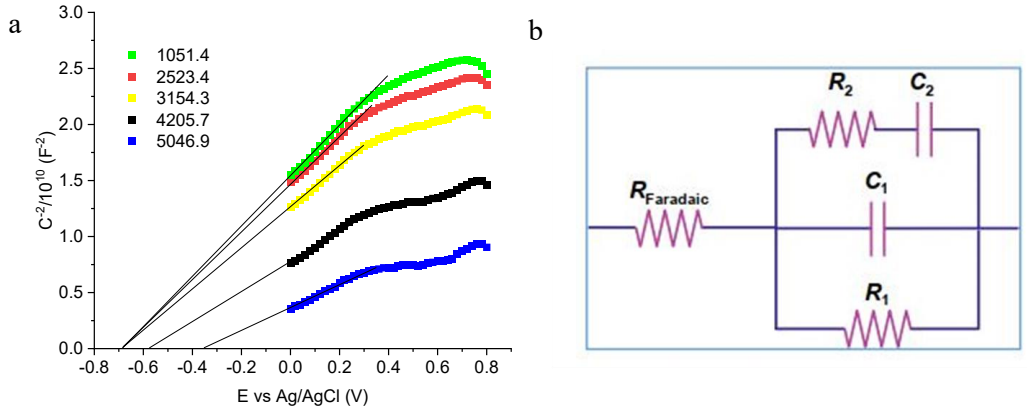

Figure 4-22 (a) The Mott-Schottky plot of β-FeOOH and (b) the equivalent circuit used to determine the slope.

The presence of surface states introduces an additional capacitance contribution to the system; therefore, the assumption which was used in the derivation of Mott-Schottky equation – that all capacitances other than that of the semiconductor can be neglected – is not valid in this case. Consequently, the experimental EIS data fitting using an equivalent circuit that accounts for this additional contribution is commonly employed to extract the semiconductor capacitance. In the literature [43], the equivalent circuit shown in Figure 4-22b is proposed. It includes an additional resistance (R_2) and capacitance (C_2) associated with the surface states, which are connected in series with each other and in parallel with the semiconductor capacitance (C_1).

However, the flat-band potential obtained from this fitting (Figure 4-21d) deviates significantly from both the theoretical value (0.44 V vs 1 M KCl Ag/AgCl) and the values determined by other experimental techniques (-0.14 V vs 1 M KCl Ag/AgCl, measured as the illuminated OCP and photocurrent onset potential). At present, no clear explanation for this discrepancy can be provided. Nevertheless, the Mott–Schottky slope obtained from this fitting will be used to calculate the donor's concentration, as it does not influence the final value of the difference between the flat-band potential and the conduction band maximum, even if it varies by an order of magnitude both in positive and negative direction.

4.4.9. Band diagram determination

The obtained value of the flat band potential was used to determine the bottom edge of the conduction band, according to the equation 4.25 [44]:

$$V_{fb} - E_{CB} = k_B T \ln \frac{n_0}{N_C} \tag{4.25}$$

where k_B is the Boltzmann constant ($1.38 \cdot 10^{-23}$ J·K^{-1}), T is temperature, n_0 is a total concentration of donor impurities in bulk and on the surface, and N_C is a density of states in the conduction band. The value of N_C is a function of the effective mass of the electron (m_e^*) in the crystal lattice (Eq. 4.26):

$$N_C = \frac{1}{\sqrt{2}} \left(\frac{m_e^* k_B T}{\pi \hbar^2} \right)^{3/2} \tag{4.26}$$

According to the literature, the m_e^* / m_o ratio for β-FeOOH is about 7.13 [41], where the effective mass of the electron m_o=9.11·10^{-31} kg. Thus, taking into account that the reduced Planck constant $\hbar$=1.05·10^{-34} Js, the calculated value of N_C for β-FeOOH is 4.79·10^{20} cm^{-3}.

On the other hand, it is assumed that the value of n_o is practically equal to the concentration of donors, N_D [44]. The latter one may be obtained from the slope of Mott-Schottky plot according to the following equation 4.27:

$$\frac{1}{C^2} = \frac{2}{e_o \varepsilon_0 \varepsilon_r N_D A^2}\left(E - E_{fb} - \frac{k_B T}{e_o}\right) \tag{4.27}$$

where e_o is the electron charge (1.602·10^{19} C), ε_0 is the vacuum permittivity (8.85·10^{-14} F·cm^{-1}), ε_r is the relative permittivity (for β-FeOOH is 4 [46]), A is the surface area of photoelectrode.

The N_D value determined for β-FeOOH from the fitting of Mott-Schottky plot with the equivalent circuit (Figure 4-21d) equals to 1.44·10^{20} cm^{-3}. Thus, the difference between the flat band potential and the bottom of the conduction band for β-FeOOH calculated from the Eq. (4.25) is about 0.03 eV. This means that the position of the E_{CB} of β-FeOOH obtained in this work may be identified with V_{fb} (0.095 V vs SHE). Since the E_g determined from Tauc plot is 2.17 eV (Figure 4-5b), the edge of the valence band is located at about 2.64 V vs SHE.

The upper edge of the valence band of β-FeOOH (vs RHE) was also determined from valence band-XPS spectra (Figure 4-23). The obtained by XPS value of significantly differ from the one obtained by electrochemical measurement of flat band potential. It also can be seen from the Table 4-5 that values of flat band potential of β-FeOOH differ a lot across the literature.

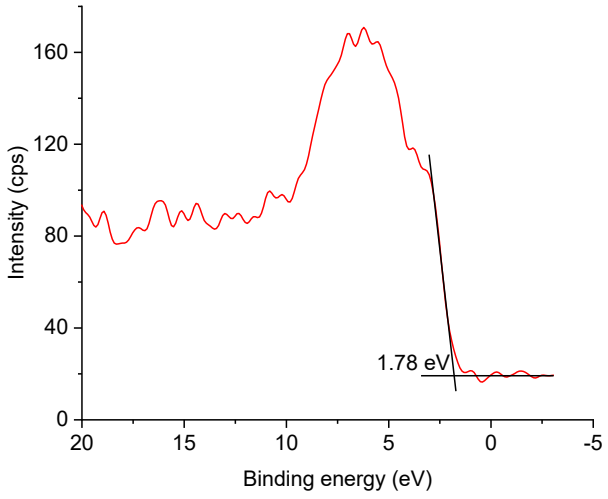

Figure 4-23 Valence band XPS spectra of FTO/β-FeOOH.

Table 4-5 Band positions of β-FeOOH determined by different methods.

VB (V vs RHE)	CB (V vs RHE)	Eg, eV	Method of determination
2.77	0.61	2.16	XPS [7]
2.95	0.81	2.14	Butler-Ginley method [12]
2.23	-0.44	2.67	DFT [45]
1.73	-0.38	2.11	Mott-Schottky [47]
2.84	0.67	2.17	Butler-Ginley method (this work)
2.68	0.51	2.17	Photocurrent onset potential and illuminated photovoltage (this work)
1.78	-0.39	2.17	XPS (this work)

4.4.10. Probe molecule experiment for HO· radicals formation

The indirect determination of hydroxyl radical formation in the system is achieved by performing oxidation experiments with terephthalic acid and detecting the corresponding oxidation product, 2-hydroxyterephthalic acid (TA-OH). Accordingly, a higher detected concentration of TA-OH indicates a higher rate of hydroxyl radical generation in the system.

Figure 4-24 presents the concentrations of TA-OH detected after 30 min of terephthalic acid oxidation under (a) photocatalytic and (b) photoelectrocatalytic conditions. Hydroxyl radical formation is observed for all investigated systems. The obtained trends are consistent with the pharmaceutical degradation results shown in Figure 4-19.

The lowest amount of hydroxyl radicals is generated on bare $BiVO_4$ under photocatalytic conditions, which corresponds to the nearly negligible degradation of all pharmaceutical compounds. Modification of $BiVO_4$ with β-FeOOH leads to a slight increase in hydroxyl radical generation, in agreement with the modest improvement observed in pharmaceutical degradation. Upon application of an external bias, bare $BiVO_4$ generates more than twice as many hydroxyl radicals as in the photocatalytic process, representing the highest hydroxyl radical production among the four investigated systems and corresponding to the most efficient degradation of all three pharmaceutical compounds. Moreover, under photoelectrocatalytic conditions, the amount of hydroxyl radicals generated on $BiVO_4$/β-FeOOH is lower than that on bare $BiVO_4$, which is consistent with the inferior pharmaceutical degradation performance observed for the modified photoanode under bias.

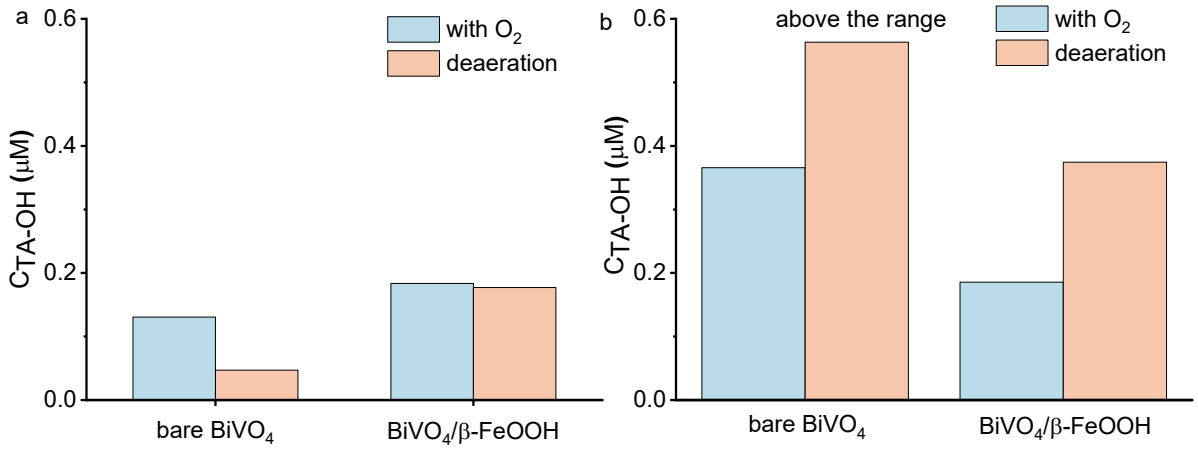

Figure 4-24 Photocatalytic (a) and photoelectrocatalytic (b) oxidation of terephthalic acid after 30 min. Normal solution (blue) and deaerated with Ar purging (orange).

As discussed in the Literature Review (Section 1.4), the formation of hydroxyl radicals on $BiVO_4$ is both thermodynamically and catalytically unfavourable. The position of the valence band is such that photogenerated holes do not possess sufficient energy to directly oxidize water to $HO^{\bullet}$. In addition, the $BiVO_4$ surface does not exhibit catalytic activity toward hydroxyl radical formation, as HO* adsorbates generated during water oxidation are strongly bound to the surface and are therefore not prone to desorption into the solution. These conclusions are consistently supported by experimental studies [48–51]. Nevertheless, hydroxyl radicals are clearly detected in the present system, raising the question of their origin.

To clarify this issue, terephthalic acid oxidation experiments are performed in deaerated solutions. Under photocatalytic conditions on bare $BiVO_4$, the formation of TA-OH is found to decrease significantly in the absence of dissolved oxygen, reaching levels comparable to those measured in the blank sample (DI water). This behavior contrasts with the results obtained in oxygen-containing solutions and indicates a key role of dissolved oxygen in hydroxyl radical formation.

Łęcki et al. [15] propose the following mechanism to explain this observation. The conduction band position of $BiVO_4$ provides sufficient reducing power to drive the reduction of dissolved oxygen to the superoxide anion radical:

$$\bar{e}_{CB} + O_{2(aq)} \rightarrow O_2^{\bullet -} \tag{4.28}$$

The formation of $O_2^{\bullet -}$ radicals is further confirmed by the authors using oxidation experiments with nitro blue tetrazolium chloride, a probe molecule for superoxide anion radicals. Subsequently, the generated superoxide anion radicals can be converted into hydroxyl radicals through the reaction pathways described in equations (2.29)–(4.31) [52]:

$$O_2^{\bullet -} + H^+ \rightarrow HO_2^{\bullet} \tag{4.29}$$

$$O_2^{\bullet -} + HO_2^{\bullet} + H_2O \rightarrow OH^- + O_2 + H_2O_2 \tag{4.30}$$

$$O_2^{\bullet -} + H_2O_2 \rightarrow HO^{\bullet} + OH^- + O_2 \tag{4.31}$$

According to this mechanism, the presence of dissolved oxygen in the solution enables indirect hydroxyl radical formation via superoxide anion radical generation on bare $BiVO_4$. In the absence of dissolved oxygen, hydroxyl radical formation is suppressed. This interpretation is consistent with the results of terephthalic acid oxidation experiments and supports the conclusion that in photocatalytic process on bare $BiVO_4$ hydroxyl radicals are predominantly generated through this indirect, oxygen-mediated pathway.

However, in the photocatalytic system employing $BiVO_4$/β-FeOOH, no decrease in TA-OH concentration is observed under deaerated conditions. Instead, the TA-OH concentration remains essentially unchanged. This behavior indicates that hydroxyl radical generation in this system proceeds via a different mechanism.

Under photoelectrocatalytic conditions, the observed behavior is more difficult to rationalize. In deaerated solutions, hydroxyl radical formation is found to be even higher than in oxygen-containing electrolytes. For bare $BiVO_4$, the generation rate of hydroxyl radicals is sufficiently high that the TA-OH concentration exceeds the detection limit within the first 15 min of the experiment. At the same time, the fluorescence spectra retain the same shape, indicating that the formation of alternative fluorescent products is unlikely. Based on these observations, an enhancement of pharmaceutical oxidation under deaerated conditions could be anticipated. However, experiments on photoelectrocatalytic degradation of PCT performed in deaerated solutions do not show any improvement compared with experiments conducted in oxygen-containing electrolytes. This apparent discrepancy suggests that the increased TA-OH signal observed during terephthalic acid oxidation under photoelectrocatalytic and deaerated conditions does not directly translate into enhanced oxidative degradation of pharmaceutical compounds. Accordingly, the elevated hydroxyl radical signal detected in terephthalic acid oxidation experiments under these specific conditions is considered to be a system-specific feature of the probe reaction rather than a general indicator of oxidative performance. At present, a definitive mechanistic explanation for this behavior cannot be provided, and further investigation is required. These results highlight the need for caution when interpreting hydroxyl radical probe experiments.

4.4.11. Quenching experiments

To identify the reactive species responsible for pharmaceutical degradation, scavenger experiments are performed. However, the results obtained are difficult to interpret unambiguously. Therefore, this section emphasizes the need for particularly careful and critical application of scavenger experiments in photo- and photoelectrocatalytic studies and outlines key considerations that must be taken into account when performing such experiments.

For the correct implementation of quenching experiments, it is necessary not only to select a highly selective scavenger with a high reaction rate toward the targeted reactive species, but also to consider potential interactions between the scavenger and the target organic pollutant, as well as between the scavenger and the photocatalyst. In addition, the scavenger concentration must be carefully optimized to ensure meaningful and reliable interpretation of the results, and it must be verified that the scavenger does not induce additional effects that influence the overall performance of the system [53].

The reactive oxygen species most likely involved in the investigated systems include hydroxyl radicals, superoxide anion radicals, photogenerated holes, and sulfate radicals. The commonly used scavengers for

these species are reviewed by Liu et al. [53]. Tert-butyl alcohol (TBA) is widely employed as a selective hydroxyl radical scavenger because it exhibits a high reaction rate with HO· and does not react with sulfate radicals. p-Benzoquinone is frequently used to quench superoxide anion radicals; however, it absorbs light in the 200-500 nm wavelength range. As a result, its presence in solution can reduce the photon flux reaching the photocatalyst surface and thereby diminish the apparent photocatalytic performance due to light-screening effects. For this reason, elimination of superoxide radical anions from solution is achieved by suppression of their formation by means of solution deaeration rather than by the addition of *p*-benzoquinone. Ethanol (EtOH) is used as a scavenger for both sulfate and hydroxyl radicals; comparison of its effect with that of tert-butanol allows to assess the contribution of sulfate radicals [54].

The use of hole scavengers in photocatalytic experiments requires careful consideration [53]. Rapid extraction of photogenerated holes from the semiconductor surface can increase the availability of electrons by suppressing electron-hole recombination [55]. As a consequence, enhanced oxygen reduction and, therefore, increased formation of superoxide anion radicals may occur [56].

Since no degradation of pharmaceutical compounds is observed in photocatalytic experiments on bare $BiVO_4$, quenching experiments are performed using $BiVO_4$/β-FeOOH under photocatalytic conditions. Sulfamethoxazole (SMX) is selected as the model organic compound.

First, the potential interaction between the scavengers and SMX is assessed by preparing solutions in which the scavenger concentration is 500 times higher than that of SMX and subjecting them to vigorous stirring under light irradiation for 2 h. No change in SMX concentration is detected, indicating that, as expected, no direct interaction occurs between SMX and either ethanol or tert-butanol.

Second, the influence of TBA concentration is investigated in order to determine an appropriate scavenger loading. The addition of TBA at a concentration 500 times higher than that of SMX results in a slight enhancement of SMX oxidation (Figure 4-25a). This effect is difficult to rationalize. It is possible that this TBA concentration is insufficient to exert a measurable quenching effect on SMX degradation, and that the observed minor increase falls within the inherent variability of photocatalytic performance, which is typical for photoactive materials. Increasing the TBA concentration to 1000 times that of SMX leads to a pronounced inhibition of SMX oxidation. However, this effect cannot be attributed solely to the quenching of hydroxyl radicals. It is observed that TBA adversely affects the stability of $BiVO_4$/β-FeOOH samples. In particular, after exposure to TBA, subsequent photocatalytic experiments performed with the same $BiVO_4$/β-FeOOH sample under standard conditions (i.e., without the addition of scavengers) show no measurable decrease in SMX concentration (Figure 4-25b). This observation indicates that contact between $BiVO_4$/β-FeOOH and TBA alters the surface properties of the photocatalyst and suppresses its ability to oxidize SMX.

The overall effect of scavengers on the photocatalytic degradation of SMX on $BiVO_4$/β-FeOOH is summarized in Figure 4-25c. In addition to the inhibition of degradation observed upon the addition of tert-butanol, complete suppression of SMX oxidation is observed under deaerated conditions. This result is not consistent with the probe-molecule oxidation experiments discussed in Section 4.5.5, which demonstrate that hydroxyl radicals are still generated during photocatalytic operation of $BiVO_4$/β-FeOOH in the absence of dissolved oxygen. At the same time, attributing this behaviour to exclusive oxidation of SMX by superoxide anion radicals appears unlikely, as numerous literature reports indicate that SMX is readily

oxidized by hydroxyl radicals. Consequently, the interpretation of the scavenger experiment results remains ambiguous. Overall, due to the coexistence of multiple competing effects influencing photocatalytic performance, the dominant oxidative species responsible for photocatalytic SMX degradation on $BiVO_4$/β-FeOOH cannot be conclusively identified based on quenching experiments.

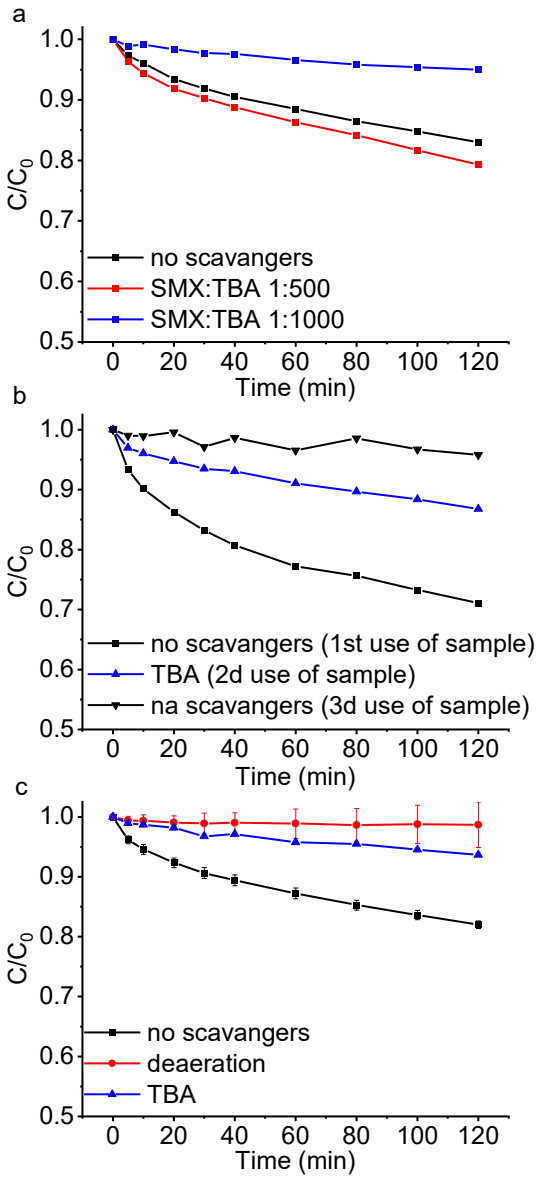

Figure 4-25 Influence of addition of scavengers on photocatalytic degradation of SMX on $BiVO_4$/β-FeOOH. (a) Influence of TBA concentration: 0 TBA concentration (black), TBA concentration 500 times higher than SMX concentration (red) and TBA concentration 1000 times higher than SMX (blue). (b) Influence of TBA on stability of $BiVO_4$/β-FeOOH: first use of freshly prepared $BiVO_4$/β-FeOOH sample (red squares), performance of the same sample in the presence of TBA (blue triangles) and performance of this sample after interaction with TBA in the absence of any scavenger (black triangles). (c) Influence of scavangers on photocatalytic oxidation of SMX on $BiVO_4$/β-FeOOH: no scavengers (black), in the presence of TBA (blue), with deaeration of solution (red).

Under photoelectrocatalytic conditions, the results are even more difficult to interpret. Figure 4-26a shows the PEC degradation of SMX on $BiVO_4$ in the presence of tert-butanol, ethanol, under deaerated conditions, and under deaerated conditions with the addition of tert-butanol. In all cases, the addition of scavengers leads to an apparent enhancement of SMX degradation performance. At first glance, this behavior could be attributed to the role of alcohols (tert-butanol and ethanol) as hole scavengers. However, chronoamperometric measurements recorded during the experiments indicate that neither tert-butanol addition nor deaeration results in significant changes in the photocurrent, whereas addition of ethanol leads to a pronounced increase in current density, approximately twofold compared with the electrolyte alone (Figure 4-26b). This observation suggests that, among the investigated conditions, only ethanol effectively scavenges photogenerated holes. Notably, even in the presence of ethanol – where hydroxyl radicals, holes, and sulfate radicals are expected to be scavenged – the SMX degradation efficiency is either slightly enhanced or remains unchanged. At the same time, attributing SMX oxidation exclusively to superoxide anion radicals appears inconsistent with the other experimental observations. If this were the case, a substantial inhibition of SMX degradation would be expected under deaerated conditions; instead, a slight increase in the degradation rate is observed.

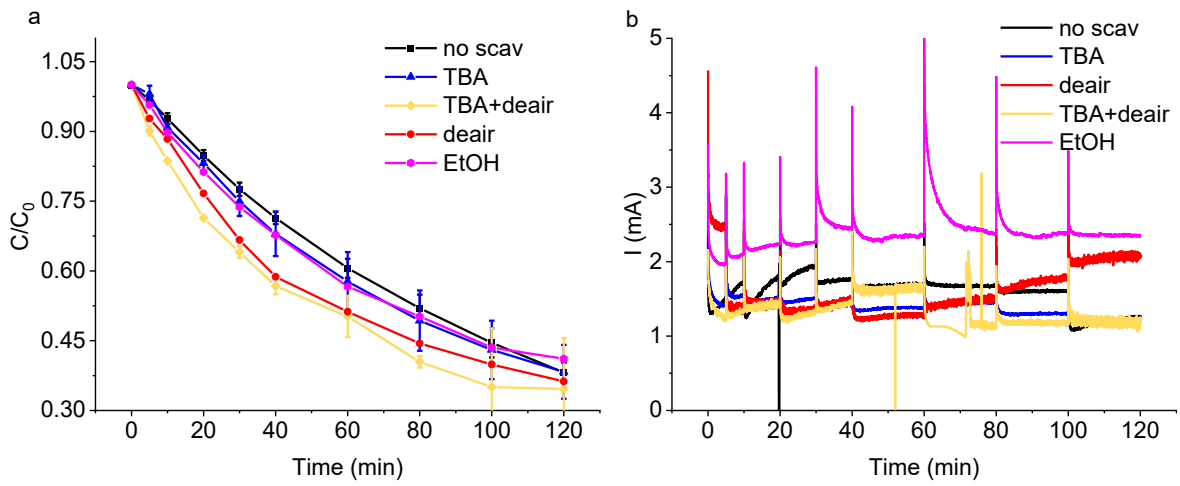

Figure 4-26 Influence of addition of scavengers on photoelectrocatalytic degradation of SMX (a) and photocurrent (b) recorded on $BiVO_4$. In the absence of any scavenger (black), in the presence of TBA (blue), under deaeration (red), under deaeration with addition of TBA (yellow) and in the presence of ethanol (pink).

Therefore, the quenching experiments performed under both photocatalytic and photoelectrocatalytic conditions do not provide a definitive identification of the dominant oxidative species responsible for pharmaceutical degradation. Rather, the results illustrate the complexity of scavenger effects and highlight the limitations of quenching experiments for mechanistic interpretation in such systems.

4.4.12. Mechanism of photocatalytic and photoelectrocatalytic degradation of pharmaceuticals

The analysis presented in the preceding sections reveals several observations that require consistent mechanistic interpretation. These include the origin of the apparent pseudo-first-order kinetics observed during pharmaceutical oxidation, the role of β-FeOOH surface modification in enhancing photocatalytic

performance and its suppression under an applied electrical bias, as well as the apparent mismatch between photocurrent density and degradation efficiency under photoelectrocatalytic conditions.

In the following section, a reaction mechanism is proposed to rationalize these observations and to elucidate the effect of β-FeOOH modification on the photoelectrochemical behavior of $BiVO_4$.

Figure 4-27 illustrates the band diagram of the $BiVO_4$/β-FeOOH photoanode together with the redox potential of formations of the main radicals and of oxidation of PCT, SMX, CBZ and terephthalic acid. Although band edge positions determined by electrochemical measurements and XPS show noticeable differences, both methods consistently indicate that the energy of photogenerated holes in β-FeOOH is insufficient to drive the direct formation of hydroxyl radicals from water (Section 4.5.4). The constructed band diagram of the $BiVO_4$/β-FeOOH system suggests that the oxidation of all three pharmaceutical compounds can proceed via direct hole transfer at the photoanode surface.

The hypothesis proposed in Introduction that modification of $BiVO_4$ with β-FeOOH may create a Z-scheme was not proved, as the electron-hole separation properties of modified photoanode remain unchanged (Section 4.5.1).

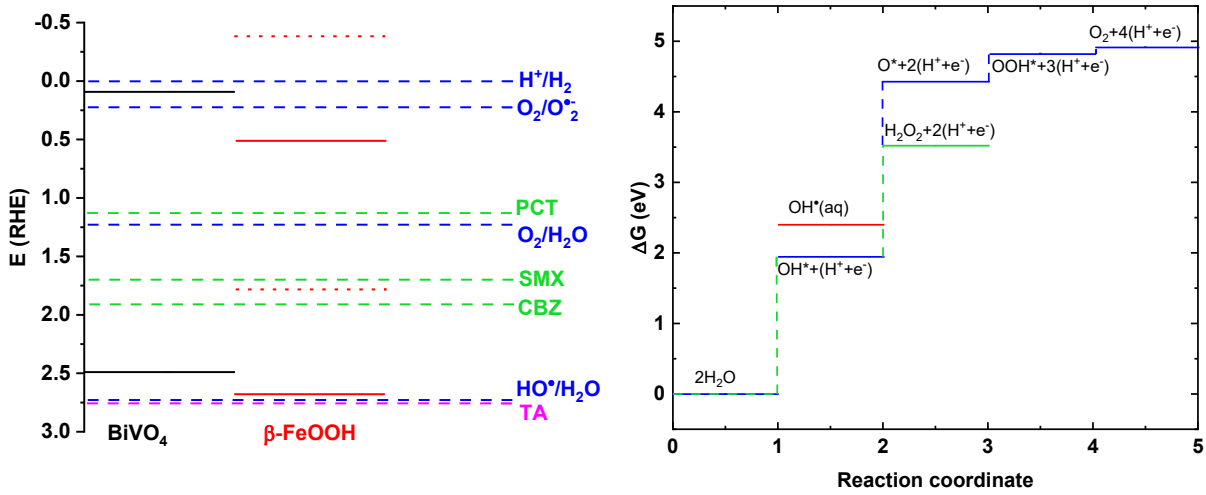

Figure 4-27 Band diagram of $BiVO_4$/β-FeOOH system (a) and free energy diagram for water oxidation reaction on $BiVO_4$ (b). Band diagram of $BiVO_4$ (black) obtained by the electrochemical measurements in previous work [15] and β-FeOOH (red) determined in this study from electrochemical measurements of flat band potential (solid lines) and VB-XPS (dotted lines). Standard potentials of radicals' formation (blue) are taken from [57]. Potentials of pharmaceuticals' oxidation (green) are evaluated in this work (Section 4.4.2). Potential of terephthalic acid oxidation (pink) calculated by DFT in [19]. Free energies are calculated by DFT in [58].

The effect of β-FeOOH modification on the photocatalytic performance of $BiVO_4$ can be explained by the reaction mechanism proposed in Figure 4-28. Under photocatalytic conditions, where both anodic and cathodic reactions take place on the surface of the photocatalyst, a Fenton-like reaction pathway may become operative. DFT calculations indicate that the $BiVO_4$ surface, despite exhibiting sluggish kinetics toward the oxygen evolution reaction, shows a tendency to oxidize water to hydrogen peroxide (Figure 4-27b). The formation of hydrogen peroxide on $BiVO_4$ surfaces has also been reported in several experimental studies [59–61].

SEM analysis of the modified $BiVO_4$/β-FeOOH photoanode reveals that β-FeOOH nanoparticles do not fully cover the $BiVO_4$ surface (Figure 4-3c). As a result, portions of the $BiVO_4$ surface remain exposed to the electrolyte, forming a $BiVO_4$/electrolyte interface. At this interface, the anodic oxidation of water to hydrogen peroxide can occur. Subsequently, Fe^{2+} ions – present in significant amounts due to oxygen vacancies in β-FeOOH, as confirmed by XPS analysis (Figure 4-4) – participate in a Fenton-like reaction with hydrogen peroxide, leading to the formation of hydroxyl radicals. The resulting Fe^{3+} species are then reduced back to Fe^{2+} by photogenerated electrons, thereby closing the catalytic redox cycle.

This proposed mechanism is consistent with the results obtained from terephthalic acid oxidation experiments (Section 4.5.5), which demonstrate enhanced hydroxyl radical formation on the $BiVO_4$/β-FeOOH surface compared to bare $BiVO_4$. Furthermore, deaeration of the solution does not suppress hydroxyl radical formation on $BiVO_4$/β-FeOOH, indicating that dissolved oxygen is not involved in the radical generation pathway. This behavior contrasts with that observed for unmodified $BiVO_4$, where dissolved oxygen plays a key role in hydroxyl radical formation (Section 4.5.5).

When an external electrical bias is applied, the photoelectrode is forced to operate exclusively as an anode, thereby suppressing cathodic reactions at the surface. Under these conditions, the Fenton-like pathway is no longer operative, and hydroxyl radical formation via this mechanism is inhibited. Consequently, $BiVO_4$/β-FeOOH does not exhibit an advantage over bare $BiVO_4$ in hydroxyl radical generation under photoelectrocatalytic conditions.

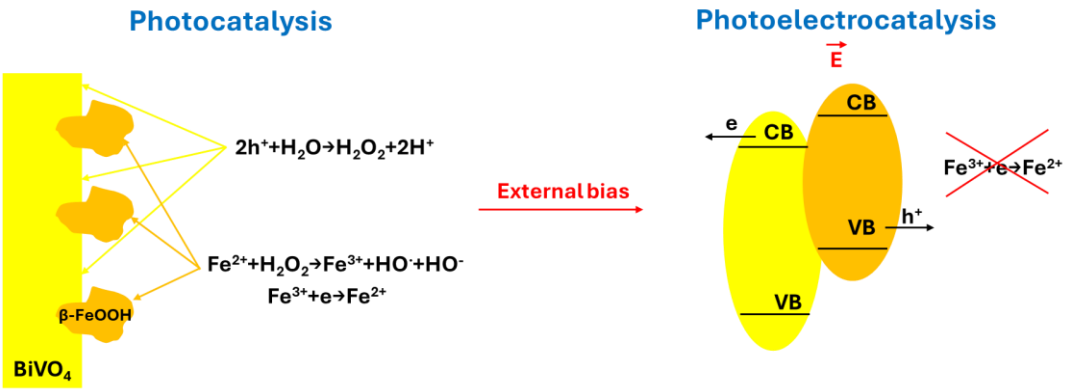

Figure 4-28 Proposed scheme to explain the improved degradation of pharmaceutical pollutants on $BiVO_4$/β-FeOOH compared to bare $BiVO_4$

In general, the mechanism of hydroxyl radical formation under photoelectrocatalytic conditions remains insufficiently understood. Since the application of an external bias does not alter the positions of the semiconductor band edges but primarily increases the number of charge carriers participating in electrochemical reactions, it is reasonable to assume that the fundamental radical generation pathways remain similar to those operative under photocatalytic conditions. Accordingly, if hydroxyl radicals are formed on $BiVO_4$ during photocatalysis via superoxide anion radicals generated through the reduction of dissolved oxygen, an analogous mechanism may also be operative under photoelectrocatalytic conditions. However, under photoelectrochemical operation, anodic and cathodic reactions are spatially separated. In such a case, superoxide anion radicals would be generated at the cathode, which remains unmodified.

Consequently, a higher photocurrent observed for the $BiVO_4$/β-FeOOH system would be expected to result in an increased flux of superoxide anion radicals at the cathode and, therefore, a higher concentration of hydroxyl radicals. This expectation is not supported by the experimental results, as demonstrated in Figure 4-24b.

An alternative explanation could involve a false detection of hydroxyl radicals in the terephthalic acid probe experiments, arising from the direct oxidation of TA by photogenerated holes, which could also lead to the formation of the TA-2OH product. The experimental determination of the oxidation potential of TA is challenging due to its low solubility and, consequently, low concentration, as well as the high potential required for its oxidation: as a result, the corresponding oxidative current is low and is consistently masked by the oxygen evolution reaction current, even on boron-doped diamond electrode [19]. Nevertheless, the oxidation potential of TA (E=2.76 V vs. SHE) has been determined by DFT calculations [19]. According to the band diagram shown in Figure 4-27a, neither bare $BiVO_4$ nor $BiVO_4$/β-FeOOH possesses sufficient valence band potential to directly oxidize TA. Therefore, there is no basis to attribute the observed formation of hydroxyl radicals product to false detection.

The absence of a direct correlation between the photocurrent generated in the system and the degradation rate can be attributed to the redistribution of the total current between organic compound oxidation and water oxidation reactions. All electrochemical characterization experiments of the photoanodes were conducted in electrolyte in the absence of organic species; therefore, these measurements predominantly reflect the kinetics of the water oxidation reaction. The experimental results clearly demonstrate that modification of $BiVO_4$ with β-FeOOH leads to a substantial reduction of catalytic barriers (Section 4.5.1). Importantly, these reduced barriers are associated specifically with the water oxidation reaction. Therefore, at the unmodified electrode, when water oxidation is kinetically sluggish, the oxidation of organic compounds competes more successfully for charge carriers. After the electrode is coated with a catalyst, the kinetic barriers for water oxidation are largely removed: most of the current now flows into that reaction, organic oxidation struggles to compete, and its current share falls. Consequently, even though the total current rises by 1.5-2 times, the partial current devoted to organic oxidation can actually decrease. This interpretation is further supported by current efficiency calculations. For example, for CBZ, for which similar removal rates are observed on both $BiVO_4$ and $BiVO_4$/β-FeOOH photoanodes, a significantly lower current efficiency is obtained in the case of the modified electrode (Section 4.4.5). This indicates that a larger fraction of the total current is consumed by the parasitic water oxidation reaction rather than by the target organic degradation process.

The analysis presented above does not allow an unambiguous identification of the reaction mechanism responsible for the observed first-order kinetics. In particular, it remains unclear whether the oxidation proceeds via direct hole transfer following a Langmuir-Hinshelwood-type mechanism or through mediated oxidation via hydroxyl radicals.

On the one hand, probe molecule experiments clearly indicate the presence of hydroxyl radicals in the system, and the obtained results are in good agreement with the pharmaceutical degradation experiments (Section 4.5.5). Furthermore, oxidation mediated by hydroxyl radicals could account for the enhanced degradation performance observed for the $BiVO_4$/β-FeOOH photoanode compared to bare $BiVO_4$ under photocatalytic conditions, which is not preserved under photoelectrochemical operation, presumably due

to the suppression of Fenton-like reactions. However, this reaction mechanism fails to explain the decrease in pharmaceutical degradation observed during catalyzed water oxidation on the $BiVO_4$/β-FeOOH photoanode. This decrease can be rationalized by the reduced availability of photogenerated holes for the target oxidation reaction, as an increased fraction of holes is consumed by the oxygen evolution reaction. Nevertheless, both experimental and theoretical studies have demonstrated that the direct formation of hydroxyl radicals from water on $BiVO_4$ (and also on $BiVO_4$/β-FeOOH) is thermodynamically unfavorable, since the energy of photogenerated holes is insufficient to drive this process. Therefore, it remains unclear how a reduction in the number of available holes influences the formation of hydroxyl radicals. Overall, the origin of hydroxyl radicals in the studied system cannot be conclusively identified.

On the other hand, the assumption that oxidation proceeds exclusively by holes also fails to explain all experimental observations. In particular, it does not account for the detection of the TA-2OH product in all investigated systems, given that photogenerated holes are not capable of directly oxidizing terephthalic acid. In addition, the observed dependence of terephthalic acid oxidation on the presence of dissolved oxygen in solution cannot be rationalized within a purely hole-driven mechanism. Moreover, since it was demonstrated that modification of $BiVO_4$ with β-FeOOH does not enhance electron-hole separation (Section 4.5.1), this modification does not result in an increased charge carrier density at the photoanode surface, making it difficult to explain the improved photocatalytic performance solely on this basis. At the same time, a hole-mediated oxidation mechanism successfully explains the decrease in degradation efficiency observed during oxygen evolution catalysis under photoelectrochemical conditions, as well as the reduction in charge-transfer resistance upon the addition of organic compounds to the electrolyte.

4.5. CONCLUSIONS

- Modification of $BiVO_4$ with β-FeOOH does not lead to improved pharmaceutical degradation performance in photoelectrocatalytic process, despite a 1.5-2-fold increase in photocurrent and enhanced photoanode stability.

- Overall, the degradation performance of the investigated pharmaceuticals (PCT, SMX, and CBZ) on both bare $BiVO_4$ and $BiVO_4$/β-FeOOH is not competitive, with removal percentages ranging from 32% to 64% after 2 h of treatment, even at a very high ratio of photoanode surface are to treated volume ($29.5 m^{-1}$).

- In contrast, the energy consumption of the investigated photoelectrochemical systems is highly competitive, remaining below 3.5 kWh/m^3 in all cases, which is approximately two orders of magnitude lower than that of conventional electrochemical oxidation processes.

- The enhanced photocurrent observed for the $BiVO_4$/β-FeOOH system does not originate from improved electron-hole separation, which would be beneficial for organic degradation, but rather from the reduction of kinetic barriers associated with the water oxidation reaction. This shift is detrimental to the degradation performance of organic pollutants.

- Although the direct formation of hydroxyl radicals from water is thermodynamically not allowed on both $BiVO_4$ and $BiVO_4$/β-FeOOH, hydroxyl radicals were detected in probe molecule (terephthalic acid) oxidation experiments. This observation indicates that mediated pathways for hydroxyl radical formation must be considered.

- This study further demonstrates that quenching experiments must be interpreted with particular caution in multiphenomenal systems such as photoelectrocatalysis, as misleading conclusions may otherwise be drawn. Specific limitations and considerations associated with such experiments are discussed in this chapter.

- In the case of organic pollutants oxidation, a higher photocurrent does not necessarily correspond to a higher degradation rate. More attention should be paid to the competition between water oxidation and target reaction of oxidation of organic compounds.

- In principle, if the target reaction is catalyzed (pharmaceuticals oxidation over water splitting) and parasitic reaction is suppressed (for example, by choosing photoanode with the valence band positioned more negatively than 1.23 V vs RHE, i. e. not allowing water oxidation reaction), one may have fast degradation rate, low photocurrent (due to the usually low concentration of pharmaceuticals pollutnats) and this low photocurrent will propagate into very low energy consumption. However, in this case stability of photoelectrode may be damaged, as if not all photogenerated holes are scavenged from the surface by electrochemical reaction, they will accumulate at the semiconductor surface, destabilizing the lattice and leading to the dissolution of photoanode material.

REFERENCES

1. Tian, T.; Jiang, G.; Li, Y.; Xiang, W.; Fu, W. Unveiling the Activity and Stability of BiVO4 Photoanodes with Cocatalyst for Water Oxidation. Renew. Energy 2022, 199, 132–139, doi:10.1016/j.renene.2022.08.138.
2. Zhang, B.; Wang, L.; Zhang, Y.; Ding, Y.; Bi, Y. Ultrathin FeOOH Nanolayers with Abundant Oxygen Vacancies on BiVO4 Photoanodes for Efficient Water Oxidation. Angew. Chemie - Int. Ed. 2018, 57, 2248–2252, doi:10.1002/anie.201712499.
3. Seabold, J.A.; Choi, K. Efficient and Stable Photo-Oxidation of Water by a Bismuth Vanadate Photoanode Coupled with an Iron Oxyhydroxide Oxygen Evolution Catalyst. 2012.
4. Weng, H.; Yang, Y.; Zhang, C.; Cheng, M.; Wang, W.; Song, B.; Luo, H.; Qin, D.; Huang, C.; Qin, F.; et al. Insight into FeOOH-Mediated Advanced Oxidation Processes for the Treatment of Organic Polluted Wastewater. Chem. Eng. J. 2023, 453, 139812, doi:10.1016/j.cej.2022.139812.
5. Jin, R.; Deng, C.; Liu, G.; Zhai, S.; Qi, D. Heterogeneous Catalysis of FeOOH In-Situ Loaded Biochar for Reactive Red X-3B: Catalytic Mechanism Based on Fenton-like System. J. Environ. Chem. Eng. 2024, 12, 111702, doi:10.1016/j.jece.2023.111702.
6. Zheng, Y.; Zhang, Z.; Li, C. Beta-FeOOH-Supported Graphitic Carbon Nitride as an Efficient Visible Light Photocatalyst. J. Mol. Catal. A Chem. 2016, 423, 463–471, doi:10.1016/j.molcata.2016.07.032.
7. Ali, F.M.; Hmadeh, M.; O'Brien, P.G.; Perovic, D.D.; Ozin, G.A. Photocatalytic Properties of All Four Polymorphs of Nanostructured Iron Oxyhydroxides. ChemNanoMat 2016, 2, 1047–1054, doi:10.1002/cnma.201600251.
8. Chang, T.; Sun, J.; Li, S.; Li, X.; Liu, J.; Hu, Y.; Cheng, H. Oxygen Adsorption and Activation Control the Photochemical Activity of Common Iron Oxyhydroxide Polymorphs in Mediating Oxytetracycline Degradation under Visible Light. J. Colloid Interface Sci. 2025, 683, 565–577, doi:10.1016/j.jcis.2024.12.199.
9. Li, Y.; Bai, B.; Zhu, M.; Li, J.; Mei, Q.; Wang, Q. BiVO4 Photoanode Modified with FeOOH Cocatalyst for Visible-Light-Driven Photoelectrocatalytic Degradation of Organic Pollutants. J. Environ. Chem. Eng. 2024, 12, doi:10.1016/j.jece.2024.113079.
10. Wen, Y.; Wang, Z.; Cai, Y.; Song, M.; Qi, K.; Xie, X. S-Scheme BiVO4/CQDs/β-FeOOH Photocatalyst for Efficient Degradation of Ofloxacin: Reactive Oxygen Species Transformation Mechanism Insight. Chemosphere 2022, 295, 133784, doi:10.1016/j.chemosphere.2022.133784.
11. Obregón, S.; Barriga-castro, E.D.; Mendoza-reséndez, R.; Luna, C. Enhanced Photocatalytic Behavior of BiVO4 through Photoinduced Charge Transfer to Amorphous β-FeOOH Nanoparticles. Ceram. Int. 2016, 42, 17773–17780, doi:10.1016/j.ceramint.2016.08.105.

12. Chowdhury, M.; Ntiribinyange, M.; Nyamayaro, K.; Fester, V. Photocatalytic Activities of Ultra-Small b-FeOOH and TiO2 Heterojunction Structure under Simulated Solar Irradiation. Mater. Res. Bull. 2015, 68, 133–141, doi:10.1016/j.materresbull.2015.03.044.
13. Liao, G.; Li, C.; Liu, S.; Fang, B. Z-Scheme Systems: From Fundamental Principles to Characterization, Synthesis, and Photocatalytic Fuel-Conversion Applications. Phys. Rep. 2022, 983, 1–41, doi:10.1016/j.physrep.2022.07.003.
14. Kim, T.W.; Choi, K.S. Nanoporous BiVO4 Photoanodes with Dual-Layer Oxygen Evolution Catalysts for Solar Water Splitting. Science (80-.). 2014, 343, 990–995, doi:10.1126/science.1246913.
15. Łęcki, T.; Hamad, H.; Zarębska, K.; Wierzyńska, E.; Skompska, M. Mechanistic Insight into Photochemical and Photoelectrochemical Degradation of Organic Pollutants with the Use of BiVO4 and BiVO4/Co-Pi. Electrochim. Acta 2022, 434, doi:10.1016/j.electacta.2022.141292.
16. Govindaraju, G. V.; Wheeler, G.P.; Lee, D.; Choi, K.S. Methods for Electrochemical Synthesis and Photoelectrochemical Characterization for Photoelectrodes. Chem. Mater. 2017, 29, 355–370, doi:10.1021/acs.chemmater.6b03469.
17. Kang, D.; Kim, T.W.; Kubota, S.R.; Cardiel, A.C.; Cha, H.G.; Choi, K.S. Electrochemical Synthesis of Photoelectrodes and Catalysts for Use in Solar Water Splitting. Chem. Rev. 2015, 115, 12839–12887, doi:10.1021/acs.chemrev.5b00498.
18. Chen, K.; Chen, X.; Xue, D. Hydrothermal Route to Crystallization of FeOOH Nanorods via FeCl3*6H2O: Effect of Fe3+ Concentration on Pseudocapacitance of Iron-Based Materials. CrystEngComm 2015, 17, 1906–1910, doi:10.1039/c4ce02504k.
19. Jing, Y.; Chaplin, B.P. Mechanistic Study of the Validity of Using Hydroxyl Radical Probes to Characterize Electrochemical Advanced Oxidation Processes. Environ. Sci. Technol. 2017, 51, 2355–2365, doi:10.1021/acs.est.6b05513.
20. Das, S.; Hendry, M.J. Application of Raman Spectroscopy to Identify Iron Minerals Commonly Found in Mine Wastes. Chem. Geol. 2011, 290, 101–108, doi:10.1016/j.chemgeo.2011.09.001.
21. Trellu, C.; Chaplin, B.P.; Coetsier, C.; Esmilaire, R.; Cerneaux, S.; Causserand, C.; Cretin, M. Electro-Oxidation of Organic Pollutants by Reactive Electrochemical Membranes. Chemosphere 2018, 208, 159–175, doi:10.1016/j.chemosphere.2018.05.026.
22. Melia Rodrigo, M.; Esteso, M.A.; Ribeiro, A.C.F.; Valente, A.J.M.; Cabral, A.M.T.D.P.V.; Verissimo, L.M.P.; Musilova, L.; Mracek, A.; Leaist, D.G. Coupled Mutual Diffusion in Aqueous Paracetamol + Sodium Hydroxide Solutions. J. Mol. Liq. 2021, 334, 116216, doi:10.1016/j.molliq.2021.116216.
23. Galindres-Jiménez, D.M.; Matias, M.F.; Paiva, I.; Fangaia, S.I.G.; Ribeiro, A.C.F.; Valente, A.J.M.; Esteso, M.A. Antibiotic–Cyclodextrin Interactions: An Effective Strategy for the Encapsulation of Environmental Contaminants. Molecules 2025, 30, 1–16, doi:10.3390/molecules30224359.

24. Mendes, F.S.; Gonçalves, A.D.A.; Guiomar, F.I.S.; Martins, R.N.; Ramalho, J.P.P.; Martins, L.F.G. On the Diffusion of Carbamazepine, Acetaminophen and Atenolol in Water: An Experimental and Theoretical Approach. Fluid Phase Equilib. 2024, 580, doi:10.1016/j.fluid.2024.114056.
25. Blangetti, N.; Freyria, F.S.; Calviello, M.C.; Ditaranto, N.; Guastella, S.; Bonelli, B. Photocatalytic Degradation of Paracetamol under Simulated Sunlight by Four TiO 2 Commercial Powders : An Insight into the Performance of Two Sub-Micrometric Anatase and Rutile Powders and a Nanometric Brookite Powder. 2023.
26. Ivanova, D.; Tzvetkov, G.; Kaneva, N. Degradation of Paracetamol in Distilled and Drinking Water via Ag / ZnO Photocatalysis under UV and Natural Sunlight. Water 2023, 15, 3549, doi:10.3390/w15203549.
27. Moctezuma, E.; Leyva, E.; Aguilar, C.A.; Luna, R.A.; Montalvo, C. Photocatalytic Degradation of Paracetamol: Intermediates and Total Reaction Mechanism. J. Hazard. Mater. 2012, 243, 130–138, doi:10.1016/j.jhazmat.2012.10.010.
28. Vogna, D.; Marotta, R.; Napolitano, A.; D'Ischia, M. Advanced Oxidation Chemistry of Paracetamol. UV/H2O2-Induced Hydroxylation/Degradation Pathways and 15N-Aided Inventory of Nitrogenous Breakdown Products. J. Org. Chem. 2002, 67, 6143–6151, doi:10.1021/jo025604v.
29. Perkampus, H.-H. UV-Vis Spectroscopy and Its Applications; 1992; ISBN 9783642774799.
30. Mezghich, S.; Ayari, F.; Sarakha, M. Photochemical Degradation of the Antimicrobial Sulfamethoxazole upon Solar Light Excitation : Kinetics and Elucidation of Byproducts Using LC / ESI + / MS2 Technique. Mass Spectrom. Purif. Tech. 2017, 3, 1–7, doi:10.4172/2469-9861.1000118.
31. Henrique, G.; Madeira, D.L. Study of the Degradation of the Antibiotic Sulfamethoxazole and Trimethoprim (ST) from Light-Mediated CuO and ZnO Nanoparticles. Harmon. Knowl. Explor. Interdiscip. Synerg. 2023, 48.
32. Almandoz, M.C.; Sancho, M.I.; Blanco, S.E. Spectroscopic and DFT Study of Solvent Effects on the Electronic Absorption Spectra of Sulfamethoxazole in Neat and Binary Solvent Mixtures. Spectrochim. Acta Part A Mol. Biomol. Spectrosc. 2014, 118, 112–119, doi:10.1016/j.saa.2013.08.060.
33. Moore, E. Photodegradation of Sulfamethoxazole: A Chemical System Capable of Monitoring Seasonal Changes in Uvb Intensity. 2006, 59, 497–502.
34. Bizi, M. Activated Carbon and the Principal Mineral Constituents of a Natural Soil in the Presence of Carbamazepine. water 2019, 11, 2290, doi:10.3390/w11112290.
35. Li, Y.; Yang, Y.; Lei, J.; Liu, W.; Tong, M.; Liang, J. The Degradation Pathways of Carbamazepine in Advanced Oxidation Process: A Mini Review Coupled with DFT Calculation. Sci. Total Environ. 2021, 779, 146498, doi:10.1016/j.scitotenv.2021.146498.

36. Sirés, I. Electrochemical Advanced Oxidation Processes for the Removal of the Drugs Paracetamol, Clofibric Acid and Chlorophene from Waters. 2006.
37. Compound, N.D.; Reactor, E.; Cotillas, S.; Westerho, P.; Garcia-segura, S. Scaling up Photoelectrocatalytic Reactors: A TiO2 Degrades Acetaminophen. Water 2019, 1–14, doi:10.3390/w11122522.
38. Butler, M.A.; Ginley, D.S. Prediction of Flatband Potentials at Semiconductor-Electrolyte Interfaces from Atomic Electronegativities. J. Electrochem. Soc. 1978, 125, 228–232, doi:10.1149/1.2131419.
39. Sayama, K.; Nomura, A.; Arai, T.; Sugita, T.; Abe, R.; Yanagida, M.; Oi, T.; Iwasaki, Y.; Abe, Y.; Sugihara, H. Photoelectrochemical Decomposition of Water into H2 and O2 on Porous BiVO 4 Thin-Film Electrodes under Visible Light and Significant Effect of Ag Ion Treatment. J. Phys. Chem. B 2006, 110, 11352–11360.
40. Xu, Y.; Schoonen, M. The Absolute Energy Positions of Conduction and Valence Bands of Selected Semiconducting Minerals. Am. Minerolagist 2000, 85, 543–556, doi:10.2138/am-2000-0416.
41. Latusek, K.; Urban, T.; Ulatowska, J.; Polowczyk, I.; Nowicki, P. Accumulation of Toxic Pb(II) Ions by the Iron - Containing Minerals in the Presence of Ionic Polyacrylamide Soil Conditioner. Environ. Sci. Pollut. Res. 2023, 30, 44553–44565, doi:10.1007/s11356-023-25502-x.
42. Online, V.A.; Hankin, A.; Bedoya-lora, F.E.; Alexander, J.C. Flat Band Potential Determination : Avoiding the Pitfalls †. 2019, doi:10.1039/C9TA09569A.
43. Dare-Edwards, M.P.; Goodenough, J.B.; Hamnett, A.; Trevellick, P.R. Electrochemistry and Photo-Electrochemistry of Iron(III) Oxide. J. Chem. Soc., Faraday Trans. 1 1983, 79, 2027–2041, doi:10.1016/c2022-0-00045-3.
44. Pleskov, Y. V.; Gurevich, Y.Y. Semiconductor Photoelectrochemistry; Springer, 1986; ISBN 978-1468490800.
45. Huang, Z.; Han, F.; Li, M.; Zhou, Z.; Guan, X.; Guo, L. Which Phase of Iron Oxyhydroxides (FeOOH) Is More Competent in Overall Water Splitting as a Photocatalyst, Goethite, Akaganeite or Lepidocrocite? A DFT-Based Investigation. Comput. Mater. Sci. 2019, 169, 109110, doi:10.1016/j.commatsci.2019.109110.
46. Meng, J. Various Electromagnetic Properties of Magnetic Fe-Based Nanorods in GHz Range. J. Alloys Compd. 2023, 960, 170805, doi:10.1016/j.jallcom.2023.170805.
47. Chang, T.; Sun, J.; Li, S.; Li, X.; Liu, J.; Hu, Y.; Cheng, H. Oxygen Adsorption and Activation Control the Photochemical Activity of Common Iron Oxyhydroxide Polymorphs in Mediating Oxytetracycline Degradation under Visible Light. J. Colloid Interface Sci. 2025, 683, 565–577, doi:10.1016/j.jcis.2024.12.199.

48. Saison, T.; Chemin, N.; Chane, C.; Brezova, V.; Jolivet, J. New Insights Into BiVO4 Properties as Visible Light Photocatalyst. J. Phys. Chem. C 2015, 119, 12967–12977, doi:10.1021/acs.jpcc.5b01468.
49. Wang, Y.; Tan, G.; Liu, T.; Su, Y.; Ren, H.; Zhang, X.; Xia, A. Photocatalytic Properties of the G-C3N4/{010} Facets BiVO4 Interface Z-Scheme Photocatalysts Induced by BiVO4 Surface Heterojunction. Appl. Catal. B Environ. 2018, 234, 37–49, doi:10.1016/j.apcatb.2018.04.026.
50. Kohtani, S.; Yoshida, K.; Maekawa, T.; Iwase, A. Loading Effects of Silver Oxides upon Generation of Reactive Oxygen Species in Semiconductor Photocatalysis. Phys. Chem. Chem. Phys. 2008, 10, 2986–2992, doi:10.1039/b719913a.
51. Ahn, H.S.; Bard, A.J. Surface Interrogation Scanning Electrochemical Microscopy of Ni1-xFexOOH (0. J. Am. Chem. Soc. 2016, 138, 313–318.
52. Nosaka, Y.; Nosaka, A.Y. Generation and Detection of Reactive Oxygen Species in Photocatalysis. Chem. Rev. 2017, 117, 11302–11336, doi:10.1021/acs.chemrev.7b00161.
53. Liu, W.; Lu, Y.; Dong, Y.; Jin, Q.; Lin, H. A Critical Review on Reliability of Quenching Experiment in Advanced Oxidation Processes. Chem. Eng. J. 2023, 466, 143161, doi:10.1016/j.cej.2023.143161.
54. Ma, J.; Trellu, C.; Skolotneva, E.; Oturan, N.; Oturan, M.A.; Mareev, S. Investigating the Reactivity of TiOx and BDD Anodes for Electro-Oxidation of Organic Pollutants by Experimental and Modeling Approaches. Electrochim. Acta 2023, 439, 141513, doi:10.1016/j.electacta.2022.141513.
55. Shkrob, I.A.; Sauer, M.C. Hole Scavenging and Photo-Stimulated Recombination of Electron-Hole. J. Phys. Chem. B 2004, 108, 12497–12511, doi:10.1021/jp047736t.
56. Photocatalysis, N.O.; Al-madanat, O.; Nunes, B.N.; Alsalka, Y.; Hakki, A.; Curti, M.; Patrocinio, A.O.T.; Bahnemann, D.W. Application of EPR Spectroscopy in TiO2 and Nb2O5 Photocatalysis. Catalysts 2021, 11, 1514.
57. Armstrong, D.A.; Huie, R.E.; Koppenol, W.H.; Lymar, S. V.; Merenyi, G.; Neta, P.; Ruscic, B.; Stanbury, D.M.; Steenken, S.; Wardman, P. Standard Electrode Potentials Involving Radicals in Aqueous Solution: Inorganic Radicals (IUPAC Technical Report). Pure Appl. Chem. 2015, 87, 1139–1150, doi:10.1515/pac-2014-0502.
58. Siahrostami, S.; Li, G.L.; Viswanathan, V.; Nørskov, J.K. One- or Two-Electron Water Oxidation, Hydroxyl Radical, or H2O2 Evolution. J. Phys. Chem. Lett. 2017, 8, 1157–1160, doi:10.1021/acs.jpclett.6b02924.
59. Fuku, K.; Sayama, K. Efficient Oxidative Hydrogen Peroxide Production and Accumulation in Photoelectrochemical Water Splitting Using a Tungsten Trioxide/Bismuth Vanadate Photoanode. Chem. Commun. 2016, 52, 5406–5409, doi:10.1039/c6cc01605g.

60. Diana, B.; Morales, G.; Mena, I.F.; Andr, O.; Olvera-vargas, H.; Andr, M. Intensifying Paired Hydrogen Peroxide (H2O2) Electrosynthesis: Influence of Electrolyte Composition and Light Irradiation. Electrochim. Acta 2025, 533, 146551, doi:10.1016/j.electacta.2025.146551.
61. Zhang, K.; Liu, J.; Wang, L.; Jin, B.; Yang, X.; Zhang, S.; Park, J.H. Near-Complete Suppression of Oxygen Evolution for Photoelectrochemical H2O Oxidative H2O2 Synthesis. J. Am. Chem. Soc. 2020, 142, 8641–8648, doi:10.1021/jacs.9b13410.

CHAPTER V: INFLUENCE OF CHLORIDE IONS PRESENCE ON SULFAMETHOXAZOLE OXIDATION: TRADE-OFF BETWEEN FASTER DEGRADATION AND TOXICITY INCREASE

5.1. INTRODUCTION

The field application of photoelectrochemical oxidation techniques for water treatment requires consideration of the inorganic compounds present in the water matrix. Chlorides are found in all types of water – both natural and wastewater – and their concentrations can vary greatly depending on the sampling location or the type of effluent. The concentration of chloride ions can widely vary from 0.5 мg/L to several grams per liter depending on the water source [1,2].

The presence of chloride ions can have both positive and negative effects. On the one hand, they can lead to the formation of active chlorine species (Cl_2, HClO/ClO^-) at the anode, which have been used for decades in processes of organic compound removal and water disinfection [3]. On the other hand, further chemical transformations may result in the formation of undesirable chlorate (ClO_3^-) and perchlorate (ClO_4^-) ions [4,5]. As shown in Table 5-1, hypochlorite and chlorite have high standard electrode potentials of formation and are characterized by low toxicity to mammals but high toxicity to microorganisms. These properties make them effective oxidants for various organic pollutants and suitable for disinfection, which explains the long-standing use of chlorination as a water treatment method. In contrast, chlorates and perchlorates have lower standard electrode potentials of formation and low acute toxicity to both mammals and microorganisms, making them ineffective for water purification. However, they exhibit chronic toxic effects for humans, including disruption of normal thyroid function and potential carcinogenicity [6]. For this reason, the provisional guideline values for chlorates and perchlorates established by monitoring agencies (WHO, US EPA) are set much lower than those for hypochlorites and chlorites, and their presence in drinking water is considered highly undesirable.

Anion	Representative acute toxicity oral LD50 (Rat)* [mg/kg]	Ecotoxicity EC50 (Daphnia magna 48 h)* [mg/L]	WHO provisional concentrations	E^0 [V] Acidic – Neutral/Basic
Hypochlorite (ClO^-)	5230 [7]	<0.02 [8]	150 мg/(kg* day) (TDI) [9]	1.63/0.89
Chlorite (ClO_2^-)	284 [10]	<1 [10]	0.7 mg/L [11]	1.64/0.78
Chlorate (ClO_3^-)	1,200-7,000 [12]	>1000 [13]	0.7 mg/L [11]	1.47/0.63
Perchlorate (ClO_4^-)	4200 [14]	> 100 [14]	0.07 mg/L [15]	1.42/0.56

Table 5-1 Properties of oxychloride compounds. (*Values are taken for sodium salts of these compounds).

The oxidation mechanism of chloride ions – and consequently, the formation of either beneficial products (active chlorine species) or harmful ones (chlorates and perchlorates) – depends on the electrode material. At active electrodes, where the oxygen evolution reaction proceeds via the lattice oxygen-mediated mechanism, chloride ions are first oxidized through a direct electron transfer to form dissolved chlorine in water (Eq. 5.1). The chlorine molecules then undergo hydrolysis (Eq. 5.2), followed by an equilibrium shift between the resulting hypochlorite species (Eq. 5.3), depending on the solution pH:

$$2Cl^- \rightarrow Cl_{2(aq)} + 2\overline{e} \tag{5.1}$$

$$Cl_{2(aq)} + H_2O \rightarrow HClO + H^+ + Cl^- \tag{5.2}$$

$$HClO \rightleftarrows ClO^- + H^+ \tag{5.3}$$

At non-active electrodes, where the oxygen evolution reaction proceeds via the adsorbate evolution mechanism, a large number of physiosorbed hydroxyl radicals are formed on the surface. In this case, the formation of active chlorine can also occur through the reaction between chloride ions and hydroxyl radicals (Eq. 5.4):

$$Cl^- + HO^{\bullet} \rightarrow ClO^- + H^+ + \overline{e} \tag{5.4}$$

In the presence of hydroxyl radicals, hypochlorite can undergo further oxidation to form undesirable chlorate and perchlorate species (Eqs. 5.5-7) [4,5]:

$$ClO^- + 2HO^{\bullet} \rightarrow ClO_3^- + 2H^+ + 2\overline{e} \tag{5.5}$$

$$ClO_3^- \rightarrow ClO_3^{\bullet} + \overline{e} \tag{5.6}$$

$$ClO_3^{\bullet} + HO^{\bullet} \rightarrow ClO_4^- + H^+ \tag{5.7}$$

As can be seen, the formation of undesirable oxidation products of chloride ions (chlorates and perchlorates) occurs mainly on non-active electrodes, where a large number of physiosorbed hydroxyl radicals are present. In contrast, such radicals are absent on active electrodes, which makes them more suitable for chlorination. Accordingly, dimensionally stable anodes (DSA) are the most widely used electrodes for chlorination in industrial applications and the high formation of chlorates and perchlorates on boron doped diamond (BDD) electrode limits its wide application. However, in practice, mixed electrode behavior is often observed, and both active chlorine species and chlorates/perchlorates can be formed in varying proportions. Therefore, before an electrode is applied in industrial processes, it must be thoroughly evaluated to determine which chlorine-containing inorganic compounds are formed on its surface and in what relative amounts.

$BiVO_4$ is considered as an appropriate photoanode for the chlorination process as its suitable band positions allow the formation of active chorine species (Figure 5-1 and Eqs. 5.1-3), while the limited generation of hydroxyl radicals is supposed to prevent formation of undesired chlorates and perchlorates (Eqs. 5.5-7) [16]. Li et al. indeed reported the suppressed formation of chlorate ions on $BiVO_4$ photoanode compared to WO_3 and TiO_2 (0.14, 2.29 and 2.74 mg/L, respectively, after 2 h at initial NaCl concentration 0.1 M) [17]. Another study of Dong et al. studied the treatment of real sewage water containing 6986 mg/L

of chloride ions by Ov-Fe_2O_3@$BiVO_4$ photoanode: after 2 h only 3.2 mg/L of chlorate was quantified [18]. It should be noted that in both studies authors did not detect formation of perchlorate ions.

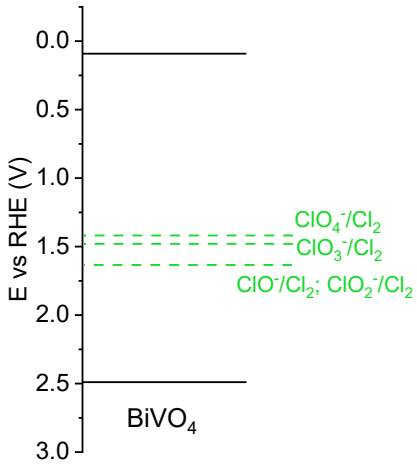

Figure 5-1 Band positions of $BiVO_4$ relative to the standard electrode potentials of oxidative chlorine species formation

A study by Gao et al. proposed that the oxidation of organic pollutants by photogenerated holes on $BiVO_4$ is limited because the $BiVO_4$ surface is highly solvated, which creates an interfacial barrier to electron transfer from non-polar and bulky organic molecules that cannot readily access the $BiVO_4$ surface [19]. In contrast, small inorganic ions can penetrate this aqueous interfacial barrier and react on the $BiVO_4$ surface, forming reactive radical species that subsequently oxidize water or organic pollutants. Therefore, the formation of active chlorine species can significantly enhance the degradation rate of organic pollutants on $BiVO_4$. Multiple studies support this hypothesis: while pristine $BiVO_4$ exhibits low degradation rates for a wide range of organic compounds, the presence of chloride ions substantially enhances its performance. For example, in the study discussed above, 10 mg/L of phenol was completely degraded within 2 h in the presence of chloride ions [17], compared with only 70% degradation after 4 h in chloride-free conditions [20]. Similarly, the chemical oxygen demand (COD) of sewage effluent decreased from 320 to 34 mg O_2/L within 2 h [18]. Enhanced degradation efficiencies in $BiVO_4$-based PEC systems have also been reported elsewhere [21–23]. Petruleviciene et al. demonstrated the formation of ClO^- and ClO_2^- in a $BiVO_4$-based PEC system, with an average Faradaic efficiency of approximately 35% [24].

However, it is well known that in the presence of reactive chlorine species (RCS) chlorinated oxidation products of the target organic compound can be formed [25,26]. Many authors have reported that such chlorinated organic by-products can be even more harmful than the initial pollutant [25,27,28]. Therefore, the formation of intermediates and the toxicity of treated solutions must be carefully monitored.

The aim of this Chapter is to determine how the presence of chlorides in the wastewater matrix affects the photoelectrochemical degradation of the antibiotic sulfamethoxazole (SMX) on $BiVO_4$ photoanode. The specific objectives of the Chapter are as follows:

- Investigate the effect of chloride presence on the oxidation rate of SMX.

- Examine how the presence of chloride influences the oxidation pathway of SMX and determine the nature of the resulting by-products.
- Assess the impact of chloride presence on the toxicity of the treated water.

The experimental work presented in this chapter is conducted during an academic mobility period at the Laboratory of Electrochemistry headed by Professor Magdalena Skompska, University of Warsaw, in collaboration with Department of Environmental Health Sciences of Medical University of Warsaw.

5.2. MATERIALS AND METHODS

5.2.1. Materials

All reagents were of analytical grade and used without further purification. Sulfamethoxazole (SMX), sodium sulfate (Na_2SO_4), sodium chloride (NaCl) and were purchased from Sigma-Aldrich. The HPLC-grade acetonitrile, trifluoroacetic acid, formic acid were purchased from Merck (Darmstadt, Germany). Aqueous solutions were prepared using deionized (DI) water (Rephile, 18 MΩ·cm).

5.2.2. Analytical methods

The concentration of sulfamethoxazole was monitored during the experiment by both UV-vis spectroscopy and high-performance liquid chromatography coupled with diode array detector (HPLC-DAD).

Spectrophotometer Lambda 12 (Perkin Elmer) working in a transmission mode was used to measure the concentration of SMX by UV-vis spectroscopy. The concentration ratio C/C_0 was obtained from the ratio of absorbances A/A_0, according to the Beer's law ($A=lc\varepsilon$). The probe times were 0, 5, 10, 20, 30, 40, 60, 80, 100 and 120 minutes.

The procedure of SMX concentration determination by HPLC-DAD is described in detail in [29]. Shimadzu (Kyoto, Japan) HPLC instrument equipped with an SPD-M10A photodiode array detector (PDA) was used to measure the concentration of SMX by HPLC-DAD. In the gradient analysis used, phase The separation process was carried out on a LichroCART 50×4 Purospher STAR RP-18 (3 μm) analytical column (Merck, Darmstadt, Germany). The flow rate was 1.0 mL min^{-1}, and the concentration of phase B changed according to the following scheme: 0 min: 15%; 1 min: 20%; 8 min: 90%; 9 min: 90%; and 9.10 min: 15%. Quantitative analysis of SMX was carried out at 268 nm. Standard curves of SMX solution was in the concentration range of 0.5-20 mg/L. The limit of quantitation was 0.5 mg/L. Aliquotes were taken at 0, 5, 10, 20, 30, 60, 80 and 120 minutes.

The structure elucidation of the SMX degradation by-product was performed by ultrahigh pressure liquid chromatography with tandem mass spectrometry as a detector by a procedure described in [30]. Instrumental analysis was performed using a UHPLC Dionex Ultimate 3000 with a Q-Exactive hybrid quadrupole-orbitrap mass spectrometer system (MS/MS) equipped with heat electrospray ionization (HESI), an online vacuum degasser, a quaternary pump, an autosampler, and a thermostated column compartment. The HESI was operated in positive mode. Full MS scans were acquired over m/z 70–850 range with a resolution of 70 000 (m/z 200). The target value was 3 x 106. Instrumental analysis was

performed using a UHPLC Dionex (Germering, Germany) Ultimate 3000 with a Q-Exactive spectrometer. Tentative metabolites were detected using Compound Discoverer Software v.3.3 (Thermo Fisher Scientific, Waltham, MA, USA). Fragmentation was performed in different runs with a normalized collision energy of 20, 40, 60 eV. The tandem mass spectrum was acquired with a resolution of 17,500 at m/z 200. The target value was 5000. Standard mass spectrometric conditions for all experiments were: spray voltage, 3.5 kV; sheath gas pressure: 60 arb; auxiliary gas pressure: 20 arb; sweep gas pressure: 0 arb, heated capillary temperature, 320 ◦C; Loop count: 3; Isolation window: m/z 1.0; and Dynamic exclusion: 6.0 s. For all full scan measurements, lock-mass ions from ambient air (m/z 445.1200 and 291.2842) were used as internal calibrants. All data collected in profile mode were acquired and processed using Thermo Xcalibur 3.0TM software, and Compound Discoverer 3.3 (Thermo Fisher Scientific, Waltham, MA, USA), respectively. Chromatographic separation was achieved with a Kinetex RP-18 column (100 mm × 4.6 mm, 2.6 μm) supplied by Phenomenex® (Torrance, CA, USA) equipped with a security guard. The column was maintained at 40 ◦C at a flow rate of 300 μL/min. The mobile phases consisted of HPLC grade water with 0.1 % formic acid as eluent A and acetonitrile with 0.1 % formic acid as eluent B. The gradient (% B) was as follows: 0 min–5 %; 1 min–5 %; 13 min–95 %.; 20 min–95 %; The re-equilibration of the column to the initial conditions lasted 5 min. The injection volume was 10 μL.

5.2.3. Photoelectrochemical degradation experiment

The synthesis procedure of $BiVO_4$ photoanode and details of experimental setup are described in previous sections (Chapter 4, Section 4.2.2 and Section 4.2.5).

The degradation experiments were performed at four initial concentrations of chloride ions – 0, 20, 200 and 600 mg/L which corresponds to 0, 0.3 mM, 3.4 mM and 10 mM concentration of NaCl. To ensure proper conductivity 0.1 M and Na_2SO_4 was added in the solution containing 0 and 10 mg/L of chloride ions, respectively. Initial concentration of SMX is 20 mg/L.

5.2.4. Toxicity test

For toxicity test the PEC degradation experiments were performed for 10 and 120 minutes for four chloride concentrations (0, 20, 200 and 600 mg/L) and 3 ml probes were taken in the end of the experiment. The control experiments without addition of SMX were performed for 600 mg/L Cl- and 0.1 M Na_2SO_4 for 10 and 60 minutes to assess the toxicity of inorganic species generated in the photoelectrochemical process. Toxicity of aqueous solutions of SMX, ClO^-, ClO_3^- and ClO_4^- was also assessed to establish their toxicity threshold for the organisms used in the test.

Microtox assay was performed according to the manufacturer's instructions using lyophilized *Aliivibrio fischeri* luminescent bacteria purchased from Modern Water (New Castle, PA, USA). The samples were incubated for 15 min and the light output of the samples was recorded with a Microtox M500 analyzer (Modern Water Inc., New Castle, PA, USA). Test was performed according to the Microtox Manual [31].

Spirotox test, which is an acute toxicity test with the ciliate protozoan *Spirostomum ambiguum*, was performed according to the standard operational protocol [32] in disposable, polystyrene 24-well microplates. The samples were incubated in the dark at 25◦C for 24 h, and the test responses, i.e. cell

deformations and lethal responses, were observed with the use of a dissection microscope (SMZ 1500, Nikon, Japan).

The toxicity values EC50 and PE express the concentration of the tested sample causing 50% of toxic effect and percent of toxic effect caused by initial concentration of the sample, respectively. For the samples before and after irradiation the EC50 and PE values are expressed in a percent of the initial concentration equal to 20 mg/L of SMX.

5.3. INFLUENCE OF CHLORIDE IONS PRESENCE ON DEGRADATION RATE OF SULFAMETHOXAZOLE IN PHOTOELECTROCHEMICAL PROCESS

5.3.1. Analysis of UV-vis spectra of SMX during photoelectrocatalytic degradation

The evolution of UV-Vis spectra during the degradation of SMX at four initial concentrations of chloride ions is presented in Figure 5-2. In the absence of chloride ions and at a low chloride concentration (20 mg/L), the spectral behavior is essentially identical: the shape of the UV-Vis spectra remains unchanged, and the main absorption peak at λ=265 nm (assigned to SMX) decreases in intensity without any shift (Figure 5-2 a,b). In contrast, at higher chloride concentrations (200 and 600 mg/L the formation of a new product is observed. This product is characterized by two absorption peaks at λ=285 nm and λ=295 nm, which significantly alter the overall appearance of the spectra (Figure 5-2 c,d). This behavior can be attributed to the formation of a chlorinated intermediate during the oxidation of SMX. The broad absorption tail of this intermediate overlaps with the main SMX peak, which likely explains the large discrepancy between the concentrations measured by UV-Vis spectroscopy and HPLC-DAD (Section 5.3.3).

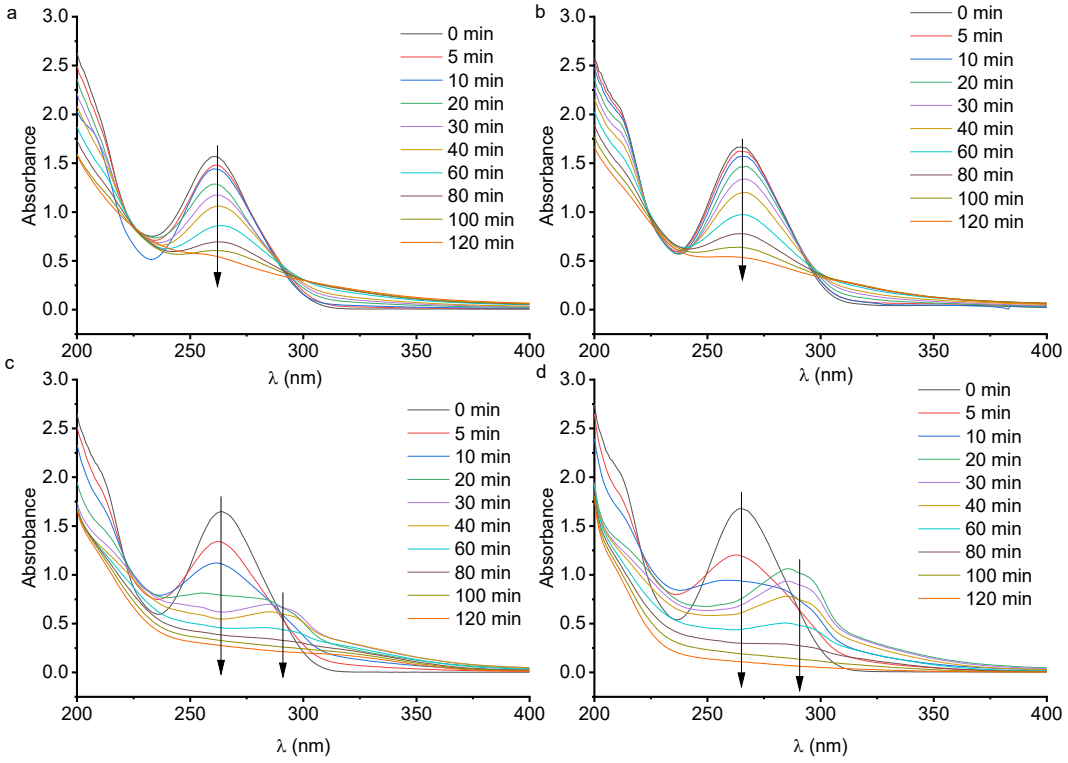

Figure 5-2 Influence of Cl- ions concentration on the shape of UV-vis spectra evolution during the SMX

degradation. In the absence of Cl^- ions in the initial solution (a), in the presence of 20 mg/L Cl^- (b), 200 mg/L Cl^- (c) and 600 mg/L Cl^- (d).

5.3.2. Analysis of HPLC-DAD chromatograms during SMX photoelectrocatalytic degradation

Figure 5-3 shows the chromatograms recorded after 120 min of degradation experiment in the presence of four concentrations of chloride ions. The results show that an increase of chloride concentration significantly enhances the overall mineralization of the initial compound. SMX has a retention time of 2.44 minutes, and this peak is still observed after 120 minutes of degradation in the water matrix containing only 20 mg/L of chloride or without chlorides at all. In contrast, for solutions containing 200 mg/L and 600 mg/L of chloride, this peak completely disappears. It is also observed that with increasing initial chloride concentration, both the number of peaks on the final chromatogram and the peaks area decrease, indicating a higher degree of mineralization. In the case of 600 mg/L of chloride, almost complete mineralization is achieved.

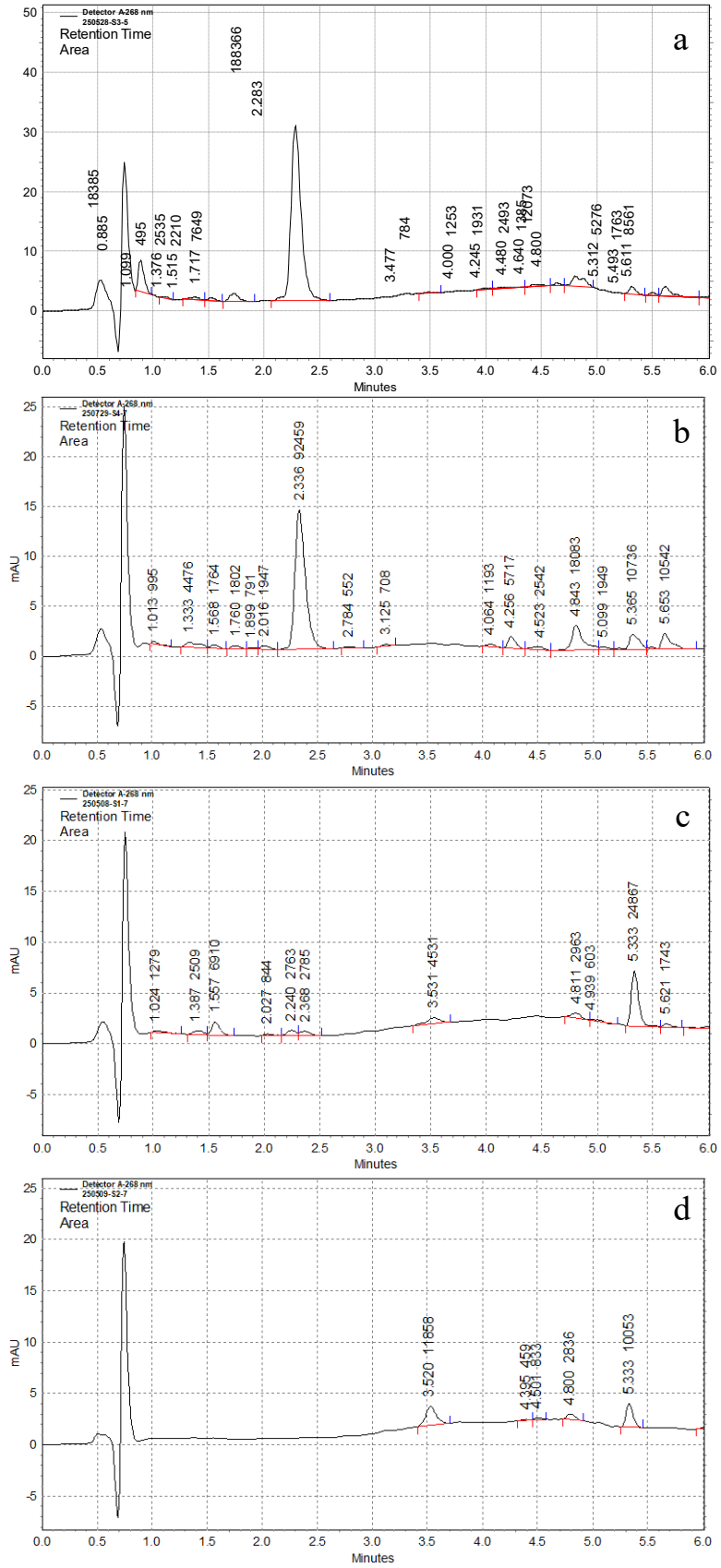

Figure 5-3 Chromatogram after 120 min of degradation in the absence of Cl^- ions in the initial solution (a), in the presence of 20 mg/L Cl^- (b), 200 mg/L Cl^- (c), 600 mg/L Cl^- (d).

5.3.3. Kinetic analysis of SMX photoelectrocatalytic degradation in the presence of Chloride ions

Kinetic analysis preformed for SMX concentration recorded by HPLC-DAD shows that SMX degradation follows pseudo-first-order kinetics, at least during the initial stage of the process (i.e., the first 40-60 minutes) (Figure 5-4). This observation is consistent with general trends reported in the literature, where the oxidation of pharmaceuticals typically proceeds according to pseudo-first-order kinetics [33]. This indicates that the concentration of oxidative species remains nearly constant during this period, implying a steady generation rate of reactive species without significant depletion. After 40-60 minutes, however, the process slows down and slightly deviates from first-order behavior. Two possible reasons may result in this behavior: (i) accumulation of reaction intermediates which also consume RCS and thus inhibit the SMX degradation (ii) the available chloride ions in the system become depleted, resulting in a reduced formation rate of oxidative species and, therefore, the deviation of their concentration from a constant value.

The comparison of apparent first-rate constants determined for SMX concentrations measured by HPLC-DAD and UV-vis methods proves one more time that the UV-vis technique gives underestimation of degradation rate of SMX due to the formation of some by-products absorbing in the same range as SMX. It is interesting to notice that in all cases the difference between apparent rate constant determined from HPLC-DAD and UV-vis spectroscopy data differs in about 2 times (1.6-2.2), even though in the case of 0 or 20 mg/L of Cl^- ions was not detected any by-product absorbing the light in the same range as SMX.

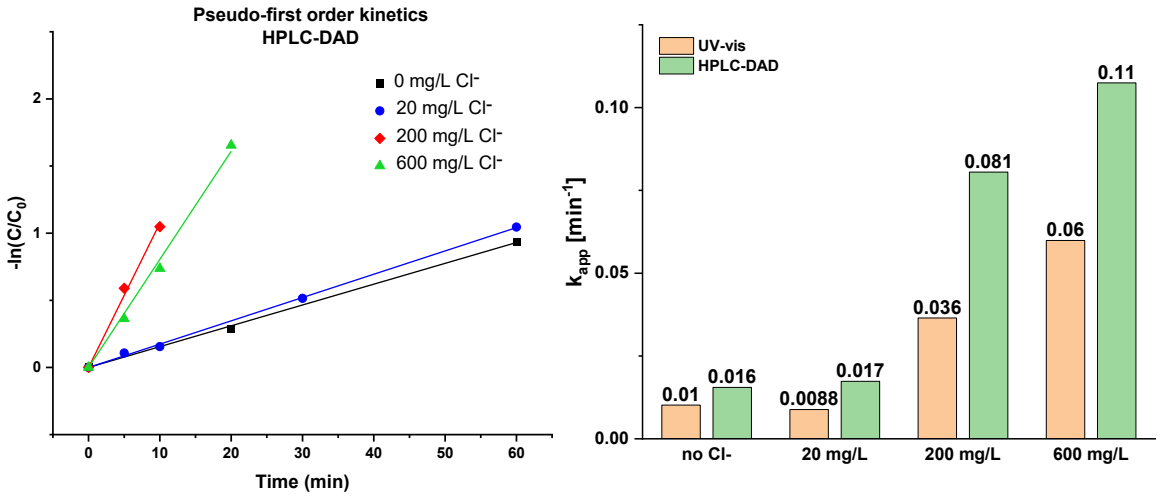

Figure 5-4 Kinetics of the SMX degradation. (a) pseudo-first order kinetics fitting according to data collected with HPLC-DAD; (b) comparison of apparent first order rate constant determined with HPLC-DAD and UV-vis spectroscopy.

5.3.4. Photoelectrocatalytic degradation of sulfamethoxazole in the presence of chloride ions

Figure 5-5a presents the SMX degradation curves based on concentrations determined by UV-Vis spectroscopy. It is observed that the degradation rate strongly depends on the concentration of chloride ions. The results indicate the presence of a minimum threshold chloride concentration that must be exceeded for the oxidation reaction to accelerate. In addition, a limiting chloride concentration is observed, above which no further increase in the oxidation rate occurs (600 mg/L in the present study).

Figure 5-5b shows the results of SMX concentration monitored by HPLC-DAD during the photoelectrochemical degradation. It has the qualitatively the same trend as concentration detected by UV-vis spectroscopy but differs quantitatively. It is seen that it indeed obeys pretty nice the pseudo-first order kinetics. It is seen that actually after 120 min of experiment the final concentration of SMX in the absence of Cl- ions is about 10% and that the addition of 20 mg/L od Cl- does not change the picture significantly. Addition of 200 mg/L and 600 mg/L of Cl- ions fasten drastically the degradation rate, reaching complete degradation in 60 and 20 minutes, respectively.

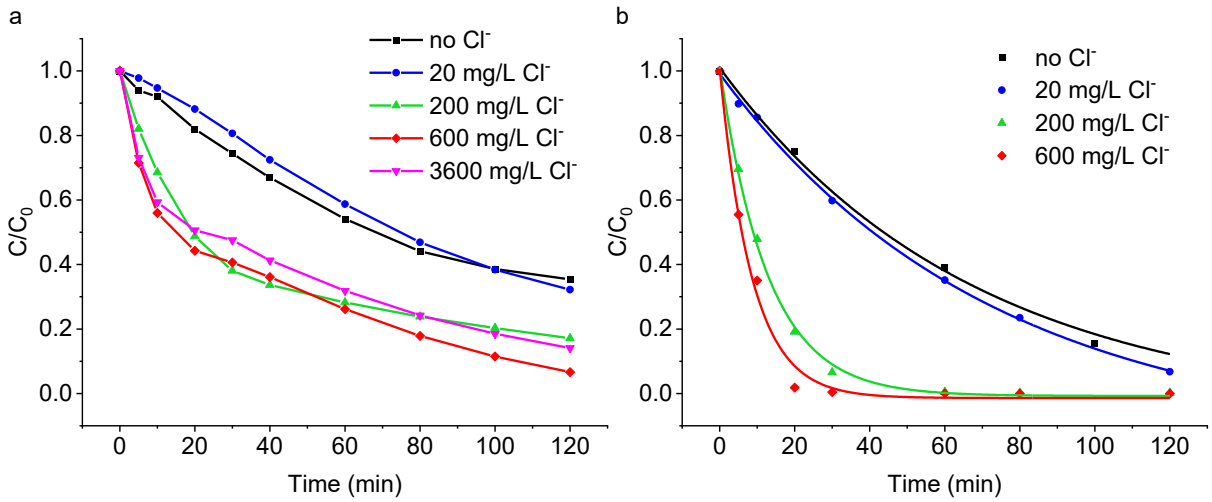

Figure 5-5 Influence of Cl- ions concentration on SMX degradation. Concentration of SMX is measured by UV-vis spectroscopy (a) and HPLC-DAD chromatography (b).

The energy consumption in the absence of chloride ions (when 0.1 M Na_2SO_4 was used as a supporting electrolyte) and in the presence of 600 mg/L chloride ions was similar as in the degradation experiments on bare $BiVO_4$ reported in previous chapters: 1.39 and 1.46 kWh/m^3, respectively. At lower concentration of chloride ions (20 and 200 md/L) energy consumption increased to 2.18 and 2.20 kWh/m^3, respectively, due to the reduced conductivity of the solution.

5.4. INFLUENCE OF CHLORIDE IONS PRESENCE ON OXIDATION PATHWAY OF SULFAMETHOXAZOLE

In this section we investigate how the presence of chloride ions and variation of their concentration affects the oxidation pathway of SMX.

In this work, a HPLC-MS chromatographic signal (peak area) is compared to the initial chromatogram: e.g., A_t/A_0 at the same retention time (where A_0 is the signal of initial solution when only SMX is present). Because authentic standards/response factors are unavailable for these by-products, these values are interpreted semi-quantitatively as “highest relative abundance change”.

The probable paths of SMX degradation in the presence of different concentrations of chloride ions (0, 20, 200 and 600 mg/L) are presented in Figures 2.3.1-2.3.4. They are proposed taking into account the most

intensive HPLC-MS peaks, and the peaks whose area markedly changed during the photoelectrocatalytic process. The chemical structures of plausible by-products were confirmed by *in-silica fragmentation*.

5.4.1. Plausible pathway of sulfamethoxazole oxidation in the absence of chloride ions

Figure 5-6 shows the plausible pathway of SMX oxidation in the absence of chloride ions. Based on detected intermediates, the proposed SMX degradation can be rationalized as three concurrent transformation pathways: (i) cleavage of the sulfonamide linkage (loss of the sulfonyl functionality), (ii) oxidative functionalization of the aromatic/isoxazole moieties (mainly $HO^{\bullet}$-driven hydroxylation followed by dehydration/rearrangement), and (iii) radical coupling/dimerization reactions.

(i) *Sulfonamide bond cleavage and desulfonation*. One primary route is hydrolytic cleavage of the S-N bond in SMX to yield 3-amino-5-methylisoxazole (**P98**) together with an aniline-sulfonyl fragment (depicted in a red dashed frame, as it was not experimentally determined but theoretically predicted) leading to formation of **P155** product. This is in accordance with DFT studies, showing that S-N bond cleavage is expectable reaction. In parallel, SMX undergoes desulfonation ($-SO_2$) to form the aniline-isoxazole fragment **P189**, which can subsequently be hydroxylated to **P190** and/or undergo intramolecular rearrangement/cyclization to **P187**. Formation of small heterocycle **P98** and aromatic sulfonamid type fragment **P155** via S-N hydrolysis and desulfonation of SMX to form **P189** are consistent with the SMX oxidation pathways proposed previously in the literature [34–36]. Considering that **P155** and **P189** have the highest relative change of chromatogram peak intensity, this oxidation route can be considered as predominant. Thus, in Figure 5-6 it is highlighted by orange arrows.

(ii) *Oxidative functionalization* ($HO^{\bullet}$ addition, dehydration, and ring modifications). A second major branch involves oxidation on the aromatic ring and/or heterocycle. Oxidation at the aromatic amine functionality of initial SMX molecule derivates **P283**, followed by $HO^{\bullet}$ attack with denitration ($+HO^{\bullet}/-NO_2$) to give a phenolic product **P254** [37]. Further multi-hydroxylation ($+2HO^{\bullet}$) with dehydration ($-H_2O$) affords more hydroxylated products such as **P270** (high relative change of peak intensity, thus, very probable pathway) or C-S bond cleavage to form **P178** – sulfamic acid derivative [35,36]. In addition, an acid/base assisted deamination pathway is indicated ($+H^+/-NH_3$) yielding **P238**, which then transforms through an oxidized intermediate (theoretically predicted) to the more oxidized/opened-side-chain product **P242**.

(iii) *Coupling reactions and dimerization*. Initial SMX molecule and product **P254** undergo dimerization to form **P502** [38] and **P500**. Separately, coupling reactions from the SMX radical occur to produce **P345**. The same **P254** radical is transformed to larger coupled/interconverted structures (theoretically predicted) and ultimately to highly hydroxylated products **P347** (high relative peak intensity change, thus, this route is considered as the dominant one) and **P363**. These routes are consistent with the general tendency of aromatic-amine-derived intermediates to form coupling products under oxidative conditions [34,35,38]. The reason of such intensive coupling/dimerization is probably in the mild oxidative strength of the system.

The most important conclusion taken from this pathway is that there is no aromatic ring opening. Although 84% of SMX removal was achieved in these conditions, the complete mineralization did not happen which is in agreement with the final chromatogram taken for this experiment that has many peaks (Figure 5-6). Only five compounds **P500**, **P256**, **P242**, **P347** and **P363** show a partial aromatic ring opening,

three of them being radical coupling products (**P347**, **P363** and **P500**). Relative change of peak intensity of **P500**, **P256** and **P242** compounds is not very large, meaning small amounts of these by-products. No end-products of aromatic ring opening is detected.

5.4.2. Plausible pathway of SMX oxidation in the presence of 20 mg/L Cl^- ions

Figure 5-7 shows the plausible pathway of SMX oxidation in the presence of low concentration of chloride ions (20 mg/L). The degradation pathway looks similar to the previous one in the absence of chlorides. However, few changes are observed. There is a slight shift of the most predominant oxidation routes – now the compounds with highest change of relative peak intensity are **P178**, **P283**, **P347** and **P363**. The addition of a new transformation pathway – chlorination has emerged. And few by-products were not detected anymore – **P269**, **P238**, **P242** and **P266** (probably, due to the shift in the effective oxidant pool toward reactive chlorine species which are more selective than $HO^{\bullet}$).

(i) *Chlorination*. In agreement with established SMX chlorination chemistry, reactive chlorine species can lead to the formation ring-chlorinated SMX products (consistent with **P287**)[39]. Further chlorination of chlorophenol yields in ring-opening and generation of highly toxic halogenated acetic acids (**P128**) [27]. This ring-opening also leads to the formation of well-established and widly reported in the literature products of benzene ring opening – maleic and fumaric acids (**P116**) [40].

(ii) *Sulfonyl/sulfonamide disruption.* A dominant pathway in chloride-containing conditions is cleavage adjacent to the sulfonyl group yielding a sulfamic-acid derivative (**P178**). Mechanistically, chlorination at the aniline nitrogen increases electron deficiency delocalized over the aromatic system and renders the α-carbon adjacent to sulfur susceptible to nucleophilic attack (by $Cl^-/ClO^-/OH^-$), thereby promoting S-C bond cleavage; subsequent hydrolysis yields a sulfamic-acid derivative together with aminophenol-type co-fragments [35,41]. The emergence of **P178** as a main by-product therefore reflects the shift from predominantly $HO^{\bullet}$-type hydroxylation pathways toward chlorination-activated sulfonyl disruption channels under chloride.

(iii) *Oxidative functionalization* ($HO^{\bullet}$ addition, dehydration, and ring modifications). Accumulation of **P283** in solution is a direct consequence of what was said above: in the presence of reactive chlorine species the aniline nitrogen is primary attacked and oxidized [37].

(iv) *Coupling reactions and dimerization*. The chloride-containing system favors formation of high-mass, highly oxygenated products (**P347** and **P363**), consistent with radical coupling followed by repeated oxygenation. Chlorination studies of SMX explicitly report that aminophenol-type intermediates formed after sulfonyl disruption can undergo dimerization/coupling, and chlorine-driven systems can generate dimeric/polymeric products from aromatic-amine motifs [35,38,41].

To sum up, we can highlight that the addition of small concentrations of Cl^- ions in solution not only lead to the small increase in percentage of removal (from 85% without chlorides to 94% in the presence of 20 mg/L in 2 hours) but also to the more complete mineralization as the products of benzene ring opening was detected. However, the price of this opening is the formation of highly toxic halogenated acetic acids.

5.4.3. Plausible pathway of SMX oxidation in the presence of 200 mg/L Cl^- ions

Figure 5-7 presents the plausible pathway of SMX oxidation in the presence of chloride ions at an initial concentration of 200 mg/L. A substantially lower number of compounds is detected and identified under these conditions. This observation is attributed to the increased oxidative strength of the system at higher chloride concentrations; consequently, the lifetime of by-products is shortened, and their detection becomes more challenging. The four main transformation pathways are discussed below.

(i) *Chlorination.* In addition to the previously detected compounds **P287** and **P128**, new chlorinated moieties are formed. In particular, chlorination of the aniline-sulfonyl product originating from S-N bond cleavage leads to the formation of **P140** and **P182**. The latter exhibits a pronounced increase in relative peak intensity, suggesting that this transformation route becomes predominant under these conditions. Chlorination of the second S-N cleavage product, **P98** (which is not directly detected at this chloride concentration), results in the formation of **P132**.

(ii) *Sulfonyl/sulfonamide disruption*. In this experiment, products of direct S-N cleavage are not detected. However, the identification of their chlorinated derivatives (**P140**, **P182**, and **P132**) confirms that S-N bond cleavage occurs and supports the conclusions of DFT calculations indicating that the S-N bond in the SMX molecule is the most susceptible to cleavage [35]. The second most labile bond is S-C, and accumulation of the corresponding product **P178** is observed, similarly to the case at lower chloride concentrations, indicating that this pathway remains dominant. No desulfonation products are detected under these conditions.

(iii) *Oxidative functionalization.* Only one oxidative functionalization product, **P283**, is detected at 200 mg/L Cl^-. This observation is attributed to the high concentration of reactive chlorine species, which is assumed to suppress the activity of other reactive oxygen species formed in the system. Due to the radical nature of these species, reaction rates between RCS and ROS are expected to be higher than those between ROS and organic molecules. As a result, ROS are likely consumed by RCS before reacting with SMX or its transformation products.

(iv) *Coupling reactions and dimerization.* In contrast to the system containing 20 mg/L Cl^-, high-molecular-mass coupling products (e.g., **P347**) are no longer dominant at 200 mg/L Cl^-, which is consistent with the suppression of radical coupling under strongly chlorinating conditions. In a detailed literature study [34], dimeric and polymeric products are reported to be detectable but represent only a minor pathway when excess chlorine promotes rapid formation of quinone-imine-type products (e.g., P140) and extensive bond cleavage reactions. Mechanistically, elevated RCS levels shorten the lifetime of aminophenol-/phenoxy-type intermediates through fast N-chlorination, oxidation, and fragmentation, thereby reducing the probability of bimolecular coupling.

At an initial chloride concentration of 200 mg/L, complete SMX removal (100%) is achieved within 1 h. The presence of chloride ions also promotes more extensive mineralization and suppresses coupling reactions. However, it leads to the formation of a limited number of chlorinated by-products, which may potentially increase the toxicity of the treated sample.

5.4.4. Plausible pathway of SMX oxidation in the presence of 600 mg/L Cl^- ions

Figure 5-8 is shown to illustrate the plausible pathway of SMX oxidation in the presence of chloride ions at an initial concentration of 600 mg/L. Trends identified under the previous conditions (20 and 200 mg/L Cl^-) are further intensified. Accordingly, only seven degradation by-products are detected, which is attributed to the short lifetime of intermediates under highly oxidative conditions.

(i) *Chlorination*. Notably, with the further increase in Cl^- concentration, fewer chlorinated by-products are detected. This outcome is attributed to their faster oxidation under strongly oxidative conditions.

(ii) *Sulfonyl/sulfonamide disruption.* The detection of **P132** and **P178** is regarded as indirect evidence that S-N and S-C cleavage is occurring in the system.

(iii) *Oxidative functionalization.* At 600 mg/L Cl^-, the availability of ROS is considered to remain strongly limited, similarly to the case at 200 mg/L Cl^-. Importantly, in multiple oxidation steps, reactive chlorine species are assumed to act as oxidants and are effectively consumed (i.e., reduced) and converted back to Cl^-, while oxygen functionality is introduced into the organic products (e.g., quinone/quinone-imine-type structures). For example, the oxidation of halides by HOCl is accompanied by Cl^- formation, which illustrates that chlorine-driven oxidation can proceed without chlorine being retained in the organic molecule [27]. In agreement with the SMX chlorination literature, excess chlorine is reported to drive the aromatic amine functionality toward strongly oxidized quinone/quinone-imine-type products [34]. As a result, only a limited set of stable deep-oxidation products associated with the aniline ring is expected to persist and accumulate; **P283** is therefore interpreted as a marker of this aniline-centered oxidation branch.

(iv) *Coupling reactions and dimerization.* o coupling products with molecular masses above 300 Da are observed under these conditions.

In the presence of 600 mg/L chloride ions, 100% SMX removal is achieved within 30 min. The increased oxidative strength of the system is further evidenced by near-complete mineralization (as indicated by an almost flat final chromatogram) and by the short lifetime of intermediates (as reflected by the smaller number of detectable by-products).

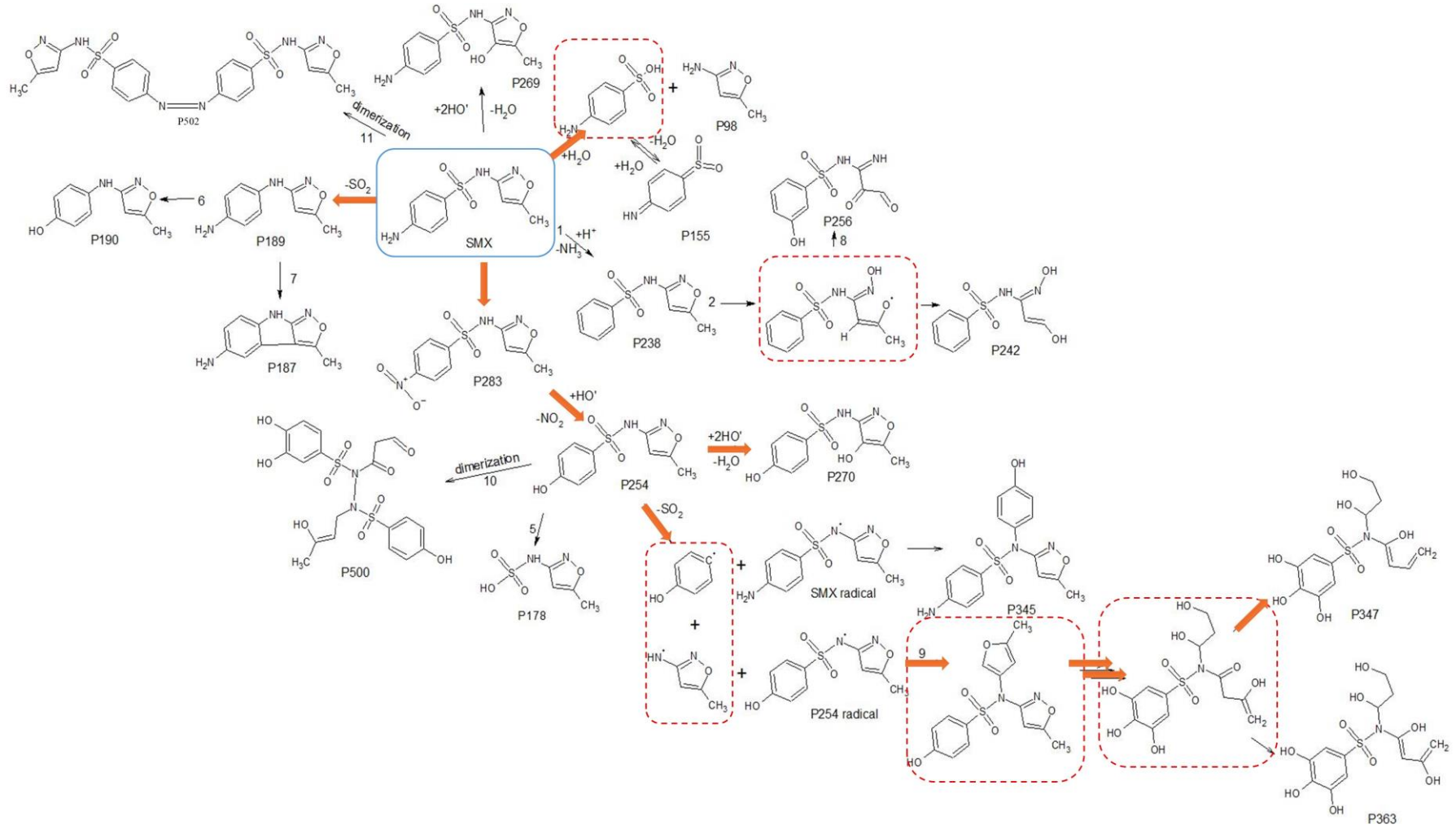

Figure 5-6 The proposed pathway of photoelectrochemical degradation of SMX in the absence of Cl^- ions with the most possible compounds detected by HPLC-MS spectroscopy or predicted theoretically (in red dashed frames). The blue frame highlights initial compound – SMX. Orange arrows show the most probable oxidation routs.

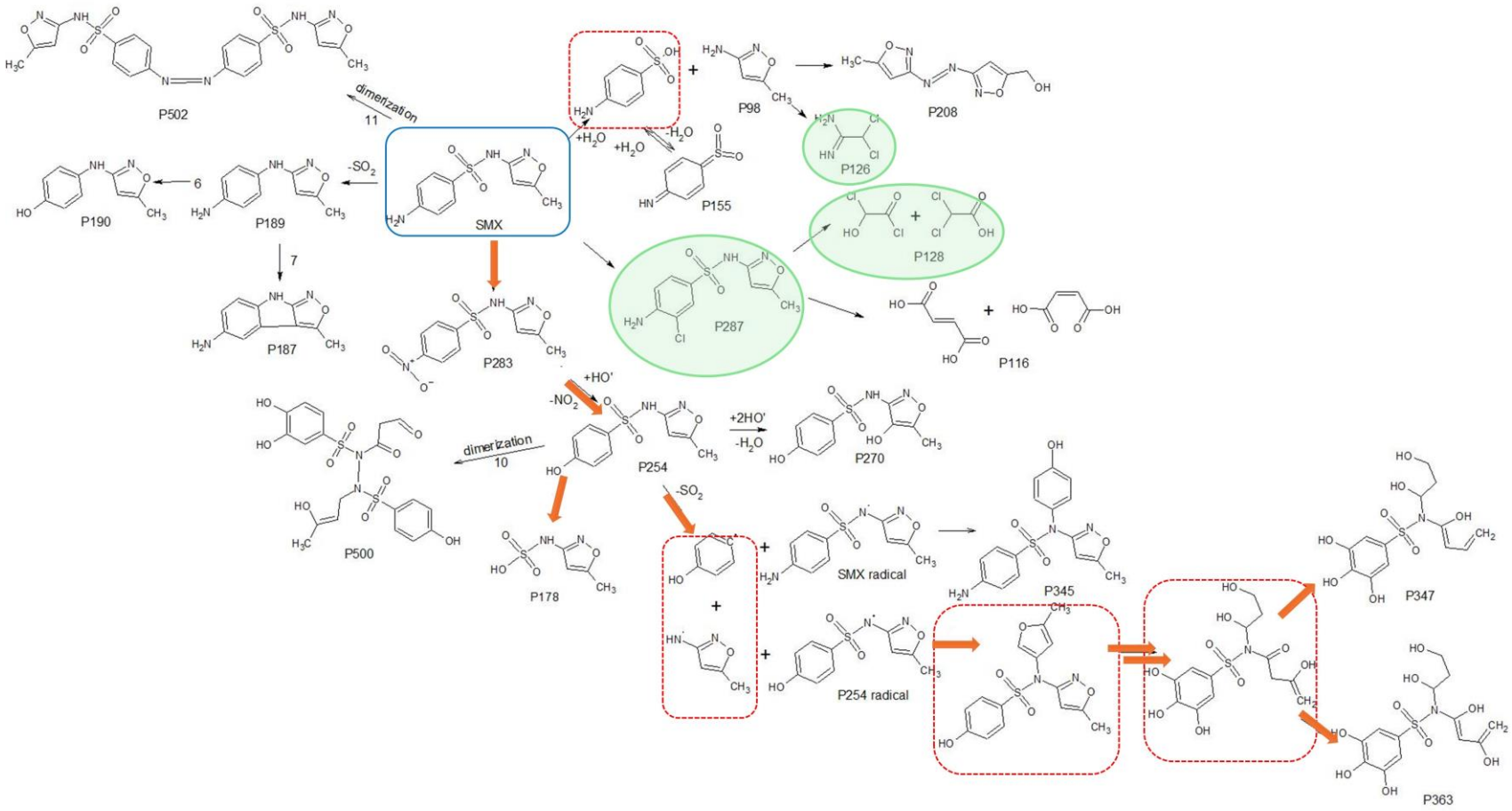

Figure 5-7 The proposed pathway of photoelectrochemical degradation of SMX in the presence of Cl^- ions (initial concentration 20 mg/L) with the most possible compounds detected by HPLS-MS spectroscopy or predicted theoretically (in red dashed frames). The blue frame highlights initial compound – SMX. Orange arrows show the most probable oxidation routs. In green bubbles chlorinated compounds are marked.

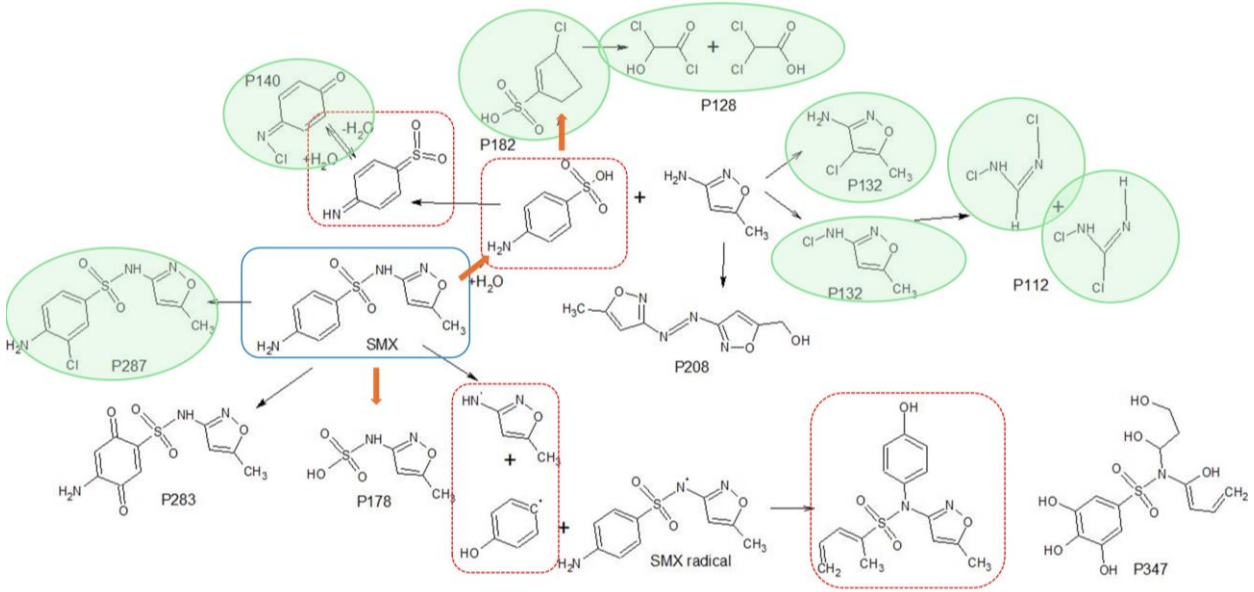

Figure 5-8 The proposed pathway of photoelectrochemical degradation of SMX in the presence of Cl^- ions (initial concentration 200 mg/L) with the most possible compounds detected by HPLS-MS spectroscopy or predicted theoretically (in red dashed frames). The blue frame highlights initial compound – SMX. Orange arrows show the most probable oxidation routs. In green bubbles chlorinated compounds are marked.

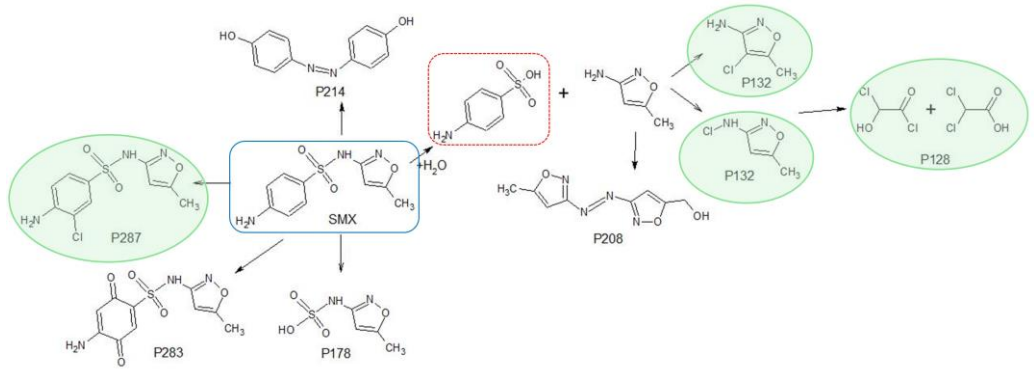

Figure 5-9 The proposed pathway of photoelectrochemical degradation of SMX in the presence of Cl^- ions (initial concentration 600 mg/L) with the most possible compounds detected by HPLS-MS spectroscopy or predicted theoretically (in red dashed frames). The blue frame highlights initial compound – SMX. Orange arrows show the most probable oxidation routs. In green bubbles chlorinated compounds are marked.

5.4.5. Summary

- Plausible SMX oxidation pathways at different chloride concentrations are found to be in good agreement with the literature on SMX degradation. Previous findings are thereby supported, according to which S-N and S-C bonds are the most susceptible to cleavage, and such bond opening is observed under all oxidative conditions, both in mild oxidative environments in the absence of chloride ions and in highly oxidative systems with an initial Cl^- concentration of 600 mg/L.
- Coupling reactions and dimerization, which are considered typical for SMX oxidation under mild conditions, are enhanced in the presence of low chloride concentrations due to an increased formation rate and higher abundance of aminophenol-/phenoxy-type radical intermediates which are building blocks for these reactions. However, at higher chloride concentrations, these reactions are suppressed because the lifetime of these intermediates is reduced, which leads to a lower probability of coupling.
- Owing to the high reactivity of both reactive oxygen species (ROS) and reactive chlorine species (RCS), reaction rates between these species are generally much higher than those between ROS and organic compounds. Consequently, ROS are scavenged by RCS, and, at high RCS concentrations, ROS activity is inhibited.
- The oxidative strength of the photoelectrocatalytic system employing $BiVO_4$ in the absence of chloride ions is insufficient for benzene-ring opening, and a satisfactory SMX degradation rate and complete mineralization are therefore not achieved. Upon chloride addition, the oxidative strength of the system is markedly increased, and both the degradation rate and the degree of mineralization are improved. However, this improvement is accompanied by the formation of a large number of chlorinated by-products, including highly toxic HAAs. As a result, an increase in the toxicity of the treated water is potentially induced.

5.5. INFLUENCE OF CHLORIDE IONS PRESENCE ON ECOTOXICITY OF TREATED WATER

Acute toxicity for fresh water and sea water ecosystems were evaluated with Spirotox and Microtox tests, respectively. The toxicity is estimated using two main metrics: percent of toxic effect caused by C_1 concentration of the sample (PE) and the concentration caused 50% of the toxic effect (EC50). Therefore, the higher PE and lower EC50, the more toxic sample is.

As expected, sulfate, chlorate and perchlorate are non-toxic in both tests up to 1000 mg/L, while hypochlorite is very toxic having the EC50=0.06 mg/L for Spirotox and EC50=0.15 mg/L for Microtox. These results are in good agreement with Table 5-2.

Because of bacteriostatic nature of SMX (i.e. this antibiotic does not kill bacteria but prevents their population grow), its solution with initial concentration of 20 mg/L does not exhibit an acute toxicity and shows no toxic effect in both tests [29].

The photoelectrocatalysis of 600 mg/L Cl^- solution in the absence of SMX drastically increases its toxicity (Table 5-2), probably due to the formation of chlorite and hypochlorite species. Despite their high

oxidative activity, ClO^- and ClO_2^- remain stable over the duration of the experiment, leading to their gradual accumulation in the solution. Consequently, an increase in toxicity is observed over time.

It is interesting to notice that the photoelectrocatalysis of 1000 mg/L SO_4^{2-} ions also induces toxicity (Table 5-2). This increase is slight in the case of marine microorganisms and more pronounced in the case of fresh water organisms. However, this increase in toxicity is smaller than in the case when Cl^- ions are present in the initial solution.

Table 5-2 Photoelectrocatalysis of the solutions of 600 mg/L Cl^- and 1000 mg/L SO_4 without addition of SMX.

600 mg/L Cl^- no SMX	***Microtox***		***Spirotox***	
	PE (C1=74%)	**EC50**	**PE (C1=100%)**	**EC50**
0 min	-	Not toxic	60%	94%
10 min	78%	18.2%	100%	16.6%
60 min	66%	7.2%	100%	4.5%
1000 mg/L SO_4^{2-} no SMX	***Microtox***		***Spirotox***	
	PE (C1=74%)	**EC50**	**PE (C1=100%)**	**EC50**
0 min	17.5%	Not toxic	0%	Not toxic
20 min	28.9%	-	75%	53.0%
180 min	29.7%	-	100%	70.7%

Table 5-3 presents the results of toxicity evaluation during photoelectrocatalytic degradation of SMX in water matrix containing different initial concentration of chloride ions (0, 20, 200, 600 mg/L of Cl^- ions). The increase of toxicity is notable in all cases. In all cases, both when chlorides were present and when they were absent in the initial solution, the presence of SMX led to a stronger increase in toxicity over time compared to the control tests without SMX. This can be explained by the formation of toxic oxidation by-products of SMX, which possess higher toxicity than the parent compound. Nevertheless, in the absence of chlorides, a significantly lower toxic effect is observed even after longer treatment times.

Interestingly, with an increase in the initial chloride concentration in the solution, the toxicity of the final sample (t = 120 min) decreases. This is most likely since a stronger oxidative environment promotes more complete mineralization, leading to the degradation of the toxic chlorination by-products of SMX as well.

Table 5-3 Photoelectrocatalysis of 20 mg/L SMX without of Cl- ions and with initial concentration of chloride ions 20, 200 and 600 mg/L.

no Cl^-	***Microtox***		***Spirotox***	
	PE (C1=74%)	**EC50**	**PE (C1=100%)**	**EC50**
0 min	14.2%	Not toxic	0%	Not toxic
20 min	53.0%	62.4%	0%	Not toxic
180 min	72.3%	36.6%	100%	70.7%
20 mg/L Cl^-	***Microtox***		***Spirotox***	
	PE (C1=74%)	**EC50**	**PE (C1=100%)**	**EC50**
0 min	1.0%	Not toxic	0%	Not toxic
10 min	86.8%	17.7%	100%	35.4%
120 min	81.8%	8.8%	100%	17.7%
200 mg/L Cl^-	**Microtox**		**Spirotox**	
	PE (C1=74%)	**EC50**	**PE (C1=100%)**	**EC50**
0 min	19%	Not toxic	90%	25%
120 min	92%	1.14%	100%	2.57%
600 mg/L Cl^-	***Microtox***		***Spirotox***	
	PE (C1=74%)	**EC50**	**PE (C1=100%)**	**EC50**
0 min	26%	Not toxic	100%	55%
10 min	100%	0.82%	100%	1.41%
120 min	100%	9.71%	100%	2.00%

5.6. CONCLUSIONS

- The presence of chloride ions in solution accelerates the oxidation of pharmaceutical pollutants, (sulfamethoxazole in this study), due to the formation of reactive chlorine species. An increase in the initial chloride concentration results in a higher degradation rate; however, this effect is limited. At low chloride concentrations (20 mg/L in this study), the influence is minor, while further increases above a threshold value (600 mg/L in this study) do not lead to additional enhancement of the degradation rate.

- Monitoring pollutant degradation using UV-vis spectroscopy may lead to an underestimation of the degradation rate, as oxidation by-products can absorb at the same wavelength as the parent compound, thereby increasing the measured absorbance at the characteristic wavelength.

- In the absence of chloride ions, and under oxidation conditions involving only reactive oxygen species and photogenerated holes, SMX does not undergo significant aromatic ring opening within 2 h of the experiment. This observation is consistent with the generally low degradation efficiency of $BiVO_4$ alone. In contrast, the presence of chloride ions promotes aromatic ring opening, with the extent of ring cleavage increasing with chloride concentration. At the highest studied chloride concentration, the highest mineralization is achieved.

- The presence of chloride ions alters the oxidation pathway of SMX due to: (i) the introduction of additional oxidative species, leading to the formation of chlorinated by-products; (ii) a decrease in the availability of ROS for the reaction with organic compounds as a result of their consumption in reactions with chloride ions and reactive chlorine species; and (iii) a reduction in the lifetime of intermediate by-products, which prevents their coupling and dimerization. The oxidation pathway does not change linearly with increasing chloride concentration; therefore, different chloride levels influence the SMX degradation mechanism and the composition of the treated effluent differently. Nevertheless, under all investigated oxidative conditions, the chemical bonds of SMX molecule what are the most susceptible to cleavage are open first, thereby defining common and invariant reaction features.

- In the presence of chloride ions, chlorinated by-products, including highly toxic halogenated acetic acids, are formed. At the highest initial chloride concentration (600 mg/L), a lower concentration of these toxic compounds is detected in the final solution compared to moderate conditions (200 mg/L), which is attributed to the higher oxidative strength of the system and the further oxidation of these intermediates.

- The presence of chloride ions leads to an increase in the toxicity of treated water samples, in agreement with the detection of chlorinated by-products. Notably, toxic oxidation by-products of SMX that contribute to increased sample toxicity are also formed in the absence of chloride ions.

- Thus, this study demonstrates that the acceleration of pollutant degradation in the chlorination process is accompanied by an increase in the toxicity of treated water due to the formation of toxic chlorinated by-products. Consequently, comprehensive monitoring of oxidation intermediates and the toxicity of the final effluent is essential when chlorine-mediated oxidation processes are applied.

REFERENCES

1. Chloride in Natural Continental Water. A Review. U. S. Geol. Surv. Water-Supply 1981, Paper 2176.
2. Water-Quality Characteristics for Selected Sites within the Milwaukee Metropolitan Sewerage District Planning Area, Wisconsin. Sci. Investig. Rep. 2007-5084, U. S. Dep. Inter. Geol. Surv. 2005.
3. Cano, A.; Barrera, C.; Cotillas, S.; Llanos, J.; Cañizares, P.; Rodrigo, M.A. Use of DiaCell Modules for the Electro-Disinfection of Secondary-Treated Wastewater with Diamond Anodes. Chem. Eng. J. 2016, 306, 433–440, doi:10.1016/j.cej.2016.07.090.
4. Sánchez-Carretero, A.; Sáez, C.; Cañizares, P.; Rodrigo, M.A. Electrochemical Production of Perchlorates Using Conductive Diamond Electrolyses. Chem. Eng. J. 2011, 166, 710–714, doi:10.1016/j.cej.2010.11.037.
5. Azizi, O.; Hubler, D.; Schrader, G.; Farrell, J.; Chaplin, B.P. Mechanism of Perchlorate Formation on Boron-Doped Diamond Film Anodes. Environ. Sci. Technol. 2011, 45, 10582–10590, doi:10.1021/es202534w.
6. Health Implications of Perchlorate Ingestion. Natl. Res. Counc. 2005, doi:10.17226/11202.
7. Plant, R.; Seaboard, E.; Estate, I.; Pluakdaeng, T.; Pluakdaeng, A.; Word, S.; Statements, H. Safety Data Sheet Sodium Hypochlorite 10 %. EcoLAB 2024.
8. Ton, S.; Chang, S.; Hsu, L.; Wang, M.; Wang, K. Evaluation of Acute Toxicity and Teratogenic Effects of Disinfectants by Daphnia Magna Embryo Assay. Environ. Pollut. 2012, 168, 54–61, doi:10.1016/j.envpol.2012.04.008.
9. (WHO), W.H.O. Chlorine in Drinking-Water Background Document for Development of WHO Guidelines for Drinking-Water Quality. Heal. criteria Support Inf. 1996.
10. Safety Data Sheet Sodium Chlorite Solution (>=25%). REDOX 2020.
11. (WHO), W.H.O. Guidelines for Drinking-Water Quality: Fourth Edition Incorporating the First and Second Agenda. 2022.
12. Ward, T.J.; Boeri, R.L. Acute Flow-Through Toxicity of Sodium Chlorate to the Daphnid, Daphnia Magna 1991, 418871–04.
13. EXTOXNET. Extension Toxicology Network Available online: https://extoxnet.orst.edu/pips/sodiumch.htm?utm_source=chatgpt.com.
14. Sodium Perchlorate Solution Safety Data Sheet. 2016.
15. (WHO), W.H.O. Perchlorate in Drinking-Water Background Document for Development of WHO Guidelines for Drinking-Water Quality. 2016.
16. Liu, J.; Wu, H.; Sun, J.; Li, S.; Hassani, A.; Zhou, M. Non-TiO2-Based Photoanodes for Photoelectrocatalytic Wastewater Treatment: Electrode Synthesis, Evaluation, and Characterization.

EES Catal. 2025, 3, 921–942, doi:10.1039/d5ey00068h.

17. Li, X.; Kan, M.; Wang, T.; Qin, Z.; Zhang, T.; Qian, X.; Kuwahara, Y.; Mori, K.; Yamashita, H.; Zhao, Y. The ClO · Generation and Chlorate Suppression in Photoelectrochemical Reactive Chlorine Species Systems on BiVO4 Photoanodes. Appl. Catal. B Environ. 2021, 296, 120387, doi:10.1016/j.apcatb.2021.120387.
18. Dong, T.; Zheng, Z.; Man, J.H.K.; Lo, I.M.C. A Low-Carbon-Emission Photoelectrochemical System Using Ov-Fe2O3@BiVO4 Photoanode for Integrated Multiple Pollutant Removal and Energy Harvesting from Real Saline Sewage. Chem. Eng. J. 2024, 499, 155840, doi:10.1016/j.cej.2024.155840.
19. Gao, X.; Wang, P.; Che, H.; Liu, W.; Ao, Y. Breaking Interfacial Charge Transfer Barrier by Sulfite for Efficient Pollutants Degradation: A Case of BiVO4. npj Clean Waters 2023, 6, 42, doi:10.1038/s41545-023-00254-w.
20. Bennani, Y.; Perez-Rodriguez, P.; Alani, M.J.; Smith, W.A.; Rietveld, L.C.; Zeman, M.; Smets, A.H.M. Photoelectrocatalytic Oxidation of Phenol for Water Treatment Using a BiVO4 Thin-Film Photoanode. J. Mater. Res. 2016, 31, 2627–2639, doi:10.1557/jmr.2016.290.
21. Davies, K.R.; Allan, M.G.; Nagarajan, S.; Townsend, R.; Asokan, V.; Watson, T.; Godfrey, A.R.; Maroto-valer, M.M.; Kuehnel, M.F. Photoelectrocatalytic Surfactant Pollutant Degradation and Simultaneous Green Hydrogen Generation. Ind. Eng. Chem. Res. 2023, 62, 19084–19094, doi:10.1021/acs.iecr.3c00840.
22. Sun, X.; Su, T.; Cui, X.; Yu, H.; Lu, Y.; Qin, W.; Huo, M. A TiO2 Nanotube Photoanode (Blue TiO2 Nanotube/RuO2/BiVO4) for Efficient Acetaminophen Degradation and Nitrogen Removal. J. Water Process Eng. 2024, 60, 105230, doi:10.1016/j.jwpe.2024.105230.
23. Cao, D.; Wang, Y.; Qiao, M.; Zhao, X. Enhanced Photoelectrocatalytic Degradation of Norfloxacin by an Ag3PO4/BiVO4 Electrode with Low Bias. J. Catal. 2018, 360, 240–249, doi:10.1016/j.jcat.2018.01.017.
24. Petruleviciene, M.; Savickaja, I.; Griguceviciene, A.; Naujokaitis, A.; Ramanauskas, R.; Juodkazyte, J. Optimization of BiVO4 Coatings for High Yield Photoelectrochemical Production of Reactive Chlorine Species. J. Photochem. Photobiol. A Chem. 2023, 443, 114842, doi:10.1016/j.jphotochem.2023.114842.
25. Panizza, M.; Cerisola, G. Direct and Mediated Anodic Oxidation of Organic Pollutants. Chem. Rev. 2009, 109, 6541–6569, doi:10.1021/cr9001319.
26. Sirés, I.; Brillas, E.; Oturan, M.A.; Rodrigo, M.A.; Panizza, M. Electrochemical Advanced Oxidation Processes: Today and Tomorrow. A Review. Environ. Sci. Pollut. Res. 2014, 21, 8336–8367, doi:10.1007/s11356-014-2783-1.

27. Lou, X.; Liu, Z.; Fang, C.; Tang, Y.; Guan, J.; Guo, Y.; Zhang, X.; Shi, Y.; Huang, D.; Cai, Y. Fate of Sulfamethoxazole and Potential Formation of Haloacetic Acids during Chlorine Disinfection Process in Aquaculture Water. Environ. Res. 2022, 204, 111958, doi:10.1016/j.envres.2021.111958.
28. Dong, H.; Qiang, Z.; Hu, J.; Qu, J. Degradation of Chloramphenicol by UV/Chlorine Treatment: Kinetics, Mechanism and Enhanced Formation of Halonitromethanes. Water Res. 2017, 121, 178–185, doi:10.1016/j.watres.2017.05.030.
29. Nałecz-Jawecki, G.; Wawryniuk, M.; Kopczynska, W.; Giebułtowicz, J. Individual and Simultaneous Photodegradation of Trimethoprim and Sulfamethoxazole Assessed with the Microbial Assay for Risk Assessment. Molecules 2025, 30, 1907.
30. Thomas, M.; Nałęcz-Jawecki, G.; Giebułtowicz, J.; Drzewicz, P. Degradation of Oxytetracycline by Ferrate (VI): Treatment Optimization, UHPLC-MS/MS and Toxicological Studies of the Degradation Products, and Impact of Urea and Creatinine on the Removal. Chem. Eng. J. 2024, 485, 149802, doi:10.1016/j.cej.2024.149802.
31. Water Quality-Determination of the Inhibitory Effect of Water Samples on Te Light Emission of Vibrio Fischeri (Luminescent Bacteria Test)- Part 3: Method Using Freeze-Dried Bacteria. ISO (International Organ. Stand.
32. Natelcz-Jawecki, G. Spirotox Test – Spirostomum Ambiguum Acute Toxicity Test. In Small-scale Freshwater Toxicity investigations; 2005; p. 563 ISBN 9781402031199.
33. Hübner, U.; Spahr, S.; Lutze, H.; Wieland, A.; Rüting, S.; Gernjak, W.; Wenk, J. Advanced Oxidation Processes for Water and Wastewater Treatment – Guidance for Systematic Future Research. Heliyon 2024, 10, e30402, doi:10.1016/j.heliyon.2024.e30402.
34. Dodd, M.C.; Huang, C.-H. Transformation of the Antibacterial Agent Sulfamethoxazole in Reactions with Chlorine: Kinetics , Mechanisms , and Pathways. Environ. Sci. Technol. 2004, 38, 5607–5615.
35. Wang, X.; Li, J.; Zhang, C.; Xue, M.; Xie, H. Degradation Products and Transformation Pathways of Sulfamethoxazole Chlorination Disinfection By-Products in Constructed Wetlands. Environ. Res. 2024, 249, 118343, doi:10.1016/j.envres.2024.118343.
36. Su, Q.; Huang, S.; Zhang, H.; Wei, Z.; Ng, H.Y. Abiotic Transformations of Sulfamethoxazole by Hydroxylamine, Nitrite and Nitric Oxide during Wastewater Treatment. Kinetics, Mechanisms and PH Effects. J. Hazard. Mater. 2023, 444, 130328, doi:10.1016/j.jhazmat.2022.130328.
37. Scholes, R.C.; Prasse, C.; Sedlak, D.L. The Role of Reactive Nitrogen Species in Sensitized Photolysis of Wastewater-Derived Trace Organic Contaminants. Environ. Sci. Technol. 2019, 53, 6483–6491, doi:10.1021/acs.est.9b01386.
38. Mao, Y.; Liang, J.; Ji, F.; Dong, H.; Jiang, L.; Shen, Q.; Zhang, Q. Accelerated Degradation of Pharmaceuticals by Ferrous Ion/Chlorine Process: Roles of Fe(IV) and Reactive Chlorine Species. Sci.

Total Environ. 2021, 787, 147584, doi:10.1016/j.scitotenv.2021.147584.

39. Queral-Beltran, A.; Marín-García, M.; Lacorte, S.; Tauler, R. UV-Vis Absorption Spectrophotometry and LC-DAD-MS-ESI(+)-ESI(−) Coupled to Chemometrics Analysis of the Monitoring of Sulfamethoxazole Degradation by Chlorination, Photodegradation, and Chlorination/Photodegradation. Anal. Chim. Acta 2023, 1276, doi:10.1016/j.aca.2023.341563.
40. Brillas, E. A Review on the Degradation of Organic Pollutants in Waters by UV Photoelectro-Fenton and Solar Photoelectro-Fenton. J. Braz. Chem. Soc. 2014, 25, 393–417, doi:10.5935/0103-5053.20130257.
41. Wang, M.; Helbling, D.E. A Non-Target Approach to Identify Disinfection Byproducts of Structurally Similar Sulfonamide Antibiotics. Water Res. 2016, 102, 241–251, doi:10.1016/j.watres.2016.06.042.

CONCLUSIONS

6.1. SUMMARY OF OBTAINED RESULTS

This thesis is focused on the investigation of the applicability of photoelectrocatalysis for the degradation of pharmaceutical pollutants. The main conclusions of the work are summarized below.

According to photoelectrochemical theory, photoelectrocatalysis is expected to be more energetically efficient than conventional electrochemical oxidation. This advantage arises from the fact that, in photoelectrochemical systems, the semiconductor band positions determine the thermodynamic feasibility of the electrochemical reaction and are not influenced by the applied potential. Therefore, when the band positions of the photoelectrode are already suitable for the target reaction, the external bias is required only to enhance charge carrier separation. However, the literature contains very limited experimentally measured energy consumption data to confirm this assumption (**Chapter 1**). In this work, the energy consumption during photoelectrocatalytic degradation of pharmaceuticals is experimentally determined and values below 3 kWh/m^3 are demonstrated (most frequently around 1.5 kWh/m^3 for bare $BiVO_4$). These values are highly competitive compared to conventional electrochemical oxidation processes, for which energy consumptions of tens to hundreds of kWh/m^3 are typically reported (**Chapters 3, 4,** and **5**).

Before the experimental evaluation a theoretical analysis of replacing the kinetically sluggish and thermodynamically demanding water oxidation reaction with kinetically and thermodynamically more favorable organic oxidation reactions is performed for the first time, to the best of current knowledge (**Chapter 2**). It is shown that, for the same photoanode, substitution of water oxidation with an organic oxidation reaction characterized by a lower ΔG leads to a decrease in solar conversion efficiency. Nevertheless, higher product fluxes may be achieved due to the faster kinetics of organic oxidation. Alternatively, organic oxidation can be performed on photoanodes with narrower band gaps than those required for water splitting, enabling absorption of a larger fraction of the solar spectrum, higher photocurrents, and consequently higher product fluxes. It is also demonstrated that the formation of hydroxyl radicals, which are among the most important reactive oxygen species, is unlikely at high fluxes in unbiased photocatalytic systems, as large band gaps (>3.2 eV) are required. Such band gaps correspond to photoanodes absorbing less than 2.8% of the solar spectrum. In contrast, the formation of chlorite and hypochlorite is possible with high maximum solar conversion efficiencies (up to 22.7% in an idealized case) on photoanodes with band gaps above 2 eV, which allows efficient solar light absorption. Furthermore, the formation of superoxide anion radicals is thermodynamically feasible on all semiconductors with appropriate conduction band position due to the low energy requirements of this reaction.

Although $BiVO_4$ possesses several favorable properties for application as a photoanode in organic pollutant oxidation – such as suitable band positions for oxidation of a wide range of organic compounds, absorption of approximately 18% of the standard solar spectrum (corresponding to a maximum theoretical photocurrent of 7.5 mA/cm^2), a wide stability window ($5 < pH < 11$), and practical advantages including simple synthesis, low cost, and non-toxicity – the degradation efficiencies obtained for a broad range of organic pollutants are not competitive (all below 60% after 2 hours of treatment) (**Chapters 3** and **4**). The

performance of $BiVO_4$ toward organic oxidation is primarily limited by its low catalytic activity, pronounced surface recombination, and photocorrosion processes (**Chapter 3**).

It is further demonstrated that photoelectrocatalytic oxidation of organic compounds follows the same general trends as conventional electrochemical oxidation of low-concentration organic pollutants: higher applied currents result in increased degradation rates, while current efficiencies decrease simultaneously (**Chapter 3**).

To enhance hole extraction from $BiVO_4$ and thereby slow down photocorrosion and potentially suppress surface recombination, surface modification with β-FeOOH is implemented (**Chapter 4**). Electrochemical characterization reveals a significant increase in photocurrent (by a factor of 1.5-2) and improved stability, confirming suppression of photocorrosion. However, this modification results in decrease of degradation rates for all three investigated pharmaceuticals and increased energy consumption. Further analysis shows that the observed increase in current and stability originates not from reduced charge recombination, but from enhanced catalysis of the water oxidation reaction. As a consequence, a larger fraction of the photogenerated charge is consumed by water oxidation, making organic oxidation less competitive. Based on these findings, β-FeOOH is concluded to be an unsuitable cocatalyst for improving the performance of $BiVO_4$ toward organic pollutant oxidation.

These results demonstrate that photocurrent alone cannot be considered a universal metric for photoelectrode selection or for predicting organic pollutant degradation performance. Particular attention must be paid to the competition between water splitting and the target organic oxidation reaction. Moreover, electrochemical characterization performed in the absence of organic compounds cannot reliably predict degradation efficiency. Catalyst design must therefore carefully avoid lowering kinetic barriers for parasitic reactions, which may increase photocurrent while simultaneously reducing organic degradation rates.

Finally, $BiVO_4$ is shown to be a potentially suitable photoanode for chlorination-based oxidation processes. The band positions of $BiVO_4$ enable oxidation of chloride ions to reactive chlorine species (chlorite and hypochlorite), which can subsequently oxidize organic pollutants. The absence or low amounts of hydroxyl radicals limits the formation of undesired chlorates and perchlorates. In addition, the band gap of $BiVO_4$ is close to the optimal value corresponding to maximum theoretical solar conversion efficiencies for Cl_2/ClO^- and Cl_2/ClO_2^- redox couples. Experimentally, the degradation rate of sulfamethoxazole is significantly enhanced in the presence of chloride ions, increasing from 90% after 120 minutes without chloride to 100% within 60 and 20 minutes at initial chloride concentrations of 200 mg/L and 600 mg/L, respectively. However, this acceleration is accompanied by the formation of chlorinated by-products, leading to increased ecotoxicity of the treated solutions. Furthermore, it is demonstrated for the first time that chloride concentration has a non-linear effect on the oxidation pathway of sulfamethoxazole, resulting in distinct degradation mechanisms at different chloride levels (**Chapter 5**).

6.2. FUTURE WORK AND PERSPECTIVES

The results presented in this thesis reveal several open questions and methodological challenges that extend beyond the specific systems investigated and are relevant for the further development of photoelectrochemical water treatment. In particular, they highlight unresolved issues related to reaction

mechanisms and process limitations at low pollutant concentrations. Addressing these challenges will require advances not only in photoelectrode materials, but also in experimental methodologies and system-level design.

The important question that must be clarified to assess the applicability of $BiVO_4$ for water treatment is whether hydroxyl radicals are actually formed on $BiVO_4$ and what the mechanism of their formation is. The current literature on this issue is highly controversial: some studies report the formation and experimental detection of hydroxyl radicals, while others report opposite results. This discrepancy primarily arises from differences in the determination of the $BiVO_4$ band edge positions. Some authors report valence band potentials more negative than the potential required for hydroxyl radical formation (determined by Mott-Schottky analysis [1–5] measurement of photocurrent onset potential [1,4] or XPS [1]) and therefore postulate that $HO^{\bullet}$ formation on the $BiVO_4$ surface is thermodynamically forbidden. In contrast, other studies report valence band positions more positive than the $HO^{\bullet}/H_2O$ redox potential (XPS [6], DFT [6,7], Mott-Schottky [8,9]) and thus conclude that hydroxyl radical formation is thermodynamically feasible.

Experimental detection of hydroxyl radicals in $BiVO_4$-based systems also yields contradictory results. Spin-trapping electron spin-resonance experiments in several studies reveal the absence of hydroxyl radicals in the vicinity of the $BiVO_4$ surface [10], whereas other reports claim their formation [11]. Similarly, probe-molecule experiments aimed at detecting hydroxyl radicals show inconsistent outcomes: some studies detect the formation of 2-hydroxyterephthalic acid and thus infer the presence of hydroxyl radicals [7,12], while others do not observe such products [4,13]. In some cases, the detected hydroxyl radicals are attributed to indirect mechanisms, such as formation via superoxide anion radicals [4] or involvement of the substrate itself [3].

Within the scope of this thesis, a definitive conclusion regarding hydroxyl radical formation on $BiVO_4$ could not be reached. However, the results obtained highlight the methodological limitations of commonly used detection approaches and emphasize the need for carefully designed experiments in divided electrochemical cells. An attempt to conduct such experiments using separated anodic and cathodic compartments connected by a salt bridge was made in the framework of this thesis; however, chloride ion leakage from the salt bridge interfered with terephthalic acid oxidation, resulting in non-interpretable data. An alternative approach would involve performing the experiments in a configuration where the anodic and cathodic chambers are separated by a cation-exchange membrane.

The results of this study indicate that $BiVO_4$ is a potentially suitable photoanode for chlorination-based oxidation processes. Therefore, more extensive studies are needed to assess its applicability in real water treatment systems, particularly with a focus on monitoring toxic chlorinated by-products and establishing mitigation approaches to avoid their formation.

An ideal photoelectrochemical system for the removal of low-concentration organic pollutants should ensure high current efficiencies, high degradation rates, and long-term photoelectrode stability. To meet these requirements, the following conditions must be satisfied:

(i) high Faradaic efficiency;
(ii) fast kinetics of the target pollutant oxidation reaction;

(iii) a balance between the flux of organic pollutants to the semiconductor surface and the flux of photogenerated holes.

Condition (i) can be fulfilled if parasitic reactions, such as water oxidation and oxidation or reduction of lattice species, are suppressed. This may be achieved thermodynamically by selecting a photoanode with a valence band position more negative than 1.23 V vs. SHE and its decomposition potential, and kinetically if the target organic oxidation reaction is sufficiently fast to efficiently scavenge photogenerated holes and outcompete parasitic reactions.

To satisfy condition (ii), a fundamental decision must be made regarding the dominant oxidation pathway: hydroxyl radical-mediated oxidation or direct heterogeneous oxidation of organic pollutants by photogenerated holes. Promotion of hydroxyl radical formation does not allow water oxidation to be avoided and may lead to the formation of undesirable chlorates and perchlorates. In addition, hydroxyl radical formation requires high energy input and can therefore only be achieved either on wide-bandgap semiconductors with low light absorption and low product flux, or on narrower-bandgap semiconductors under high external bias, resulting in increased electrical energy consumption. Nevertheless, hydroxyl radical oxidation is non-selective and enables degradation of a wide range of organic pollutants without the need for catalyst design for each contaminant or continuous monitoring of wastewater composition. In contrast, direct oxidation by holes may offer improved selectivity but requires tailored catalyst design. Enhanced selectivity can be advantageous, as real wastewaters typically contain high concentrations of non-toxic, biodegradable organic matter compared to ones of contaminants of emerging concern, and, thus, they may be preferentially oxidized. Moreover, the energy input for oxidation of organic compounds by holes is lower than the one, requiring for water oxidation or hydroxyl radicals formation, therefore, this reaction can be employed in systems with semiconductor of narrow bandgap which are not able to drive water splitting reaction ensuring the high flux of product, low electric energy consumption and high faradic efficiency (for example, crystalline silicon [14]). In all cases, rapid removal of photogenerated holes from the semiconductor surface by the target reaction is essential, as it suppresses parasitic reactions and mitigates photocorrosion.

For low-concentration pollutants, fast oxidation kinetics may lead to rapid transition of the process into the mass-transport-limited regime, resulting in violation of condition (iii). This may cause accumulation of holes at the semiconductor surface, increased photocorrosion, and additional energy losses due to charge recombination. A similar limitation is well known and extensively studied in conventional electrochemical oxidation, where insufficient mass transport reduces energy efficiency. Several strategies have been proposed and implemented to overcome this limitation, including continuous adjustment of the applied current to the limiting currentv[15], enhancement of fluid dynamics to improve mass transport [16], and implementation of preconcentration step [17].

In photoelectrocatalytic systems, photoelectrodes effectively act as current sources, with the current primarily determined by light irradiation. As a result, direct and rational current adjustment is less straightforward. Furthermore, at pollutant concentrations in the μg/L range, the limiting current typically lies in the range of tens of $\mu A/cm^2$. Adjusting the operating current to such low values would result in very low system productivity.

Experience from electrochemical oxidation indicates that diffusion limitations associated with low pollutant concentrations can be most effectively suppressed in flow-through reactor configurations employing porous anodes. (the order of magnitude of mass transport coefficients are 10^{-6} m/s in mixed tanks, 10^{-5} m/s in flow-by cells and 10^{-4} m/s in flow-through cells) [17]. However, fabrication of photoactive electrodes in porous configuration remains challenging due to the nature of commonly used substrates (ofthen coated glass), which are difficult to render porous.

Implementation of a preconcentration step therefore appears to be the most realistic approach for photoelectrocatalytic treatment of low-concentration pollutants. Nevertheless, this strategy inevitably leads to additional capital and operational costs.

In conclusion, the results of this thesis suggest that, at the current stage of development, photoelectrocatalysis is only conditionally applicable to the removal of low-concentration persistent organic pollutants. In addition, the results highlight fundamental differences between radical-based and non-radical oxidation strategies and emphasize that their benefits and drawbacks are strongly application-dependent. Nevertheless, the underlying theoretical concepts of photoelectrocatalytic process for water purification are highly promising. Realizing this potential will depend on integrated evaluation and transparent reporting of photoelectrocatalytic systems, with particular attention to reaction pathways, energy efficiency, mass transport, and long-term stability under realistic process constraints.

REFERENCES

1. Nurain, S.; Nasir, S.; Aida, N.; Azri, M.; Firdaus, M.; Noh, M.; Affiqah, N.; Asri, M.; Teridi, M. Direct Extrapolation Techniques on the Energy Band Diagram of BiVO 4 Thin Films. Phys. B Phys. Condens. Matter 2021, 604, 412719, doi:10.1016/j.physb.2020.412719.
2. Fuentes-Camargo, I.; Carrera-Crespo, J.E.; Vazquez-Arenas, J.; Romero-Ibarra, I.; Rodriguez, J.L.; Lartundo-Rojas, L.; Cardoso-Mart, J. Pulse-Plating Electrodeposition of Metallic Bi in an Organic-Free Aqueous Electrolyte and Its Conversion into BiVO4 To Improve Photoelectrochemical Activity toward Pollutant Degradation under Visible Light. J. Phys. Chem. C 2020, 124, 1421–1428, doi:10.1021/acs.jpcc.9b09898.
3. Carrera-Crespo, J.E.; Fuentes-Camargo, I.; Palma-Goyes, R.E.; García-Perez, U.M.; Vazquez-Arenas, J.; Chairez, I.; Poznyak, T.; AChairez, I.; Poznyak, T. Unrevealing the Effect of Transparent Fluorine-Doped Tin Oxide (FTO) Substrate and Irradiance Configuration to Unmask the Activity Of. Mater. Sci. Semicond. Process. 2021, 128, 105717.
4. Łęcki, T.; Hamad, H.; Zarębska, K.; Wierzyńska, E.; Skompska, M. Mechanistic Insight into Photochemical and Photoelectrochemical Degradation of Organic Pollutants with the Use of BiVO4 and BiVO4/Co-Pi. Electrochim. Acta 2022, 434, doi:10.1016/j.electacta.2022.141292.
5. Kim, T.W.; Choi, K.S. Nanoporous BiVO4 Photoanodes with Dual-Layer Oxygen Evolution Catalysts for Solar Water Splitting. Science (80-.). 2014, 343, 990–995, doi:10.1126/science.1246913.
6. Cooper, J.K.; Gul, S.; Toma, F.M.; Chen, L.; Glans, P.A.; Guo, J.; Ager, J.W.; Yano, J.; Sharp, I.D. Electronic Structure of Monoclinic BiVO4. Chem. Mater. 2014, 26, 5365–5373, doi:10.1021/cm5025074.
7. Wang, Y.; Tan, G.; Liu, T.; Su, Y.; Ren, H.; Zhang, X.; Xia, A. Photocatalytic Properties of the g-C3N4/{010} Facets BiVO4 Interface Z-Scheme Photocatalysts Induced by BiVO4 Surface Heterojunction. Appl. Catal. B Environ. 2018, 234, 37–49, doi:10.1016/j.apcatb.2018.04.026.
8. Zhang, Y.; Wang, D.; Zhang, X.; Chen, Y.; Kong, L.; Chen, P.; Wang, Y.; Wang, C.; Wang, L.; Liu, Y. Enhanced Photoelectrochemical Performance of Nanoporous BiVO4 Photoanode by Combining Surface Deposited Cobalt-Phosphate with Hydrogenation Treatment. Electrochim. Acta 2016, 195, 51–58, doi:10.1016/j.electacta.2016.02.137.
9. Li, T.; He, J.; Peça, B.; Berlinguette, C.P. Curing BiVO4 Photoanodes with Ultraviolet Light Enhances Photoelectrocatalysis Angewandte. Angew. Chemie - Int. Ed. 2016, 55, 1769–1772, doi:10.1002/anie.201509567.
10. Saison, T.; Chemin, N.; Chane, C.; Brezova, V.; Jolivet, J. New Insights Into BiVO4 Properties as Visible Light Photocatalyst. J. Phys. Chem. C 2015, 119, 12967–12977, doi:10.1021/acs.jpcc.5b01468.

11. Wang, K.; Liang, G.; Waqas, M.; Yang, B.; Xiao, K.; Zhu, C. Peroxymonosulfate Enhanced Photoelectrocatalytic Degradation of Ofloxacin Using an Easily Coated Cathode. Sep. Purif. Technol. 2020, 236, 116301, doi:10.1016/j.seppur.2019.116301.
12. Kohtani, S.; Yoshida, K.; Maekawa, T.; Iwase, A. Loading Effects of Silver Oxides upon Generation of Reactive Oxygen Species in Semiconductor Photocatalysis. Phys. Chem. Chem. Phys. 2008, 10, 2986–2992, doi:10.1039/b719913a.
13. Cheng, B.; Wang, W.; Shi, L.; Zhang, J.; Ran, J.; Yu, H. One-Pot Template-Free Hydrothermal Synthesis of Monoclinic BiVO4 Hollow Microspheres and Their Enhanced Visible-Light Photocatalytic Activity. Int. J. Photoenergy 2012, 2012, 28–33, doi:10.1155/2012/797968.
14. Ko, M.; Lee, M.; Kim, T.; Jin, W.; Jang, W.; Hwang, S.W.; Kim, H.; Kwak, J.H.; Cho, S.; Seo, K.; et al. Coupling Furfural Oxidation for Bias-Free Hydrogen Production Using Crystalline Silicon Photoelectrodes. Nat. Commun. 2025, 16, 2701, doi:10.1038/s41467-025-58000-4.
15. Panizza, M.; Kapalka, A.; Comninellis, C. Oxidation of Organic Pollutants on BDD Anodes Using Modulated Current Electrolysis. Electrochim. Acta 2008, 53, 2289–2295, doi:10.1016/j.electacta.2007.09.044.
16. Trellu, C.; Chaplin, B.P.; Coetsier, C.; Esmilaire, R.; Cerneaux, S.; Causserand, C.; Cretin, M. Electro-Oxidation of Organic Pollutants by Reactive Electrochemical Membranes. Chemosphere 2018, 208, 159–175, doi:10.1016/j.chemosphere.2018.05.026.
17. Ganiyu, S.O.; Hullebusch, E.D. Van; Cretin, M.; Esposito, G.; Oturan, M.A. Coupling of Membrane Filtration and Advanced Oxidation Processes for Removal of Pharmaceutical Residues : A Critical Review. Sep. Purif. Technol. 2015, 156, 891–914, doi:10.1016/j.seppur.2015.09.059.

LIST OF ACRONYMS

AMR	Antimicrobial Resistance
AOPs	Advanced Oxidation Processes
APEB	Absorbed Photon Energy Balance
BDD	Boron-doped diamond
CBZ	Carbamazepine
CECs	Contaminants of Emerging Concern
CV	Cyclic Voltammetry
DFT	Density Functional Theory
DMPO	5,5-Dimethyl-1-pyrroline N-oxide
DMSO	Dimethyl sulfoxide
DOS	Density of States
DSA	Dimensionally Stable Anode
EAOPs	Electrochemical Advanced Oxidation Processes
ECSA	Electrochemically active Surface Area
EDS	Energy Dispersive electron Spectroscopy
EIS	Electrochemical Impedance Spectroscopy
EPR	Electron Paramagnetic Resonance
ERE	External Radiative Efficiency
FTO	Fluorine-doped Tin Oxide
HAAs	Halogenated acetic acids
HMF	2,5-hydroxymethylfurfural
HPLC-DAD	High Performance Liquid Chromatography with Diode Array Detector
HPLC-MS	High Performance Liquid Chromatography – Mass Spectrometry
ITO	Indium Tin Oxide
LHE	Light Harvesting Efficiency
LSV	Linear Sweep Voltammetry
MDB	Modified Detailed Balance
NHE	Normal Hydrogen Electrode
OCP	Open Circuit Potential
OER	Oxygen Evolution Reaction
PC	Photocatalysis
PCT	Paracetamol

PEC	Photoelectrocatalysis
PFAS	Per- and polyfluoroalkyl substances
PL	Photoluminescence
RCS	Reactive Chlorine Species
RHE	Reversible Hydrogen Electrode
ROS	Reactive Oxygen Species
SCE	Solar Conversion Efficiency
SEM	Scanning Electron Microscopy
SHE	Standard Hydrogen Electrode
SILAR	Successive Ionic Layer Adsorption and Reaction
SMX	Sulfamethoxazole
STH	Solar-to-Hydrogen conversion efficiency
TA	Terephthalic acid
TA-OH	2-Hydroxyterephthalic acid
TBA	Tert-butyl alcohol
TOC	Total Organic Carbon
US EPA	United States Environmental Protection Agency
WHO	World Health Organization
XPS	X-ray Photoelectron Spectroscopy
XRD	X-ray Diffraction

LIST OF FIGURES

LIST OF TABLES

PUBLICATIONS

"Mathematical modeling of the anodic oxidation of organic pollutants:a review", Ekaterina Skolotneva, Andrey Kislyi, Anastasiya Klevtsova, Davide Clematis, Semyon Mareev, Marco Panizza. *Environmental Chemistry Letters*. – 2024. – V. 22. – p. 1521-1561. DOI: 10.1007/s10311-023-01693-0

"Impact of catalyst, chelating agent and light irradiation on Electro-Fenton performance under not optimal conditions", Davide Clematis, Ekaterina Skolotneva, Davide Cademartori, Marco Panizza. *Chemosphere.* – 2023. – V. 344. – 140480. DOI: 10.1016/j.chemosphere.2023.140408

"Highly efficient anodic oxidation of organic pollutants using Ti_4O_7 particle anode: Experimental and theoretical study of the operational and structural parameters influence", Andrey Kyslyi, Vera Guliaeva , Yuriy Prokhorov, Victoria Plis, Iliya Moroz, Anastasiya Klevtsova, Ekaterina Skolotneva, Davide Clematis, Marco Panizza, Semyon Mareev. *Separation and Purification Technology*. – 2025. – V. 359. – 130820. DOI: 10.1016/j.seppur.2024.130820

"Theoretical analysis of efficiency in photoelectrochemical cells employing organic oxidation as an anodic half-reaction", Ekaterina Skolotneva, Davide Clematis, Marco Panizza. *Under submission*

"Photocurrent Is Not a Reliable Predictor of Pollutant Degradation: A Case Study of β-FeOOH-Modified $BiVO_4$", Ekaterina Skolotneva, Davide Clematis, Marco Panizza, Magdalena Skompska. *Under submission*

"Influence of Chloride Ion Concentration on Sulfamethoxazole Photoelectrochemical Oxidation on $BiVO_4$: Nonlinear Pathway Shifts and the Trade-Off Between Faster Degradation and Increased Toxicity", Ekaterina Skolotneva, Grzegorz Nałecz-Jawecki, Joanna Giebułtowicz, Davide Clematis, Marco Panizza, Magdalena Skompska. *Under submission*

CONGRESS CONTRIBUTIONS

"Critical Analysis on Efficiency in Photoelectrochemical System for Organic Oxidation", Ekaterina Skolotneva, Davide Clematis, Marco Panizza – Days of Italian Electrochemistry, 15-19 September 2025, **Oral presentation**.

"Effect of β-FeOOH modification on the photocatalytic and photoelectrocatalytic performance of $BiVO_4$ in the degradation of pharmaceuticals", Ekaterina Skolotneva, Davide Clematis, Marco Panizza, Magdalena Skompska – 9 International Conference on Semiconductor Photochemisrty, 8-12 September 2025, **Flash oral and poster presentation**.